UNIVERSITY OF BIRMINGHAM

NANOTEXTURISATION OF GOLD SURFACES AND ITS APPLICATION TO NEURAL IMPLANTS

by

ANDREAS FROMMHOLD

A thesis submitted to

The University of Birmingham

for the degree of

DOCTOR OF PHILOSOPHY

Department of Electrical, Electronics and Computer Engineering

College of Engineering and Physical Science

The University of Birmingham

August 2010

ABSTRACT

The objective of this thesis was to develop a new methodology for the improvement of the interface properties of gold electrodes for neural implants. The goal was to increase the surface area without a change in geometrical footprint of the electrode with nanofabrication tools. A process has been created that uses Nanosphere Lithography for masking layer deposition and anisotropic etching to fabricate nanostructures on the surface of the electrodes. Optimisation of the process parameters led to a control of structure morphology, which allowed the production of a variety of shapes. The effect of the nanostructures on the interface was investigated by impedance spectroscopy and additional electrochemical measurements. It showed that the interface impedance could be decreased significantly by up to a magnitude of scale with the surface modifications. In addition a porous columnar form of sputtered gold was found that also showed decreased interface impedance compared to standard gold films. A set of neural implants was designed and fabricated to test the effect of surface modification in-vitro in neurological tissue. The surface modification process was successfully implemented in the device fabrication. The in-vitro assessment showed signs of improved interface performance compared to unmodified devices.

ACKNOWLEDGEMENTS

I am grateful to my supervisor, Dr Edward Tarte, for granting me the opportunity to explore a field so completely new to me. As we were both from different backgrounds it was a journey we have taken together to learn many new things. His constant encouragement has been a great help for me and the freedom to explore my own interests was much appreciated.

As the topic was very multidisciplinary there is a large number of people who have contributed to this thesis in small and not so small ways. I would like to thank Professor Richard Palmer and his Nano-scale Physics group for providing access to their clean room facilities for the development of the nanostructure process. I am thankful to Dr Alex Robinson for introducing me to nanosphere lithography and for useful advice for improvements of my own work as well as taking a general interest in my progress. Further I would like to acknowledge Mi Yeon Song and Jedsada Manyam who did their best to keep the clean room equipment running and provided an enjoyable atmosphere to work in. Thanks are also owed to Ahmed Abdela and Tianluo Pan for help with the STM characterisation.

From the School of Chemistry I would like to thank Professor Trevor Rayment and Dr Sarah Horswell for useful discussion about electrochemical measurements and use of the potentiostat equipment and electrochemical cell. Dr Richard Wiltshire took it upon himself to introduce me to the use of the potentiostat and helped with first measurements.

I am indebted to Professor John Jefferys for the opportunity to test the devices in-vitro in slice cultures in his laboratory as well as offering his perspective on the implant devices from a clinical perspective. My gratitude is also extended to Dr Premek Jiruska who sacrificed his spare time to perform the in-vitro testing.

I would also like to thank the project manager, Dr Stephanie Lacour, and the other team members of the microchannel interface project for support and general advice.

I am thankful to Dr Zoe Barber and Dr Kartik Senapati from the Department of Materials Science and Metallurgy of the University of Cambridge, who produced the titanium nitride samples.

My thanks go to Dr Maolong Ke for gold deposition with his evaporator and and discussions of other issues of microfabrication. I would also like to acknowledge Donna Holdom, the group's technician, who maintains the clean room and lab facilities and also provided training on the equipment. I am thankful to my fellow students Samia Benmerah and Richard Barrett for sharing their expertise on polyimide and providing samples to me.

Finally I would like to thank my parents for their support and for having me let my way. My wife Lucy endured my grumpiness when research was not going well and suffered the loneliness of endless evenings and weekends without complaint while I was busy working in the lab. Without her care, support and love it would have been a much harder experience and I am forever grateful to her.

CONTENTS

LIST OF FIGURES

LIST OF TABLES

1. INTRODUCTION

Neural implants in general are briefly discussed as an introduction to the topic. Some examples are given and major types described. The requirements for neural interfaces are then elaborated in detail and the aim of this thesis is presented. At the end the further content of the individual chapters is outlined.

1.1 Motivation

In simplest terms a neural interface is a device that allows connection to and communication with the nervous system using electronics so that the electrical signals in the brain or nerves coordinating all actions in living beings can be extracted and analysed. Also the opposite is possible, where an external signal is applied through the neural interface to elicit a biological reaction. A pacemaker for example would not be possible without such an interface that monitors the electrical activity in the heart's muscle cells for a regular beat to decide and provide the electrical shocks when necessary. The aim of most applications is to help people with severe impediments to reach a better quality of life. One experiment demonstrated the ability to control an artificial limb with thoughts alone [1]. The participant was completely paralysed from the neck downwards because of a spinal cord injury so that he had no control over his body. Through a neural interface in the form of a silicon chip implanted into the surface of his brain he could open and close an artificial hand hooked up to the implant just by thinking of the corresponding action. Recently researchers presented results that went even further with a test person connected to a robotic hand for a whole month [2]. The subject lost his forearm during an accident. The neural interface was formed by electrodes implanted in the nerves of the remains of the arm. It allowed the patient to perform complex movements like moving fingers

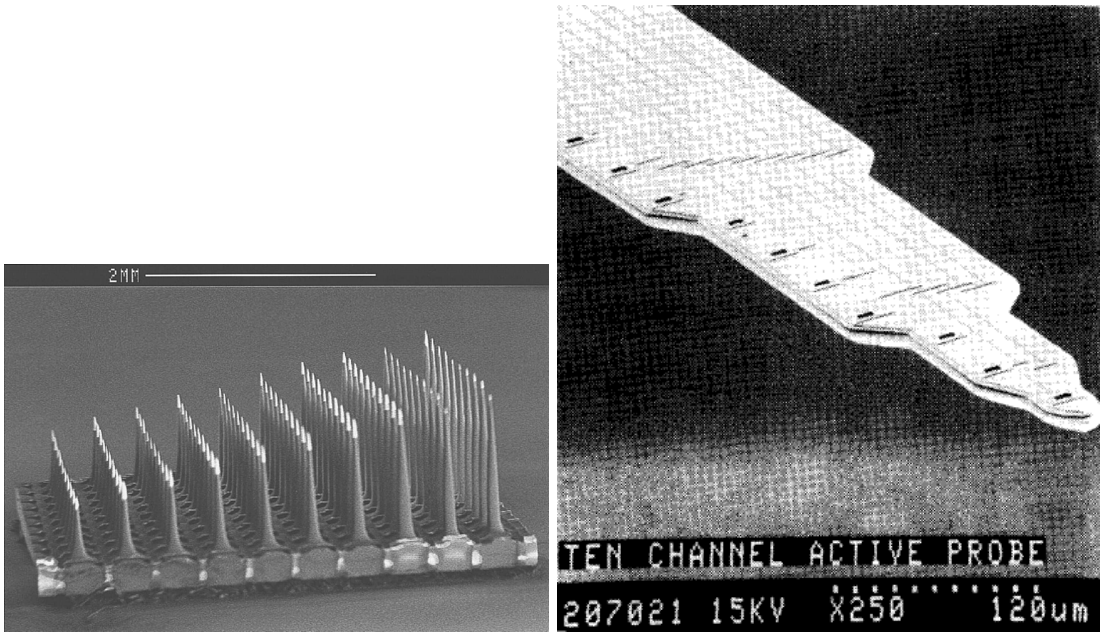

(a) (b)

Fig. 1.1: SEM images of (a) Utah array [4] and (b) Michigan probe [5]

independently or grabbing objects. Through sensors build into the prosthesis he also received tactile feedback from the hand giving him even a sense of touch. Neural interfaces can also help people with visual impairment. A microchip with 1,500 photo detectors has been successfully connected to the optic nerve to give test subjects who suffer from retinitis pigmentosa a rudimentary vision that lets them distinguish basic shapes and navigate in a room [3]. Auditory implants can also be included into the group of neural interfaces when directly connected to the nerve to restore impaired hearing function. Another application is deep brain stimulation where electrodes are implanted into the brain to stimulate parts of the brain in order to treat the effects of Parkinson disease or prevent epileptic seizures. All these examples illustrate the significance of the field of neural interfaces and the impact it can have on the quality of daily live.

The two most established neural interfaces in the field are the Utah array [6] and the Michigan probe [7]. Both are designed for direct implantation into the brain. The Utah device consists of an array of spikes that have been machined from silicon chips. Metal electrodes are created by coating the spikes and insulating them except for the spike tips. It is a three-dimensional

device, which is pressed on to the surface of the brain for implantation. The depth of implantation is controlled by the height of the spikes. Different heights have been implemented in the same device to map different layers of the brain simultaneously. The Utah array was used for example in the experiment with the paralysed person described earlier. The Michigan Probe on the other hand is a planar device fabricated on the surface of silicon wafers. The electrode sites are distributed along a shaft so that there are multiple electrodes on a single shaft. The shaft possesses a sharp tip so that it can be inserted with the shaft axis perpendicular to the tissue surface. By combining many shafts it is possible to form 2- and 3-d multi-arrays to achieve geometries similar to the Utah array. The advantages of microfabricated electrodes are the excellent control over device shape and size, which allows accurate positioning of the electrodes with minimal damage to the tissue. For this reason they are often used in electrophysiology research to study the function of the brain. For peripheral neural interfaces there is no common widely used device. Instead a variety of designs exist based on cuffs [8] that wrap a flexible sheet containing planar electrodes around a nerve fibre or sieve-type devices [9], which are thin sheets of materials with holes machined into it. The electrodes are metal rings deposited around each hole. The injured nerves then grow through the holes making contact with the electrodes in the process.

In an collaborative effort, to which the work in this thesis contributed, between the group at the Electrical Engineering Department of the University of Birmingham, Kings College London, Nanoscience, Material Science and the Brain Repair Centre all of the University of Cambridge a novel peripheral neural interface, the polyimide microchannel device, was developed [10]. Its aim was to realise the project's concept of axonal amplifiers [11] to boost recording signal quality of peripheral neural implants. The device is made from polyimide making it flexible but rigid enough without the need for further mechanical support. The structure consists of a thin polymer sheet with long channels on top. At the bottom of the channels are electrodes for recording and stimulation. The channels are necessary to guide the axons and ensure intimate contact to the electrodes. The device's most important feature is the creation of a real three-dimensional device by a two-dimensional fabrication process and subsequent rolling of

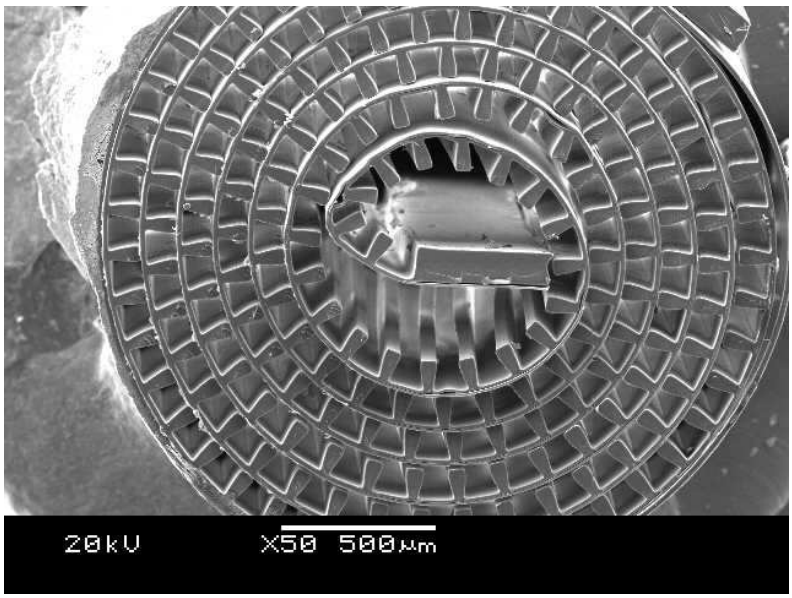

Fig. 1.2: Cross section of the rolled up polyimide device

the polyimide sheet (figure 1.2). The fabrication process is discussed in more detail in chapter 7. The task of the research documented in this thesis was to explore ways to improve the performance of the channel electrodes of this device.

1.2 Objectives and goals

When designing such a long term implant one often encounters the dilemma of selectivity versus sensitivity. The aim is to decrease the interface impedance in order to improve signal-to-noise ratio associated with thermal noise (eq. (1.1)). Small electrodes are desired to address as few neurones as possible per electrode site in order to achieve high selectivity in conjunction with high density integration of as many electrodes as possible. Smaller electrode areas result in larger electrochemical interface impedance because the two quantities are inversely proportional. But higher impedance is associated with larger thermal noise leading to a loss in sensitivity. The amplitude of the extracellular signals of interest are of small values in the microvolt range and can be interfered by the noise. As a numerical example, for a typical electrode impedance of 2 MΩ the thermal noise amplitude would be 3.3 μV for a 100 kHz bandwidth of

interest for neurological signals and increases steadily with shrinking electrode sizes to 10.51 μV for 20 MΩ. Typical neurological signal amplitudes can be below 10 μV so that the thermal noise becomes as serious problem for signal detection when the impedance increases until they fail to record any viable signals. In this way selectivity and sensitivity are competing agendas. When increasing the sensitivity of any given device, at the same time the geometric footprint of the electrode has to be maintained in order to preserve its selectivity to ensure that each electrode is connected to a limited neurone population in order to distinguish between different neurones. One solution is to increase the surface area locally through nanostructures to create a three-dimensional surface while the actual electrode size is not changed.

$$V_{noise} = \sqrt{4\,k_B\,T\,Z\,\Delta f} \tag{1.1}$$

Since the device should remain in the body for a long period of time, only biocompatible materials that do not corrode or release toxic substances can be used for the implant. There are two possible routes for improving the interface characteristics. Either the application of a coating with an intrinsic highly porous structure or the mechanical structuring of the electrode material can be used to enhance the surface area without enlarging the actual electrode size. Both have their advantages and disadvantages, which are reviewed in more detail in chapter 4. A suitable method needs to be mechanically stable in order to withstand wear through natural microscopic movements that are experienced by the devices during their life-cycle upon implantation into the neural tissue. It should not degrade over time to preserve device characteristics during use so that function is maintained. The electrode material for the neural implants in this work was gold. It is a biocompatible material with excellent chemical stability. The decision was made to directly shape the surface rather then apply coatings since the target device is rolled for assembly. This exerts additional mechanical stresses on the device, which increases the risk of delamination of coatings. A new process was developed to pattern the surface of gold electrodes with various kinds of nanostructures. The ability to use these structures to engineer the interface impedance was successfully demonstrated.

1.3 Overview of thesis

After the introduction, chapter 2 gives a brief overview of the biological aspects involved in neurological signal formation and conduction to establish an understanding of the requirements for the design of neural implants. The electrochemical aspects of interface formation in neural implants are summarised in chapter 3 to illustrate its importance for device operation. A literature survey of the different methods that have been developed up to date to improve neural electrode performance is presented in chapter 4. In chapter 5 the approach used to improve the interface impedance by increasing the surface area on a nanometre scale is described. The characterisation of the modified surfaces by electrochemical impedance spectroscopy to determine the influence of the surface structure on the interface properties is the subject of chapter 6. The details of the design and fabrication of neural implants for incorporation of nanotexture are given in chapter 7. The implants were used to record neurological signals from slice cultures of rat brains and their performance is analysed in chapter 8 before the final chapter summarises the main results and presents the conclusions.

2. THE ANATOMY OF A NERVE FIBRE

This chapter introduces the underlying biology of the nervous system needed to develop an understanding of the fundamental requirements for the design of neural recording devices and a perception for the environment in which they are to operate. Since all neural devices are made to record from and stimulate populations of neurones, the structure and components of neurones are discussed first, followed by a simple model for the propagation of the electrical signals between cells. In the last section the structural differences between brain and peripheral nerves are detailed. All the information presented here is compiled from [12] and [13] unless referenced otherwise.

2.1 The neurone

In the nervous system there are only two types of cells, glia cells and nerve cells. Glia cells are non-conductive and provide support to the nerve cells. They are a special kind of connective tissue that nourishes and protects the nerve cells. The Neurone Doctrine [14] states that neurones, which is another name for nerve cells, are the basic signalling units in neural tissue. It is estimated that there are about 100 billion (10^{11}) neurones in the human brain. Their task is to transmit and process information within the body by generating and processing electrochemical pulses. There are three different kinds of neurones: sensory, motor and inter-neurones. Sensory neurones are responsible for carrying information from receptors into the nervous system while motor neurones are responsible for controlling muscles and glands. Inter-neurones act as relays and provide pathways for signal distribution either locally or to distant parts of the body.

All of them share common structural features which can be divided into three parts: the soma (cell body), the dendrites and the axon (figure 2.1). The soma contains the nucleus with the DNA

and the cell metabolism needed to maintain their life cycle. Its diameter varies roughly between 10 to 100 μm. The dendrites are short processes emerging from the cell body and developing into a network of fine branches. They are responsible for collecting the signals from other neurones and transferring them to the soma. The axon is a single long fibre also growing out of the cell body. It transmits signals away from the cell body to other neurones or muscles. Many axons possess a Myelin sheath which is formed by Schwann cells in the peripheral nervous system or oligodendrocytes in the central nervous system, which wrap themselves around the axon. This sheath is regularly interrupted by gaps called nodes of Ranvier. This influences the conduction properties since the Myelin has insulating character so that electrical signals jump from gap to gap rather than being conducted continuously speeding up signal conduction. Axons have a diameter between 0.2 and 20 μm and can be up to 2 metres long in human beings. Near their ends axons can branch out to form connections to various targets. In the tips they have pre-synaptic terminals. A nerve pulse reaching this terminal will trigger the release of a chemical transmitter that crosses the synaptic cleft to reach receptors in the post synaptic terminal of the neighbouring cell causing a new nerve pulse in that cell. All neurones are connected this way through what is called a synapse. The post synaptic terminal can be in a muscle fibre causing a muscle to contract or in the dendrites transmitting the signal from one cell to the next.

What allows a neurone to transmit electrical signals is the fact that their cell membrane is excitable. It is made of phospholipid molecules. They possess a phosphoric head that is hydrophilic and a glyceride tail, a fatty acid that is hydrophobic. These polarising properties cause it to assemble in a bilayer configuration. Furthermore ion channels in the form of macro-pores allow the flow of ions like sodium, potassium, chloride and calcium through the membrane, which are dissolved in the liquid inside and outside the cell. These macro-pores are formed by special ion-selective proteins who have variable permeability depending on the voltage across them. The voltage is called the transmembrane voltage and defined as the potential on the inner surface (Φ_i) relative to the potential on the outside membrane surface (Φ_o) in the form of $V_m = \Phi_i - \Phi_o$. Under resting conditions (no nerve signals) a specialised protein serves as a

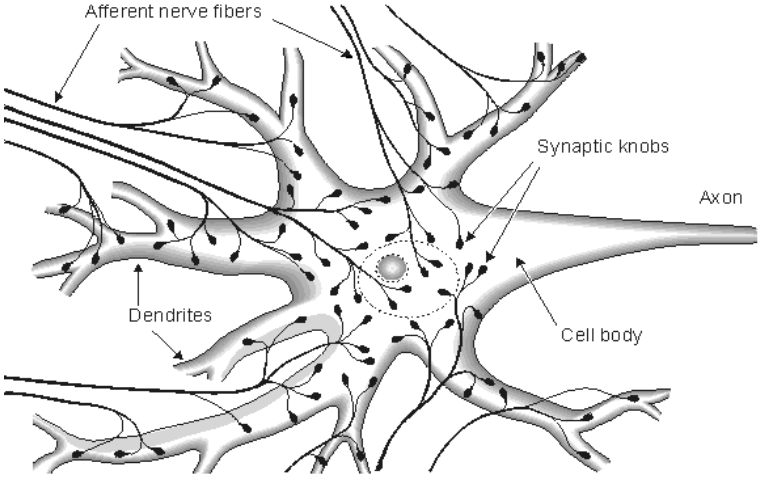

Fig. 2.1: The components of a nerve cell schematic [12]

Sodium (Na) - Potassium (K) pump maintaining a high concentration of sodium outside the cell and a high concentration of potassium inside the cell. Because of the resulting concentration gradients and the selective permeabilities for each ion species there is a voltage of usually about -65 mV across the membrane, which is called the membrane resting potential. The membrane can be stimulated to form a nerve pulse if the transmembrane voltage rises above a certain threshold. This causes the sodium permeability to increase and the sodium to flow into the cell making the inside of the cell more positive. In response the K-ion channels open up and K-ions flow out of the cell membrane returning the potential on the inside to its resting value. The rising and falling potential as a consequence of the ions flows constitutes the nerve pulse. Subsequently the Na-K pump finally restores the initial concentration gradients. During this refractory period the membrane is not able to fire again and becomes insensitive to new stimuli.

The signal is conducted along the membrane because the local nerve pulse also perturbs its nearest neighbourhood causing the same process to be triggered there. So the signal propagation is not a real conduction but the recreation of the pulse over and over again along the membrane. There is no distortion in the signal and all the pulses are identical. Therefore in neural networks information is not encoded in the signal shape but in the frequency of their appearance and the time period between signals. A strong sensational stimulus will cause a greater number of action

potentials with smaller time delay between the pulses than a minor stimulus. There are a couple of important features in this mechanisms. Stimulation can be either excitatory by making the inside of the cell more positive than the outside (depolarisation). It is then easier for the cell to exceed the threshold and hence increases the probability of firing. Or it can be inhibitory by making the inside more negative (hyperpolarisation), which reduces the probability for firing. In this way a nerve cell can be either silenced or activated. Another property of nerve excitation is that it is a so-called all-or-none process. The stimulus is either strong enough to depolarise the cell over the threshold to cause the release of an action potential with a shape independent of how far it crossed the threshold. Or it will be too weak to exceed the limit value and the signal will be non-propagating with the stimulus simply decaying.

The basic chain of events for the cell to release an action potential then summarises as follows. First the dendrites pick up incoming signal pulses via chemical signalling in their synapses. This triggers local signals (1-10 mV) in the dendrites, which then travel to the soma. All incoming signals are integrated there and once a certain threshold is reached, an action potential (~100 mV) is released at the axon hillock to propagate along the axon to the next synapse. There the incoming action potential causes the release of a transmitter to transfer the signal on to the next cell. The action potentials are the part of the signal pathways that neural devices aim to record as they have the biggest amplitudes present, which makes them easier to detect and they are an important part of the signal coordination in nerve cell networks. Additionally axons can regenerate after injury while a damaged cell body will cause cell death. Regenerative devices like the Cambridge implant make use of the axon's ability to regrow in the device design.

2.2 The Hodgkin Huxley membrane model

In the previous section the biological mechanisms for the creation and propagation of nerve signals were introduced. This section will describe a model that incorporates all these mechanisms and can be interpreted as an electrical equivalent circuit. It is an empirical model that was developed by Hodgkin and Huxley [15] out of their experiments on Giant Squid axons. They

chose this particular species because the relatively large size of their axons with a diameter of a few millimetres and centimetre-sized length made it easier to perform the necessary experiments. While the numerical values are determined for the Giant Squid the basic mechanism is present in all neurones, so it can be readily adapted to human neurones. First the conditions for membrane equilibrium have to be established, which sets the value of resting potential, and then the dynamics of the channel mechanism are added.

As a result of the different ion concentrations inside and outside the membrane in conjunction with the ion specific permeability diffusion occurs due to the concentration gradients. As a consequence ions accumulate on the inner and outer surface on the membrane setting up an electric field. An equilibrium is reached when the electrical forces are balanced by the diffusional forces. For the sum of the two currents due to the electrical field described by Maxwell's Law of Electrostatics and diffusion expressed as Fick's Law becoming zero, one arrives at the equation for the Nernst potential, which is the potential due to an ion concentration gradient separated by a semi-permeable membrane, for a specific ion species as

$$V = -\frac{R\,T}{z\,F} ln \frac{c_i}{c_o} \tag{2.1}$$

with R the gas constant, T the absolute temperature, z the valence of the ion species, F the Faraday constant, c_i the concentration inside and c_o outside the membrane. Now the origin of the resting membrane voltage becomes clear. If the ion concentration inside and outside were the same then the resting voltage would be zero. But because the Na-K pump maintains a stable ion concentration gradient, the voltage is different from zero. It should be denoted that the pump consumes energy from the metabolism of the cell. Important to notice is that while the total current is zero, it is actually a steady-state, the diffusional current in one direction being counterbalanced by the electrical current in the opposite direction.

As explained in the previous section, more than one ion species is able to pass through the membrane is found in the vicinity of the membrane. So the picture has to be expanded to the case of multiple permeable ions. The independence principle, formulated by Hodgkin and Huxley in 1952, states that the flux of each ion species is independent of the others since each channel is ion specific. In this case there is an equilibrium potential V_k for each species

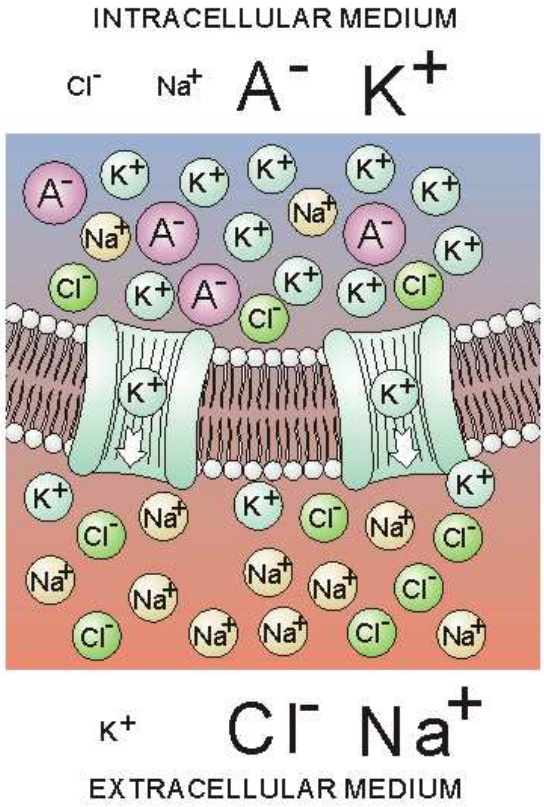

Fig. 2.2: Illustration of the membrane with ion channels. The size of the symbols corresponds to the ion concentration. A^- symbolises large immobile and impermeable molecules that are important for electroneutrality [12]

k as well as the overall membrane potential V_m formed by the sum over all the different ion channels. The driving force for each species is then $V_m - V_k$. Assuming a constant field across the membrane and maintaining that at resting potential the sum of the ion currents from all ion species must be zero the equation for the membrane voltage becomes

$$V_m = -\frac{RT}{F} ln \frac{P_K\, c_{i,K} + P_{Na}\, c_{i,Na} + P_{Cl}\, c_{o,Cl}}{P_K\, c_{o,K} + P_{Na}\, c_{o,Na} + P_{Cl}\, c_{i,Cl}} \tag{2.2}$$

with P_k the membrane permeability of the corresponding k^{th} ion species. This equation is called the Goldman-Hodgkin-Katz equation. It shows that for multiple ion species present the contribution of each species to the resting voltage is weighted by its membrane permeability.

In the next step the dynamics of the ion channels are added to obtain a model describing the constitution of the nerve pulses. The first model to describe these dynamics was formulated by

A.L. Hodgkin and A.F. Huxley in 1952 awarded with the Nobel Prize in 1963. For their experiments they used a technique called voltage clamp that allows one to set any desired value for the membrane voltage and measure the correspondent ion flow for each constituent ion species by chemically blocking the other channels allowing one to study the response of the channels in detail. It is a phenomenological model with a set of equations that allow for theoretical calculations of action potentials. It does not strive to be an accurate picture of the processes occurring in the membrane. Their work is based on the assumption of separated ion-conducting branches called the parallel conductance model. Each of its four components represents a specific ion channel type for sodium, potassium and leakage current from other ion species as well as a capacitive current for the charge separation by the membrane. Each branch is composed of electric circuit components as shown in figure 2.3. The conductances represent the different ion permeabilities of the membrane for each species as

$$G_{Na} = \frac{I_{Na}}{V_m - V_{Na}} \tag{2.3}$$

$$G_K = \frac{I_K}{V_m - V_K} \tag{2.4}$$

$$G_L = \frac{I_L}{V_m - V_L} \tag{2.5}$$

and the voltage sources are the Nernst voltages as defined by the corresponding Nernst equation (2.2). Conductances and currents are defined per unit area as the model represents a small patch of the overall membrane. The sodium and potassium conductances are dependent on time and transmembrane voltage while the leakage conductance is constant. The total membrane current is the sum of the branch currents

$$I_m = C_m \frac{dV_m}{dt} + (V_m - V_{Na})G_{Na} + (V_m - V_K)G_K + (V_m - V_L)G_L \tag{2.6}$$

An expression for the conductivities is needed in order to solve this expression. Hodgkin and Huxley proposed a gating mechanism in the channels to this end. They postulated the presence of ion specific charged particles inside the membrane that do not act as carriers in the ion flow. Instead they allow ion passage through the membrane depending on them occupying specific sites in the membrane. The rate of movement of these particles would then determine the rate

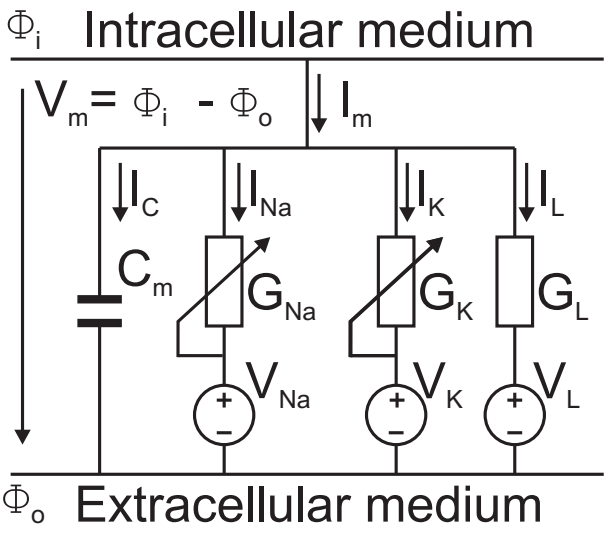

Fig. 2.3: The equivalent circuit of the Hodgkin-Huxley model for a membrane patch [12]

at which the ion conductances approach their maximum values. Hodgkin and Huxley did not explore the nature of these particles and only used them do define the fraction of open to closed channels giving the probabilities to find a certain configuration.

Starting with potassium, they found during their experiments that the time variation of the conductance can be fitted to a fourth-power variable that changes according to first-order kinetics. They then supposed an electrically charged n-particle that controls the potassium channels by being either in open position or closed position and moving between these two states (figure 2.4). The probability to find the particle in the open state is defined as n and the probability for a closed state is $(1-n)$ with $0 \leq n \leq 1$. A change in membrane potential then results in a change of the distribution of the charged particles. Voltage dependent transfer rates α_n for transition from closed to open state and β_n for the reverse case are defined to describe this process. For a given initial n its time evolution is described by a differential equation as

$$\frac{dn}{dt} = \alpha_n(1-n) - \beta_n n \tag{2.7}$$

The dependency of the conductivity on the fourth power suggests that a channel is only open when four n-particles are in the open state. If the probability of any of the particles to be open is not dependent on the other ones then the probability for the channel to be open is n^4. The

Tab. 2.1: Rate transfer coefficients of the Hodgkin Huxley model

$$\alpha_n = \frac{0.1 - 0.01(V_m - V_r)}{e^{1-0.1(V_m-V_r)} - 1} \qquad \alpha_m = \frac{2.5 - 0.1(V_m - V_r)}{e^{2.5-0.1(V_m-V_r)} - 1} \qquad \alpha_h = \frac{0.07}{e^{0.05(V_m-V_r)}}$$

$$\beta_n = \frac{0.125}{e^{0.0125(V_m-V_r)}} \qquad \beta_m = \frac{4}{e^{(V_m-V_r)/18}} \qquad \beta_h = \frac{1}{e^{3-0.1(V_m-V_r)} + 1}$$

potassium conductance per unit area is then the maximum conductance (when all channels were open) multiplied by the number of open channels

$$G_K = G_{K,max} \cdot n^4 \tag{2.8}$$

For sodium the situation is more complex because the rise in conductivity is not maintained but falls off again after a certain time. Therefore in addition to a sodium channel-activating m-particle they also introduced an inactivating h-particle with h the probability that the particle is in a non-inactivating state. Both particles follow first-order kinetics and their time evolution can be described as

$$\frac{dm}{dt} = \alpha_m(1 - m) - \beta_m m \tag{2.9}$$

$$\frac{dh}{dt} = \alpha_n(1 - h) - \beta_h h \tag{2.10}$$

with α and β the corresponding voltage dependent transfer rate coefficients. By fitting the experimental data it was determined that a channel is open when three m-particles occupy open state sites and is not blocked by one h-particle in the inactivating state, so that the sodium conductance then is

$$G_{Na} = G_{Na,max} \cdot m^3 h \tag{2.11}$$

The reason for the pulse-like behaviour is the difference in time constants of the parameters m and h. A short time constant of m causes the channel to open quickly while h has a longer time constant, which results in a delay before the channel closes again. The rate transfer coefficients themselves do not directly depend on time, only on the voltage.

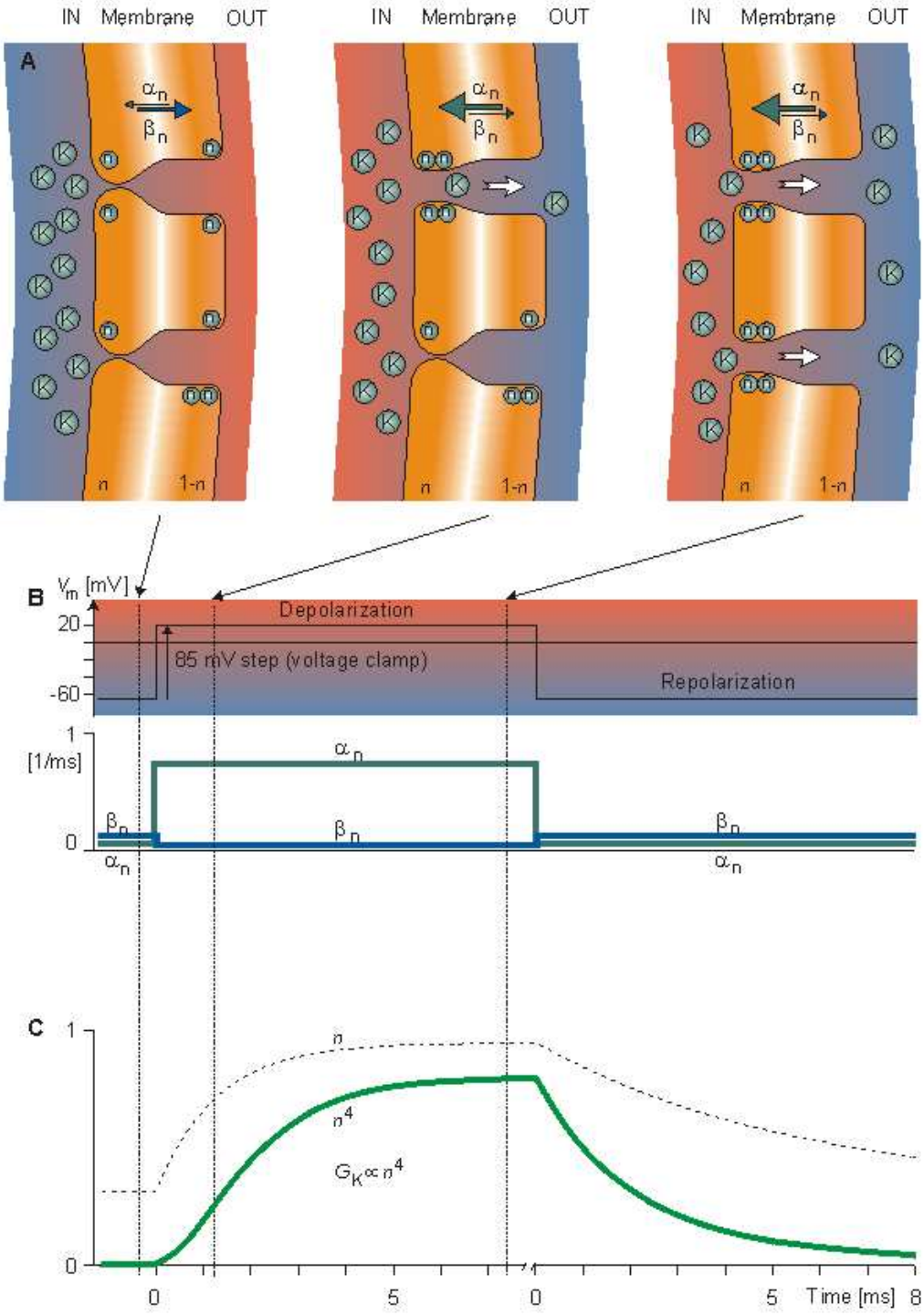

Fig. 2.4: Gating mechanism for the potassium channels with corresponding transfer rate coefficients [12]

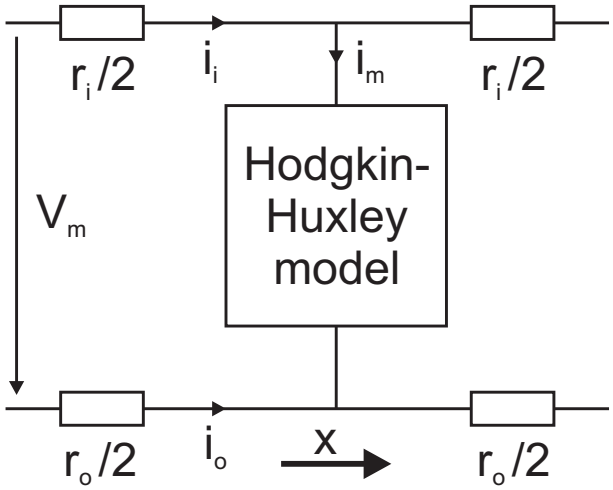

Fig. 2.5: Circuit model for propagating action potential [12]

Hodgkin and Huxley also developed equations describing these voltage dependencies based on their measurements. They are shown in table 2.1 and are only valid for the Giant Squid axon at a temperature of 6.3° C. By choosing values for the constant parameters C_m, $V_r - V_{Na}$, $V_r - V_K$, $V_r - V_L$, G_{Namax}, G_{Kmax} and G_L the model that describes the membrane dynamics, which lead to action potential formation is complete.

However, it does not describe propagation yet since Hodgkin and Huxley studied the membrane under conditions of fixed voltage or stimulation across an entire axon neglecting propagation. For propagation an axial component in the transmembrane current needs to be considered as well. Figure 2.5 shows an equivalent circuit for a unit length of axon. The resistance per unit length on the inside and outside of the axon are represented by r_i and r_o with the Hodgkin-Huxley model connecting the inside with the outside. The total membrane current obeys the cable equation

$$i_m = \frac{1}{r_i + r_o} \frac{\delta^2 V_m}{\delta x^2} \tag{2.12}$$

Substituting equation (2.12) into the left-hand side of equation (2.6) gives a partial differential equation that models propagation as well since it is dependent on the x-coordinate along the axon as well as on time. With a mathematical software package like *MATLAB* [16] the equations can then be solved for the membrane voltage in the presence of an excitation to plot action

potentials and study the influence of the variables. An example is shown in figure 2.6. The source code for the computation was taken from [17].

For regenerative implants it is not possible to place electrodes on the inside and outside to directly measure the membrane voltage. Problems would be accurate positioning as well as puncturing of the axon leading to its inevitable death. Instead a single electrode is brought close to the axon to detect changes in potential difference with regard to a reference like an external ground or a position proximal along the axon, which is then interpreted as the passing of an action potential. This is called extracellular recording. A difficulty for the design of neural implants is that in practice the value for the resistance of the external medium is much smaller than the resistance of the internal medium. As the outside resistance is very small only a minute potential develops, that quickly fades away as the distance to the axon increases. The extracellular potential change is only in the microvolt range compared to the millivolt amplitude of the action potential. This requires very good amplifiers to reliably detect action potentials and it is furthermore necessary to avoid any loss in the conduction path, especially the interface. One way of relaxing this limitation is to confine the extracellular space to a small region in order to increase the extracellular resistance r_o and hence amplify the external potential value [11] as is practised in the polyimide microchannel implant device.

A final comment on the nature of channel behaviour. While Hodgkin and Huxley modelled the opening and closing of channels by a time-dependent differential equation, later research using patch clamp technique revealed that they are of a digital nature. Patch clamping allows one to look at a very small area of membrane isolating a few or even a single channel at a time. It was found that they can only be either in open state or closed state with no transitional states in between. Hodgkin and Huxley's presumption of conductance varying with time because of channels slowly opening up or closing is actually the averaged behaviour of a large amount of individual channels opening or closing over a certain membrane area.

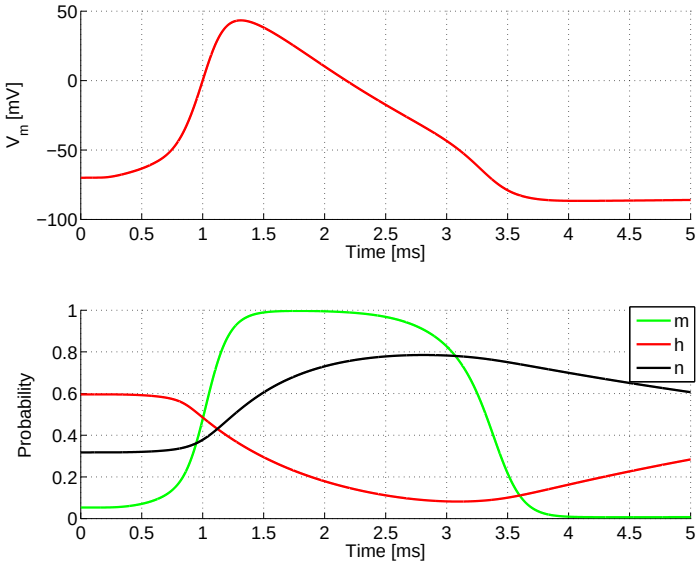

(a)

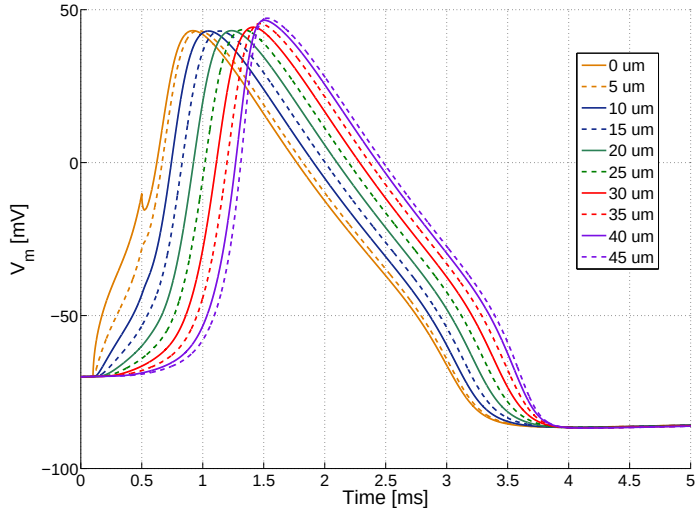

(b)

Fig. 2.6: Computation of an action potential using the Hodgkin-Huxley model. (a) Action potential at the middle of a 50 μ long axon with the corresponding gating parameters, (b) Propagation of the action potential along the axon with the voltages plotted at 0, 5, 10, 15, 20, 25, 30, 35, 40 and 45 μm. A clear time delay is visible as the nerve pulse travels along the axon. The first node shows an artefact from the stimulation pulse.

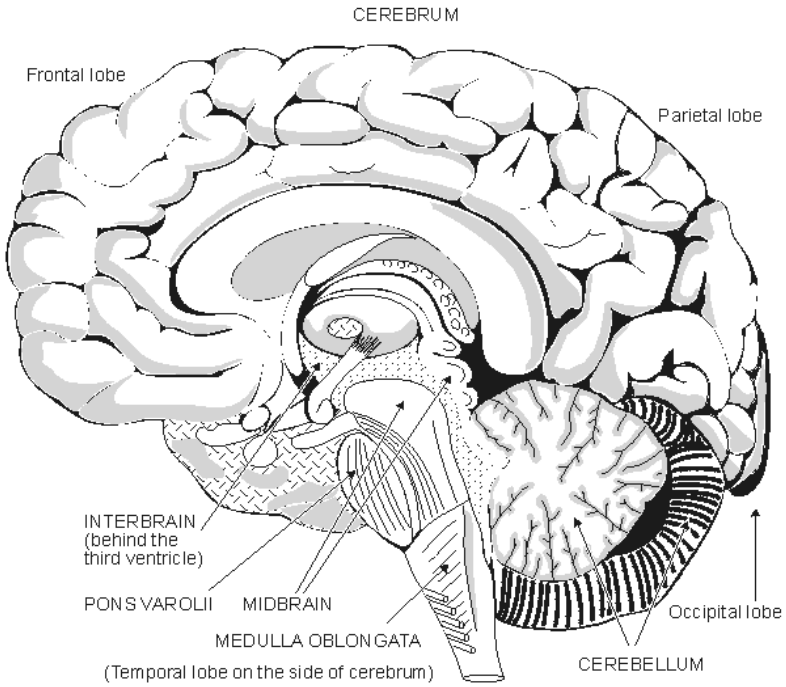

Fig. 2.7: The anatomy of the brain [12]

2.3 Differences in brain and peripheral nerves

The brain is part of the central nervous system together with the spinal cord. It consists of the cerebrum, the inter-brain, the mid brain, the pons Varolii, the cerebellum and the medulla oblongata (figure 2.7). It is protected by the skull bone and encased in three layers of meninges (skins), which are the dura mater, the arachnoid mater and the pia mater. As the name suggests the dura is a very durable, tough and almost leather-like white tissue protecting the underlying layers. The arachnoid is a thin layer with a cobweb-like structure and fine strands that are attached to the innermost layer. The space between the arachnoid and the pia is filled with cerebrospinal fluid. This fluid acts as a cushion to protect the brain from mechanical damage. It also contains blood vessels to support the brain. The thin and delicate pia mater is the innermost layer and runs closely over the entire surface of the brain down into the fissures. The cerebrum is the largest part of the brain and is divided into two hemispheres by a deep fissure in the middle running from the front of the head to the back. Its surface is extremely rugged so that the actual surface area is about 1600 cm^2. The outermost layer of the cerebrum forms the

cerebral cortex, a very important part responsible for much of the higher brain functions like memory, consciousness, language and thought. The left hemisphere contains the sensory system and the right hemisphere the motor cortex. Each specific function is mapped to a certain area within the cortex (figure 2.8). The cortex is about 3 mm thick and consists of six layers, each with different types of neurones. It is composed of grey matter, which is formed of neurones and unmyelinated fibres whereas the white matter below it contains mostly myelinated fibres responsible for connecting the different regions of the central nervous system. Inside the brain are three ventricles that also contain cerebrospinal fluid.

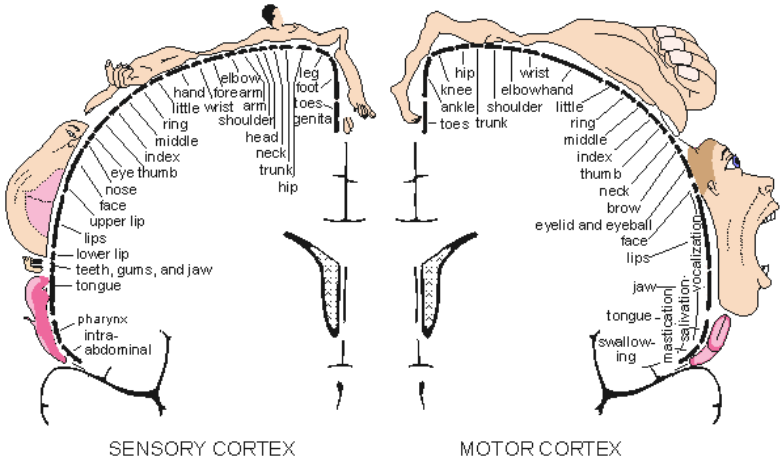

Fig. 2.8: The mapping of the brain functions to the cortex [18]

In contrast to the complex structure of the brain the peripheral nerves are mostly bundles of axons that connect the neurones in the central nervous system with the sensory and motor units in the human body for sensation and actuation. Unlike the brain it is not protected by bone leaving it vulnerable to mechanical injury. One remarkable feature is that while neurones can not be regenerated because they do not undergo mitosis (cell division) and die upon injury, axons in the peripheral nervous system (unlike in the central nervous system) can actually regrow. If a nerve is cut and the two ends are placed close to each other the side still connected with the nervous system grows back towards the severed stump and function can be partially restored over time. This is common surgical practice when dealing with nerve injuries and allows for regenerative neural implants to interface with the nervous system and guide the regrowth of

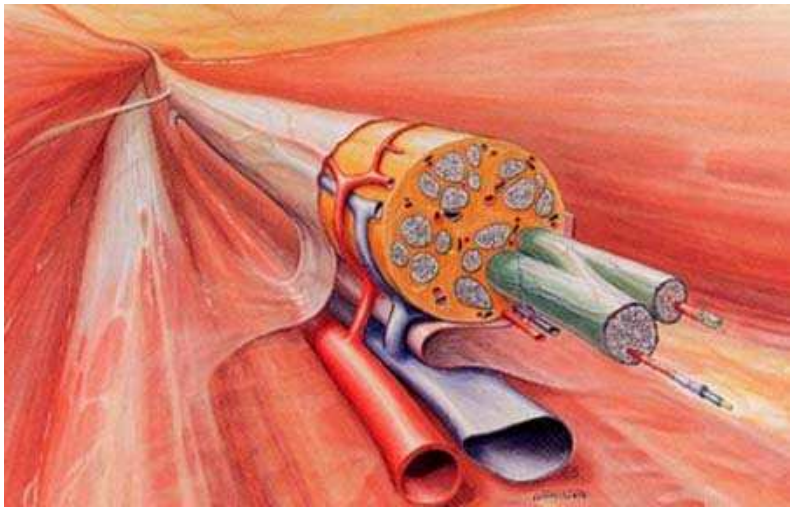

Fig. 2.9: Illustration of a peripheral nerve with supporting blood vessel [19]

nervous fibres. As within the brain it needs to be in the vicinity of blood vessels to be supported with oxygen and nutrients (figure 2.9). The individual axons are grouped together in fibre bundles called fascicles. These are encapsulated by a sheath of connective tissue called the perineurium. The fasciles are formed on the basis of their destination rather than their function. They are bound together by a collagen matrix called epineurium that gives them mechanical stability and protection. Within the fascicles each individual fibre is surrounded by connective tissue called endoneurium. The fibres follow an undulating course allowing them to be stretched within a certain limit without injury. Also Schwann cells are present in the bundles producing the myelin sheath around the myelinated axons.

3. THE ELECTRODE-TISSUE INTERFACE

As discussed in the previous chapter, signal conduction in the axon is an ionic transport mechanism. The axons in the tissue are surrounded by salt solution, the electrolyte, which allows the ionic charge carriers to move through the membrane. The electrodes on the other hand are made from metals and based on electron conduction. As a consequence an electrochemical interface is formed between the solution and the electrode. This chapter will describe the structure of this interface and the its different components. The information presented in this chapter can be found in standard text books on electrochemistry [20, 21, 22] while the style of presentation is mainly borrowed from [23].

The task of the interface is the conversion of bioelectric signals from ionic charge carriers to electronic signals carried by electrons or vice versa. This can happen either by capacitive coupling or by charge transfer reactions of electrons or ions to/from the solution. While electronic conduction is characterised by high carrier mobilities allowing for very high frequencies, electrodes as transducers operate with frequencies up to 10-100 kHz since biological signals are mostly present in this range due to the low mobility of their ionic carriers. Typically there are two different scenarios for electrode applications in biological tissue. They are either operating in the small-signal regime where capacitive effects dominate and charge transfer is negligible (neural signal recording). Or they work in large-signal mode with significant currents flowing through carrier exchange at the interface (nerve stimulation). While for small-signal operation the interface can be represented by linear circuit elements, for large-signal operations additional non-linear effects appear and have to be considered.

3.1 The charge double layer

When a metal electrode is put into solution without a voltage applied, a chemical reaction can spontaneously occur where metal ions go into solution leaving behind electron charges spread out across the surface due to repellent forces. This continues until enough potential has accumulated for the reverse reaction to happen where a metal ion recombines with a free electron to form a neutral atom on the surface. The reverse reaction is of electrochemical nature because it is driven by the potential difference between the metal and the charge layer in the solution. After a while an equilibrium is reached when the rates of the forward and reverse reactions balance each other out so that there is no net current flow across the interface. The surface charges of the metal then attract dissociated ions in the electrolyte, which varies the ion concentration from a maximum value near the electrode to the bulk concentration in the solution. The closest approach of ions to the metal is determined by the hydration sheath. It is formed because of polar water molecules that collect around the ions and the metal surface with the poles oriented correspondingly to the charges of the ions and electrons. This is often referred to as the double layer with the hydration sheath termed the Inner Helmholtz Plane (IHP) and the first layer of ions called the Outer Helmholtz Plane (OHP). Since the hydration sheath has a very small thickness of a few angstroms the potential difference between ions and metal surface drops over a very small distance causing a high electrical field strength. For this reason the electrochemical reactions usually take place in that region. With the ions being kept separated from the metal by a thin layer of water molecules in effect a capacitor arrangement forms with negative electron surface charges on the metal and positive ion charges in the solution separated by a dielectric layer of water molecules.

The simplest way to model this capacitance is by assuming a two-dimensional configuration with the charge concentrated on the Outer Helmholtz Plane and the metal surface of the electrode was proposed by Helmholtz and Perrin. It uses the well-known capacitance formula of a parallel-plate capacitor:

$$C = \frac{\varepsilon_r \, \varepsilon_0 \, A}{d} \tag{3.1}$$

with ε_r the relative dielectric permittivity of water (~80 at 20° C), ε_0 the dielectric permittivity

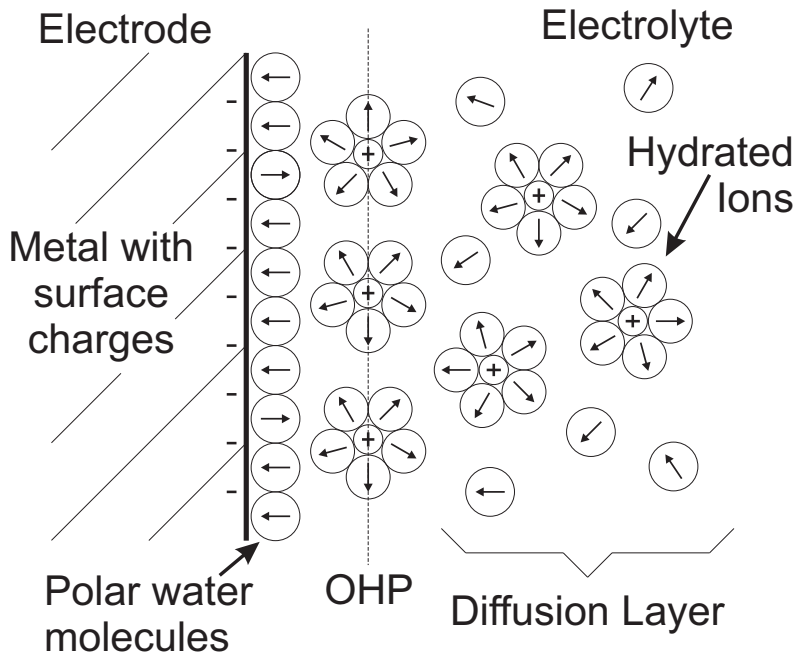

Fig. 3.1: Structure of the electrochemical interface

of vacuum, A the surface area of the electrode and d the spacing between electrode and OHP. Normalised to the electrode area the Helmholtz capacitance is

$$C_H = \frac{\varepsilon_r \, \varepsilon_0}{d} \tag{3.2}$$

The normalisation is useful to compare different materials regardless of the particular area of the electrode since researchers use various electrode sizes. While being a good first approximation, the parallel-plate configuration is not a valid assumption. The value of the Helmholtz capacitance with a double layer thickness in the typical angstroms range is too high compared to real electrodes. For example bright platinum electrodes routinely used in neurophysiological measurements because of their good recording capability have 0.2 pF/μm^2 [24] compared to a theoretical value of 1.39 pF/μm^2 for 5 Å. As illustrated in figure 3.1 the charge is actually not solely concentrated on the Outer Helmholtz plane but spreads into the solution thus lowering the capacitance. Furthermore it does not take into account the voltage dependence that arises from charges packing closer to the electrode surface for higher voltages and therefore reducing the thickness of the double layer.

Gouy and Chapman proposed a different approach by modelling a diffusive space charge layer rather then having the ions stuck on a rigid plane. This leads to a potential distribution described by

$$\frac{tanh\left(\frac{zeV(x)}{4\,k_BT}\right)}{tanh\left(\frac{zeV_0}{4\,k_BT}\right)} = e^{-Kx} \tag{3.3}$$

with

$$K = \sqrt{\frac{2\,n^0 z^2 e^2}{\varepsilon_0 \varepsilon_r k_B T}} \tag{3.4}$$

where V_0 is the potential at the electrode, $V(x)$ the potential at distance x, k_B the Boltzmann constant, T the temperature, e the electron charge, n^0 the bulk number concentration of the ion species and z the ion charge. For $z\,e\,V(x)/4k_BT \leq 0.5$ it becomes

$$V(x) = V_0\,e^{-Kx} \tag{3.5}$$

so that the potential drop is exponential and not linear as in the parallel plate model. The drop occurs in close vicinity to the electrode surface and is confined even more for increasing applied voltage. Using Gauss's law on the region near the electrode with the exponential potential distribution a formula for the space charge capacitance can be derived as

$$C_D = \sqrt{\frac{2\,n^0 z^2 e^2 \varepsilon_0 \varepsilon_r}{k_B T}} cosh\left(\frac{zeV_0}{2\,k_BT}\right) \tag{3.6}$$

In contradiction to experimental measurements this formula however also overestimates capacitance values as it does not show a finite plateau with increasing voltage as observed in real systems thus indicating a flaw in the model.

The Stern model combines the rigid ion plane of the Helmholtz-Perrin model with the diffusive space charge layer of the Gouy-Chapman model as a series combination of the two capacitances to result in an interfacial capacitance of the form

$$\frac{1}{C_I} = \frac{1}{C_H} + \frac{1}{C_D} = \frac{d_{OHP}}{\varepsilon_0 \varepsilon_r} + \frac{1}{\sqrt{\frac{2\,n^0 z^2 e^2 \varepsilon_0 \varepsilon_r}{k_B T}} cosh\left(\frac{zeV_{OHP}}{2\,k_BT}\right)} \tag{3.7}$$

with d_{OHP} the position of the OHP where the transition from C_H to C_D takes place and V_{OHP} the potential at this position. In figure 3.2 the total interfacial capacitance is plotted against the

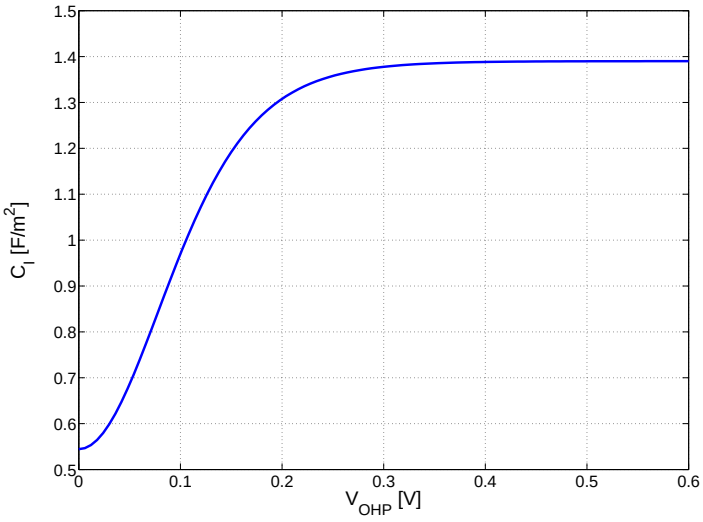

Fig. 3.2: Plot of the interfacial capacitance according to the Stern model

Outer Helmholtz potential with d_{OHP}= 5 Å for physiological saline (bulk concentration 0.154 mol/L, z = 1). It starts from a minimum value at zero applied potential rising with increasing voltage to pass over into a plateau set by C_H. The model is still an approximation but helps to understand and illustrate the processes involved. It is sufficient to describe neural electrode behaviour.

3.2 The charge transfer resistance

The charge transfer resistance, in simple terms, gives a measure of the difficulty to place or remove a charge from the electrode. It provides a highly nonlinear DC current path. In the process of moving the charge to or from the electrode, the electrode potential is altered and moved away from its equilibrium value, V_o. The resulting potential difference is called the overpotential and is defined as

$$\eta = V - V_o \tag{3.8}$$

It can be split into four terms each accounting for a different process that can alter the overpotential. These are η_t due to charge transfer across the electrode double layer, η_d due to diffusion

of reactants to or from the electrode surface, η_r due to chemical reactions at the electrode and η_c due to crystallisation or exchange of metal atoms with the ions. The sum of these components forms the total overpotential η. The most important component for the use of electrodes as biological transducers is η_t, which describes the charge transfer resistance, while η_r and η_c are negligible in this case.

Under equilibrium conditions the current of oxidation is balanced by the reduction current. The current density with regards to the surface area in this case is called the exchange current density, J_0. Its value depends on the electrode material and the reactions involved. The effect of an externally applied current on the overpotential is evaluated by its magnitude in comparison to the exchange current density. If the current is small with regards to J_0 then the electrode will not shift significantly from equilibrium and behave linearly. If, on the other hand, the current is of similar magnitude or above the value of J_0, nonlinearities are introduced and the charge transfer resistance falls off exponentially with applied potential.

The relationship between the current density and the overpotential is given by the Butler-Volmer equation

$$J = J_0 \left(e^{\frac{(1-\beta) z\, \eta_t F}{RT}} - e^{\frac{-\beta z\, \eta_t F}{RT}} \right) \tag{3.9}$$

in A/cm^2 with J_0 the exchange current density, z the ion charge, F the Faraday constant, R the molar gas constant, T the temperature and β the symmetry factor. One exponential term symbolizes the current of oxidation while the other represents the current of the reduction reaction. It is similar to the formula for the current of two diodes in an anti-parallel set-up with each diode only allowing one current direction to pass through. The symmetry factor accounts for differences in the energy barriers for oxidation and reduction. Therefore it determines the symmetry in the I-V characteristics. When both reactions proceed at the same rate, β is 0.5. A plot illustrating the influence of the parameters J_0 and β on the Butler-Volmer equation is shown in figure 3.3. It is noteworthy that for noble metals such as gold the charge exchange reactions occur through the presence of impurities rather than by the metal itself [25].

For the case of a symmetry factor equal to 0.5 where the oxidation matches the reduction

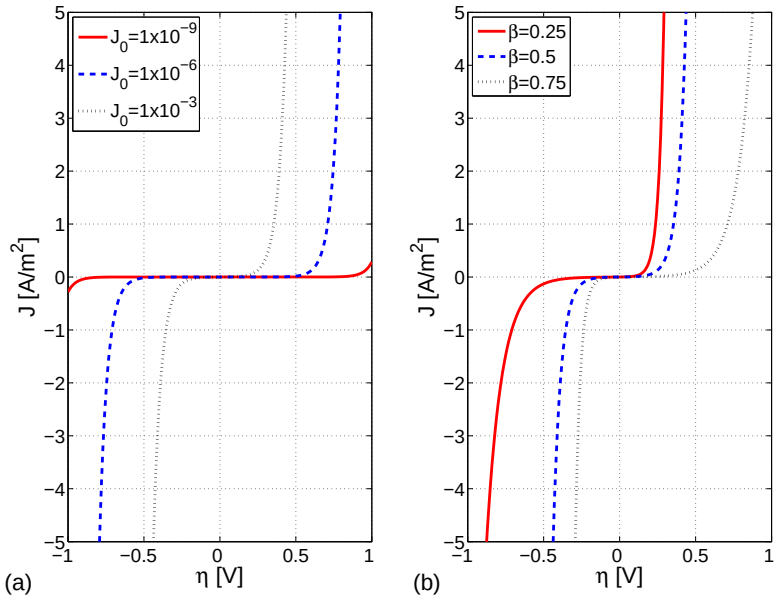

Fig. 3.3: Plots of the Butler-Volmer equation for (a) different exchange current densities and (b) various symmetry factors

reactions, equation (3.9) can be expressed using the hyperbolic sine function to give

$$J = 2\, J_0 sinh\left(\frac{zF\eta_t}{2RT}\right) \tag{3.10}$$

The charge transfer resistance is than defined as the differential

$$R_t = \frac{\partial \eta_t}{\partial J} = \frac{J_0 zF}{RT}\left[cosh\left(\frac{zF\eta_t}{2RT}\right)\right]^{-1} \tag{3.11}$$

in $\Omega \cdot cm^2$. For the case of a small overpotential a low-field approximation can be made where

$$sinh\left(\frac{zF\eta_t}{2RT}\right) \approx \frac{zF\eta_t}{RT} \quad \text{for } \frac{zF\eta_t}{RT} \ll 1$$

so that the expression for J in relation to η_t simplifies to

$$J = J_0 \frac{zF\eta_t}{RT} \tag{3.12}$$

and the charge transfer resistance becomes a linear term of the form

$$R_t = \frac{RT}{J_0 zF} \tag{3.13}$$

The limit for this approximation is assumed in [20] as

$$\frac{zF\eta_t}{2RT} < \frac{1}{5} \tag{3.14}$$

for an error due to the approximation to be less than 1%. It is interesting to note that the linearity limit is only determined by the overpotential and completely independent of J_0. By inserting the values for the constants and rearranging for the overpotential, this leads to

$$\eta_t < \frac{0.0103}{z} \tag{3.15}$$

as the limiting condition. For a one-electron-transfer reaction the maximum value for the overpotential in order to assume linearity is then roughly 10 mV. For reactions involving higher electron transfers this value is diminished further. The low field approximation thus holds for the case of extracellular neural recording since spike amplitudes normally are below this threshold so that the linearised charge transfer resistance can be used.

The high-field approximation assumes that for large values of η_t in either direction the opposite polarity contribution is negligible small so that it essentially behaves exponentially. As shown for the positive part the expression for J in relation to η_t becomes

$$J = J_0\, e^{\frac{(1-\beta)zF\eta_t}{RT}} \tag{3.16}$$

and is valid to describe the electrode in neurological stimulation applications.

The system's response to a sinusoidal signal with increasing signal amplitudes is shown in figure 3.4 by substituting $\eta_t = ksin(t)$ into equation (3.10) with k the voltage amplitude. As can be seen, above a certain voltage limit the current response signal does not follow a pure sinus curve and harmonic distortion is evident.

3.3 Chemical processes at the electrode

For high current densities a saturation in the current density can occur because of the increase in chemical reaction rate, which can locally deplete the reactants and cause a concentration gradient from the electrode to the bulk solution. In consequence the reaction rate and hence

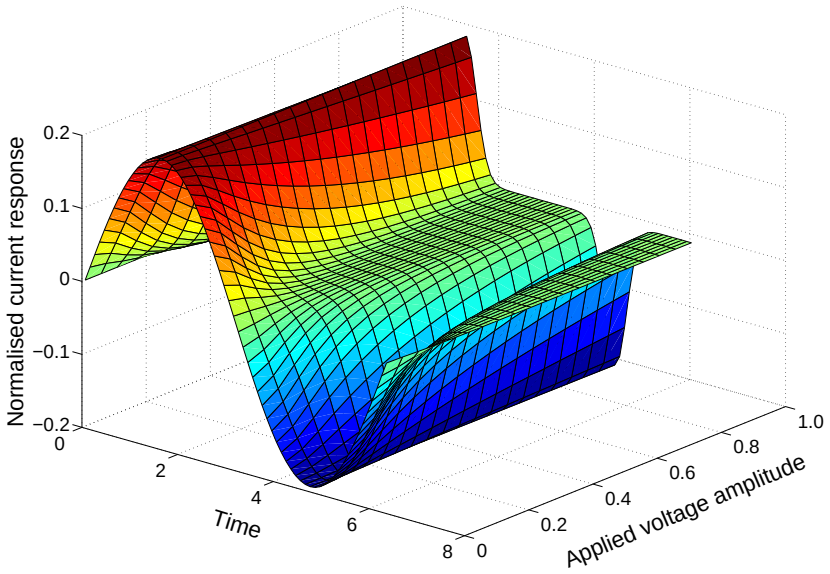

Fig. 3.4: Current response to sinusoidal signal for different voltage amplitudes. The current responses have been normalised by their maximum amplitudes to show the effect of nonlinearities

the current density is limited by the diffusion rate in order to supply new reactants. This is expressed by the overpotential η_d due to diffusion.

In the case of very low frequencies near DC it is a steady-state diffusion and the relation between the overpotential and the current density is given by

$$J = J_s \left(1 - e^{\frac{\eta_d z F}{RT}} \right) \tag{3.17}$$

where J_s is the saturation current density leading to a diffusion resistance of

$$R_d = \frac{RT}{zF} \left(J_s e^{\frac{\eta_d z F}{RT}} \right)^{-1} \tag{3.18}$$

For the case of time-varying signals with higher frequencies a different approach is necessary. In 1899 Warburg proposed that the diffusion impedance for a sinusoidal signal varies with frequency. The model assumes a sinusoidally varying spatial concentration in response to a sinusoidal potential applied to the electrode. This variation is largest near the electrode and

falls off with distance away from the interface. For increasing frequency it is damped so that it reaches less far into the solution and hence increases the concentration gradient. He solved the diffusion equation under these assumptions to arrive at a frequency dependent impedance, which he modelled as a R-C-series circuit. The impedance can be expressed in the form

$$Z_w = \frac{A_w}{\sqrt{\omega}} - j\frac{A_w}{\sqrt{\omega}} \tag{3.19}$$

while

$$A_w = \frac{RT}{n^2F^2\Theta C\sqrt{2D}} \tag{3.20}$$

with R the ideal gas constant, T the temperature, F the Faraday constant, n the valency, Θ the fraction of ion species present, C the concentration of the electrolyte and D the diffusion coefficient. The Warburg impedance is often represented as a parallel R-C circuit combination with equal frequency-dependent magnitude to show that it has a constant phase angle of $-45°$. One shortcoming of the Warburg model is that for the limiting case of $f \to 0$ it does not give the DC diffusion resistance as shown above.

One more point to consider about the chemical reactions taking place at the interface is the distinction between reversible and irreversible reactions. While for neural recording applications the reactions at the interface are negligible, for neural stimulation they need to be considered for safety reasons. In reversible reactions the chemical species remain localised at the electrode surface and do not diffuse away during stimulation. In irreversible reactions on the other hand new species evolve that are not bound to the electrode. Electrodes made from noble metals usually act as electron donors or acceptors rather than participating directly in the reactions. For a long term implant only reversible reactions are to be allowed since irreversible reaction products would severely effect the surrounding tissue. For this reason charge injection limits are specified and charge-balanced stimulation pulses are used to avoid irreversible reactions.

3.4 The solution resistance

The solution resistance accounts for the resistance experienced by the current as it spreads out into the solution. It depends on the shape of the electrode and the conductivity of the solution. The solution's conductivity is determined by the ion concentration of the constituent species and the temperature. In order to determine the conductivity of a given solution one works with the molar conductivity Λ defined as

$$\Lambda = \frac{\sigma}{c} \tag{3.21}$$

with σ the conductivity in S/m and c the ion concentration in moles. Kohlrausch established that for dilute solutions it varies only weakly with concentration in the form

$$\Lambda = \Lambda_0 - k\sqrt{c} \tag{3.22}$$

where k is a constant and Λ_0 is the limiting molar conductivity at infinite dilution. For solutions with a concentration of up to ~1 mM and equal charges for the anion and the cation, the constant k can be derived by thermodynamic arguments to form the Debye-Huckel-Onsager equation

$$\Lambda = \Lambda_0 - (A + \Lambda_0 B)\sqrt{c} \tag{3.23}$$

At a temperature of 25° C assuming monovalent ion species A has a value of 60.20 and B is 0.229 [26]. The conductivity for different ion species varies with their size but Kohlrausch described the limiting molar conductivities of the ions involved in conduction in the solution to be independent so that

$$\Lambda_0 = \Lambda_0^+ + \Lambda_0^- \tag{3.24}$$

These values are tabulated at 25° C in standard texts such as [26]. To account for their temperature dependency it is necessary to adjust the conductivity values for body temperature by approximately +2%/° C. With this information it is then possible to calculate the conductivity of normal 0.9% saline often used in medicine because it mimics the chemistry in the body. It is produced by mixing 9 grams of sodium chloride in one litre of water, which results in a solution with a concentration of 0.154 M. The limiting molar conductivity for this solution is

$$\Lambda_0^{Na^+} + \Lambda_0^{Cl^-} = 126.4 \cdot 10^{-4} \, {}^{\mathrm{S \cdot m^2}}/_{\mathrm{mol}} \tag{3.25}$$

Inserting this value into (3.23) gives a approximate molar conductivity of

$$\Lambda = \Lambda_0 - (60.2 + 0.229\Lambda_0)\sqrt{c} = 91.4 \cdot 10^{-4}\ {}^{\mathrm{S\cdot m^2}}/_{\mathrm{mol}} \tag{3.26}$$

so that the conductivity of the solution is

$$\sigma = \Lambda \cdot c = 1.408\ {}^{\mathrm{S}}/_{\mathrm{m}} \tag{3.27}$$

Adjusting for body temperature this corresponds to a conductivity of $1.76\ {}^{\mathrm{S}}/_{\mathrm{m}}$.

When idealising the electrode as a point source the solution resistance can be calculated by integrating over the series resistance of infinitesimal shells of solution in the manner

$$R_s = \int_{x=0}^{x=\infty} dR_s \tag{3.28}$$

with x perpendicular to the shell surface. For a planar disc electrode geometry the solution resistance is given by

$$R_s = \frac{1}{4\,\sigma\,r} \tag{3.29}$$

where σ is the electrical of the conductivity of the solution in $(\Omega \cdot cm)^{-1}$ and r is the disc radius [27].

3.5 Equivalent circuit model

After discussion of the processes involved in the electrochemical interface, an equivalent circuit model of the interface that accounts for all contributing processes is formed. The charge double layer is represented by a capacitive element in parallel with a branch symbolising the path of direct charge transfer. This branch is formed by the charge transfer resistance in series with the Warburg impedance. The series combination is justified by the diffusion processes limiting the amount of charge transfer possible at a time. The Warburg impedance is chosen over the DC diffusion resistance as the signals in neural recording applications are frequency dependent. The parallel circuit is then connected in series to the solutions resistance. The complete circuit diagram is shown in figure 3.5.

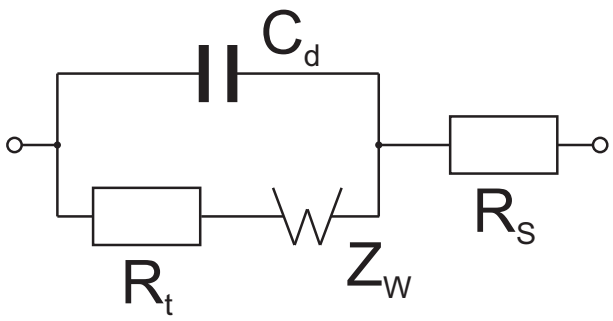

Fig. 3.5: Equivalent circuit of the electrochemical interface

From the equivalent circuit two special cases can be distinguished with regards to electrode polarisation (figure 3.6). The term electrode polarisation here means to alter the potential difference across the interface. For the interface to be polarisable means to be susceptible to changes in potential difference. For the case of an infinitely large charge transfer resistance the lower path in the parallel circuit is blocked and the behaviour of the electrode is dominated by the capacitance. The result is an ideally polarisable interface because any charge build up is stored in the capacitor, which causes a potential difference across the interface. On the contrary if the value of the charge transfer resistance tends towards zero, it bypasses the capacitance and any potential difference or stored charge is quickly neutralised. This is called an ideally non-polarisable interface.

For applications in the neuroscience a non-polarising interface is favourable as build up

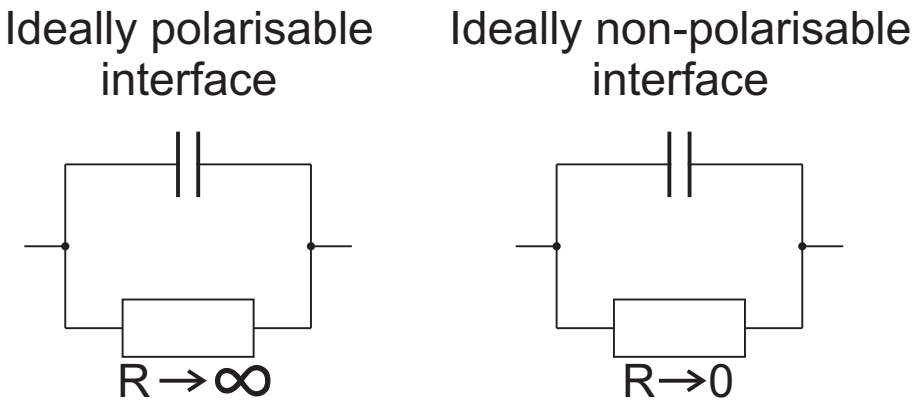

Fig. 3.6: Types of Polarisation for the interface

potential moves the interface away from equilibrium and into non-linear behaviour. It also makes irreversible reactions more likely to happen. Real electrode systems are assumed to be non-polarising if the current density is small in comparison to the exchange current density J_0. This has to be determined experimentally since J_0 depends on electrode material as well as the reactions involved. Often they show mixed behaviour somewhere in between the limiting cases. In the case of neural recording charge transfer plays no major role and polarisation is negligible since the signal is of such small amplitude that equilibrium can be assumed. Any process that does not involve electron transfer between the electrode and the solution is called a non-faradaic process. Neural stimulation on the other hand makes use of charge transfer to stimulate neural tissue and is termed a faradaic process. In this scenario attention has to be paid to electrode polarisation so as not to cause irreversible reactions.

4. REVIEW OF METHODS FOR MODIFICATION OF NEURAL IMPLANT SURFACES

The following chapter reviews the different approaches that are traditionally used to improve the properties of neural electrodes as well as recently reported research results. These latest developments show that it is an active area of research with great importance to the field of neural implants. The main objective most of the time is to lower the electrode impedance. For recording this provides better quality signal acquisition with increased sensitivity while in stimulation it reduces the need for higher stimulation currents because of smaller losses in the stimulation site.

4.1 Porous materials

One of the oldest methods in electrophysiology is the coating of electrode tips with platinum black, a rough form of platinum, through platinisation [28]. In this method platinum is non-perfectly deposited from solution onto a platinum substrate. It possesses a bubbly, corrugated surface that gives rise to an increased surface area. Like most electrochemical deposition methods for porous materials, it suffers from poor adhesion and mechanical stability so that it detaches from the surface during use. This can be improved by carrying out the process in an ultrasonic bath, which removes loosely attached deposits while the particulates with better adhesion remain on the surface [29]. Literature reports for a circular electrode with a 500 μm diameter a decrease of impedance from 40 kΩ to 1 kΩ at 1 kHz [30], but because of the high porosity it is still subject to degradation. From the same field stems a similar material that is produced by chloriding of silver wire which creates a silver-silver chloride interface [31]. It offers a low stable electrode potential, a small value of charge transfer resistance and a small

interface impedance due to rough surfaces. On the downside it has a low conductivity so that for thicker coatings the total impedance increases. It also degrades with time because of its porosity and is not suitable for long-term application because of the leakage of silver, which leads to poisoning of the body.

A material highly regarded for neural stimulation is iridium oxide (IrOx) because of its excellent charge transfer capacities [32]. This is associated with the porous, hydrous multilayer structure of the oxide film and the nature of the reaction with the oxide that allows higher maximum charge delivery compared to other materials with higher safe charge delivery limits because of the reversible faradaic reaction it undergoes

$$IrO_{n-1}(OH)_{4-n} \Leftrightarrow IrO_n(OH)_{3-n} + H^+ + e^- \tag{4.1}$$

Reports also state that the impedance is even smaller compared to platinum black and in particular maintains a lower value in the frequency range < 10 Hz [33] because of the low charge transfer resistance of the faradaic reaction. Iridium oxide films can be obtained in various ways. It is possible to electrochemically deposit them from solution or they can be created from iridium films that are oxidised through an activation process during which the electrode potential is cycled between a positive and a negative limit with each cycle causing further oxide to grow. Also IrOx can directly be produced during iridium sputtering by adding oxygen to the chamber during deposition. On the downside it is reported to suffer from poor adhesion to substrates as well as low structural and chemical stability that tends to get even worse during electrode operation because of an increasingly thick oxide layer forming [34, 35].

A material with even higher porous surface area due to its columnar microstructure is titanium nitride [36]. However, it is used less in neurostimulation because it lacks the reversible Faradaic charge transfer mechanism. Titanium nitride is formed by reactive sputtering of titanium in an mixed argon-nitrogen atmosphere that forms a mechanically robust film. For a 900 nm thick layer an impedance of 150 kΩ at 1 kHz is stated for a 80 μm^2 electrode in contrast to 2900 kΩ for a bare gold electrodes of the same size. The process is compatible with integrated circuit fabrication processes and unlike iridium oxide does not need activation. Its biocompatibility is uncertain as reports exist that indicate increased cell death while it is used routinely

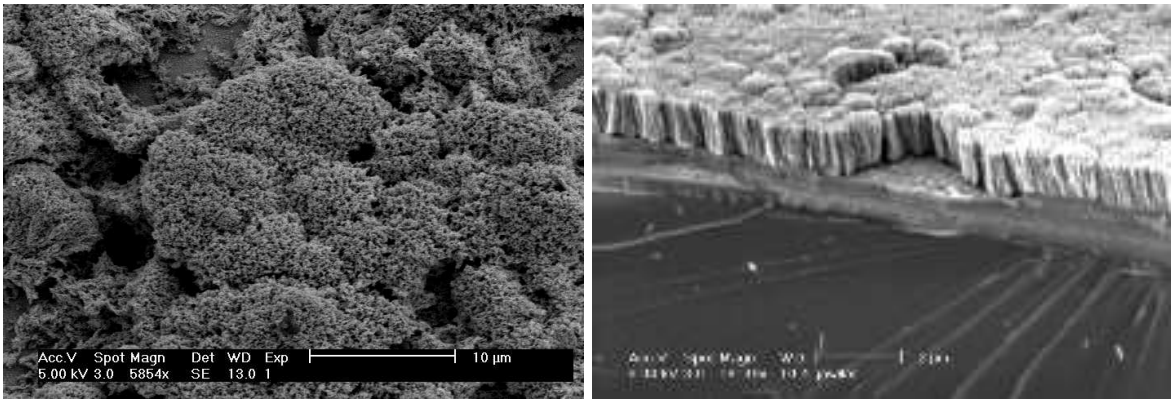

(a) (b)

Fig. 4.1: a) SEM image of Platinum Black deposit b) Columnar structure of Titanium Nitride [37]

as pacemaker material. Diverging reports about its electrical properties indicate that it is very sensitive to the growth parameters impeding reproducibility [37]. As it is a ceramic its extreme hardness might induce additional mechanical stresses when applied to compliant devices based on polymeric substrates compared to softer materials like gold.

Another interesting type of coating is the employment of conducting polymers [38]. Many different polymers exist that exhibit electrical conduction. However, for neural probe application essentially two materials have been explored that are suitable for this purpose. At first polypyrrole (PPy) was most intensively studied for use on neural electrodes [39]. It was later complemented by Poly(3,4-Ethylenedioxythiophene) (PEDOT) [40]. Polypyrrole is reported to be mechanically more stable while PEDOT has superior electrical properties. They are deposited by electrochemical synthesis through electropolymerisation. The reason these materials can conduct electricity derives from conjugated double bonds in their backbone with overlapping π-orbital, so that through doping with other molecules they can become p- or n-type doped materials. Through appropriate incorporation of dopants like poly(styrene sulfonate), para-toluenesulfonate or salts like lithium perchlorate conductivities up to 1.6 S/m have been achieved. The films possess a high surface area because of their porous structure which in turn decreases their impedance. Reports show that PEDOT can even be deposited in the form of polymer nanotubes through a fibre template process which further decreases the impedance

[41]. As a negative side effect these polymers can be brittle and prone to delamination and cracking [42] as the low impedance is directly correlated to the film softness. Another reason for their attractiveness in neural devices is that they premeditate the transduction of ionic current into electronic current through a efficient reversible redox reaction which minimises the charge transfer reaction much like in IrOx. This also contributes to the overall low impedance. Since the charge transfer reaction dominates low-frequency behaviour it also makes them excellently suited to record local field potentials because of reduced low frequency drift.

The electrochemical stability of the material can be a problem, in particular PPy is reported to retain only 5% of its charge after polarisation over 16 hours because of irreversible oxidation. Maintaining a high capacitance over long periods is a requisite to record long-term chronic neural activity. PEDOT retains 89% of its electrochemical activity but is a much more brittle material. In an effort to fuse the mechanical stability of PPy with the electrochemical properties of PEDOT layering has been shown to be a suitable method to combine the advantages of both materials [43]. A further attractive feature of this material class is the ability to incorporate biomolecules and drug release to enhance cell attachment or reduce the inflammatory tissue response through the release of anti-inflammatories [44, 45]. As no long-term studies are available it remains to be seen how the tissue reaction changes once the molecules are consumed up. Some researchers hypothesise that the beneficial effects will wear off. Initial toxicity assessments are favourable showing an overall good biological performance [46]. Long-term assessment of actual devices in their operating environment is still needed to gain a better understanding of changes polymers undergo in-vivo. Especially the leaching of unlinked monomers and dopants must be avoided as they can show moderate toxicity. Further research and long-term studies are required for a safe and durable long-term implant based on these materials.

So far studies of PEDOT films [47] and nanotubes [48] for implantation periods of 6 weeks have been conducted. PEDOT films were grown on 703 μm^2 iridium sites of Michigan probes and the impedance monitored over the whole implantation period for coated versus uncoated control sites. The initial impedance after implantation at 1 kHz was 0.98 ± 0.08 MΩ and 0.13 ± 0.06 MΩ for uncoated and coated sites respectively giving a ratio of 7:1. During the

assessment the impedances of both types increased due to biological reactions in the tissue associated with scarring and inflammatory response. At the end of the experiment the ratio dropped to only roughly 2:1 as the measured impedances were 1.5 $\pm$ 0.3 MΩ for uncoated sites and 0.81 $\pm$ 0.3 MΩ for coated sites showing that the lower impedance could not be fully maintained during implantation. Also noise levels, signal amplitudes and signal-to-noise ratio (SNR) were monitored during the implantation. At the end of the 6 week period noise levels were 13.1 $\pm$ 0.9 μV and 12.7 $\pm$ 0.8 μV for control versus coated sites with signal amplitudes of 113 $\pm$ 13 μV and 129 $\pm$ 15 μV respectively. This translates into a SNR of 4.3 $\pm$ 1.0 for the bare iridium sites and 5.1 $\pm$ 1.2 for the modified PEDOT sites. The PEDOT nanotubes study found similar results as 1250μm^2 gold recording sites were modified with polymer fibres and their impedance monitored. Right after implantation measured impedance was 905$\pm$ 5 kΩ for bare sites and 87 $\pm$ 8 kΩ for nanotube sites. After 49 days the corresponding values had risen to 980 $\pm$ 15 kΩ for the control sites and to 521 $\pm$ 18 kΩ for the nanotube modified electrodes. Again an increase in SNR was found.

The impedance of the coatings is expected to drop with increased deposition thickness. However it was shown that beyond a certain limit no further drop in impedance can be observed while at the same time the mechanical stability decreases. During the polymerisation of the precursor the film not only grows thicker but also spreads laterally. While this contributes to surface area increase by extending the original electrode footprint this also makes it more prone to detachment and hence reduces mechanical stability.

The next promising material for neural application is carbon nanotubes (CNT). They have made an impact in a broad range of fields and are also suitable candidates for neural prostheses. With diameters down to tens of nanometres and the ability to be grown in lengths up to the μm range they possess a large surface area with tube densities of about 10^9 per cm^2 being reported [49]. They are grown by chemical vapour deposition from ethylene gas in an hydrogen precursor. The need for elevated temperatures of 700 - 900° however makes them incompatible with polymer substrates. They can be grown either as dense mats or vertically aligned fibre arrays forming real three-dimensional electrodes [50]. For insertion type devices this might

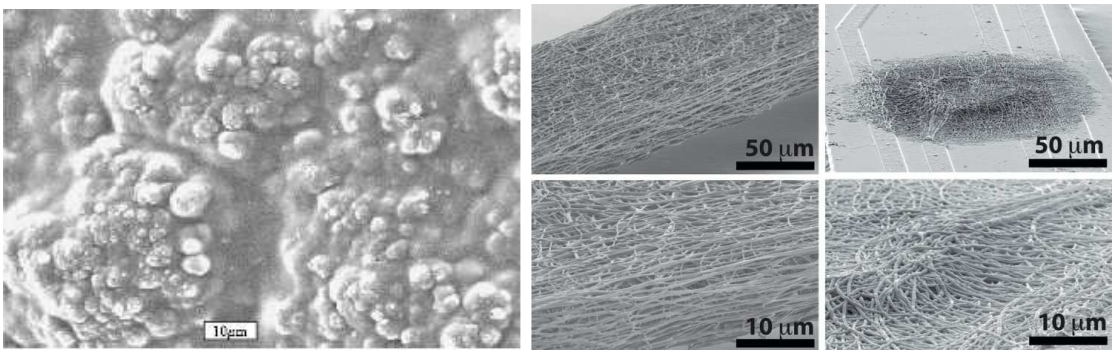

(a) (b)

Fig. 4.2: SEM images of (a) Polypyrrole [39] and (b) PEDOT nanotubes [48]

be a problem as their micrometre size could potentially increase tissue damage compared to planar electrodes. Another issue is the need for metal catalyst islands to initialise CNT growth. Metals that are not biocompatible have to be used, like iron or nickel. They require careful insulation so as not to come into contact with the body where they could release toxic traces or corrode. CNTs themselves have superior mechanical strength, but the catalyst islands anchoring them on the substrates provide a weak spot that could potentially result in detachment during excessive wear experienced in long-term devices. Reports suggest that further modification of as-grown nanotubes is necessary to have access to the full surface area. It was stated that their hydrophobic nature prevents the influx of electrolyte into dense fibre bundles and as a result they showed poor electrochemical properties, which were similar to planar electrodes. It was overcome by soaking them in cell culture medium to cause nonspecific adsorption of proteins, which made them more hydrophilic. Investigations show that CNTs offer lower noise recording compared to TiN electrodes [50] and are viable for neural stimulation with charge injection limits of 1 - 1.6 mC/cm^2 exceeding the safe charge delivery threshold of 1 mC/cm^2 for biological tissue [51]. In addition the charge transfer seems to be completely capacitive which excludes any adverse faradaic reactions. Impedances as small as 10 kΩ have been reported for 80 μm diameter electrodes coated with nanotube mats of 10 μm average height at 1 kHz [50]. Despite the fact that it was possible to successfully culture functional neuronal cells on microelectrode arrays containing carbon nanotubes, there are still concerns about implantation

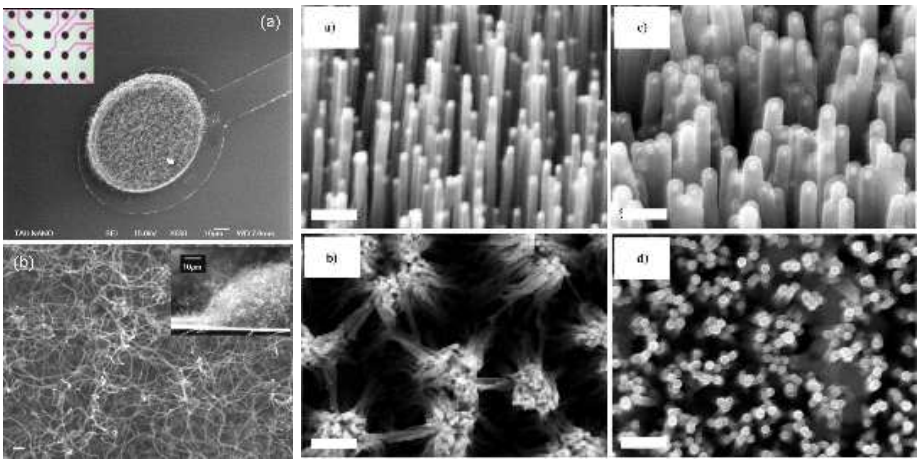

(a) (b)

Fig. 4.3: SEM images of (a) electrode coated with random deposited carbon nanotubes [50] and (b) vertically aligned grown fibres [49]

of such devices into the body as investigations on nanotubes showed adverse effects on the body [52, 53, 54]. Because of their small size they can easily pass barriers inside the body. For example they were observed to penetrate the membranes of cells causing cell death [55].

In an effort to combine the advantages and to alleviate some of their disadvantages composite coatings of polymers together with carbon nanotubes have been suggested. The first indications of the potential of this material mix were observed from the increase of electrochemical capacitance of a coating made up of carbon nanotubes and polypyrrole for super-capacitor application [56]. Recently this material combination was further investigated for the use in neural interfaces [57]. The addition of carbon nanotubes to the polypyrrole raised the conductivity of the film by about 50% and reduced the loss of electroactivity as described earlier by providing a conductive path that is not affected by irreversible oxidation. The material was assembled either through a layer-by-layer (LBL) approach or by co-deposition during electropolymerisation. While the LBL growth resulted in improved properties, the co-deposition resulted in values worse than pure polypyrrole. It was suspected that the carbon nanotubes interfere with the polymerisation process causing incomplete polymerisation. As there is still concern about the effect of nanotubes on the body, safely trapping them in the polymer is desirable but long-term

studies are still missing. It is also expected that the composite film benefits from the superior mechanical strength of the nanotubes to reinforce the conductive polymers. In another study a LBL composite of multi-walled CNTs, dispersed in PSS, and poly vinyl alcohol was compared to PEDOT and IrOx [58]. The material consists of intertwined bundles of nanotubes that give rise to an increased surface area. A single bilayer had an approximate thickness of 7 nm and the overall thickness could readily be increased by adding subsequent layers. It was found to have impedances lower then PEDOT and IrOx. The materials were coated on ball-shaped tips of 75 μm diameter Platinum/Iridium wires. For a coating thickness of 700 nm a reduction from 17.4 kΩ to 277 Ω is stated at 1 kHz. Also charge injection capacity was found to be superior with only a 5% loss of the original value after 300 cycles. The multilayer structure also enhanced the material's mechanical strength and ensures intimate adhesion to the substrate. Again biocompatibility is unclear and long-term tests are needed. A potential disadvantage of the process is the LBL approach, which does not allow for selective deposition making it difficult to apply to microelectrode arrays.

4.2 Electrode roughening

In contrast to the deposition of materials with intrinsic enhanced surface areas there have also been efforts to add porosity to noble metal electrodes through specific fabrication methods. One of the earliest methods was to increase the surface roughness through etching methods such as chemical etching with potassium iodine, electrolytic etching in sodium chloride or argon sputter etching. A comparison of these methods can be found in [59]. The report stated that this results in a increase of surface roughness from 5.5 nm for a 1 μm^2 area to up to 42.2 nm and is accompanied by a drop in interface impedance. While it is a simple method to apply to any neural device it lacks control over the surface features. Scalability is limited as prolonged etch times result in smooth surfaces. This is explained by the increased etching of the roughened features because they expose a larger surface area for the etchant to attack.

Another way to improve the performance of neural devices is to incorporate microstructures using conventional microfabrication and photolithography tools to create three-dimensional sur-

faces. For example grooves can be machined into silicon substrates prior to metal deposition to increase the exposed surface area. Other shapes include micro-posts [60] and pyramid-shaped microelectrode arrays that possess a two times lower impedance compared to planar devices [61]. These approaches are limited by the size of the electrodes, which are on the micrometre scale as well and hence put restriction on the area available for microstructuring. To preserve selectivity of the device the electrode surface should not extend too far into the nerve tissue. A near-planar shape is also required to minimise tissue damage. As a general rule to prevent bulky devices a maximum aspect ratio of roughly 10:1 should not be exceeded. For a 30 micrometer wide electrode the height of the microstructure has to be kept below 3 microns according to this rule. The use of nanostructures instead of microstructures can mitigate these limitations allowing higher densities but new tools have to be developed.

The nanostructuring of conductive, doped poly-silicon by reactive ion etching in a plasma of hydrogen bromide with the addition of a small amount of oxygen has been reported to increase the surface area by about 20 times [62]. The treatment resulted in 300 nm tall pillars with diameters between 20 and 100 nm. This was possible because the oxygen passivated the polysilicon during the etch, with dust particles and native oxide acting as micro masks for the pillar structures. In addition to the surface area increase a strong attachment of cellular material to the structured electrodes was observed indicating improved tissue integration. A report on nanoflake electrode fabrication has recently been published [63]. Bare gold electrodes were modified by electrochemical deposition of gold in the form of flake-like spikes that produced sharp tips and valleys. For the electrodeposition of gold in polyvinylpyrrolidone a small voltage window from 0.3 to 0.4 V exists that results in these structures. With increasing voltage inside this window the structures becomes more heterogeneous and exhibits higher surface area but became, as typical in nanoporous materials, mechanically more unstable and poorly attached. Also non-uniformity in large scale application increased. For a 30 μm diameter electrode a reduction of impedance from 1.15 MΩ to 26.7 kΩ at 1 kHz is stated. For smaller sized electrodes the impedance reduction was even greater as the shape of the electrode after electrodeposition became curved further increasing the available surface area compared to planar electrodes.

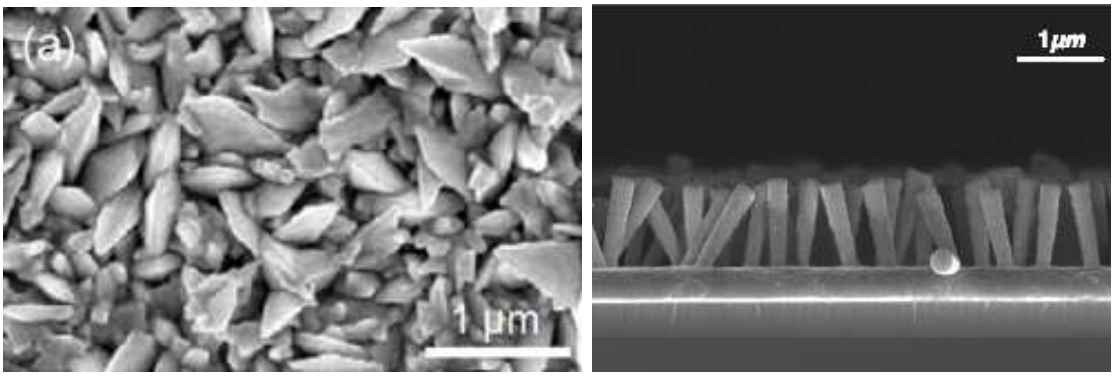

(a) (b)

Fig. 4.4: Electroplated gold nanoflake structures [63] (a) and templated gold pillars [65] (b)

While successful in-vitro cultivation of neural cells on microelectrode arrays was demonstrated, the rugged, sharp edge structures might cause problems in long-term implant devices. Micromovement of the device in conjunction with the sharp, spiky shapes could potentially cause constant microscopic injuries to the surrounding tissue resulting in inflammatory responses.

A de-alloying technique was recently reported for the manufacture of nanoporous gold electrodes [64]. At the beginning gold and silver were simultaneously deposited on the electrode through sputtering to form a gold-silver alloy. The silver was then selectively etched out of the compound with nitric acid to leave a porous gold film. For a 304 nm thick film and and an electrode diameter of 32 μm a change of impedance from 850 kΩ for a gold control electrode to 30 kΩ for a porous electrode at 1 kHz was stated. Caution has to be exerted towards these numbers as the methods section of that article described the use of an unusual large AC signal amplitude of 200 mV for impedance spectroscopy. It is common to use smallest possible amplitudes of 5-10 mV to avoid driving the interface into its non-linear operation regime which causes distortion of the test signal. A further concern is the 5% residual silver content remaining in the gold film. During in-vitro culture assessment no adverse effects were observed, but a long-term implant is exposed to wear and tear, which carries the potential of silver poisoning.

The last method to be discussed in this review is template filling, in which a nanoporous membrane is used as a mask for the aligned growth of nanowires or tubes by filling the pores through electrodeposition. The membranes are selectively etched away afterwards to leave

free-standing nanostructures behind. There are two main materials actively used as templates at the moment, alumina and polycarbonate membranes. These materials can either be obtained commercially as free-standing membranes or formed in-situ on the desired substrates. Free-standing membranes have to be mounted on to the substrates for use in patterning making them difficult to use in device fabrication. For flexible substrates bonding the polymeric polycarbonate templates is more suitable then ceramic alumina membranes. Occasionally the metal film to be patterned is directly deposited on one side of the membrane. In-situ membrane formation requires the use of high cost, access limited ion accelerators in the case of polycarbonate membranes for ion track etching to form the pores. The substrates have to withstand harsh treatment during the anodisation of aluminium in strong acids to create nanoporous alumina.

Using lithography-assisted bonding of polycarbonate templates, the modification of neural probes has been reported [65]. The membrane had a typical pore density of maximum 10^8 cm^{-2} and pore diameters between 10 and 1,000 nm. Photoresist was used to stick the membrane to the substrate surface and holes were opened lithographically in the templates for electrodeposition. Because the diffusion rate for the transport of developer necessary for the dissolution of the exposed photoresist parts down the holes decreased with pore sizes, pores of small sizes (10 to 35 nm) could not be opened even after extended soaking in developer (t > 1 hour). Large tilt from vertical direction was observed for the wires because the angle of the ion beam trajectories used to etch the pores typically experiences a large spread. Electrodes of 50 μm diameter on polyimide substrates decorated with Au nanowires were reported to show a significant impedance reduction and to increase the surface area by almost ten times compared to planar electrodes. Reports also stated that an aspect ratio below 4 must be kept in order to have sufficient mechanical stability and avoid breakage of the structures when removing the template [66]. For porous alumina templates also successful gold nanowire and nanotube fabrication has been reported [67].

5. FABRICATION OF NANOSTRUCTURED SURFACES

In the following sections of this chapter the methodology for the creation of surface nanotexture is detailed. In the previous chapter a range of surface modification techniques were discussed. Here a new technique using *Nanosphere Lithography* (NSL) is described. It allows for an inexpensive, parallel patterning of nanometre-sized structures with low equipment requirements where more traditional nanostructuring technologies like electron-beam lithography, scanning tunnelling microscopy or direct laser scribing suffer from limited process speeds due to their serial operation mechanism. Together with X-ray lithography they also require elaborate, expensive equipment. On the downside NSL is restricted to a limited amount of possible pattern shapes. Furthermore the creation of highly regular periodic arrays of large size is challenging. So far NSL has been used in a broad range of applications like the fabrication of magnetic structures [68], high-T_c Josephson devices [69], GaAs-based quantum dots [70] and optical applications [71, 72]. What has hindered a wider spread of this technique is that most applications require highly ordered layers of single crystal material. For the purpose of nanostructuring to increase surface area and to modify interface properties a highly monocrystalline structure would also be beneficial but is not a strict prerequisite. Therefore it is an attractive method and considered to be suitable for this application. It is the first time it is being used for the purpose of neural implant modification. The developed process presented here uses a simple bench-top method for the initial nanopattern generation. The first section describes the necessary process steps to sculpture thin films into textured surfaces. A description of various approaches to the NSL technique follows and explains the principal operating mechanism. Sections 3 and 4 explore in more details the two most important manufacturing steps, masking and etching. The next section contains the analysis of the fabricated structures with regards to their topology. In the final section possible alternative routes are discussed.

5.1 Process steps

The developed process consists of the following main steps:

- Nanosphere array deposition
- Etch mask deposition
- Nanosphere removal
- Ion beam milling
- Etch mask removal

illustrated in figure 5.1. The nanosphere deposition is done through assembly at the air-water interface as described in section 5.2 The sample is then loaded into a physical vapour deposition (PVD) system to coat it with a metal layer of suitable thickness. At the interstices the metal attaches to the substrate while the spheres block the rest of the area. The spheres are then removed in two steps. First scotch tape is used to lift off the main portion of the metallised spheres then any remains are dissolved in chloroform or tetrahydrofuran in an ultrasonic bath for 3 to 30 minutes. This leaves small metal spots on the otherwise clear gold surface. In the next step these metal islands serve as an etch mask to protect the underneath gold from the ion beam while unmasked areas are milled. After milling the remains of the titanium etch mask are removed by wet-etching in a commercial solution containing nitric acid and ammonium fluoride. The result is a gold surface covered with nano structures.

5.2 Nanosphere Lithography

NSL takes advantage of micro- and nanometre sized particles that are suspended in a solution, usually water. A broad range of materials in a wide spectrum of sizes is available. Some of the most common particle materials are latex polymers and silica. Upon evaporation of the solvent they assemble into close-packed hexagonal lattices. One of the first works to utilize this is described in [73] where a monolayer array of nanospheres was used as a metal deposition mask. Later it was extended by Deckman & Dunsmuir [74] as a micro- and nanofabrication

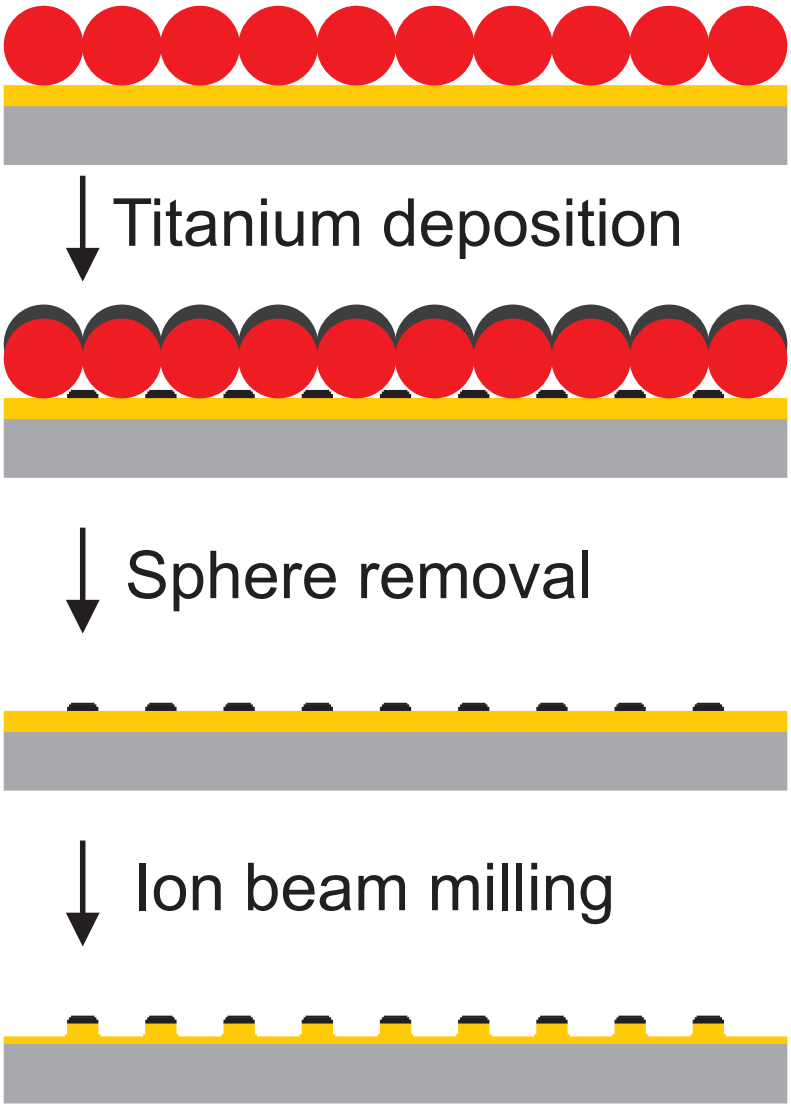

Fig. 5.1: Illustration of the four main process steps for nanostructuring

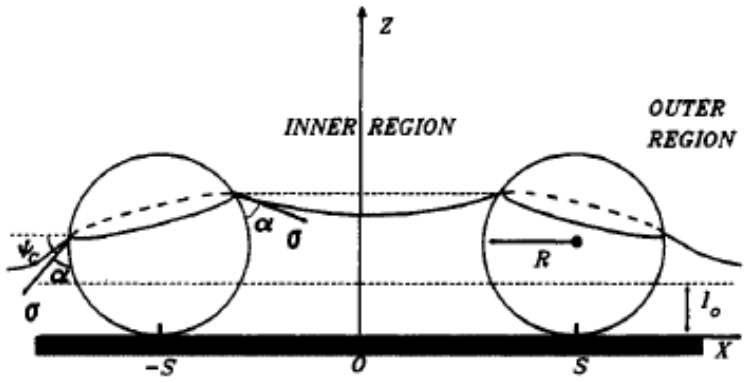

Fig. 5.2: Spheres partially immersed in liquid layer on a substrate [76]

tool for deposition and etching. They used the term *Natural Lithography* for their work before it finally became widely known as *Nanosphere Lithography* coined by Hulteen & Van Duyne [75], who expanded the method using bilayers of spheres and performed extensive studies on generated deposition pattern.

The basic mechanism for the nanoparticles to assemble into close-packed arrays was described by *Denkov et al.* [76]. Through optical observation of particle dynamics during solvent evaporation they found the process to be governed by contact forces between solvent and particles as well as convective solvent flux. The process starts when enough solvent has evaporated so that the spheres are not fully immersed any more and partially protrude from the liquid (see figure 5.2). As can be seen a difference in liquid meniscus shape between the inner and the outer region of two neighbouring particles exists. For this reason the orientation of the surface tension force σ differs between the two regions so that the horizontal component of the surface tension force is bigger on the inside than the outside. It is also oriented towards the opposing sphere causing a strong inter-particle attraction. Therefore the two particles are driven towards each other since the capillary forces are several orders of magnitude larger than the thermal energy of the spheres. A nucleus is thus formed by the spheres coming together at the particular site where the liquid layer was thin enough at first. In the second stage this colloidal crystal continues to grow through the transport of new spheres from the surrounding solution towards

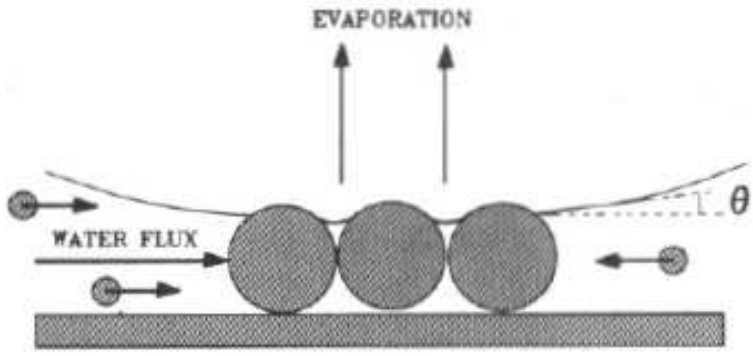

Fig. 5.3: Convective solvent flux towards assembled spheres [76]

the ordered array. This transport mechanism however is not governed by capillary forces as the surrounding liquid layer thickness is still too big so that the particles are completely immersed. Instead it can be explained by a convective inflow of liquid towards the nucleus. This inflow is caused by evaporation of water trapped between the ordered spheres creating a suction force that draws in liquid from the surrounding layer with the suspended spheres as illustrated in figure 5.3. It is then easy to see that the main control parameter for array formation must be the evaporation rate. Together with the sphere concentration it allows the speed to be set with which array formation proceeds. Slow crystal growth is preferable as it leads to better crystal quality with larger monocrystalline domains and substrate coverage. However it also makes the formation of bilayers more likely.

The idea pursued here for the texturing of gold films is to use NSL for the deposition of an etch mask of nanoscopic features on top of the gold film, which is then subjected to an anisotropic etch to transfer the feature pattern into the underlying material. By analysing the geometry of the sphere array an estimate of the increase in surface area can be derived. Figure 5.4 shows the particles assembled into a close packed hexagonal array. Connecting the centres of the spheres by lines forms triangular unit cells. The interstice for material deposition is defined by the contact points of the sphere circumferences and the corresponding arc segments connecting these points. The centres all have the same distance from their nearest neighbours, which is the sphere diameter. Therefore the triangles are equilateral and their inner angles are

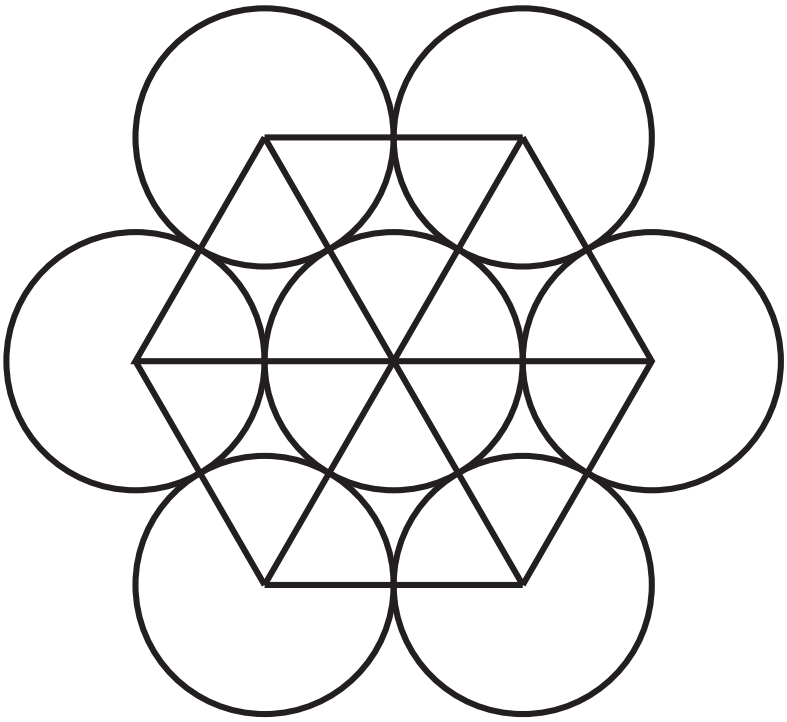

Fig. 5.4: Geometric outline of assembled sphere array

$60°$. With the spheres blocking a substantial part of the surface, material will only be deposited in the interstices and will mostly take the form of the interstice shape. Transferring this shape into the underlying film by the etching process creates a pillar or cone-like three-dimensional structure. With the top of the structure fixed in area the process increases the surface by adding the sides of the pillars. For each interstice the vertical side wall area is defined by the interstice circumference composed of the three arc segments multiplied with the height of the structure. As each corresponds to an opening angle of $60°$, the sum of the angles over the arc segments is $180°$, which is equivalent to half the circumference of one of the spheres so that

$$A_{side} = \frac{1}{2}\pi dh \tag{5.1}$$

where d is the sphere diameter and h is the height of the pillar. As the gold surface outline can be completely reconstructed by unit cells, the difference in area between an unstructured unit cell and a structured unit cell also applies to the film in total. The area difference is used to define a surface gain g_s. The area of a plain unit cell is given by the triangle area, whereas the

nanostructured unit cell is composed of the triangle area (the top of the structure is maintained) together with the side walls so that g_s is

$$\begin{aligned} g_s &= \frac{A_{triangle} + A_{side}}{A_{triangle}} \\ &= \frac{\frac{d^2}{4}\sqrt{3} + \frac{1}{2}\pi dh}{\frac{d^2}{4}\sqrt{3}} \\ &= 1 + \frac{2\pi h}{d\sqrt{3}} \end{aligned} \tag{5.2}$$

For a sphere diameter of 500 nm and a pillar height of 50 nm the surface gain according to equation (5.2) is 1.36 corresponding to 36 percent additional surface area. Due to imperfections in the fabrication process, which does not create ideal geometric shapes, these values can only be of a theoretical nature and are considered an approximation. However, it illustrates how the increase in surface area depends on the parameters of sphere diameter and structure height. In order to maximise the surface gain the height should be increased, while it scales inversely with the sphere diameter. The relation between surface area and height is easy to understand whereas the scaling argument for the diameter seems counterintuitive at first glance since a reduction in diameter reduces the length of the arc segments. But due to denser packing of smaller spheres more interstices are created within the area of the original unit cell, which overcompensates for the shrinkage in arc length illustrated in figure 5.5. The spheres are overlaid by another array with half the diameter for comparison. Instead of one large interstice now there are four smaller interstices present in the unit cell. In this case the total arc circumference for the larger spheres is $1 \times \pi \cdot d$ and for the smaller ones $4 \times \pi \cdot d/2$, which is equal to $2 \times \pi \cdot d$. Therefore the effective circumference doubled by halving the sphere diameter as suggested by the surface gain formula.

So far various methods have been reported for the deposition of mono- and multilayers of sphere arrays on to substrates. One of the first methods to be explored was *Spin Coating* [74]. The sphere solution is simply spun on to the substrate using a spinner that is commonly used to coat samples with photoresist in lithography. The rotation helps to spread the solution over the substrate and aids in the evaporation of the solvent. Another method is *Electrostatic*

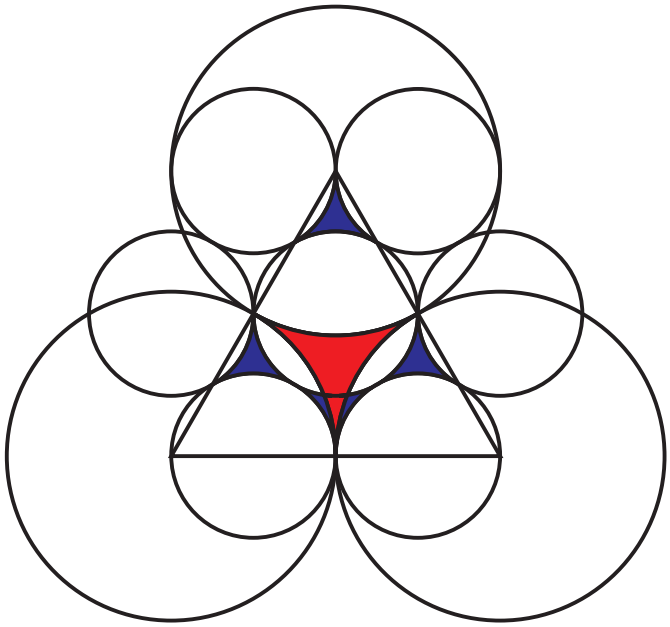

Fig. 5.5: Overlay of sphere arrays with diameters d and 2×d - corresponding interstices are marked by different colours

Deposition [77] which utilises the creation of attractive surface charges on the particles and the substrate. The result is however not periodic arrays but random deposits. A similar technique is *Electrophoresis* [78] where electrical currents are used to guide the deposition of the spheres and is therefore limited to conductive samples. *Dip Coating* [79] is an evaporative method where a substrate is dipped into a heavily loaded sphere solution and then withdrawn at a low constant velocity. The thinning of the water film along the contact line between solution surface and substrate during withdrawal causes the formation of nuclei as described above that subsequently grow as the substrate is further retracted from solution. Closely related to that is a process using a liquid meniscus of sphere solution which is dragged across the substrate with the help of an inclined glass slide [80]. The deformation of the water film with the help of the glass slide directs the crystallisation along the drag axis. Another possibility is *Self-assembly at an interface* [81]. In this process the solution is placed at the interface between two immiscible liquids or a liquid and a gas phase. This constrains the solution into a two-dimensional plane. After assembly the array can be transferred to the desired substrate by dipping it into the liquid

and bringing it up from underneath the array. A similar technique uses the *Langmuir-Blodgett* process [82]. Here nanospheres assemble on the water surface in a special trough, then they are compressed by a movable barrier and finally transferred to the substrate by vertically dipping at the end of the trough followed by slow retraction. Other evaporation techniques control the parameters by placing the substrate with the solution into airtight containers with reduced temperatures to lower the evaporation speed of the solvent [83]. Pre-patterned substrates have been used to shape the geometry of deposits as spheres seem to preferentially settle at corners or in grooves [84]. In combination with flow cells streams of sphere solution were guided along such pre-patterned substrates for deposition.

For this work the focus was put on three approaches that do not require special equipment and are easy to implement. It has been investigated whether they are suitable for the use on neural implants. The main criteria for the evaluation of these methods was a large area coverage with a close packed mono-layer and that it can be applied to gold surfaces. The three methods chosen were deposition by spin coating, evaporation in a closed container and the assembly of sphere arrays at an air-water interface. All three methods can be employed using only standard cleanroom equipment. For experimentation 10 mm x 10 mm sized chips were cut from 4-inch silicon wafers. The chips were first immersed in isopropyl alcohol (IPA) and put in an ultrasonic bath for 5 min to remove any particles from the surface. Then a 1:1 mixture of sulphuric acid and hydrogen peroxide (piranha solution) was prepared and the chips immersed for 10 min immediately after solution preparation as it is an exothermic reaction that quickly cools off. The piranha removes organic contamination and additionally makes the surface hydrophilic through hydroxylation. This helps the solution to spread across the sample and wet the entire surface. To produce gold samples, the cleaned chips were coated with gold of desired thickness by either sputtering or thermal evaporation. Gold does not stick very well to other materials necessitating a thin adhesion layer. Usually chromium layers of 5 to 20 nm thickness are used to provide adhesion. But chromium is toxic to the human body, so titanium was used instead as adhesion promoter. Titanium performs less well than chromium so that thicker layers between 15 and 40 nm have to be deposited. The spheres used in the experiments were 0.132 μm, 0.204 μm and

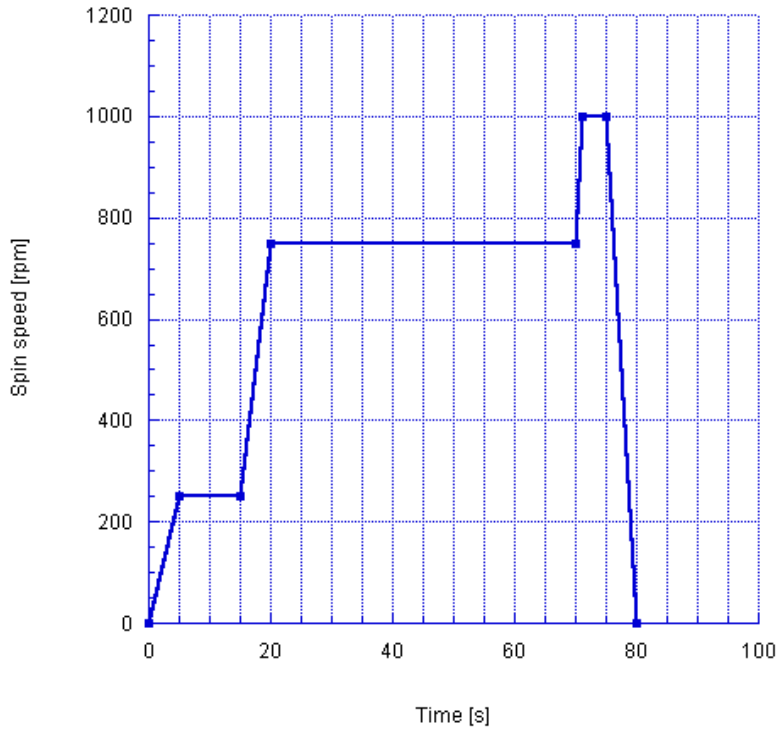

Fig. 5.6: Optimized spin speed profile for improved substrate coverage

0.520 μm diameter polystyrene latex particles in 1% wt concentration from Agar Scientific and particles of 0.2 μm diameter from the 5000 series latex microsphere suspension with a 10% wt concentration and size distribution $\leq 5\%$. A high size uniformity is important to avoid ordering defects that disrupt crystallinity.

5.2.1 Spin coating

Experiments were conducted on silicon and gold substrates. In the beginning silicon was used to gain control of the process parameters, which were then applied to gold surfaces. Naturally gold is hydrophobic causing water drops to ball up with a large contact angle on the surface. For sphere arrays to be formed the water needs to spread out into a thin layer in order to start the assembly process. Therefore the gold surface needs to be chemically treated. One possibility is the use of piranha solution. But the violent exothermic reaction sometimes causes the gold to peel off the silicon chip because of the poor adhesion. Other researchers reported the addi-

tion of a small amount of the surfactant triton-X dissolved in methanol to the sphere solution [85]. However, during testing it was observed that this interferes with the SEM imaging of the spheres as the images appear blurry, a effect often associated with electron charging in insulating substrates. After coating these samples with a thin metal film by sputtering, the image quality could be restored to some extent. But this step consumes additional time and the sample cannot be used for further processing afterwards.

Better results were obtained with ethanol mixed with the sphere solution in a 1:1 ratio. Ethanol is an organic solvent that spreads well on the gold surface. The prepared substrate is placed on the vacuum chuck of the spinner and a small amount of solution (5-10 μl) is applied with a pipette. The spin program is then started immediately. A variety of spin speeds is reported throughout the literature. The main task is to find a suitable spin speed profile for this application to achieve optimum spread and sphere assembly. A series of trials was performed varying the spin speed and spin duration. The sample needs to be spun until the solution is completely evaporated. Higher spin speeds cause the solvent to evaporate quicker but also throw off sphere solution. A two step profile was applied. The initial step spreads the sphere solution over the entire substrate and the second step served to completely evaporate the solvent. Ramps between the spin steps were included to slowly bring the sample to the desired revolutions to reduce the amount of solution spun off immediately because of high velocity gradients. Based on the area coverage with densely packed spheres the spin profile pictured in figure 5.6 gave the best results. Areas on the order of 10,000 μm^2 (figure 5.7) can be achieved. The islands show sufficient ordering with intermediate small defects or gaps. But the position of the areas is random and they are separated by large voids making it unreliable for coating micro-devices and therefore not suitable for the intended application. Especially incorporation into a batch-fabrication process would be difficult as the device structures would hinder the solution flow and cause preferred nucleation along the edges of the device layers.

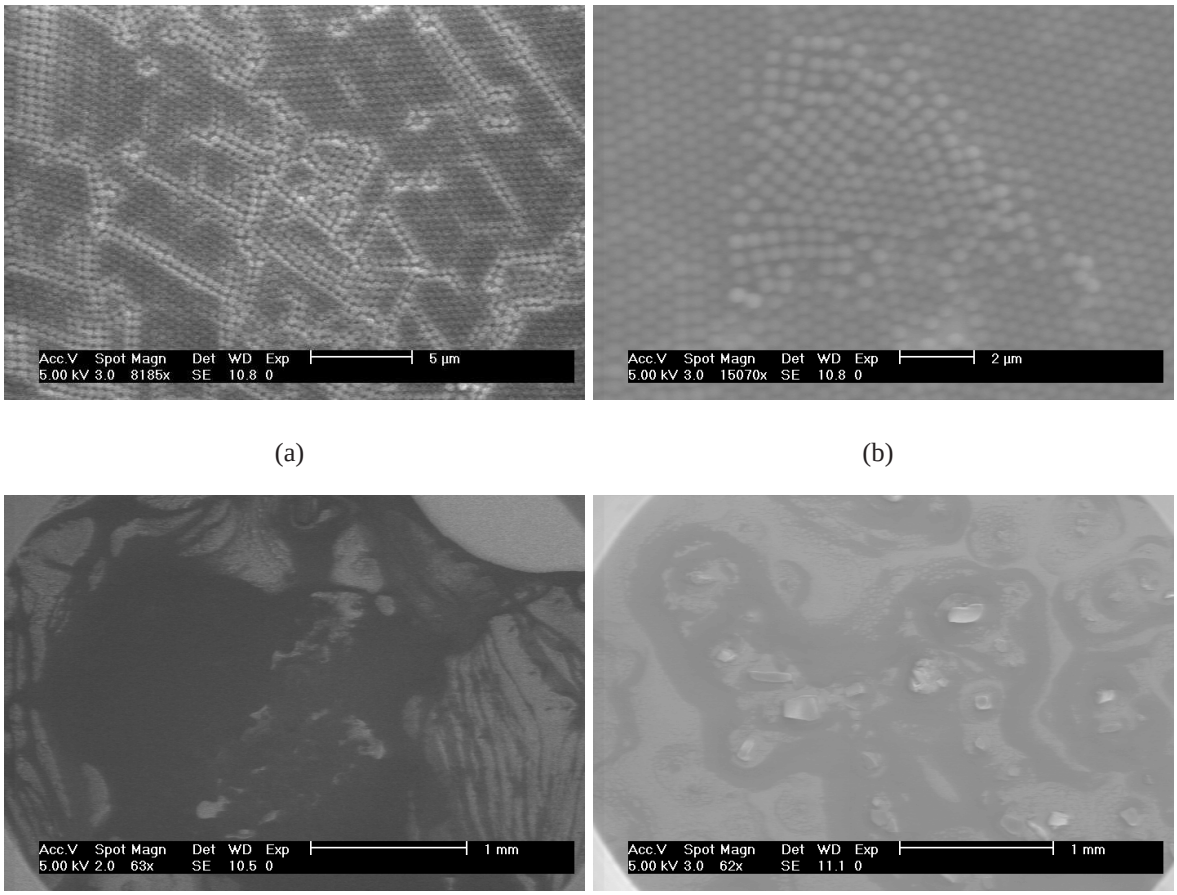

Fig. 5.7: SEM graphs of sphere assembly by spin coating: (a) 500 nm particle assembly with a variety of defects like gaps and disordering, (b) well ordered layer with intermittent double layer arrangement, (c) large area coverage with dark parts representing particle arrays and light parts blank area, (d) typical drying topology with nucleation centres formed by lumped particles and circularly surrounding monolayers

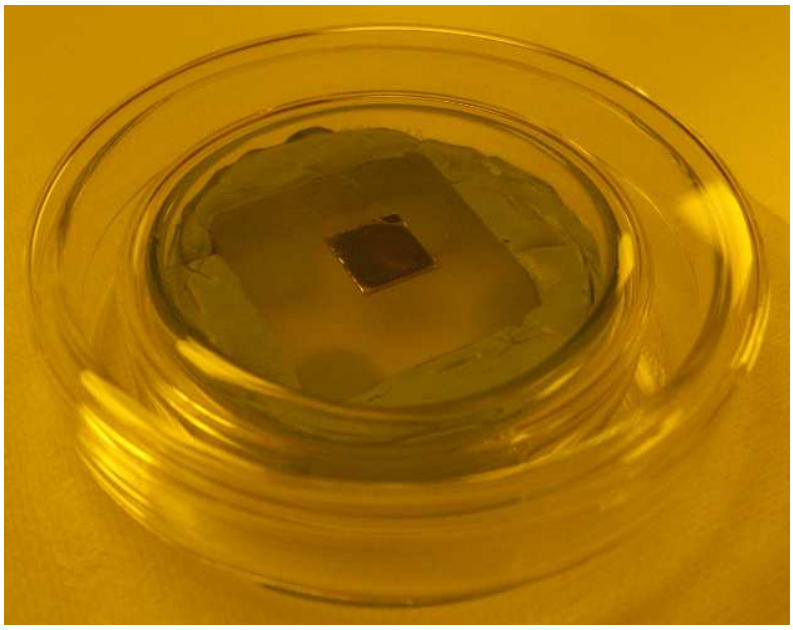

Fig. 5.8: Experimental set-up for evaporative technique

5.2.2 Controlled Evaporation

For this method custom-made boxes are used to control the evaporation rate of the solvent. As described earlier the rate has a strong influence on the ordering of the sphere array. The boxes are sealed air-tight to have their own microclimate. During solvent evaporation the confined air becomes saturated and further evaporation is slowed down. In addition the sample is often cooled to further reduce the rate of evaporation. This can be done by placing the substrate on a heat sink like a block made from a good thermal conductor like copper. A Peltier cell is attached to the copper brick acting as a thermal pump. The other side of the Peltier element is cooled by a water-flow cell to remove the excess heat. Through the voltage applied to the Peltier cell, the temperature can be set within a certain range. During experimentation it was found that a much simpler set-up without any cooling is sufficient to achieve acceptable results. Two sets of Petri dishes were used as the container. Confinement was done by putting one dish upside down on top of the other and placing it inside the other Petri dish set in the same manner as shown in figure 5.8. A perspex block was stuck to the bottom of the first Petri dish to act as the substrate holder. The block had an angle machined into it to slant the resting plane of the

sample to deform the solution drop from its equilibrium shape so that the film was thinner at the top and crystallisation proceeds in a directional manner toward the bottom. The angle should be chosen carefully to prevent the drop from completely sliding down the surface and collecting at the bottom.

The volume of the container is an important parameter as smaller volumes saturate faster and hence the evaporation rate is lower. Therefore the Petri dish was of smallest possible size so that it is just big enough to accommodate the substrate holder. The volume of the inner set was further reduced by filling the available space with an adhesive plasticine mass called Blu-Tack. The drop amount of solution on the substrate also influences the evaporation rate. A larger amount of solvent will take longer to evaporate. In contrast to spin coating the whole amount of solution remains on the sample for evaporation, which means that the number of particles placed on the substrate is fixed. This is important because the particle number determines the arrangement into separated islands, closed mono- or multilayers. For a monolayer the amount of particles has to be sufficient to cover the entire substrate once. The number of particles in the solution is given by the concentration of spheres in the solution. For different drop amounts this concentration has to be adjusted to maintain the desired particle number. This can be done using some simple calculations. A rough estimate of the amount of particles needed to cover the sample is calculated by

$$n = A_{sub}/A_{sphere} \tag{5.3}$$

with n the number of particles, A_{sub} the substrate area and A_{sphere} the cross-sectional area of a sphere. The desired concentration is

$$c = \frac{n}{V} \tag{5.4}$$

in particles per ml with V the drop volume in ml. Companies often supply their sphere solutions with the concentration given in weight percentage. Duke Scientific states a formula to translate their weight percentage into molar concentration as

$$c^* = \frac{6 \cdot \rho_{solvent}}{\pi d^3 \left(\rho_{solvent} + \frac{\rho_{beads}}{\omega} - \rho_{beads} \right)} \tag{5.5}$$

where $\rho_{solvent}$ and ρ_{beads} are the densities of the solvent and the sphere material, d the sphere

diameter in centimetre and ω the concentration in weight percentage. For 200 nm diameter polystyrene spheres (ρ = 1.05 g/cm^3) dissolved in water in a ratio of 10 % wt this gives a concentration of 22.85 x 10^{12} particles per ml. After obtaining the value, the solution needs to be adjusted to the desired value. For 1 ml of new solution the desired concentration is divided by the supplied concentration to give the amount of sphere solution needed, which is then filled up to 1 ml with solvent. To assist the spreading of the drop, ethanol is used as filling liquid.

After identification of all relevant process parameters the right set of values to create a suitable assembly have to be determined. The parameters studied were chamber volume, slope angle, amount of liquid placed on the sample and number of particles. The chamber volume was modified by packing with Blu-Tack as already described. Different configurations of plasticine in the dish were tested. The Petri dish was either left empty, filled to the height of the sample holder or packed up to the glass rim. An empty chamber resulted in an evaporation rate that is too fast for continuous coating of the sample. This is observed through a pattern described by slip-stick motion where the spheres assemble in stripes. When the evaporation rate increases because of film thinning, sphere ordering is disrupted and the stripe is followed by an uncoated area. As evaporation slows down stripe formation starts again until the next rupture occurs leading to the observed pattern. For a completely filled Petri dish the evaporation rate is too slow and the formation of double and multilayers is observed.

The best result was achieved with an intermediate fill level as large area monolayers were created through fine tuning of the evaporation rate by controlling the drop volume and particle number. Optimum conditions were found to be a 10 μl drop with twice the number of particles needed for monolayer coverage. The 10 μl evidently set the right rate of evaporation compared to 5 μl and 15 μl which were also tested. Doubling the particle number resulted in larger covered areas compared to the single amount. A certain portion of particles deposit in thick drying rings at the edges of the sample. The reason for this behaviour is that at the start of the evaporation the curvature of the drop along the edges is larger, which locally increases the surface area and subsequently the rate of evaporation. As a result a large amount of spheres is drawn in to the edges where they then settle into thick stacks and circumvent an even distribution due

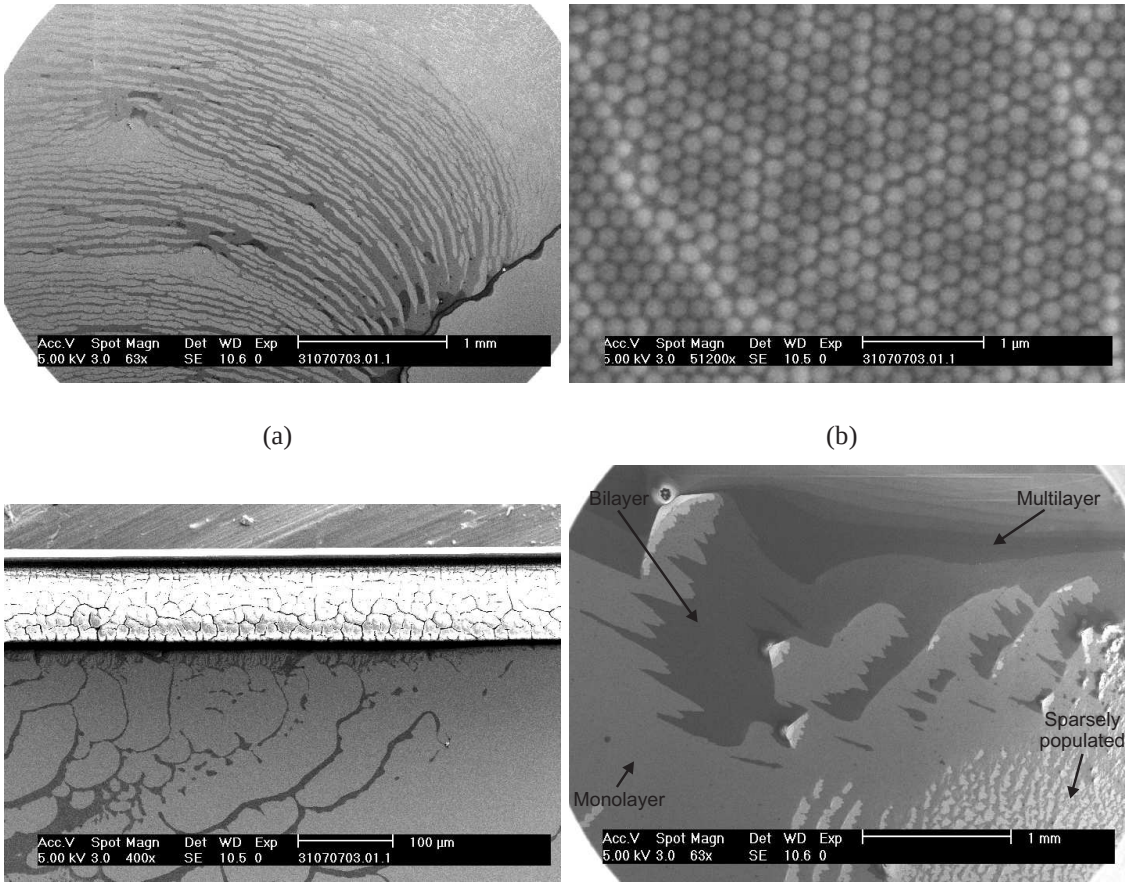

Fig. 5.9: Evaporative coating results: (a) typical stripe formation for too high evaporation rates, (b) monolayer of 200 nm particles, (c) drying ring on the edge of the sample that consumes a large amount of particles, (d) different film morphologies present in large area coverage

to the non-available spheres. Increasing the particle numbers compensates for this effect. The studied substrate angles were 5°, 10° and 15°. They were set by using different sample holders manufactured with the corresponding angles. The holder with the best results had a 5° angle.

Using the optimised values for the parameters led to a rate of solvent evaporation that facilitated the coverage of large portions of the samples with areas of continuous monolayers with intermediate parts of bilayer arrangement and uncoated gaps in between. They offer better ordering than the spin coated samples, which is attributed to the increased control over the evaporation process. For small samples this procedure is well suited. Larger samples pose certain

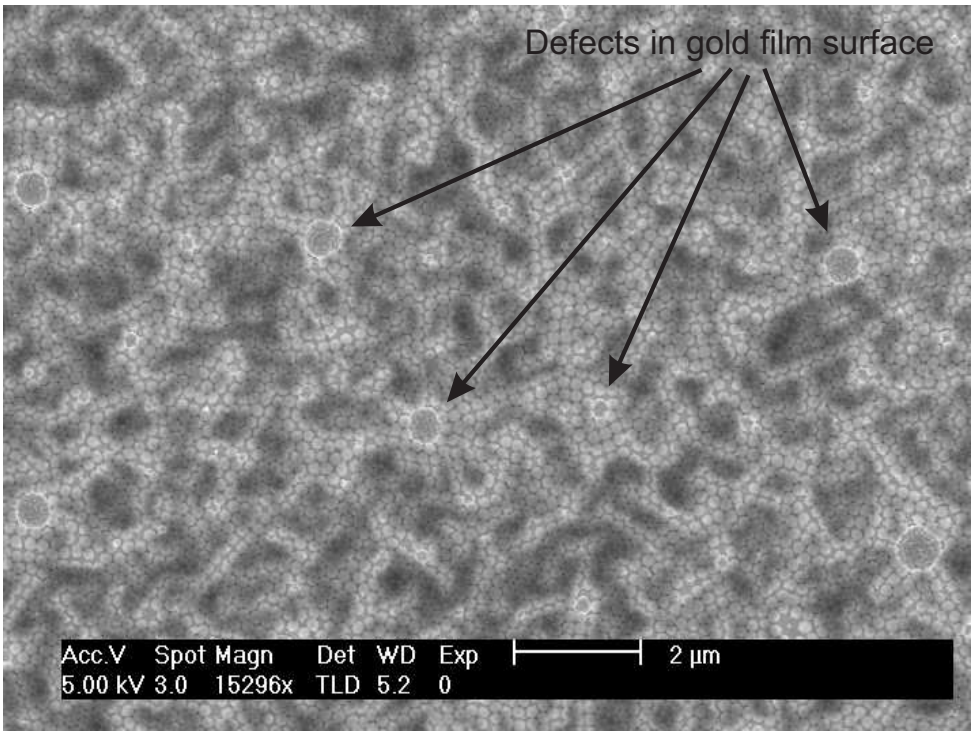

Fig. 5.10: Defects in the gold film hindering the assembly of spheres

limitations since they cannot be fitted into Petri dishes and would require the use of beakers or specially made boxes. The larger volumes of these containers change the evaporation conditions, so the parameters would have to be readjusted for each sample size. Furthermore figure 5.10 illustrates why the substrate should be really planar. Even the minute defects in the gold film structure led to disordering and the spheres were not able to cover them. Structured device layers would hence prove insurmountable obstacles for the film formation process. Single devices might be coated using this technique but it is not suited for wafers with large amounts of devices.

5.2.3 Assembly at the air-water interface

Through this method nanospheres are trapped at the air-water interface and then left to assemble into monolayers on the water surface. A beaker was used as vessel for the assembly. It was cleaned with ethanol and then rinsed in deionised water before filling up to 70% of its volume

with deionised water to allow for enough space to submerge a piece of silicon sufficiently well. A portion of the 10% wt solids solution of 200 nm spheres was mixed in equal ratio with ethanol. 30 μl of the mixture was then applied to a 30 mm x 30 mm piranha cleaned silicon substrate via pipette and left for a few seconds in order to spread over the entire chip and then carefully immersed into the water in the beaker with tweezers. During immersion the solution transferred to the surface of the water. Once a cloud of sphere solution formed in the water just in front of the substrate immersion was stopped and the silicon removed from the water. The cloud is an indication of the surface being tightly packed with spheres because any additional spheres could not transfer to the surface and were dragged into the water by further immersion. Some of the spheres were unavoidably dispersed into the water from the film but the whole water surface was covered. Attempts to directly apply the solution on to the water surface via syringe achieved less favourable results as the forces seemed to be too large, the main portion of the mixture dissolved in the water and only sparsely distributed islands of spheres were formed.

After application of the solution the beaker was covered with a Petri dish to protect it from external air flows while the remaining ethanol evaporated. A clean, hydroxylated sample was then slowly dipped into the water and subsequently placed underneath the floating sphere array. Slow and careful retraction from the water transferred the spheres on to the sample. A thin water layer was trapped between sample and spheres that needed to evaporate in order for the spheres to stably settle on the samples. The sample was then ready for inspection and further processing. In this procedure the spheres benefited from sustained mobility on the water surface in comparison to solid substrates as they remained mobile on the water interface the whole time. The method was successful in completely covering the entire samples with a monolayer except for the part covered by the tweezers. The spheres were densely packed and exhibited good ordering. However small cracks between the sphere islands were present. These are believed to be caused during the retraction of the sample from the water by small vibrations and strongly depend on the skill of the experimenter.

The method was also tested for compatibility with smaller spheres of 137 nm diameter since the previous methods experienced difficulties. Because the 137 nm suspension had a

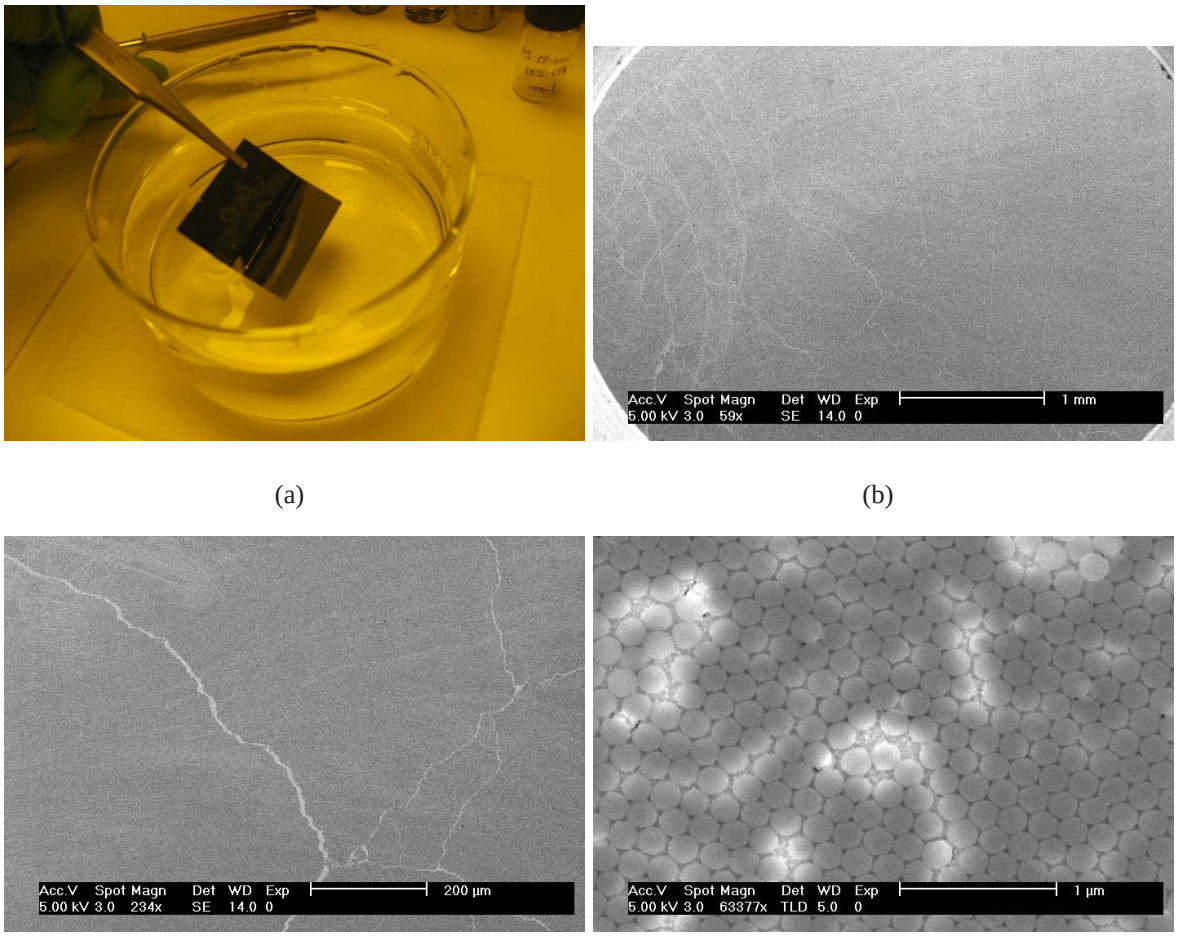

(a) (b)

(c) (d)

Fig. 5.11: Floating technique results: (a) solution transfer to the water surface, (b) uniformly coated large area, (c) magnification of cracks separating sphere islands, (d) sphere arrangement through interface transfer

1% wt concentration it had to be concentrated by placing 10 ml of solution in an open vial on a hotplate at 60° C and let it evaporate until the volume is reduced to about 1 ml. This is necessary to ensure that close packed arrays form, otherwise the number of spheres on the water surface is too low and no array formation is observed. The same steps as described above were performed and similar results were achieved demonstrating that it is also viable for smaller size preparations. However, for routine use a commercial 10% wt solution should be used because during boiling down coagulation occurred causing intermediate lumped deposits. Small particle size solutions with narrow size distributions are harder to obtain as the controlled chemical synthesis is more difficult. An advantage of interface assembly is the easy scalability using larger beakers and increased amount of solution. Devices with large aspect ratios can be coated without problems as will be shown in chapter 7 by simple dipping.

In summary the assembly at the interface was the most suitable method for the intended use as it combines sphere assemblies of good quality with a versatile coating mechanism that is suited for small chips as well as microfabricated devices. All further investigations were carried out with samples prepared using this method. After solvent evaporation the spheres adhere to the substrate very well so that in the next step they can be used as masks for metal deposition under vacuum.

5.3 Masking layer deposition

One of the most important steps for the process is the deposition of the mask layer. This determines the shape of the resulting structure as the milling step transfers the etch mask pattern into the gold. Even though directional deposition methods were used, at some point the interstice became clogged through material build up. This prevents further metal from reaching the substrate and hence limits the possible thickness. Initially sputtering in a Edwards Auto 306 rack with FL400 chamber was used for mask deposition. The working principle of sputtering however causes the sputtered atoms to have trajectories that are not strictly perpendicular to the substrate surface, which makes interstice clogging more likely. The reason is that once the atoms leave the titanium target they have to pass through the plasma in order to reach the sam-

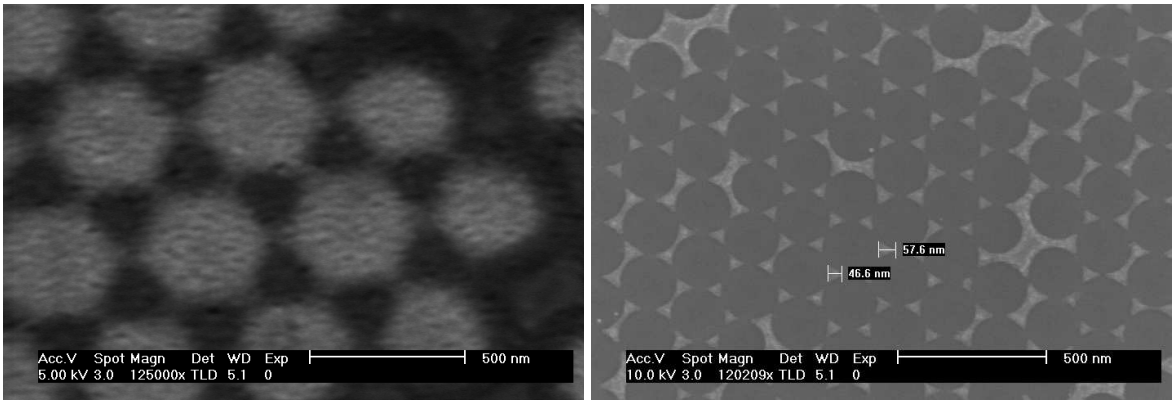

(a) (b)

Fig. 5.12: Comparison of the deposition patterns generated by (a) sputtering and (b) E-beam evaporation

ple. In the plasma they are subjected to collisions with gas atoms deflecting them from their path. To overcome this problem deposition was changed to e-beam evaporation in an Edwards Auto 500 E-beam and filament evaporation system. Here the metal atoms travel by line-of-sight in vacuum after leaving the source and better results were achieved (see figure 5.12). In order to reduce the probability of impacts and collisions with residual molecules, the mean free-path length was extended by evacuating the chamber to a pressure of at least 2 x 10^{-6} mbar.

Clogging still occurred eventually. The installation of a collimator between source and substrate can be considered. It acts as a spatial filter to let only particles through that travel perpendicular to the substrate, which should improve deposition but has not been used during this work. Instead the interstice size was enlarged by subjecting the sphere array to an oxygen plasma. This reduces the sphere diameter by etching the outer polymer layers away. A small plasma power allows to fine tune the interstice size. Two different machines were used for the plasma etching, a 100-E Plasma system from Technics Plasma and a Plasmalab NGP80+ from Oxford Instruments. Surprisingly even though the same process parameters, 100 W RF power and 30 sccm oxygen gas flow, were used in both etchers the obtained results were not equal. Apart from different reactor geometries the only visible difference was the cooling of the substrate in the Oxford machine, which was set to 20° C. A sufficient substrate cooling seems necessary for the etching as elevated heating can cause the polymer material to re-flow and

form connected polymer areas as was experienced during the experiments when using the 100-E Plasma system, which has no cooling for the substrate holder. Alternatively short etch steps with intermediate pauses for cool down might be used. It was also noticed that the etch rate for both systems differs significantly. As for the Technics Plasma system etching proceeded slower so a higher RF power of 150 W was additionally tested. The initial sphere diameter was 200 nm. The averaged sphere diameters after etching in both systems are summarised in tables 5.1 and 5.2. The amount of sphere material removed was plotted versus etch time. The slope of the graphs corresponds to twice the etch rate because the spheres are etched from both sides (figure 5.13). Both show almost linear behaviour. Comparing the results obtained from both systems a substantial difference in the morphology of the spheres after etching is observed (figure 5.14). The Plasmalab NGP80+ produced smooth surfaces with no protrusion between the spheres. They possess an oval shape and are well separated from each other. The Technics Plasma system in contrast created slightly more deformed spheres and they stayed connected through thin polymer bands between their former contact points.

Tab. 5.1: Sphere diameter after etching - 100-E Plasma

	etch time [sec]		
RF power [W]	60	120	180
100 W	176 nm	155 nm	142 nm
150 W	162 nm	148 nm	128 nm

An important point to bear in mind when reducing the sphere diameter is that this also reduces the limit of possible material deposition before it forms a closed layer that traps the spheres underneath and prevents them to be removed. If interstice clogging is neglected, the

Tab. 5.2: Sphere diameter after etching - Plasmalab NGP80+

etch time [sec]				
10	20	30	40	60
175 nm	152 nm	132 nm	110 nm	55 nm

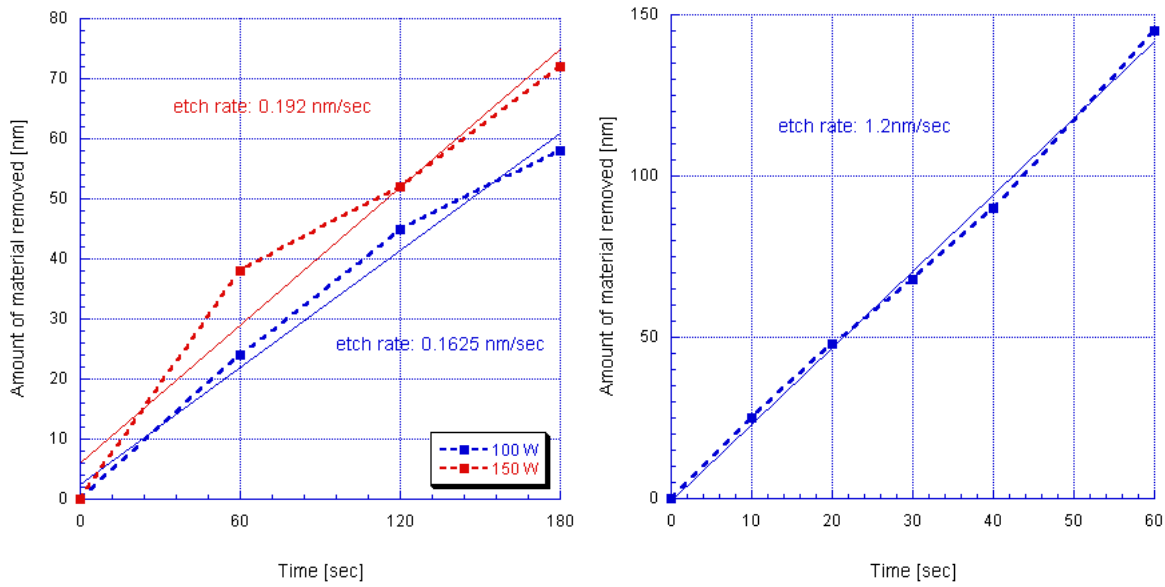

(a) (b)

Fig. 5.13: Extracted etch rates from curve fitting of etch data for (a) Technics Plasma and (b) Oxford systems

maximum theoretical thickness to be deposited is smaller then half the sphere diameter. After filling the interstice to half the sphere diameter, the material growing up from the bottom connects with the layer on top of the spheres to form a continuous closed film. A positive aspect of the sphere etching is the increase in circumference of the created nanostructures thus increasing their surface area while maintaining the packing density.

The etched spheres are then used as a mask during titanium evaporation (figure 5.15). Depending on the amount of sphere diameter etched a variety of structures can be achieved. While short etch times lead to triangular titanium islands, for longer etch times the metal islands can connect with each other to form nano rings first and later thicker, pore-like patterns. For the Technics Plasma system this is prevented by thin polymer residue between the spheres, which keeps the islands from linking up. As mentioned earlier for prolonged etching the metal layer thickness is sufficient to form closed layers that trap the spheres with no possibility of removal. A thickness of 70 nm was deposited on all samples. For longer etch times more material is

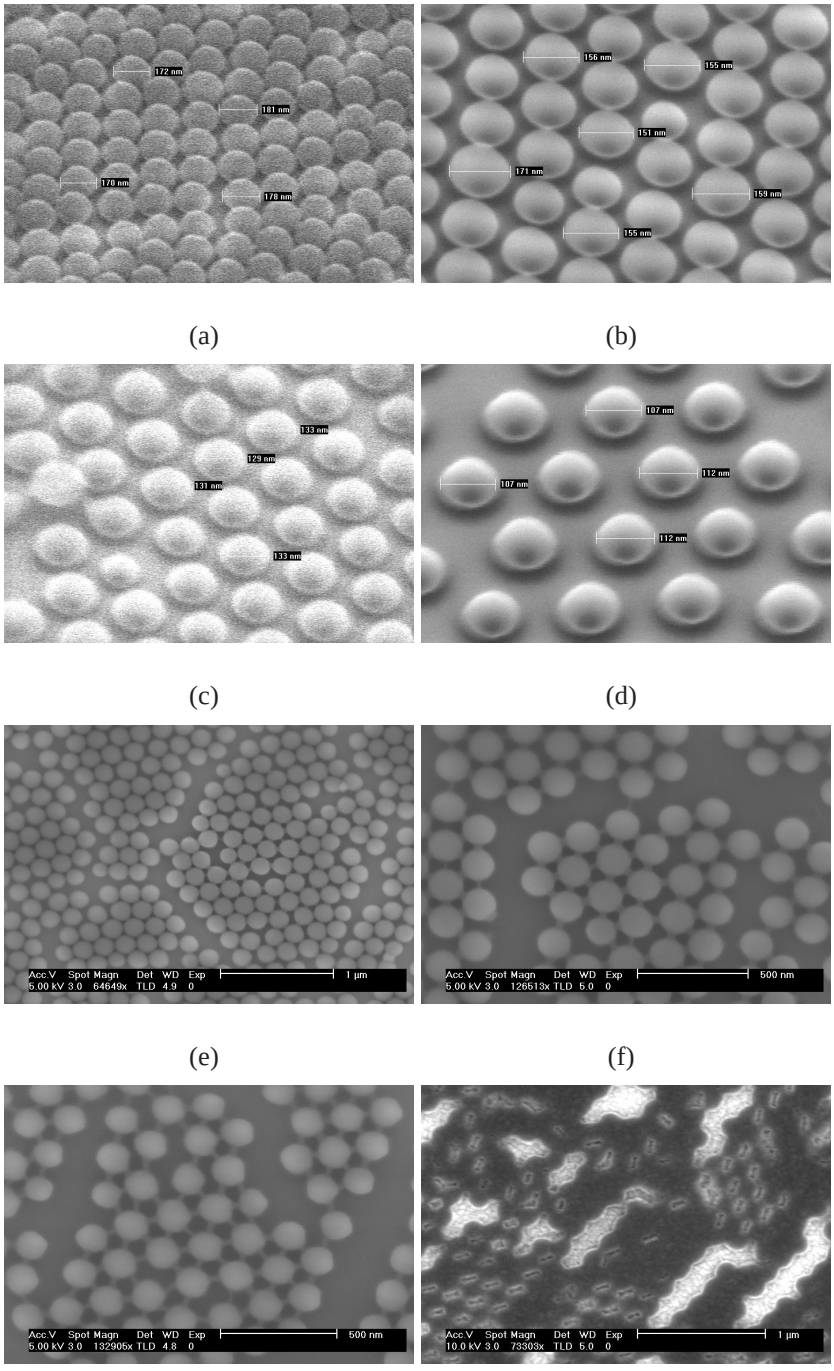

(a) (b)

(c) (d)

(e) (f)

(g) (h)

Fig. 5.14: Sphere etching results with Plasmalab NGP80+ at 100 W for (a) 10 sec, (b) 20 sec, (c) 30 sec, (d) 40 sec and with 100-E Plasma at 100 W for (e) 1 min, (f) 2 min, (g) 3 min; (h) Polymer re-flow due to heating

actually deposited on the substrate because of larger interstices and slower onset of clogging. The material thickness is monitored during deposition in the e-beam chamber by a quartz micro balance. Confirmation of these values by SEM revealed them to be consistent within a 10% error limit.

5.4 Ion beam milling

In order to achieve aspect ratios larger than 1 as well as scalability the etching method has to be anisotropic. For gold this is only achievable with dry etching methods. A number of etch gas compositions have been reported for the use in reactive ion etching (RIE) that combines chemical and physical etching in a dry gas phase of the etchant. Because these gas mixtures contain toxic, corrosive chlorine gas [86, 87] or more exotic gases [88], it was not possible to use them in the existing equipment even though especially the later one appears very attractive because of its high selectivity for noble metals over titanium masks. Instead ion beam etching (IBE) had to be used. Based on the milling rates reported for titanium and gold [89] a selectivity of roughly 1:4 is anticipated. IBE is a purely physical etch process using argon ions extracted from an argon plasma, which are accelerated and focused into a beam through a set of charged metal grids in a vacuum chamber. The kinetic energy of the argon ions causes them to knock out atoms of the sample surface upon collision. The main parameters for ion milling are the beam current, etch time and beam angle.

The milling angle is an important parameter for the general shape of the structures and material re-deposition has to be taken into account as well. At the beginning the angle was set to 90° in order for the milling to be perfectly anisotropic. But the structures turned out as round dome shapes. Conversely at a milling angle of 45° on the other hand the structures show cylinder shapes with nearly vertical side walls. Therefore it is possible to tune the slope of the side walls via the milling angle to create different shapes (figure 5.16). The reason for this behaviour is a combination of angle dependent sputtering yield and re-deposition [90]. The slope of the side wall will then be the same as the angle with the highest sputter yield. Changing the milling angle acts like the addition of an offset sputter angle, so that if the highest sputter

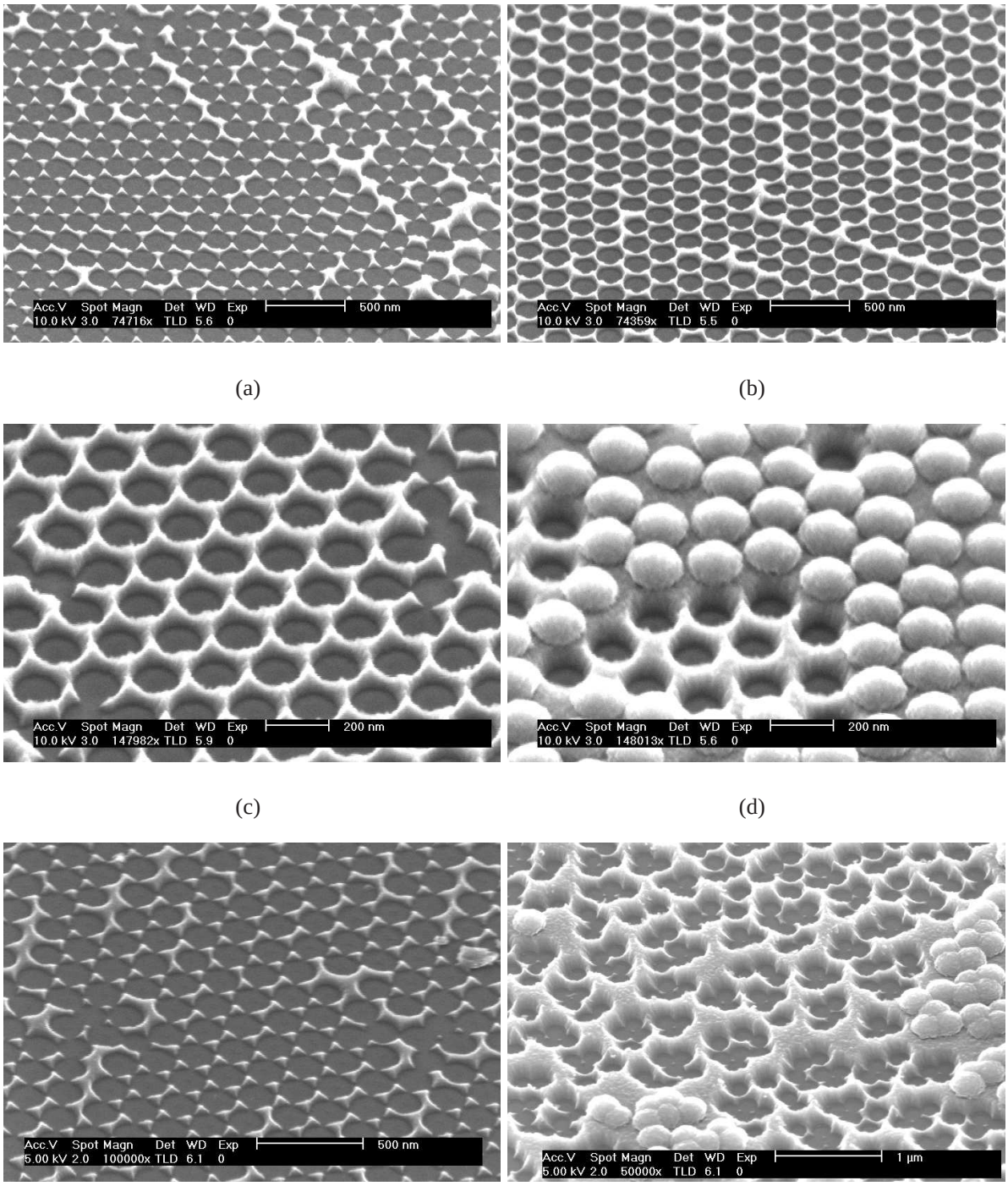

Fig. 5.15: Titanium deposition on spheres etched with Plasmalab NGP80+ at 100 W for (a) 10 sec, (b) 20 sec, (c) 30 sec, (d) 40 sec and with 100-E Plasma at 100 W for (e) 1 min, (f) 2 min

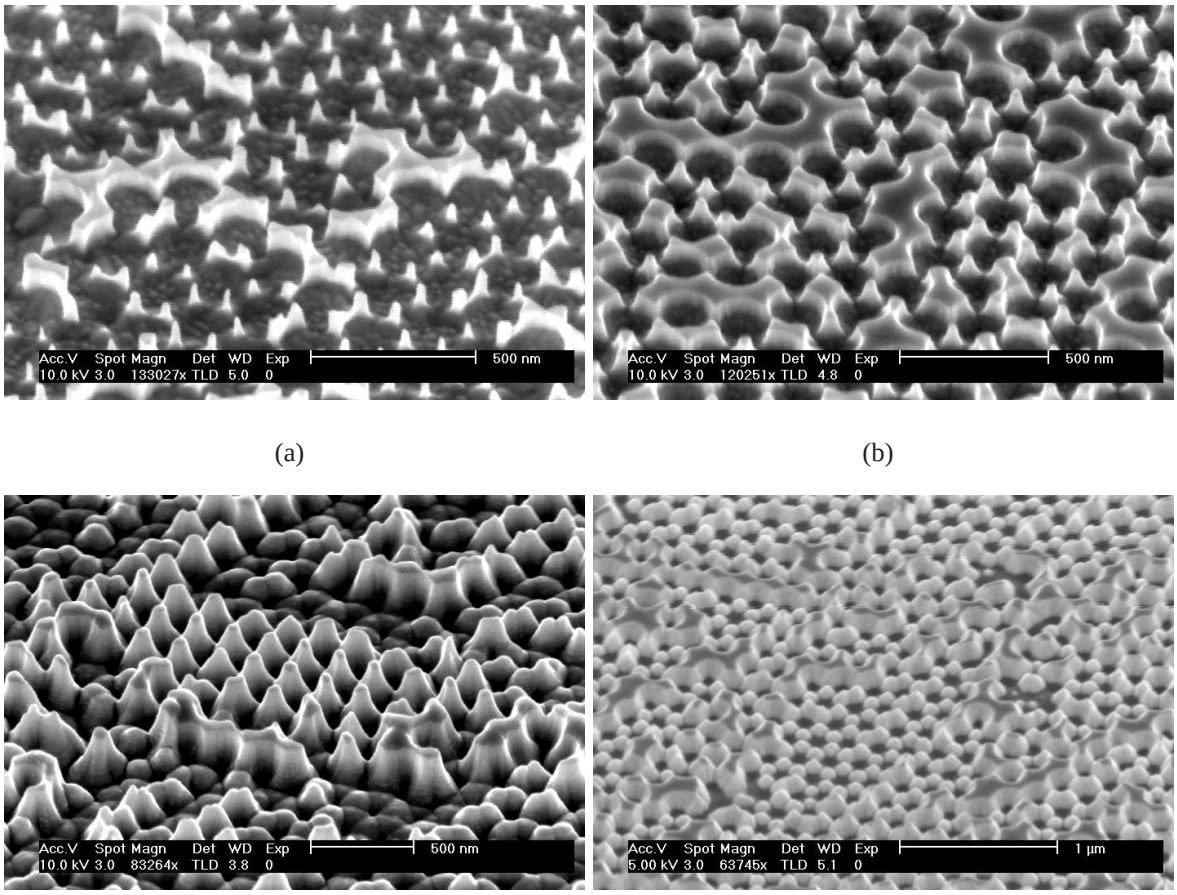

Fig. 5.16: Patterned gold surfaces for different milling angles: (a) 45°, (b) 55°, (c) 65°, (d) 90°

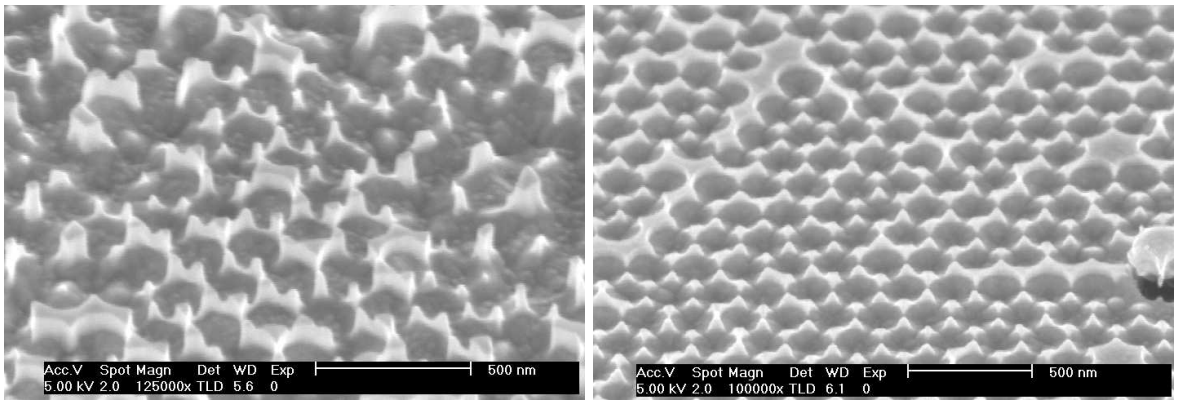

Fig. 5.17: Comparison of results for 45° milling with (a) Millatron IV and (b) IM150

yield angle for perpendicular beam incidence was 45°, rotating the sample an additional 45° would create side walls with 45° + 45° = 90°. While at 90° only low aspect ratios with limited scalability are produced, almost vertical side walls at 45° allow for better scaling. Intermediate angles combine scalability with an increase in side wall area through the slope.

To reduce the chance of re-deposition of milled particles the substrate holder is rotated at a constant speed around the axis perpendicular to the sample surface during milling. In the beginning a Millatron IV Ion Beam Milling System from Commonwealth Scientific Corp. was used to pattern the samples. It uses a magnetic field to curve the electron trajectory to increase the number of collisions required for plasma generation. The first samples that were fabricated using this machine showed no problems with material re-deposition and offered high aspect ratios. Unfortunately the system broke down and could not be restored because of the age of the equipment as spare parts were not available any more. Another type of miller located in the Physics Department had to be used to continue experiments. The machine used for later samples was an Oxford Applied Research IM150 ion milling system, which uses an RF power source to excite the gas for plasma generation. Here re-deposition was more severe as the material visibly accumulated at the base of the structures (figure 5.17) limiting the possible height of the pillars to a maximum of around 120 nm. The reason remains unclear as the principle operation in both systems is the same. The only noticeable difference was the etch rate. The older machine had a considerably lower etch rate compared to the newer one. It was investigated whether a change in etch rate significantly influences the re-deposition behaviour. Changing the RF power to influence ion generation or different voltages applied to the grids adjusts the kinetic energy and hence the beam current. A higher beam current increases the etch rate. While the nominal value of the RF power used for fabrication was 150 W, it was set to 100, 120 and 180 W for the experiment while the grid voltages were maintained at nominal values for plasma generation. The screen grid was supplied with 500 V and the accelerator grid value was 200 V. No significant change in material re-deposition was observed so that the difference in etch rate between the two systems can not serve as an explanation for the stronger re-deposition of milled material in the later one.

5.5 Surface structure characterisation

One of the first things to notice is that the patterned samples display a red colour under optical inspection instead of the typical clear golden shine. It is well known that colloidal gold with particle dimension below 100 nm shows an intense red colour due to light scattering [91]. This already indicates that the samples possess well defined features below that threshold just by looking at them. Another indirect indication of successful patterning is the change in wettability of the gold surface. Pure gold is a hydrophobic material resulting in water drops to ball up rather then spread out on the surface. Patterning the surface with sub-micrometre structures can change the wetting behaviour of surfaces. Indeed it is observed that on the gold samples prior to the modification water does not spread but is partially de-wetting while for the substrates after processing the water wets the whole surface.

To characterise the surfaces in more detail SEM was used to take images under a 45° angle with a slanted sample holder. Cross sections were taken by cleaving the sample with a diamond pen and setting the view angle to 90° by rotating the sample holder. The interplay of milling angle and sphere mask diameter allows for a variety of surface structures. Reducing the diameter of the masking particles transforms the structures from separated nanopillars through intermediate states of closer packed larger features to the creation of nanopore arrays. As described in the previous section the milling angle changes the slope of the side walls from near vertical to lower angles tapering the structure shape with a broader base and smaller top. Prolonged milling times increase the height of the structure with mask erosion limiting the maximum etch time. Examples are shown in figure 5.18 with process details summarised in table 5.3. Even

Tab. 5.3: Summary of fabrication parameters for different surface structures

Morphology	process details
singular vertical structures	10 sec oxygen plasma, mill angle 45°
tight packed structures with sloped side walls	15 sec oxygen plasma, mill angle 65°
pore-like configuration	20 sec oxygen plasma; mill angle 75°

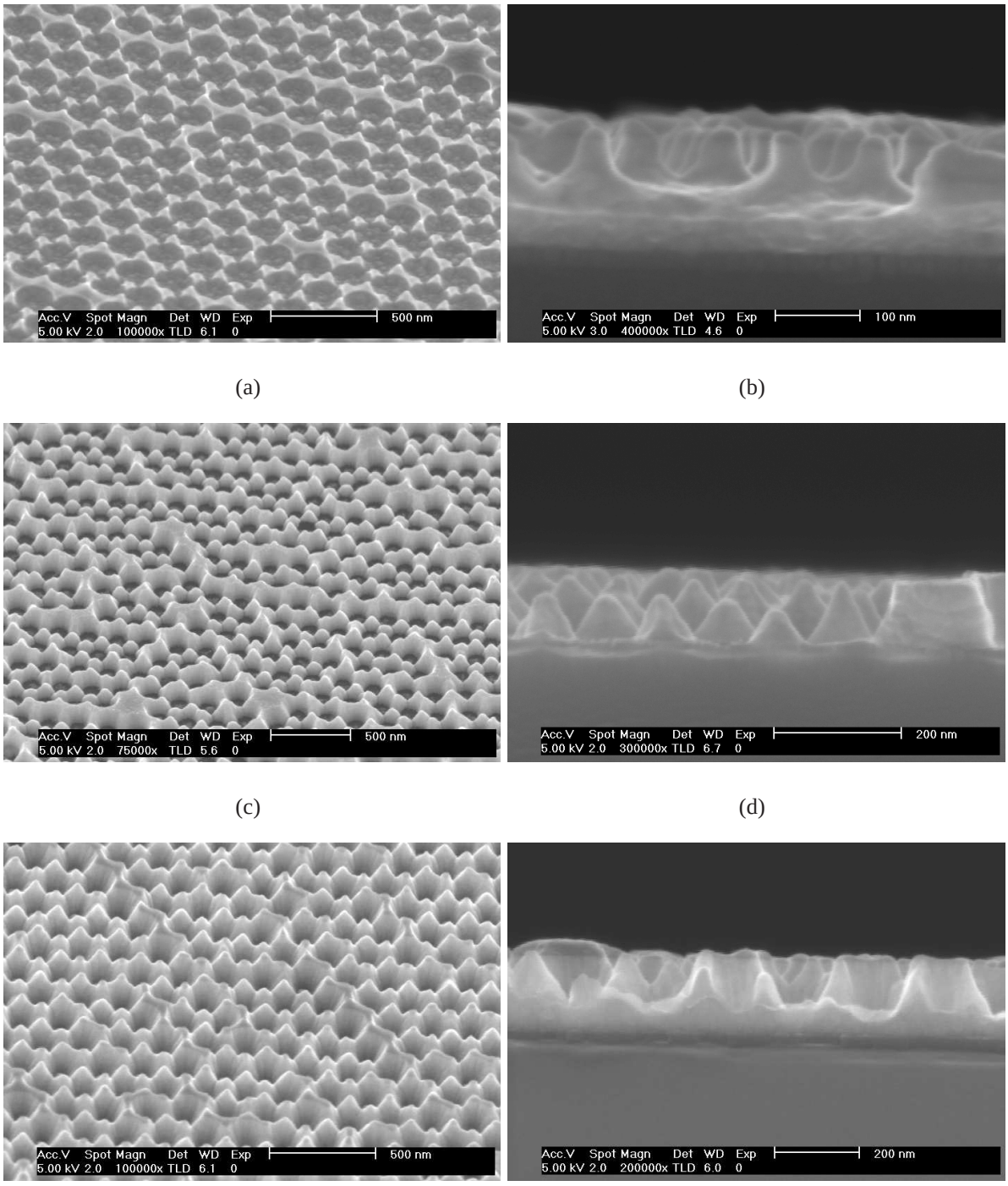

Fig. 5.18: Examples of the surface morphologies: (a,b) vertical pillars, (c,d) tight packed features, (e,f) nanopores

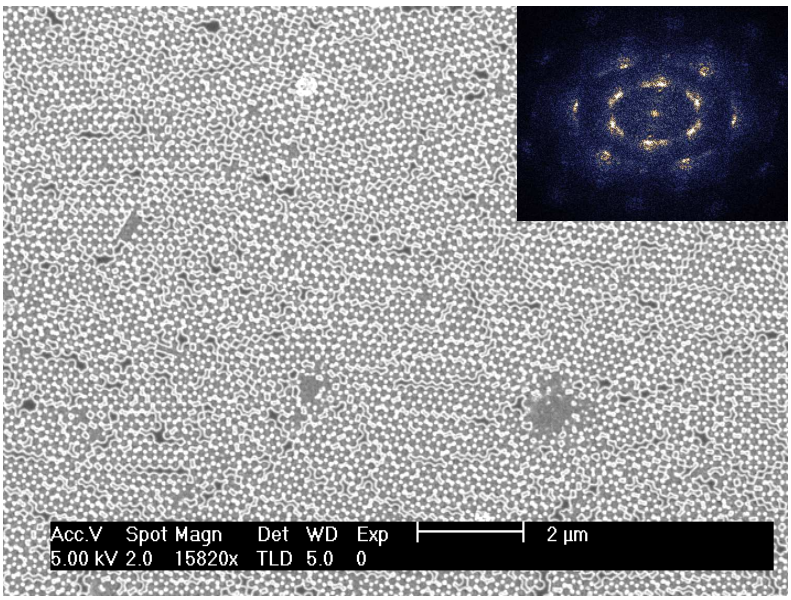

Fig. 5.19: Example of milled surface in top view with the Fourier transformation shown in the inset

though the mask deposition was done with non-perfect sphere ordering, Fourier transformation performed on SEM top views of the milled samples showed that they still exhibit periodic arrangements evidenced by the presence of distinctive spatial frequencies seen as bright spots in figure 5.19.

With a Digital Instruments Dimension 3100 Scanning Tunnelling Microscope (STM) surface roughness measurements were performed and the increase in surface area probed. For reference a plain film of gold was measured as deposited. An unpatterned sample milled together with a masked one was used to show that the milling itself does not induce any surface roughening and additional surface area is solely created by the nanostructuring process. For a 5 μm by 5 μm scan the surface area was 25.35 and 25.41 μm^2 with a root-mean square roughness of 1.87 and 1.95 nm respectively. The small roughness is attributed to the gold deposition process. Measurements performed on a sample with isolated pillar features (figure 5.20) showed a boost of surface area to 49.98 μm^2 effectively doubling the amount of surface area and an increase in surface roughness to 40.7 nm. Another sample (figure 5.21) with more closed, tighter packed structure had a smaller measured area of 32.22 μm^2 even though from the SEM image it must be deduced that the surface is actually larger then in the previous sample. The expla-

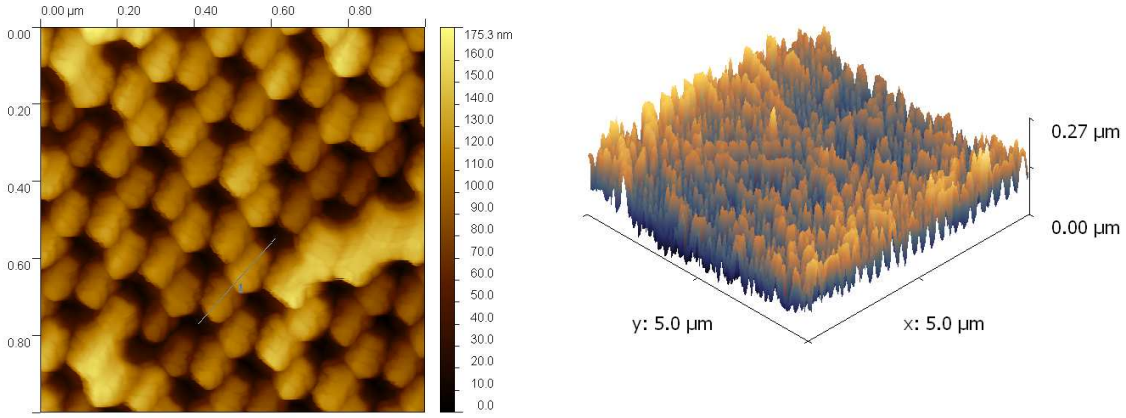

(a) (b)

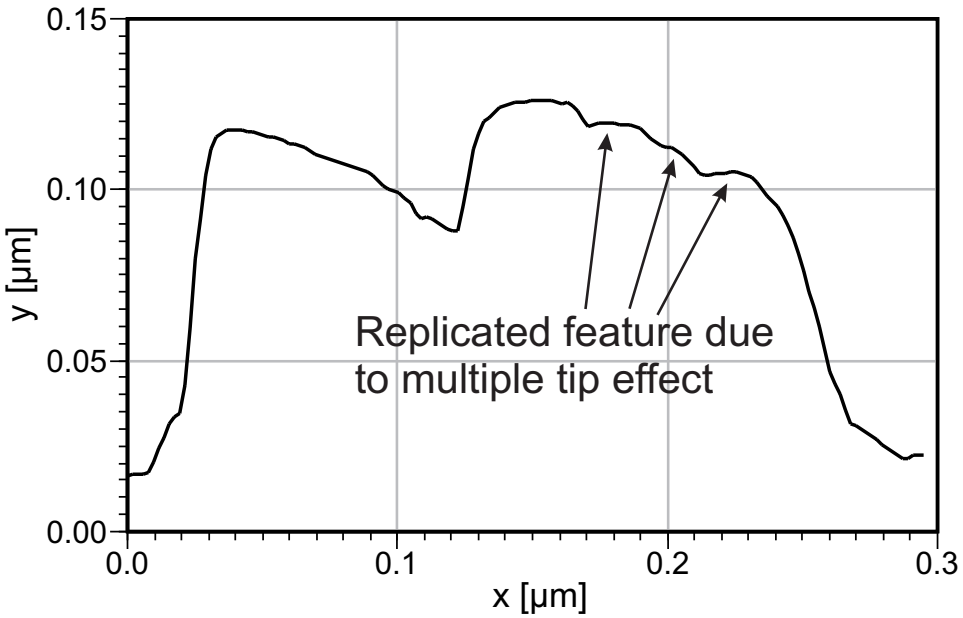

(c)

Fig. 5.20: Surface characterisation of vertical structures: (a) STM scan, (b) 3D view, (c) line profile

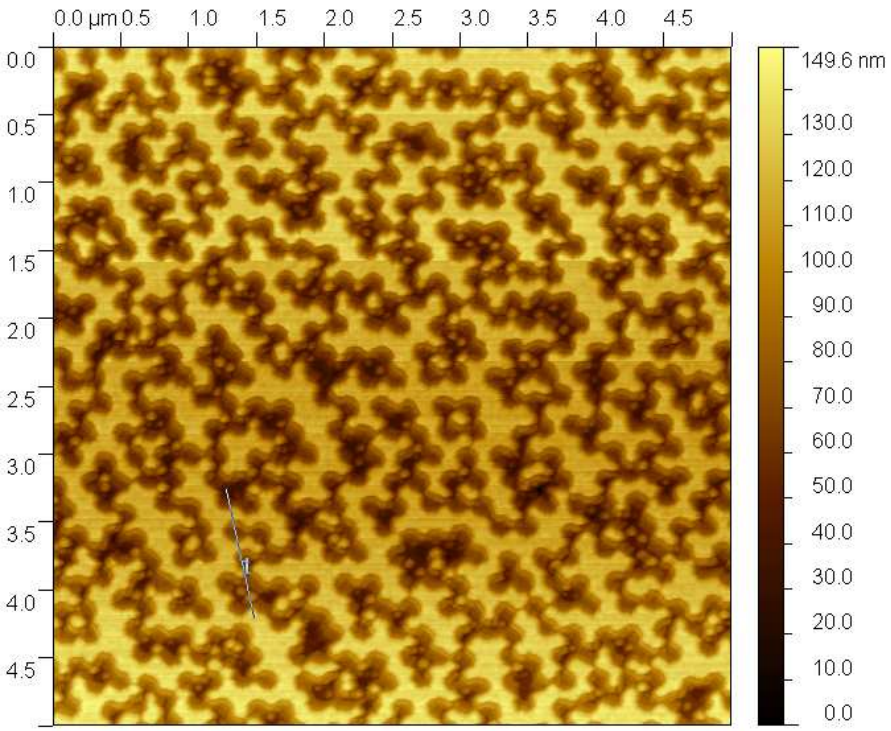

(a)

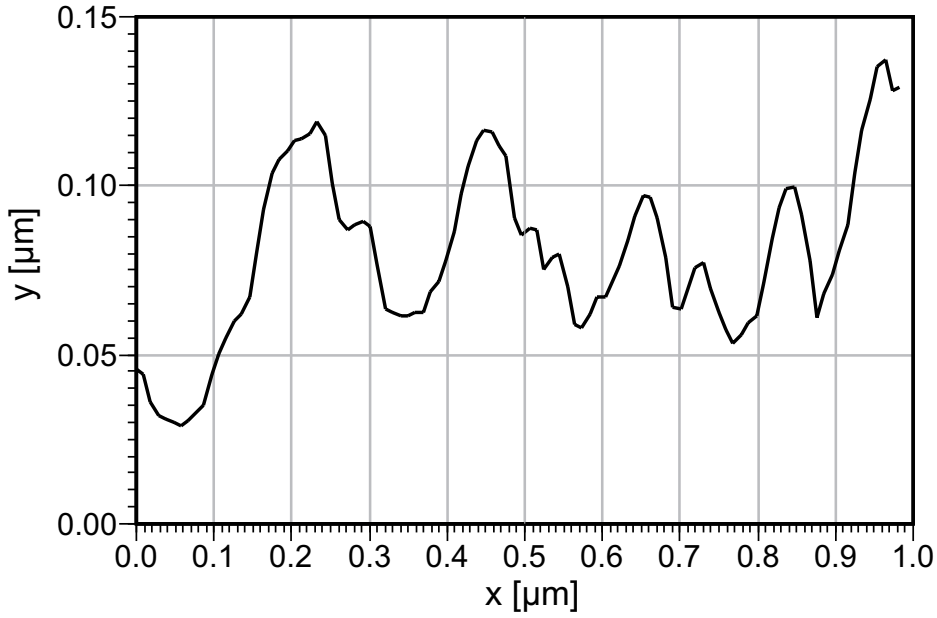

(b)

Fig. 5.21: Surface characterisation of tight packed structures: (a) STM scan, (b) line profile

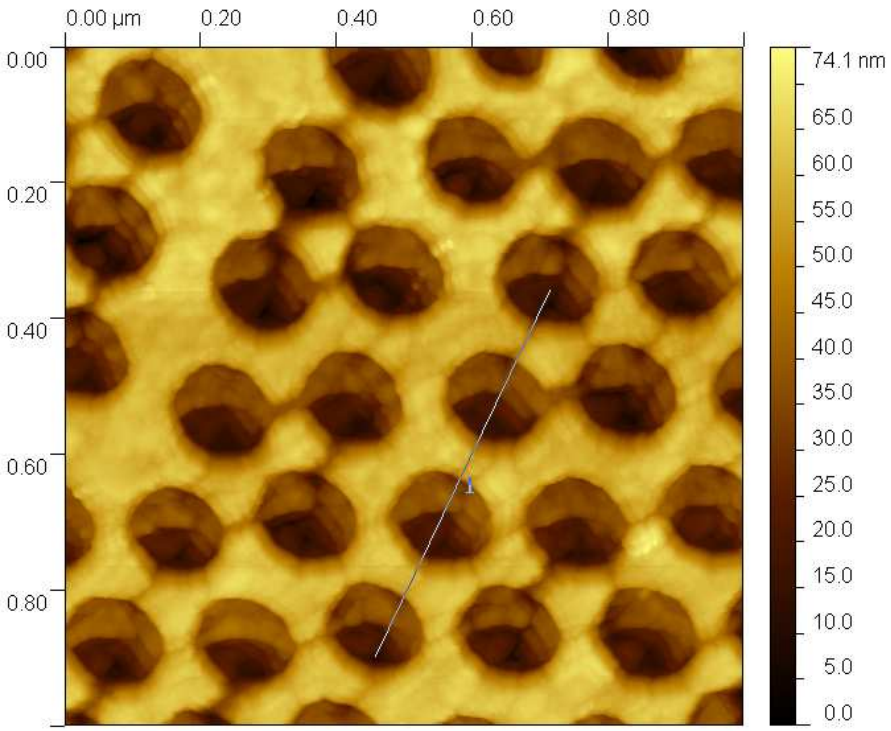

(a)

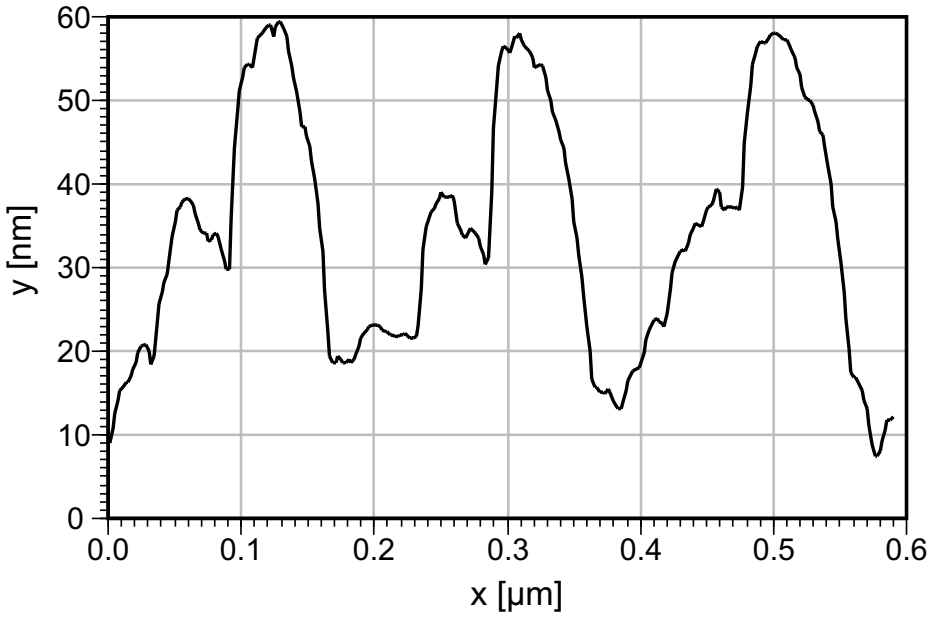

(b)

Fig. 5.22: Surface characterisation of nanopore structures: (a) STM scan, (b) line profile

nation for this is that the finite size of the STM tip prevents it from reaching to the bottom of confined spaces because of interactions between the side of the tip and the elevated structures. The zero level is shifted to the lowest point measured but does not necessarily coincide with the actual sample bottom. Furthermore both samples show a multiple tip effect. When the STM tip is cut from a Platinum-Iridium wire one often does not get a clean single tip but ends up with an ensemble of features that can all act as tips for signal acquisition. In the measurements this can be identified as a repetition of the same feature displaced by an offset and decreased amplitude as the tip is scanned along the surface. This is further demonstrated by a third sample with a nanopore structure (figure 5.22) with shallower structures compared to the second sample (feature heights were 50 nm and 120 nm respectively determined by SEM) but measured surface areas were comparable as 32.22 μm^2 and 31.1 μm^2, which is obviously false. Line profiles support this as they showed that the higher structures were not measured correctly and that tip effects were present. The STM measurements clearly confirm the increase in surface area but the absolute numbers must be taken with care as the tip influences the data acquisition substantially.

5.6 Alternative approaches

The nanostructure fabrication process presented above has some limitations that are addressed in this section and alternative approaches still utilising NSL are described. The first problem is the obvious discrepancy between predicted theoretical shape of the features (see surface gain equation (5.2)) and actual structure. The cause for this is the ion beam milling in conjunction with the non-ideal metal deposition causing interstice clogging. The circumference of the spheres is not preserved and the result is smaller, singular structures. The second issue is concerned with the initial gold film thickness. As the proposed process is a subtractive top-down method, thicker films have to be deposited to maximise pillar height and surface area. Gold is an expensive material and during milling a large portion of the deposited gold is removed again making it less economical.

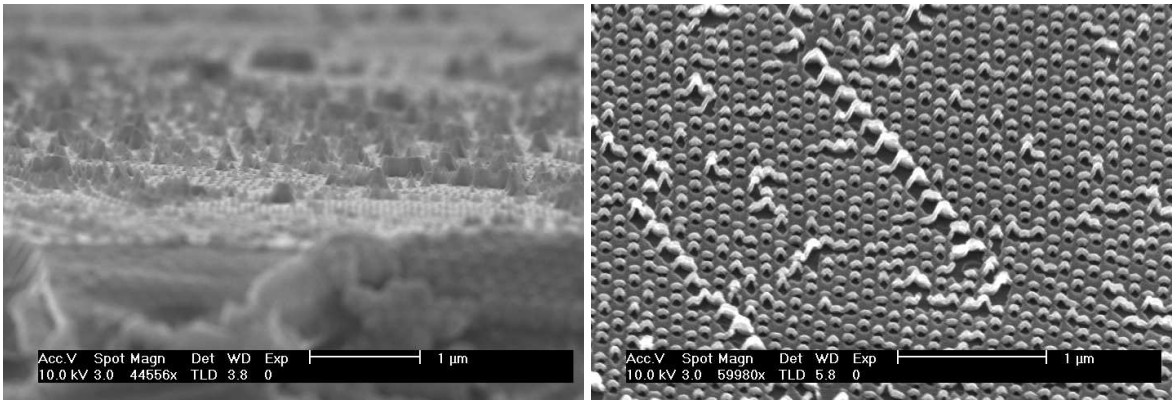

(a) (b)

Fig. 5.23: SEM images of (a) aluminium sacrificial layer and (b) titanium film after aluminium removal

5.6.1 Image reversal

To preserve a larger portion of the sphere circumference for surface area increase it was tried to perform an image reversal. In this case instead of titanium material covering the interstice it is deposited in the footprint area of the spheres. The size of the nanostructure is then exactly the diameter of the spheres. In order to achieve image reversal a sacrificial layer of aluminium was deposited in the interstices of the sphere array (figure 5.23a). After removal of the spheres a second deposition is performed. Titanium was evaporated with the sample held at an angle of 60° with respect to the material flux. The titanium then does not form a closed film and only coated the side of the aluminium pillar exposed to the flux. Afterwards the sample was placed in a solution of 1 mM tetramethylammonium hydroxide (TMAH), which selectively etches aluminium without attacking the gold or titanium. However, it also etches silicon, so that the sample should not be immersed for extended periods of time. The sample submerged in the solution was placed in an ultrasonic bath for 2 minutes to help remove the sacrificial layer. SEM inspection showed that the aluminium could be successfully removed. But the titanium covering the side of the aluminium pillar remained on the substrate as well. It was assumed that the free-standing titanium part, which should be only weakly attached to the titanium layer on the gold, would come off as a result of the ultrasonic treatment. Instead a kind of hollow pyramid was formed (figure 5.23b) so that milling was not possible.

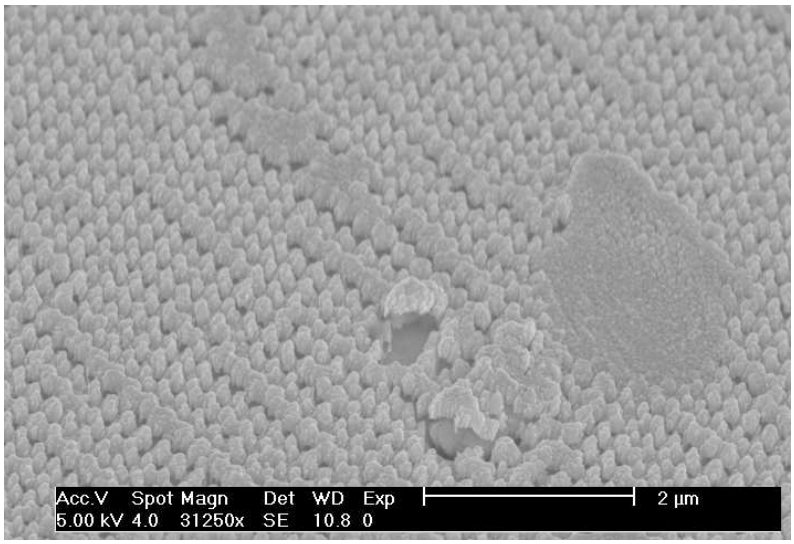

Fig. 5.24: SEM image of gold surface after removal of sacrificial aluminium

Instead it led to the idea to use this technique to fabricate a hollow structure of gold on the sample surface. This way there is no need to mill the sample and the hollow structures have a larger surface then the conventional pillar features. The process was repeated but gold was evaporated in the place of titanium. In contrast to the use of titanium the final gold film showed only little evidence of hollow structures present. In the SEM it was not certain whether the structure is hollow as the gold seems to have wrapped itself around the aluminium structure almost completely (figure 5.24). Gold is known to have the tendency to migrate around the substrate surface most likely because of weak bonding to other materials combined with high surface mobility. The sample surface showed traces of porosity but whether the aluminium was completely removed is not possible to conclude from SEM inspection. Measurement of the electrochemical impedance has to show whether it was successful.

Image reversal could not be achieved by the proposed method. Further work would be needed to optimise the process. The influence of the deposition angle has to be investigated further to find an optimum value that allows the method to succeed.

5.6.2 Nanomoulding of SU8

So far the feature height was limited by the gold film thickness. Another idea is to nanostructure the polymer surface of the implant before the deposition of the electrode material instead. Only a thin layer of gold has to be coated conformally on to the surface to cover the polymer nanostructures reducing the necessary amount of gold.

During experimentation with the nanospheres they showed potential to be used as masks for reactive ion etching (RIE) of silicon. Depositing an array of spheres on a silicon chip and subjecting it to a RIE process with a mix of sulphur hexafluoride (SF_6) and octafluorocyclobutane (C_4F_8) gas resulted in the fabrication of silicon nanopillars. The gases were fed into the chamber at flow rates of 20 sccm for SF_6 and 30 sccm for C_4F_8. While the SF_6 is etching the silicon, the C_4F_8 covers the side-walls with a thin polymer film to improve etch anisotropy. The chamber was kept at a pressure of 15 mTorr and the sample was cooled to 10° C. For plasma generation an inductively coupled plasma (ICP) power of 220 W and 20 W RF power were used. An etch duration of 2 min resulted in silicon pillars of ~440 nm height. The shape of the pillar is slightly tapered as the spheres were etched also during the process. The spheres are still visible on top of the pillars with diameters of ~100 nm while the pillar tops had a width of ~130 nm (figure 5.25). Optimisation of the etch parameters should result in even higher aspect ratios. The size of the pillars can be adjusted using an oxygen plasma to reduce the sphere diameters as described earlier. In conjunction with the etch time this enables the shape of the nanostructure to be tuned from dense nanopillars over cones to well separated sharp thin needles (figure 5.25).

Reproducing these features in polymer substrates used for the implants described in chapter 7 the resultant surface would be predestinated to test the idea suggested above. In order to transfer the silicon pattern to the polymer a negative mould was produced from polydimethylsiloxane (PDMS) by mixing 184 Dow Corning elastomer precursor with the accompanying curing agent in a ratio of 10:1 and pouring it over to the structured silicon chip. It was then placed in a vacuum desiccator. This removes air bubbles trapped during mixing or pouring and ensures close contact between the silicon surface and the liquid PDMS. It is left overnight in the desiccator to fully cross-link and harden to become a flexible rubber. Since PDMS contains silicon

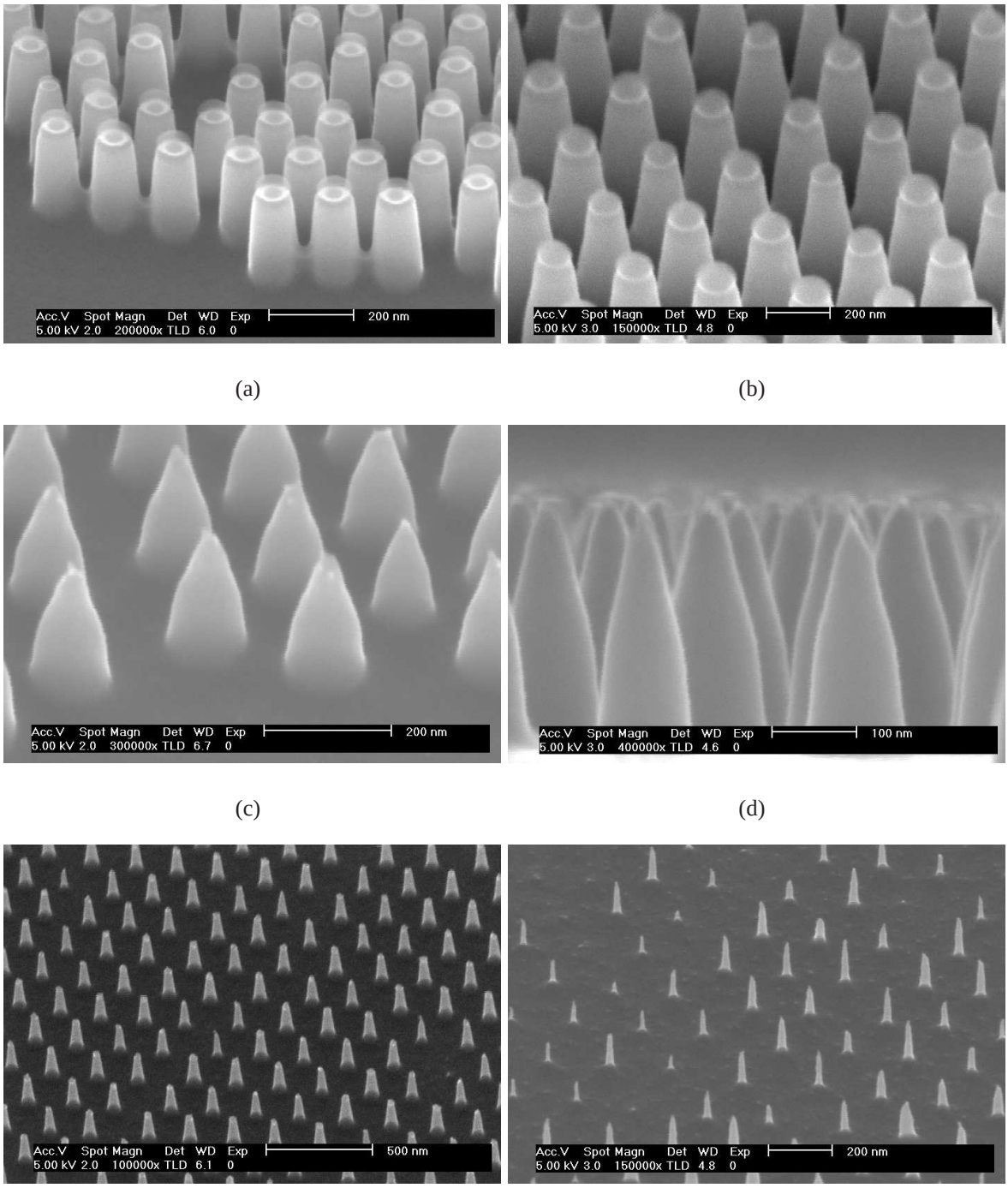

Fig. 5.25: SEM images of silicon pillars etched with (a) no prior oxygen thinning for 2 min; (b) 15 sec O_2, 2 min; (c) 30 sec O_2, 2 min with (d) a cross section of (c); (e) 60 sec O_2, 1 min; (f) 60 sec O_2, 2 min

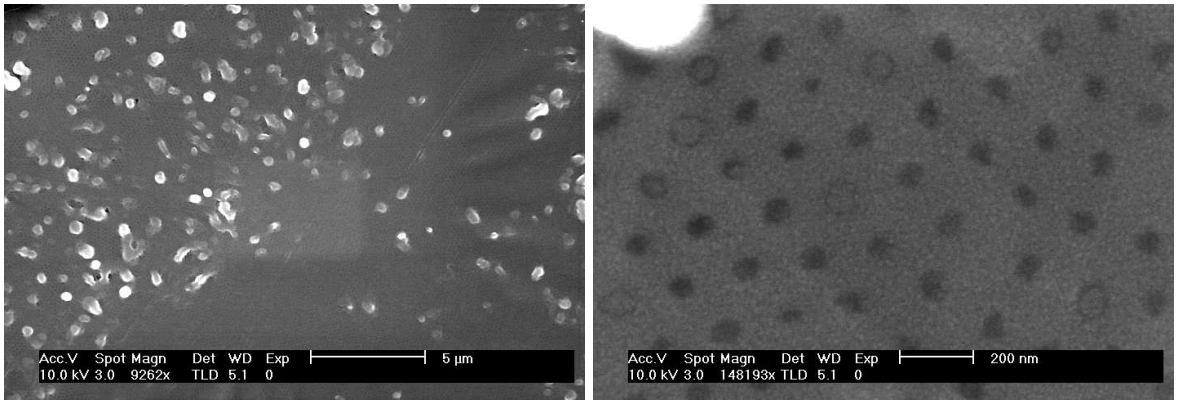

(a) (b)

Fig. 5.26: SEM images of the PDMS mould surface

groups it bonds very well to any surface that also contains silicon. Therefore prior to pouring of the PDMS on to the silicon its surface needs to be passivated with trichloro(1H,1H,2H,2H-perfluorooctyl)-silane. This was done by evaporating a drop of the solution in a small vessel containing the chip and sealing it under vacuum.

Once the PDMS is set, it was carefully peeled off the silicon chip. It is difficult to image the surface of PDMS in SEM as the thick dielectric material is prone to electron charging. A metal film deposited to counter this effect has to be very thin to prevent sealing the narrow channels in the PDMS. Silver paint was additionally used to connect the metal film on the PDMS to ground via sample holder but the image quality remained poor. Nevertheless periodic arrays of holes in the PDMS were visible (figure 5.26). Because of the soft elastic material property no viable cross sections of the moulded features could be produced. During cutting the rubber was torn apart and no clean cutting edge was obtained. In evidence of the observed holes the mould is assumed to be successful even though proof of channels in cross section is missing.

The PDMS template was then used to cast a polymer resist. The material used was SU8 2002 because of its low viscosity, which is necessary to fill the pores. The low surface energy of PDMS prevents the poured SU8 from covering it properly. An oxygen plasma treatment of the PDMS creates bonding sites on the PDMS surface, which the SU8 can link to and supports

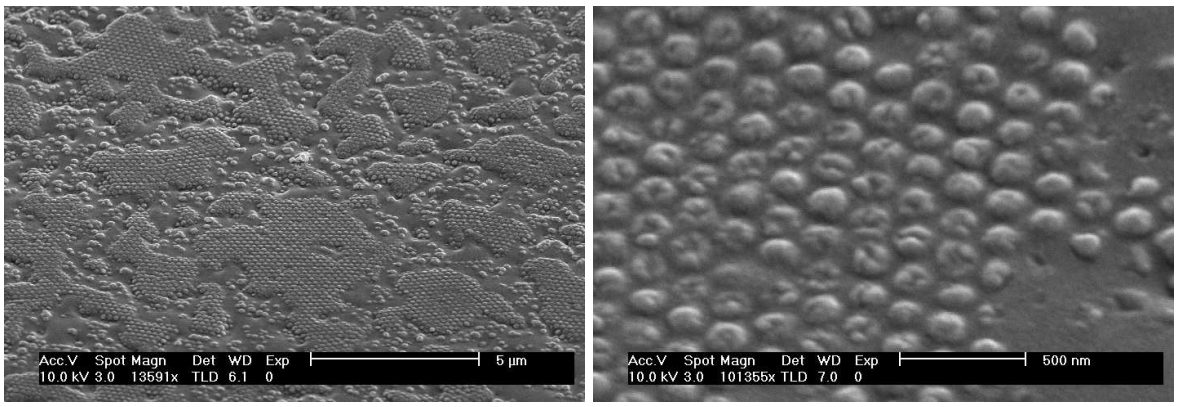

(a) (b)

Fig. 5.27: SEM images of SU8 surface after peeling from the PDMS template

the wetting. As the effect of the oxygen plasma is of short duration, plasma treatment and pouring have to be done in immediate succession. It was poured on to the PDMS until the entire surface was covered using the minimum amount possible as SU8 2002 is designed for thin films (~2 μm). It was then pre-baked according to data sheet specifications. Next step was a 3 min exposure to UV light in the mask aligner followed by the post bake to completely cross-link the material. After cool-down the hardened SU8 was peeled off from the PDMS and covered with a thin chromium film for SEM inspection. The SU8 surface did not display replicas of the silicon pillars. Only periodic bumps were covering the surface (figure 5.27). Assuming a viable mould there are two possible explanations. Trapped air might have prevented the liquid from entering the pores so that no SU8 pillars could be formed. Unlike in PDMS moulding the SU8 cannot be poured under vacuum as this causes the solvent to quickly evaporate out of the resist leaving a very viscous mass with bad flow properties behind. The other possibility is that the pillars were ripped off during peeling. Judging from the appearance of the bumps and the likeliness that ripping should have left at least some pillars or stumps of different sizes, entrapment of air is the more likely explanation.

Instead of casting the SU8 it was tried further to stamp the structures into the polymer expecting that the applied force would pushes the SU8 into the pores and squeeze out trapped

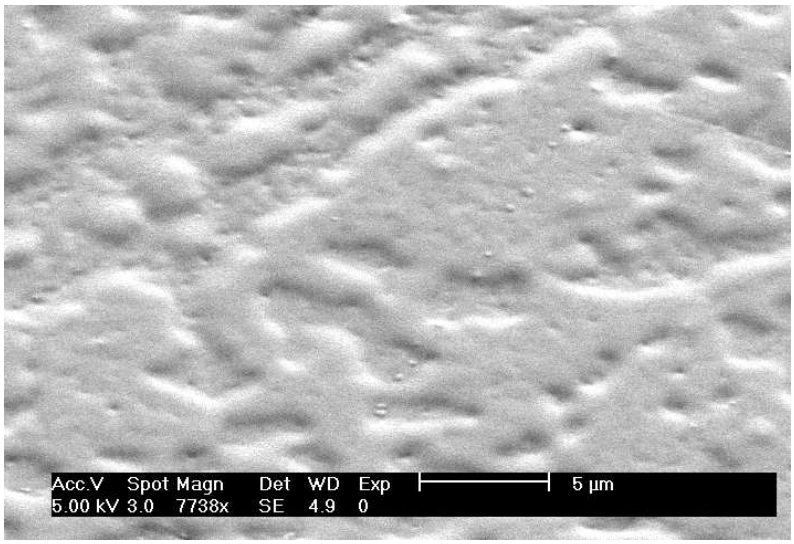

Fig. 5.28: SEM image of the SU8 surface after stamping

air. This approach resembles microcontact printing but used more simplistic tools. A thin film of SU8 was spun on to silicon samples. The PDMS template was then placed on the sample with the feature mould side facing the SU8. A piece of microscope glass slide on top of the PDMS was used to sandwich PDMS and SU8 between glass and silicon. The use of glass was necessary to allow subsequent UV exposure. The assembly was clamped with two bulldog clips, which applied a constant force and fixed them into position. After performing the pre-bake, 5 min UV light exposure through the glass slide and PDMS and post bake the clips were removed. The PDMS was carefully peeled from the the SU8 and the sample was coated with a thin metal film for SEM. The result of the stamping is shown in figure 5.28. No structures were found on the surface. Even the bumps previously observed were absent. This suggests that the force was too small to imprint the SU8 with the mould features.

The nanometre sized features were unable to be reproduced in SU8 with the available equipment. A professional microcontact printing system or a nano-imprinter might be able to achieve this as they can supply higher forces without breaking the samples and often also incorporate the UV exposure in the printing process.

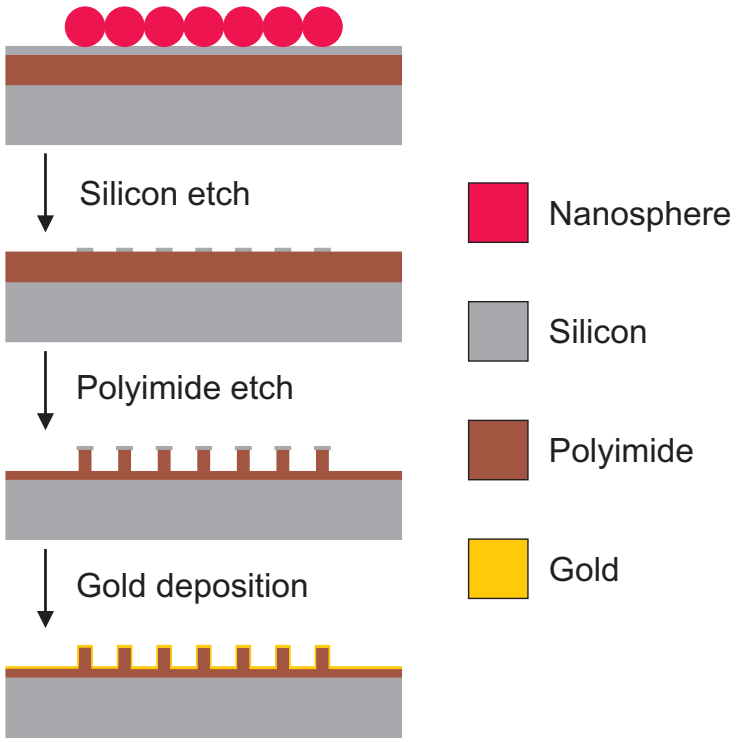

Fig. 5.29: Process steps for polyimide pillar fabrication

5.6.3 Polyimide nanopillars

As the SU8 moulding did not work, an alternative was suggested. The silicon pillars could act as an etch mask for polyimide substrates since the they are resistant to the oxygen plasma. Unlike SU8, polyimide is readily dry etched by oxygen plasma. Polyimide is biocompatible and has been used in neural interfaces before. Furthermore one of the implants described in chapter 7 is fabricated from polyimide, which makes it a primary target for surface nanostructuring.

A 20 μm thick PI2611 polyimide layer was spun on to silicon substrates and baked according to instructions (figure 5.29). Then a ~400 nm thin film of silicon was deposited on top by sputtering at 2x10^{-2} mbar with 300 W RF power for 10 min. Afterwards the sample was coated with nanospheres. Surprisingly the sputtered silicon film showed hydrophilic behaviour in contrast to standard silicon wafers. Therefore pretreatment of the silicon was unnecessary. After nanosphere deposition the sample was transferred into the etch system. First the sphere diameter is altered by oxygen plasma etching to define the size of the silicon features and sub-

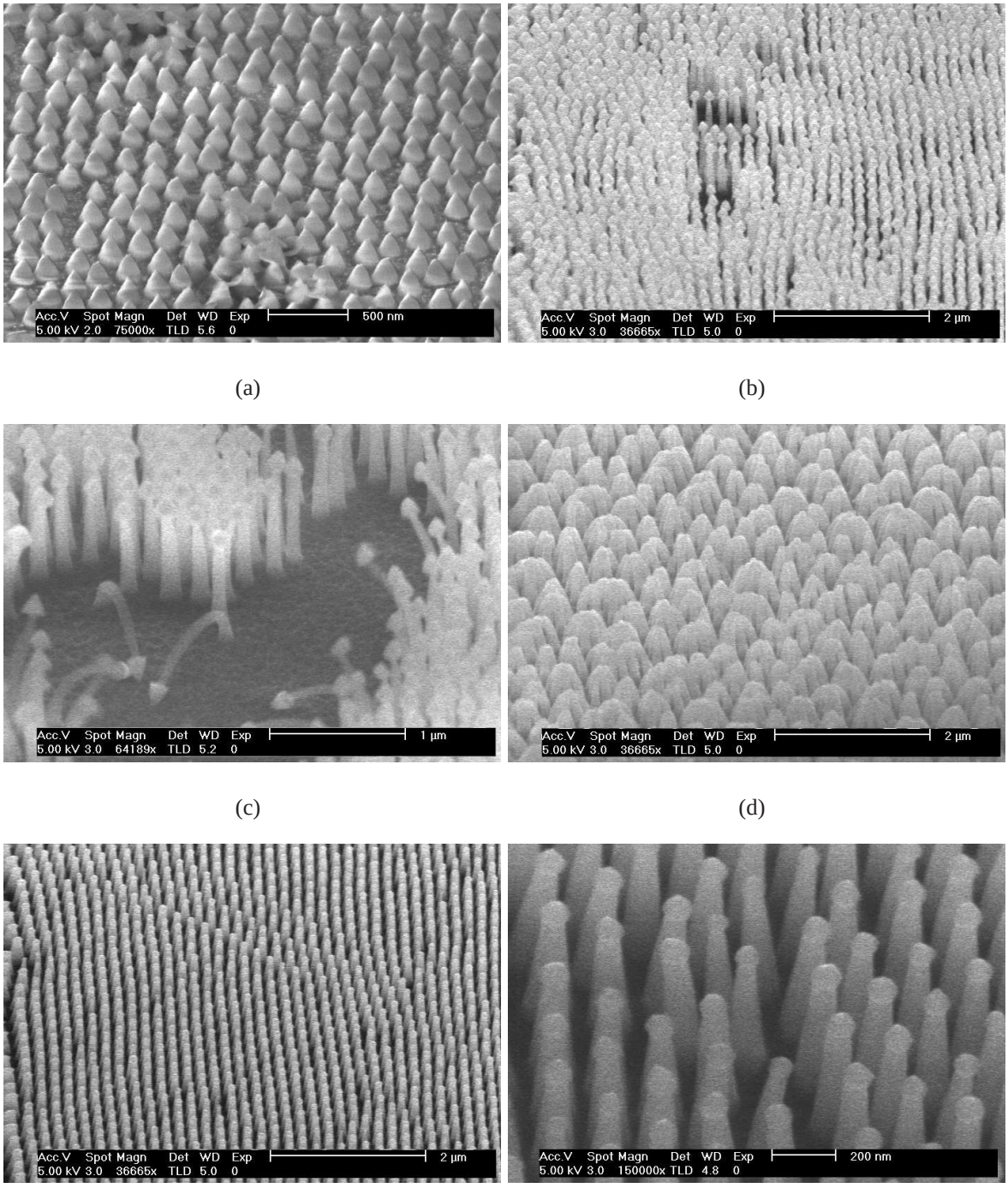

Fig. 5.30: Polyimide nanopillars: (a) silicon mask after 2 min 30 sec of etching; (b,c) nanopillars after 3 min of O_2 plasma with 15 sec initial sphere thinning; (d) polyimide pillar bundles after wet processing; (e,f) pillars after 2 min oxygen etching with spheres initially etched for 30 sec

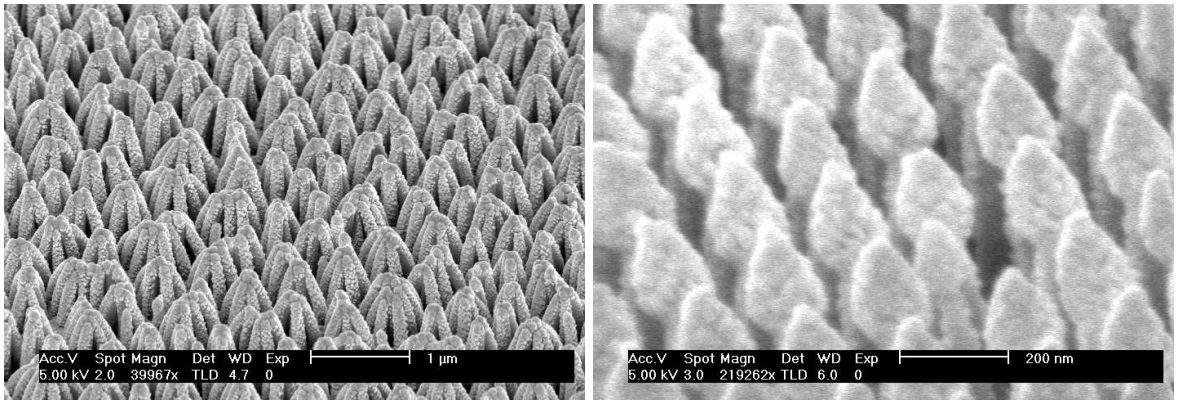

(a) (b)

Fig. 5.31: SEM images of surfaces after gold deposition for (a) sample with wet etch silicon mask removal and (b) dry etched sample

sequently the diameter of the polyimide pillars. A sufficient spacing between the features is required to ensure conformal coating of the structures during later gold deposition. Etch times were chosen as 15 and 30 s, respectively. The next step is the etching of the silicon layer. A combination of SF_6 and C_4F_8 was used as previously described. After 3 min of etching the polyimide underneath was exposed. It was then followed by oxygen etching of the polyimide. The process conditions were 100 W RF power, 100 W ICP power and 30 sccm oxygen flow at a pressure of 10 mTorr. For best verticality of the side walls and avoidance of polyimide heating the sample was cooled to 1° C and a helium backing pressure of 15 Torr was used. The feature height can be tuned via etch time. One sample was etched for 3 min resulting in roughly 900 nm high pillars while for a second sample exposed to oxygen plasma for 2 min a height of around 450 nm was measured. Results for both samples are shown in figure 5.30. They have a slightly tapered profile caused by undercutting and stand upright (bending in figure 5.30c was due to electron charging) with aspect ratios of ~10:1 and 5:1, which can be increased further by longer etch times.

The remaining silicon mask on top of the pillars should be removed to allow for better access to the bottom of the polyimide layer for gold coating. One sample was immersed in TMAH solution for 3 min to completely remove the silicon top. However, the wet processing

caused the pillars to bundle up during drying so that the area inside the bundle cannot be coated with metal. Alternatively a further SF_6/C_4F_8 etch was performed on the other sample for 1 min. The polyimide does not seem to be affected significantly by the etch gas. Some of the silicon remained but was thinned enough to allow for a more open structure. The gold coating was done by Dr Maolong Ke in a specially fitted thermal evaporator. During evaporation the sample was held at an angle of 5° to the vertical and slowly rotated to coat the side walls all around. The thickness as measured by the quartz crystal balance was 62 nm of gold over 5 nm of chromium for better adhesion but must assumed to be thinner as the material was spread out due to sample rotation. SEM could not confirm whether the pillars were covered successfully due to decreased gap size between the structures after evaporation. The observed roughness on the sides that was not present before as well as sporadic diameter measurements on single pillars indicate that indeed they were covered with a thin gold film. Final confirmation has to be carried out through electrochemical impedance spectroscopy where a fully coated pillar surface should display a substantial decrease in interface impedance.

A potential advantage of this method is the flexibility of the polyimide pillars. The pillars can bend easily when exposed to forces or strain reducing the risk of breaking compared to high aspect ratio solid metal structures. The area increase can be simply controlled by pillar height. They might even possess less inflammatory response. The stiffness of the substrate seems to play an important role in foreign body reactions. The cells constantly probe their surroundings for tensile strength [92]. When encountering surfaces that do not display the typical softness of tissue a foreign body reaction can be triggered. Due to the pillars bending under the probing force, the cell should potentially interpret this as a surface softer than that displayed by bulk polyimide. In conclusion the nanostructuring of polyimide surface is a promising approach towards the improvement of neural electrodes.

5.7 Conclusion

The capabilities of Nanosphere Lithography for the purpose of nanostructuring were thoroughly investigated and the suitability of three different methods for sphere deposition were analysed.

As a result the method of sphere assembly at an interface was deemed the most appropriate and a process for nanostructuring thin gold films using Nanosphere Lithography was successfully developed. The surface characterisation showed that the surface area could readily be doubled with the technique. To address the problem of limited aspect ratio, alternative processes were investigated. This resulted in the fabrication of higher aspect ratio polyimide nanopillars using Nanosphere Lithography with subsequent metallisation, which poses a strong alternative to the nanostructured thin film process.

6. ELECTROCHEMICAL MEASUREMENT AND IMPEDANCE SPECTROSCOPY

After introducing the developed methods for nanostructuring the surfaces are assessed by electrochemical impedance spectroscopy for their potential to change interface properties through the increase in surface area. This is complemented by the use of the electrochemical methods of chronoamperometry and cyclic voltammetry. All measurements were carried out with a potentiostat (Autolab PGSTAT 12) and an additional frequency response analyser module for the impedance. The experimental set-up and operational principle of a potentiostat are described in section 1 of this chapter. The results obtained from samples with plain and structured gold surfaces are analysed in section 2. During experimentation on the nanostructured samples a porous form of gold was found that showed significantly reduced impedance and corresponding results are presented in section 3.

6.1 Operational principles

The basic elements for the acquisition of electrochemical characteristics are an electrochemical cell and a potentiostat. A electrochemical cell consists of a chamber holding the electrolyte and three electrodes necessary for the measurement, which are the reference electrode (RE), the counter electrode (CE) and the working electrode (WE). The name potentiostat is derived from its basic operational mode. The potential difference between WE and RE is kept constant and the current flowing between CE and WE is measured (figure 6.1). To keep the potential constant, RE is connected to the inverting input of an operational amplifier with a signal source connected to the non-inverting input while the output of the amplifier is connected to CE. This way the current injected by CE is automatically adjusted to keep the potential at WE at a constant level.

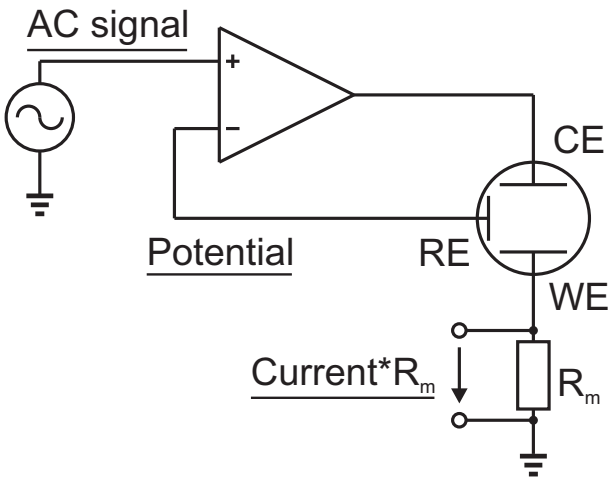

Fig. 6.1: Operational diagram of a potentiostat

The cell current is measured through the voltage difference developed across a reference resistor attached to WE. RE needs to have a stable, well-defined potential in the electrolyte in order to only reflect potential changes at WE. Hence only materials with stable electrode potentials like silver chloride or mercury are used and all measured potentials are then defined relative to this reference. WE is the electrode under study while CE is normally made of inert materials like platinum or graphite.

The electrochemical cell used for the measurements (figure 6.2) consists of a custom-made Teflon block with a chamber and openings for the three electrodes machined into it. A large platinum sheet served as the CE and a silver/silver-chloride electrode was used as RE. The hole intended for the WE is surrounded by an O-ring, against which the samples acting as the WE were pressed by a clamp. The exposed sample area is fixed by the hole diameter to a value of 0.283 cm^2. The samples were connected to the instrument by a flattened gold wire clamped between sample and Teflon block outside the O-ring. During measurement the whole block was placed in a closed metal box connected to the potentiostat's ground to shield it from external noise sources. Physiological saline was used as electrolyte to mimic the environment that neural implants are exposed to. It comprises of 8.6 g of sodium chloride, 0.3 g of potassium chloride and 0.33 g of calcium chloride dissolved in one litre of deionised water.

For impedance spectroscopy a sinusoidal voltage signal of 10 mV amplitude is used to probe

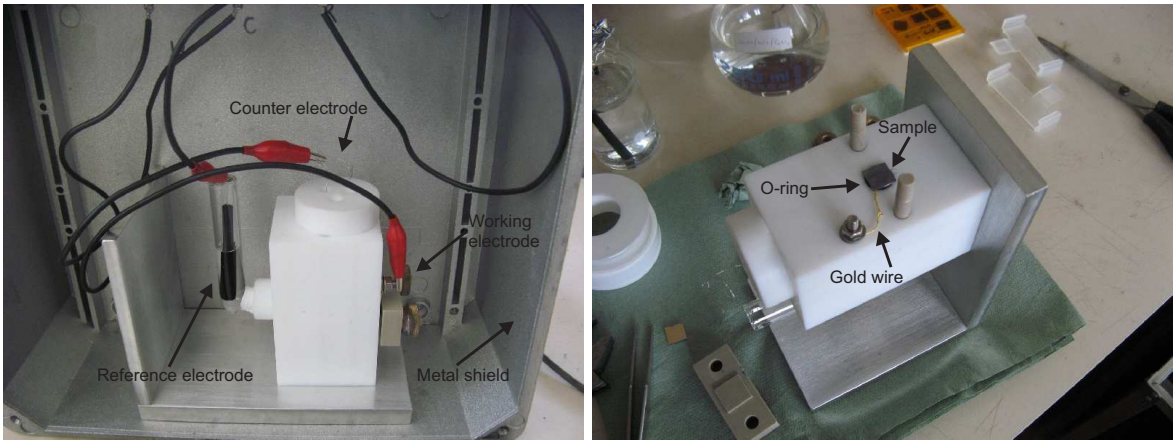

(a) (b)

Fig. 6.2: Electrochemical cell (a) assembled for electrochemical measurements and (b) mounting of the sample as working electrode

to impedance at 51 frequencies in the range from 0.1 Hz to 10 kHz spread logarithmically over each decade. A small amplitude must be chosen to stay within the limit of linearity of the sample's interface response. The impedances are automatically calculated by the Autolab software from the current and voltage values and the phase shift between the two quantities.

The values of the equivalent circuit components of the interface vary with frequency as well as surface area. The scaling law for each element can be deduced from the constituent equations shown in chapter 3 and they are summarised in table 6.1 where k is a proportionality constant, f the frequency and A the surface area. All of them are inversely proportional to the electrode's surface area and benefit from a surface increase. In this case the charge transfer resistance for example would be reduced because more electro-active sites become available. With the exception of R_t the impedance values decrease with increasing frequency.

Once the impedance spectroscopy has been performed the measured curves have to be fitted to equivalent circuit models in order to obtain specific values for the various components. The complexity of the fitting increases with the number of circuit elements involved. Therefore it is useful to analyse the measurements before fitting to deduce, which interface components are present and to choose appropriate initial guesses for the parameter values. The influence of the various components on the impedance curves is discussed in the following. The simplest case is

Tab. 6.1: Impedance scaling of the interface components

Symbol	circuit element	scaling dependency
C_d	interfacial capacitance	$\mid Z \mid = \frac{k}{Af}$
R_t	charge transfer resistance	$\mid Z \mid = \frac{k}{A}$
Z_w	Warburg impedance	$\mid Z \mid = \frac{k}{A\sqrt{f}}$
R_s	solution resistance	$\mid Z \mid = \frac{k}{\sqrt{A}\sqrt{f}}$ (for symmetrical shapes)

a series combination of the solution resistance R_s and the double layer capacitance C_d assuming that the direct current part can be neglected because of very high charge transfer resistance. In practise the double layer will never show pure capacitive behaviour. Instead a constant phase element (CPE) has to be used whose impedance is described by

$$Z_{CPE} = \frac{1}{Q_0(j\omega)^n} = \frac{1}{Q_0\omega^n} e^{-j\frac{\pi}{2}n} \tag{6.1}$$

with n an empirical constant having values between 0 and 1. The cause for this non-ideal capacitive behaviour is assumed to be surface inhomogeneities and the value of n a measure for the size of the surface roughness. Only for n equal 1 this element represents an ideal capacitance and Q_0 = C so that a fitted value of Q_0 can only be an approximation for the capacitance for values of n close to 1. The variation of the impedance and phase with the value of n is plotted in figure 6.3 with Q_0 corresponding to 20 μF for n = 1. R_s is chosen to be 50 Ω and accounts for solution as well as connection resistances. The plots of impedance magnitude show changes in the slope of the frequency dependent part of the curve and the frequency cut-off shifting to higher frequencies, while the phase decreases from -90° for ideal capacitance to smaller values with decreasing n. In the Bode plot representation it is often hard to distinguish different system behaviours. For this reason in electrochemistry it is common to plot the data in Nyquist form instead with the real part of the impedance on the x-axis and the imaginary part on the y-axis. In this form (figure 6.4) the data is represented by straight lines. For n = 1 the line is perpendicular to the x-axis. With the real part completely set by the series resistance, the imaginary part is solely a function of capacitance and frequency. As the value of n decreases the lines tilt over

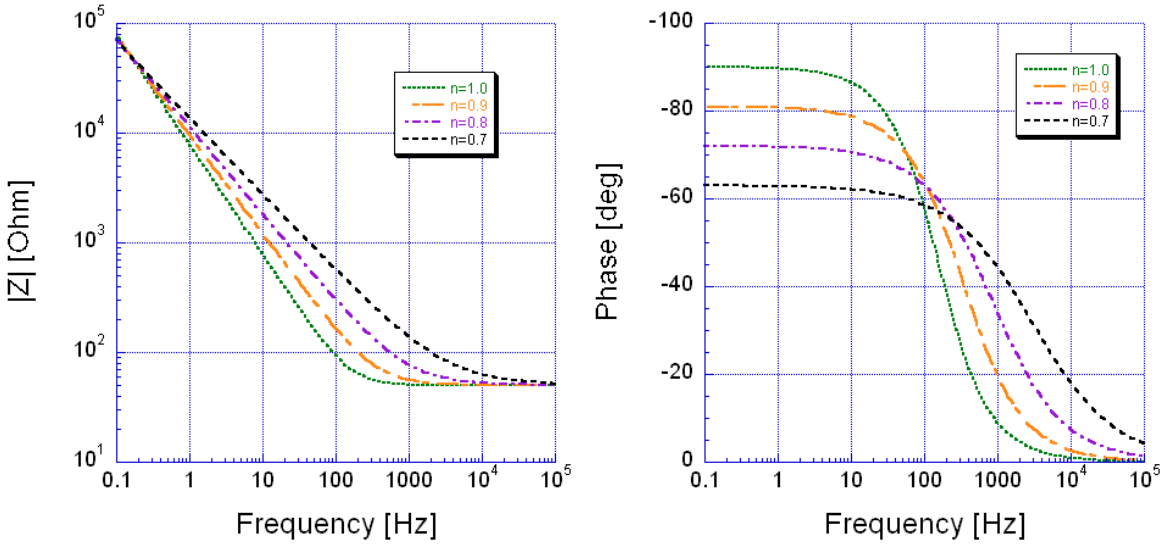

(a) (b)

Fig. 6.3: Simulated Bode plots for a constant phase element in series with a solution resistance

with the base anchored at the value of the series resistance. The constant phase element now has a real and an imaginary part in its impedance. It also demonstrates why it is called constant phase element as the phase angle between the graph and the x-axis does not vary with frequency. The phase angle only depends on the value of n as can be seen from equation (6.1).

In the next step the circuit model is expanded to feature a charge transfer resistance in parallel. It provides a current path at low frequency where the capacitive impedance is very high. The total impedance plateaus at the value of R_t for small frequencies then transitions into the capacitive slope and flattens out for higher frequencies to the series resistance (figure 6.5). This behaviour is mirrored in the phase plot with the phase angle tending towards zero for low frequencies and hence being dominated by the resistive path. Following this is the capacitive regime for mid-frequencies before going back to zero as the impedance value of the capacitive decreases with rising frequency. The values of R_t are chosen to demonstrate cases ranging from significant influence for low values to mixed situations up to high values with minor impact on the system's behaviour. In the Nyquist plot the presence of an appreciable charge transfer resistance is expressed as a semi circle with the diameter being determined by the value of R_t (figure 6.6). The effect of $n < 1$ is to depress the ideal semi circle of $n = 1$ into a more convex

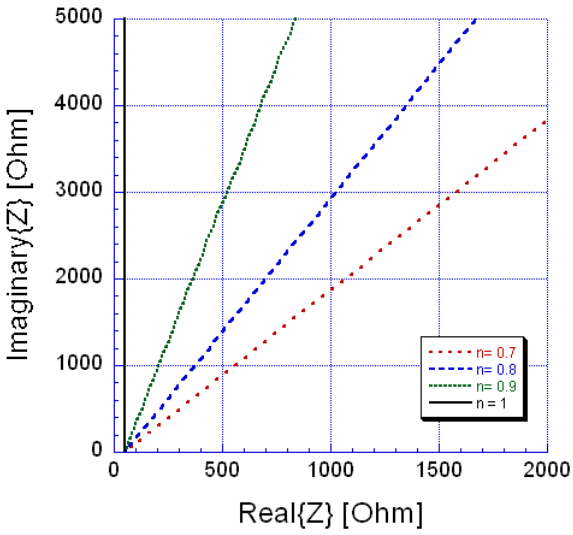

Fig. 6.4: Corresponding Nyquist plot for R_s in series with CPE

shape.

The Warburg impedance as the last influence on the system's behaviour is added to the circuit model. Since the diffusion resistance can only be of importance if there is a sufficient reaction rate the charge transfer resistance was set to a comparably low value of 1,000 Ω. The value of n for this preliminary analysis was chosen as 0.8 to give a realistic situation. Because the Warburg impedance is frequency-dependent the plateau observed for a singular charge transfer resistance is replaced with a steadily varying curve of fixed slope for values lower than the impedance of the capacitive branch (figure 6.7). In the phase plots the influence of Z_w is seen at low frequencies. Small values of Warburg impedance do not significantly show in the curve and the phase is determined by R_t with an angle close to zero. As Z_w increases it starts to shift the phase closer to its native phase angle of -45°. Because the Warburg impedance is frequency-dependent the phase falls off towards zero with increasing frequency as the charge transfer resistance becomes the limiting element again. For high values the Warburg impedance blocks the charge transfer branch and the constant phase element is the dominant component with a phase closer to -90°. In the corresponding Nyquist plot low values of Z_w show the typical semi circles of charge transfer resistances while high Z_w leads to constant phase behaviour (fig-

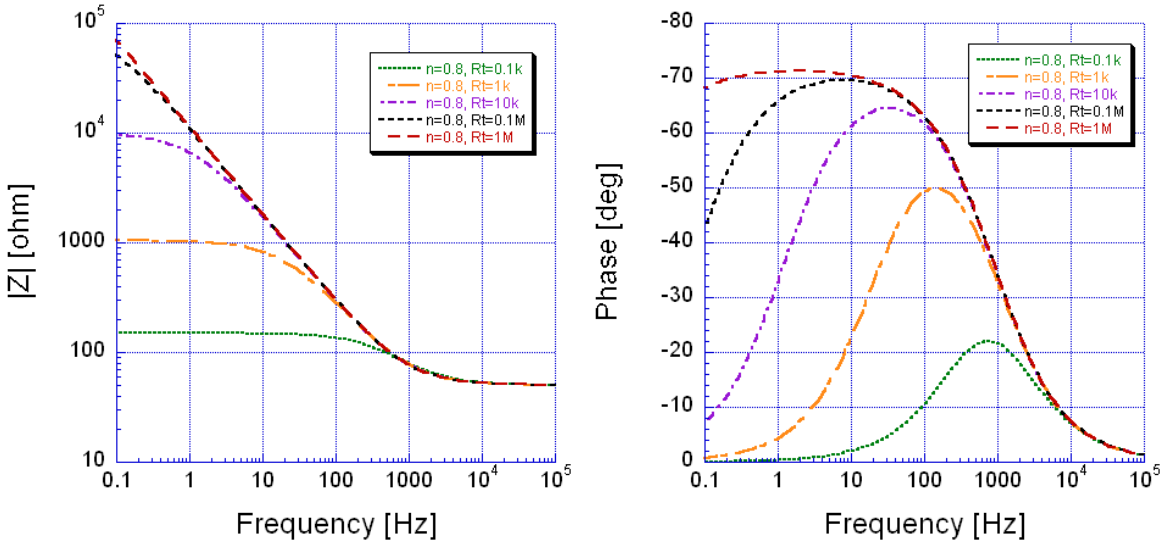

(a) (b)

Fig. 6.5: Simulated Bode plots with a charge transfer resistance in parallel with the constant phase element

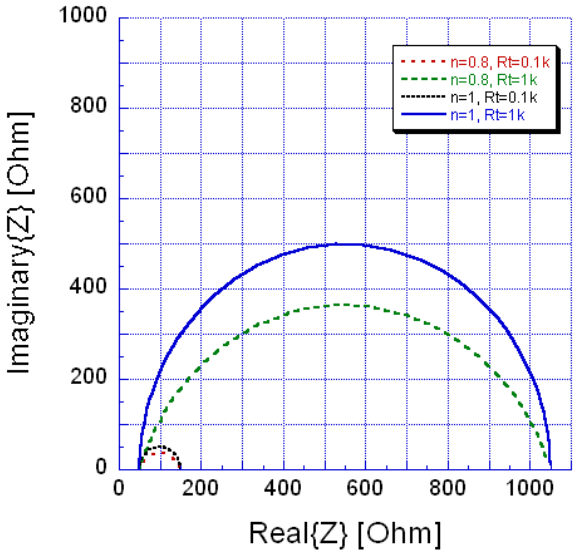

Fig. 6.6: Corresponding Nyquist plot for added charge transfer resistance

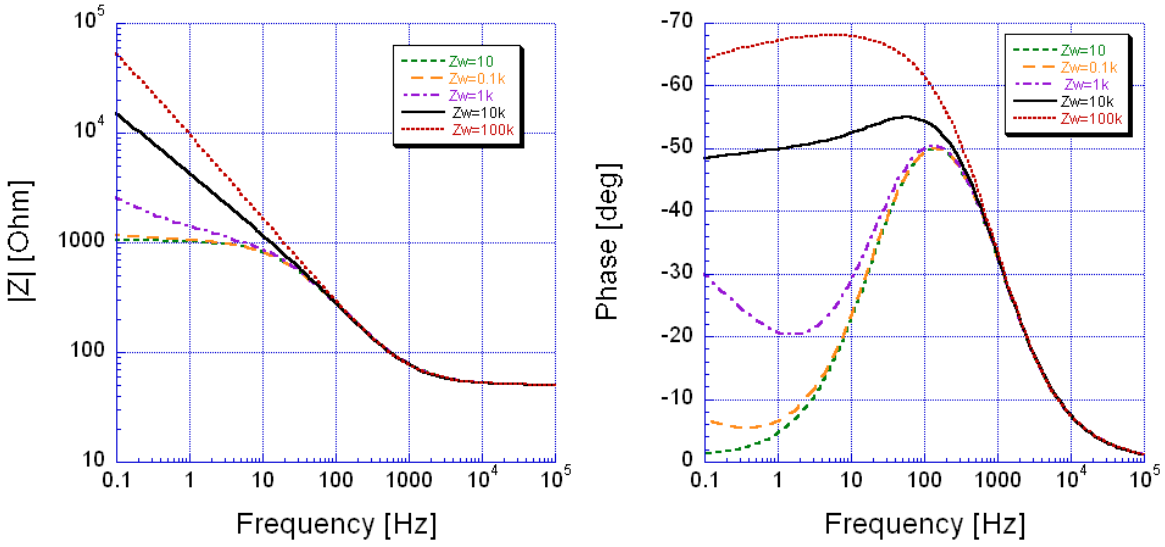

(a) (b)

Fig. 6.7: Simulated Bode plots with Warburg element added in the charge transfer branch

ure 6.8). As the Warburg element starts to dominate it breaks up the semi circle into a straight line with a 45° angle to the x-axis before it transitions to straight lines of higher slope set by the CPE. It is therefore only necessary to consider a Warburg element for fitting when one observes the break up of the semi circle or straight lines with an angle of around 45° in the Nyquist plot representation of the measured data. When using equivalent circuit models for data fitting it has to be considered that they are not unique and different circuit models can produce the same results. Also the components do not always represent real physical entities (like the constant phase element) but might fit the data very well.

Complementary to impedance spectroscopy, chronoamperometry is performed by applying a potential step to the electrode and measuring the current response over time. The current response consists of two parts, the charging of the double layer and the diffusion of charge carriers with respect to the electrode. As the discharge current is exponentially proportional with time, it quickly decays compared to the slower diffusion process. The diffusion current is described by the Cottrell equation in the following form as

$$\mid I \mid = \frac{n\,F\,A\,C_0^i\,\sqrt{D_i}}{\sqrt{\pi t}} \tag{6.2}$$

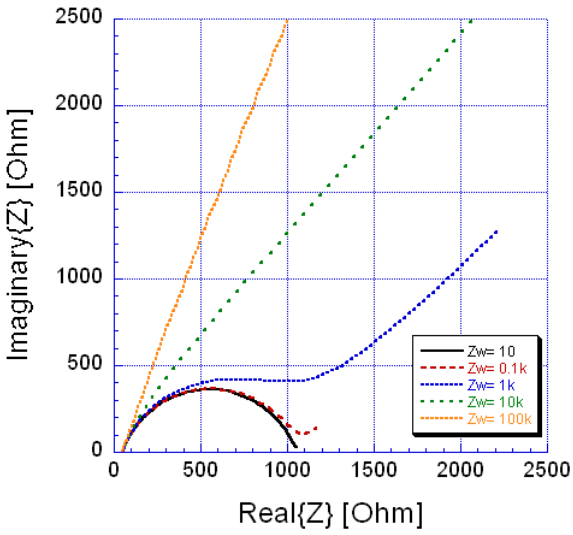

Fig. 6.8: Corresponding Nyquist plot with Warburg impedance

with n the numbers of electrons transferred per molecule, F the Faraday constant, A the surface area, C_0^i the bulk concentration and D_i the diffusion coefficient for each species. As the same solution composition was always used for the measurements, the only parameter varying is the surface area. Hence the size of the peak gives an indication of the surface area with respect to the different samples. However as the Cottrell equation assumes an ideal interface structure it can at best only be used semi-quantitatively. In the measurements the potential was stepped from 0.5 V to 0 V and the response measured for 3 s after a conditioning phase of 1 s.

Cyclic voltammetry is often used to determine the stimulation efficiency of neural electrodes, which is the amount of charge delivered per voltage pulse. In cyclic voltammetry the electrode voltage is swept at a constant rate between two potentials and the resulting current is measured. Integration of the area under the obtained curves gives the amount of charge injected. Broader voltammogramms along the current axis hence correspond to increased charge injection. For the measurements in this work the voltage was cycled between -0.2 and 0.6 V for 10 times to reach a steady state and the last scan was used for analysis.

Tab. 6.2: Process parameters used for the manufacturing of the analysed samples

Sample	nanostructure modification
S1	plain reference surface
S2	80 nm sacrificial aluminium + 50 nm gold
S3	1 min O_2, milling: 6 min @ 45°
S4	14 sec O_2, milling: 6 min @ 65°
S5	20 sec O_2, milling: 3 min @ 65°
S6	20 sec O_2, milling: 6 min @ 65°
S7	bundled Au coated PI Pillars (15 sec & 3 min O_2)
S8	straight Au coated PI Pillars (30 sec & 2 min O_2)

6.2 Modified gold surface

As shown in the previous chapter the nanostructuring process is capable of producing a variety of different surface morphologies. A representative set of samples was chosen for investigation of the influence of the surface structure on the interface impedance (figure 6.9). The details of fabrication are summarised in table 6.2. Sample S1 is a deposited gold film with no further modification and acts as reference for the other samples. S2 results from the attempt to produce hollow gold nanostructures as described in section 5.6. The conditions for S3 were chosen to create prototypical pillar shapes. S4 is an example of a shape in a transitional stage between pillar and honeycomb-like structure while S5 and S6 represent such a honeycomb shape for different milling times. S7 and S8 are the polyimide pillar samples discussed in section 5.6. Ideally a number of samples for each structure type should have been produced and measured to account for statistical variations in fabrication and measurement. Because of time constraints and limited access to the potentiostat only one sample of each type could be analysed. However, general tendencies of the nanotextures should still be observable. To minimise variations all samples stem from the same gold deposition, were processed together and measured in a single session except for the polyimide pillars.

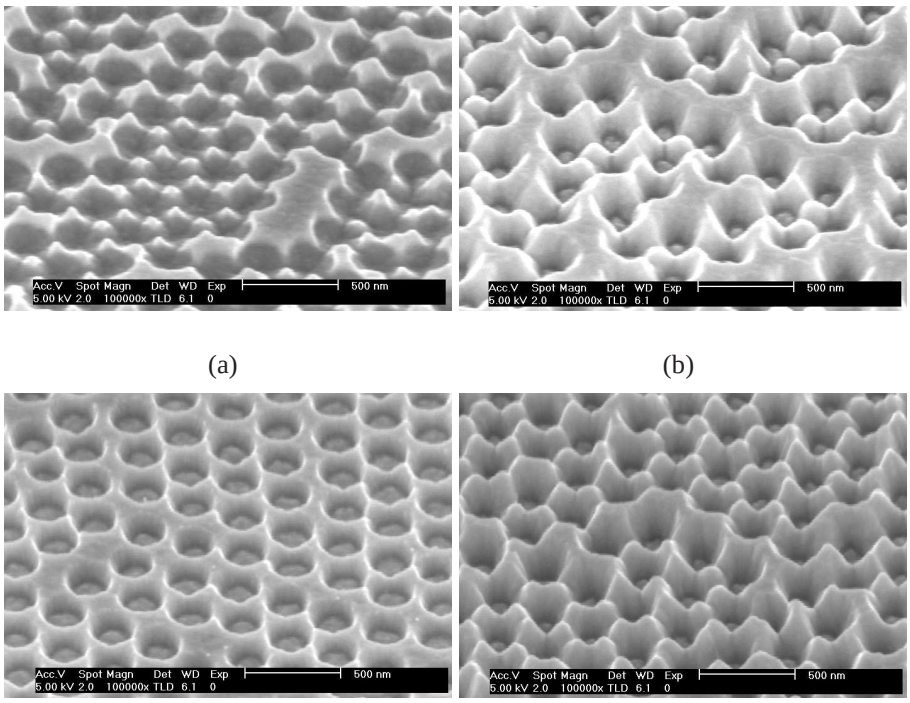

Fig. 6.9: SEM images of the analysed sample surfaces: (a) S3, (b) S4, (c) S5, (d) S6

First the effect of different surface structure is demonstrated by comparing samples S3, S4 and S6 with the reference S1. All structures were milled for 6 min and SEM confirmed that they possess similar heights of around 110 nm. From the plot shown in figure 6.10a it must be concluded that S4 features the largest accessible surface area as it shows the lowest impedance of the three structures while S3 and S6 show similar results. This is in agreement with SEM images of the structures taken earlier where the features of S4 have larger circumferences compared to S3. They also form almost closed circles. As the spheres for S6 were etched for a longer time in oxygen plasma the resulting pore sizes are smaller than in S4. Hence S4 should have the largest surface area of the three structures and the EIS data supports this supposition. The structure possessed by S4 is therefore the most effective for impedance reduction of the available surface topologies. The amount of reduction is assessed by plotting the ratio of impedances between S1 and S4 (figure 6.10b) with a maximum of 2.25 around 20 Hz which lies in the capacitive region of the interface behaviour. The scaling of the impedance with feature height is illustrated

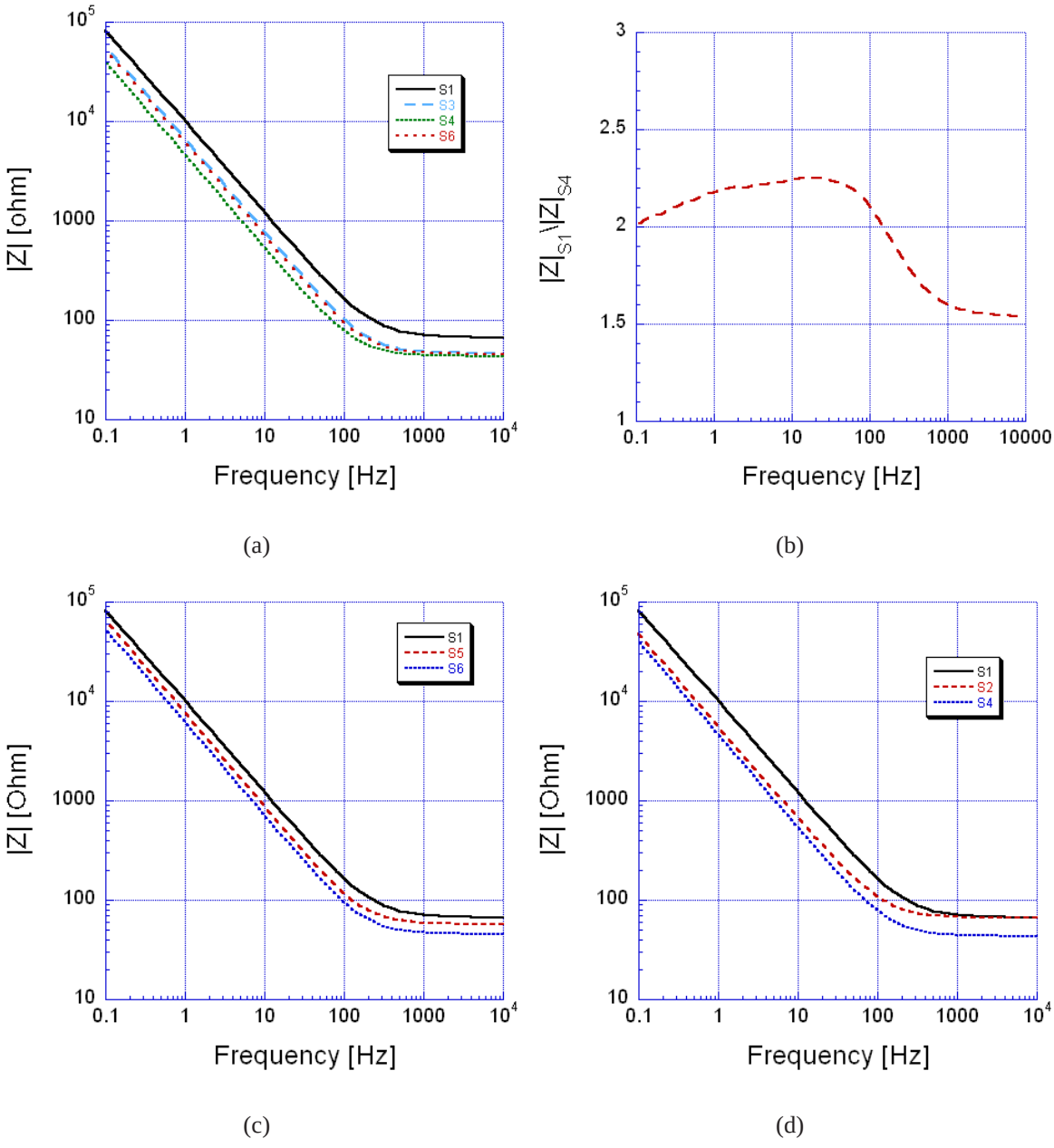

Fig. 6.10: Evaluation of the influence of the surface structure on the interface impedance

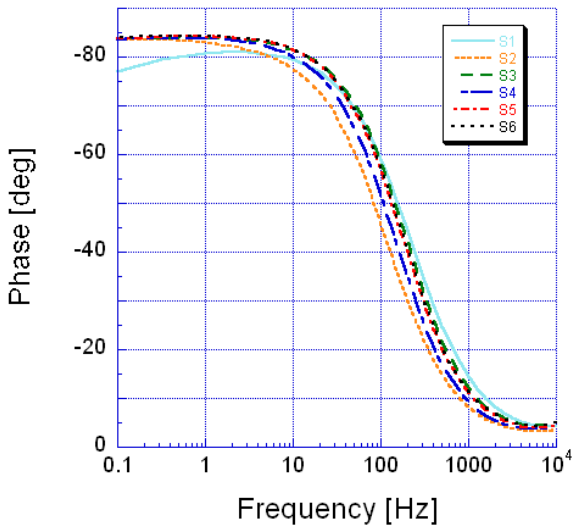

Fig. 6.11: Phase of the measured impedance for S1-S6

in figure 6.10c where the curves of S5 and S6 are plotted. The milling time for S5 was half that of S6 consequently resulting in half the feature height. While S5 still shows a reduction in impedance, it is approximately half the size achieved with S6 confirming the dependency on structure height. An exception is S2 because it was not produced by milling. It shows a reduced impedance (figure 6.10d) in the capacitive branch similar to S4 but then plateaus for higher frequencies at a value similar to S1 in opposition to the scaling conventions. While the rough outer gold surface leads to a decreased impedance similar to S4, the reduction is not sufficient enough to assume the successful creation of hollow gold structures. The phases for all six samples were similar with maximum values around -80° for low frequencies (figure 6.11).

To extract equivalent circuit parameters from the measured impedance curves the data has to be fitted to a matching circuit model. A freely available program called *EIS Spectrum Analyser* was used for this purpose. It specialises in fitting to and simulation of electrochemical circuit models. Four different fitting algorithms are included that can be used in combination with three weighting options to allow for easy data fitting to user-defined electrochemical circuit models. At the beginning a circuit model has to be chosen to which the data is fitted. The Nyquist plot representation is used to deduce the most likely combination of circuit components as described

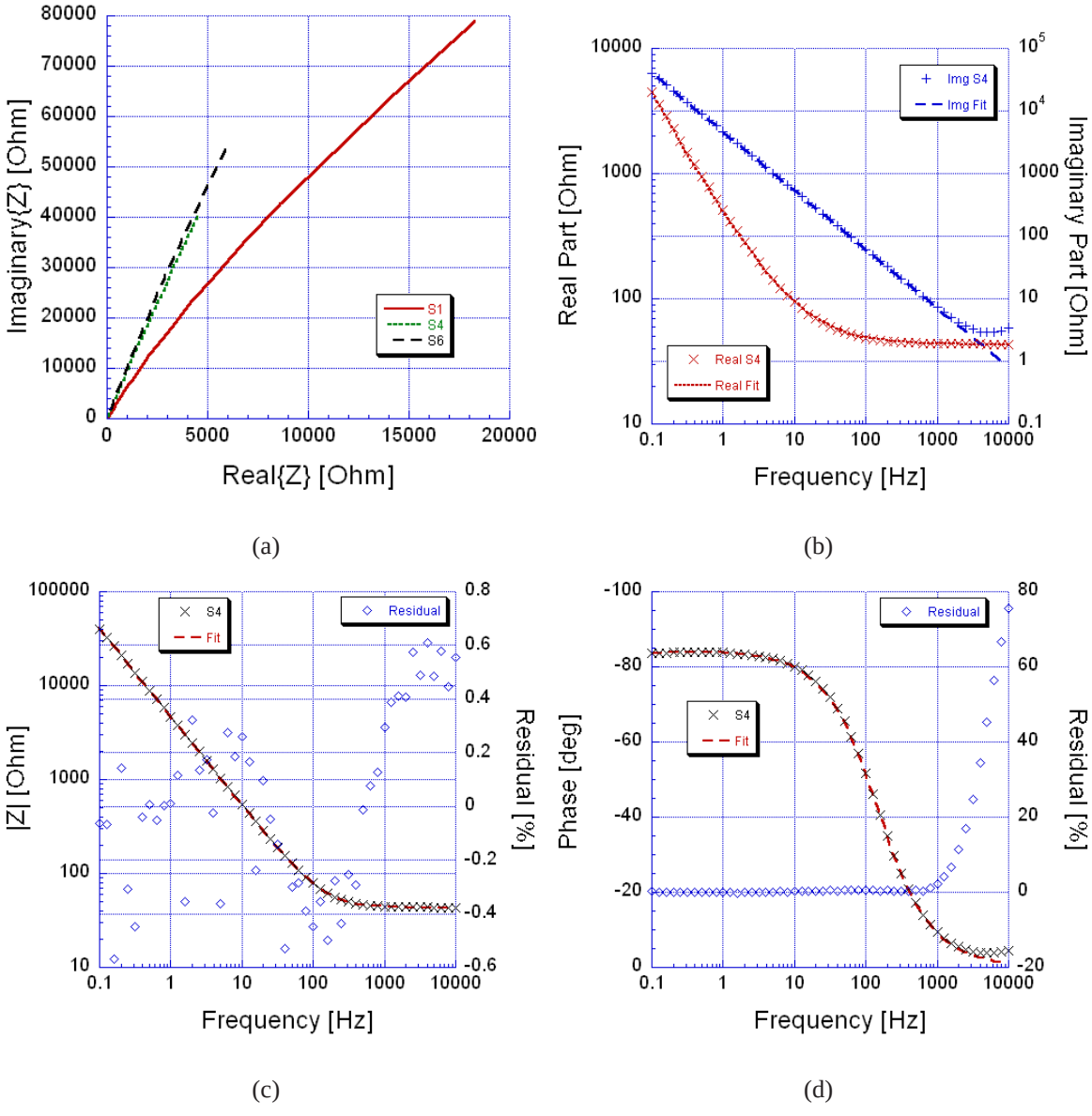

(a) (b)

(c) (d)

Fig. 6.12: Example of data fitting for S4 with Nyquist plot (a), comparison of fitted values to measurements of the real and imaginary parts of the impedance (b), and the residual errors for fitting total impedance magnitude (c) and phase (d)

Tab. 6.3: Results of equivalent circuit fitting for samples S1-S6 with relative errors

Sample	R_s [Ω]	CPE		R_t [Ω]
		Q [$S \cdot s^n$]	n	
S1	66.66 (0.81%)	18.45 x 10^{-6} (0.56%)	0.92 (0.14%)	0.8 x 10^6 (7.91%)
S2	65.97 (0.6%)	32.43 x 10^{-6} (0.47%)	0.93 (0.13%)	10 x 10^6 (-)
S3	46.28 (0.82%)	26.59 x 10^{-6} (0.59%)	0.94 (0.14%)	2.61 x 10^6 (808%)
S4	43.1 (0.69%)	38.24 x 10^{-6} (0.53%)	0.94 (0.13%)	2.55 x 10^6 (-)
S5	56.61 (0.68%)	23.01 x 10^{-6} (0.5%)	0.94 (0.12%)	3.2 x 10^6 (138%)
S6	45.22 (0.8%)	28.35 x 10^{-6} (0.59%)	0.94 (0.14%)	2.8 x 10^6 (-)

above. Examples are shown in figure 6.12a as almost straight lines with slight bends. This points to a constant phase element in parallel with a relatively high charge transfer resistance. After deciding on a circuit model the fitting routines are tested to see which one gives the best initial result. Attention has to be paid as some of the algorithms require a good initial parameter guess in order to find a global minimum. It is also checked whether fits improve with choice of weighting option. The program supplies a relative error estimate of the calculated parameters. These errors are summarised together with the parameters in table 6.3 but as it is not explained how the errors are exactly calculated the minimisation of the residuals is used instead for identification of the best possible fit. The last step was manual parameter optimisation to further improve results if possible. As an example for data fitting the results for S4 are shown in figure 6.12b-d. The relatively high residual in phase for high frequencies is caused by the small values at these points so that even slight deviations show as large percentage error. The Nelder-Mead algorithm with box constraints and amplitude weighting was found to give best results for fitting and was used for all six samples. The data could be fitted reasonable well to the model for all samples and the calculated parameters in general follow the scaling trend observed from the impedance curves. Sample S4 shows the highest equivalent capacitance value in correspondence with the lowest impedance. It is important to bear in mind that the models used for the data fitting can only approximate the system behaviour. A good fitting result does

not necessarily mean that the system is exactly described by the single components of the model. They only show trends of system behaviour. As gold is an chemically inert material and the low amplitude of the applied voltage signal does not allow reactions to occur, charge transfer is negligible, which is evidenced by the high values of R_t for all samples. Still the use of a charge transfer element improved fitting accuracy. Alternatively the curve bending attributed to charge transfer could also be caused by measurement errors in the system like drift in the open circuit potential. The fitted model is only valid for the investigated frequency interval and cannot be used to predict system behaviour outside that interval.

Complementary chronoamperometry and CV measurements confirm the improvement of the electrochemical properties of the electrodes. For matter of clarity only S1 and S4 are compared so the plots stay comprehensible as the values lie close together (figure 6.13). In the chronoamperometry the peak current value of the modified surface is slightly larger than for the reference indicating an increase in surface area. For other samples the value is similar to the reference. From the values only moderate increase is seen but as mentioned in the introduction chronoamperometry is not very precise for this purpose. The CV also shows improved characteristics as the area enclosed by the curve of S4 is larger than for S1 corresponding to more charge injected into the solution, which is important for neural stimulation. The exact values can be calculated by integrating the area under the curve. The values for S4 are 36.36 μC for positive current and -68.66 μC for the negative current direction which corresponds to a total increase by around 50% compared to 25.58 μC and -44.54 μC for S1. While the increase is not as strong for the other samples, they also feature higher amounts of charge.

In summary an impedance reduction of half an order of magnitude has been achieved. The measurements demonstrate that the developed nanopatterning method is capable of modifying the interface behaviour. To realise the full potential of this method and increase the improvement of interface properties the height of the nanostructures has to be maximised. Optimisation of the process is necessary to combine the process advantages with impedance reductions comparable to or even higher then those reported in the literature.

Samples S7 and S8 are discussed separately because of their inherently different structure.

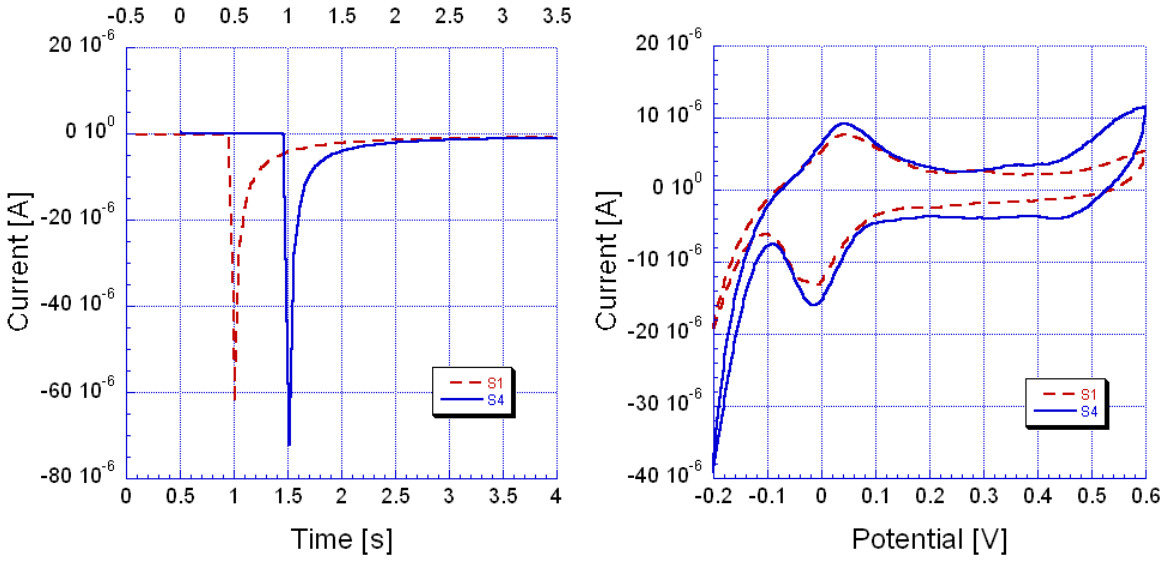

(a) (b)

Fig. 6.13: Comparison of the results of (a) chronoamperometry and (b) cyclic voltammetry for S1 and S4

Comparing them with S1 showed a considerably lower impedance for both PI samples (figure 6.14). The increase of impedance at higher frequencies is attributed to the small thickness of the gold film, which reduces the bulk conductivity. The low frequency impedance of S8 is similar to the nanostructured metal film sample S4 indicating that the PI pillars were not completely coated with gold as a successful coating would have resulted in a lower impedance demonstrated by S7. The evaporation has to be optimised by increasing the spacing between pillars through reduction of pillar diameter and using different coating angles. But S7 demonstrates the improved performance of this type of nanostructuring even though it did not possess the maximum surface area possible because of pillar bundling. The readily achievable aspect ratios and the reduced amount of gold necessary make this the most promising route for electrode nanostructuring. CV and chronoamperometry further prove the good properties of the interface modified with this method. The CV shows a large increase in injected current because of the large accessible surface area with a total charge of $3.1\ \mathrm{mC}$ compared to $70.1\ \mu\mathrm{C}$ for S1. The sharp peaks in the CV scans are most likely due to the adsorption and desorption of chloride ions from the electrolyte on the gold surface [93]. As the peak remains stable for many cycles

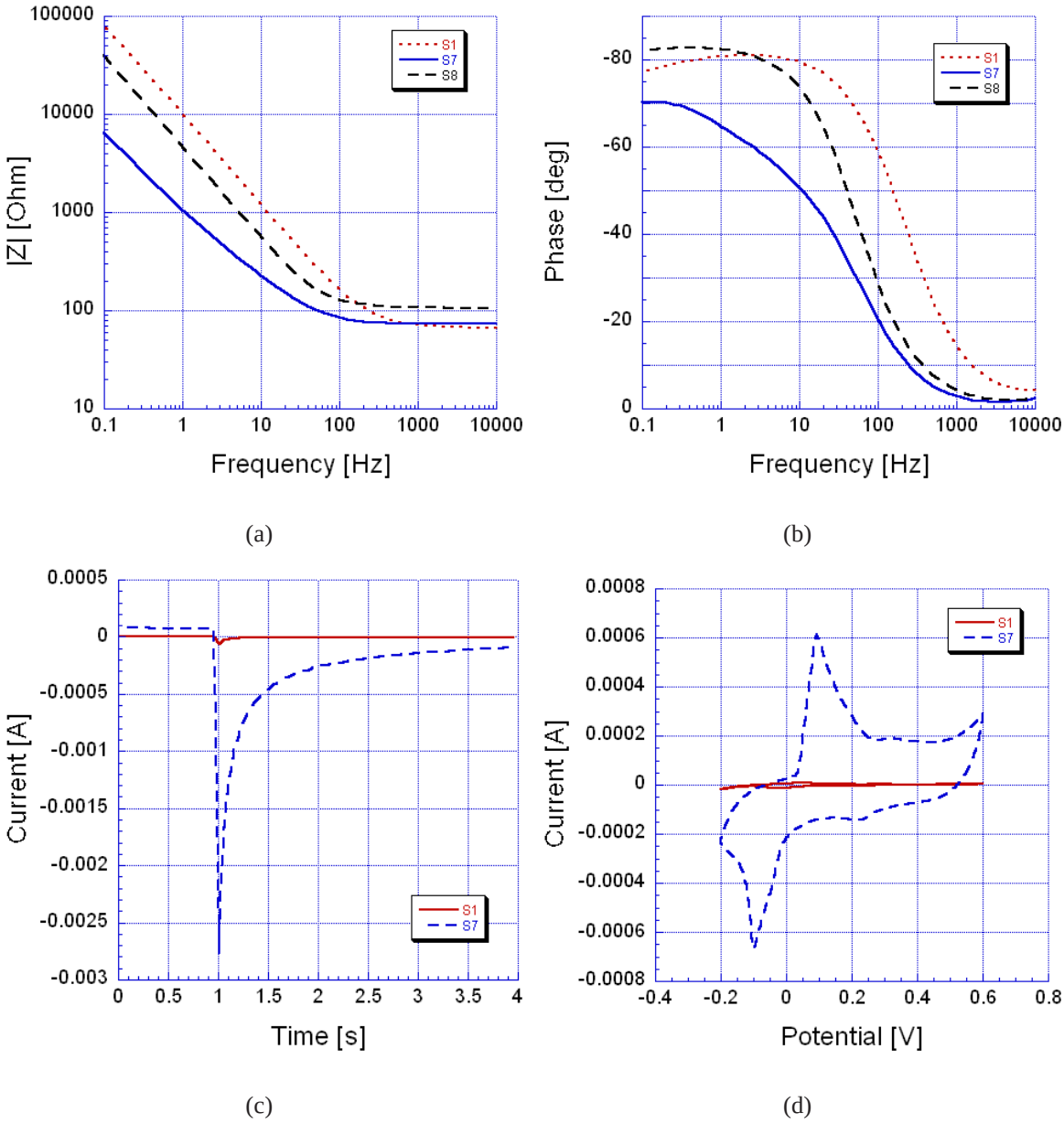

Fig. 6.14: Results for the polyimide pillar samples for (a) impedance magnitude, (b) phase, (c) chronoamperometry and (d) cyclic voltammetry

it potentially offers an additional current injection path for stimulation. The data for S7 was fitted with a series combination of solution resistance and a constant phase element without further circuit components. The obtained values were R_s = 71.357 Ω (1.29%), Q = 228.2 S·s^n (1.29%) and n = 0.77 (0.5%). S8 was not further investigated as it showed similar behaviour to S4. Future work should focus on the PI pillar method for optimisation as the electrochemical measurements for this structure type are superior to the patterned metal films.

6.3 Microcolumnar gold

During the measurement of the first nanostructured samples unexpected results were obtained. Instead of reduced impedances these actually offered higher impedance compared to plain gold surfaces even though both samples originated from the same gold deposition. Hence any difference in gold composition should be excluded. In order to identify whether the gold undergoes any changes during the fabrication process a plain gold sample was treated using the same steps as a modified chip except for the titanium masking. Impedance spectroscopy then showed results as expected that the modified samples have half the impedance of non-patterned samples. Noticing then that samples with increased coating thickness caused lower impedance led to the presumption that the gold might exhibit an intrinsic porosity. This was confirmed by SEM inspection of film cross sections prepared by cleaving the gold coated silicon chips. They possessed a distinct columnar structure with voids separating the columns in contrast to gold films deposited by thermal evaporation or electroplating which possess a dense grainy structure. The explanation can be found in the work of Thornton [94] who extended the standard structure zone model [95] to take into account the argon pressure for sputter deposition. It exhibits a zone that is characterised by matchstick topology with voided columnar grains. While it is known that many other metals show this kind of behaviour there seems to be no report on columnar gold or its exploitation as a neural electrode material.

To study this film structure further two different sets of samples were investigated. The deposition pressure is the parameter responsible for the change in surface structure and therefore the samples were prepared using two pressure settings that were on the edge of the operational

limits of the sputter coater. For low pressure deposition 0.9 Pa were used, which was about the smallest possible value that still maintains an argon plasma. The high deposition pressure was set to 2.8 Pa because higher pressures cause a fault in the backing pump that cuts off the plasma. Silicon squares of 10 mm side length were used as sample substrates. Prior to deposition they were cleaned in IPA in an ultrasonic bath. For gold adhesion to the silicon surface a thin titanium layer was coated first. Gold was deposited at 100 W for 3, 6 and 9 min for both pressures. This resulted in films of 90, 160 and 215 nm thickness independent of the deposition pressure. The difference in structure can be seen even under optical inspection. The low pressure films possess the metallic shine and reflectance commonly associated with gold. The high pressure films on the other hand have a darker, more matt appearance and are less reflective. SEM imaging of the low pressure samples show a film structure that is typical for evaporation or electroplating processes (figure 6.15). They are densely packed with small sized grains of random orientation and the surface is composed of a closed film with nodular growth.

The films grown at higher pressure have a rougher, more porous surface with voids clearly visible (figure 6.16). In the cross section it can be seen that these films are composed of columnar features running completely through from bottom to top so that their height is equal to the film thickness. The width of the individual columns is between 10 and 20 nm. The formation of columns is caused by substrate shadowing effects where high points on the substrate are exposed to a higher coating flux than the valleys. These high points can be created by initial surface roughness, preferential nucleation or inhomogeneities. The shadowing effect is enhanced by the oblique component in the coating flux present for sputter deposition. For low deposition pressures this effect is countered by surface diffusion as the ions possess high energies due to the electrical field in the plasma discharge. These energies give them a high surface mobility so that they can move around on the surface after impact and cancel out differences in coating. The low pressure ensures that the metal atoms travel almost collision-free through the plasma similar to line-of-sight transport in evaporation explaining the similar film structure. For higher argon pressures the atoms collide more often with the gas particles as they pass through the plasma which reduces their energy. The resulting reduced mobility limits surface diffusion so

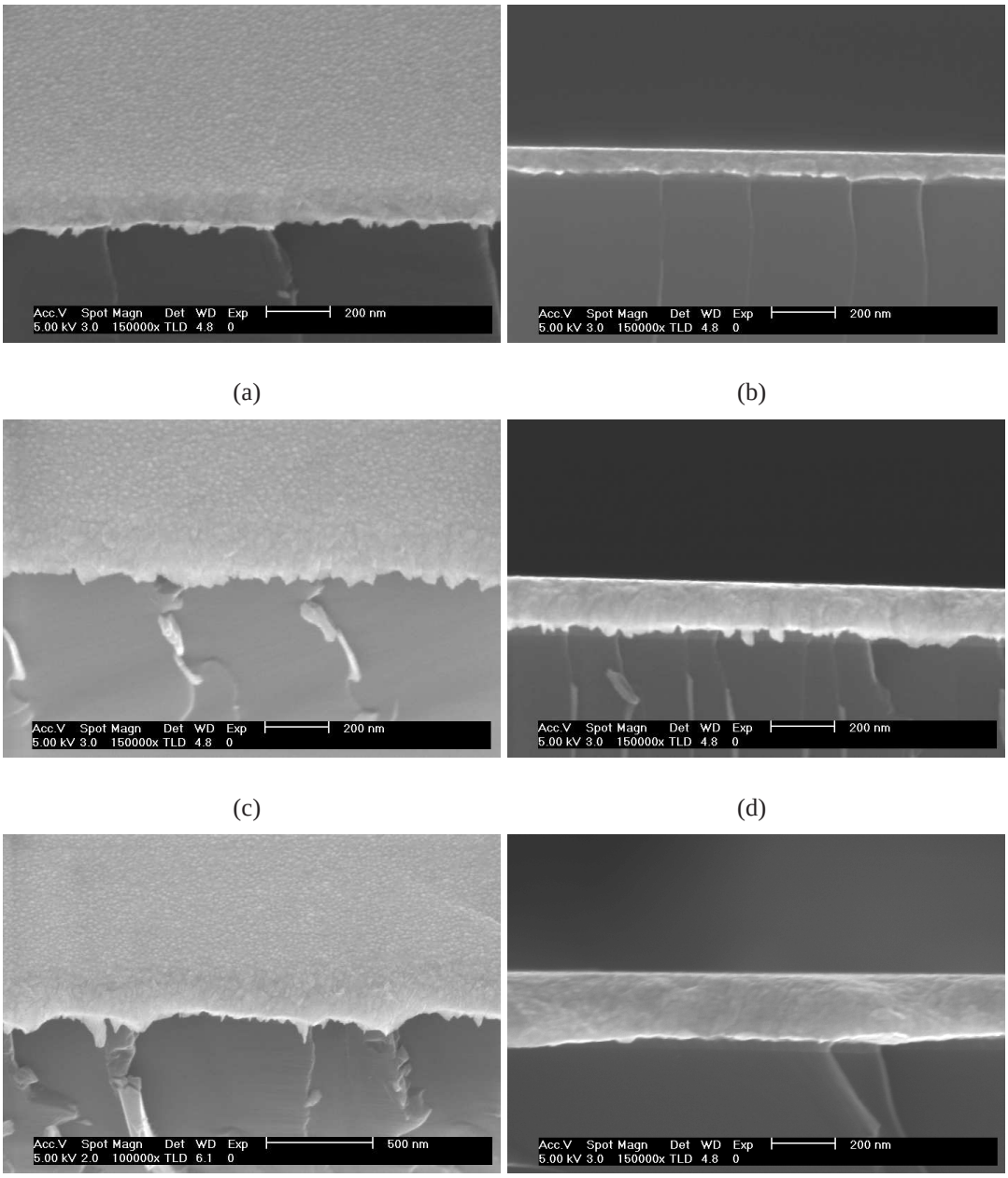

Fig. 6.15: SEM images at 45° angle showing the top of the samples deposited at 0.9 Pa for a) 3 min c) 6 min and e) 9 min and corresponding cross sections (b,d,f)

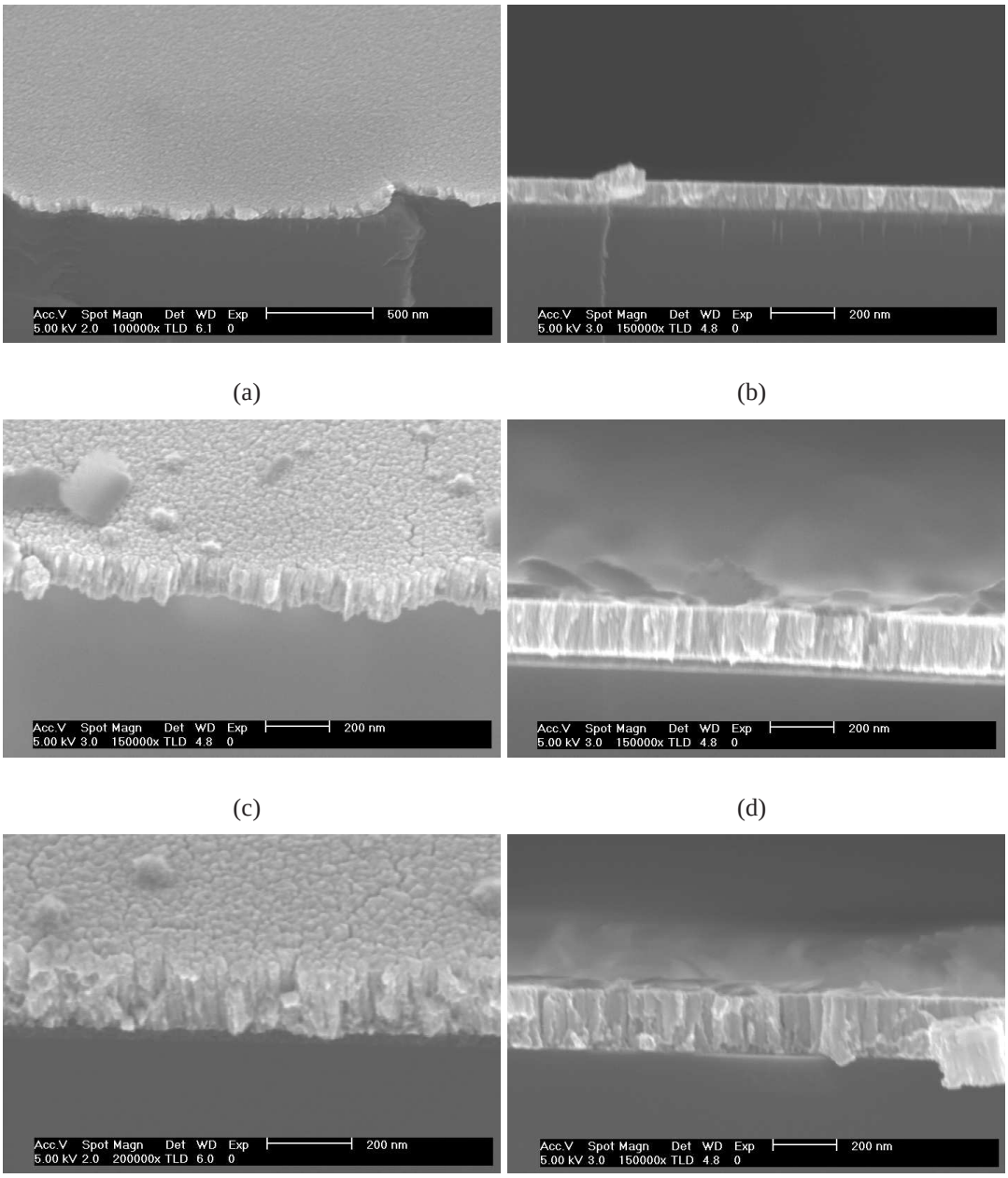

Fig. 6.16: SEM images at 45° angle showing the top of the samples deposited at 2.8 Pa for a) 3 min c) 6 min and d) 9 min and corresponding cross sections (b,d,f)

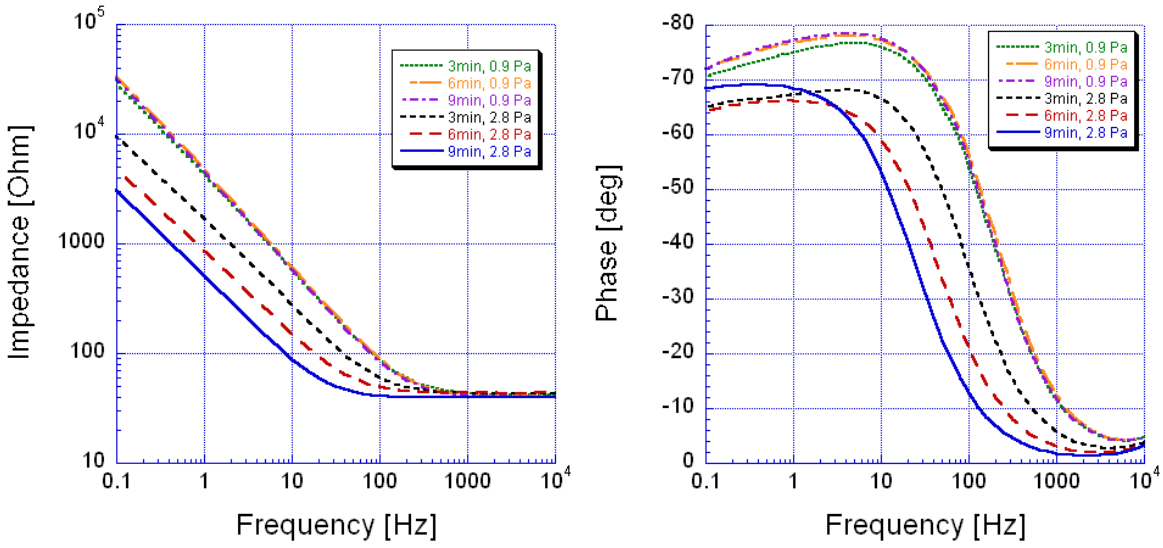

(a) (b)

Fig. 6.17: Comparison of (a) impedance spectra and (b) corresponding phase plots for gold films deposited at low and high pressures

that the effect of shadowing is predominant and leads to the columnar structure.

In the analysis the EIS data of the samples display the typical behaviour of a double layer interface. The impedance decreases approximately inverse with frequency until it saturates above a certain cut-off value. The curves are interpreted as capacitive behaviour of the interface dominating at low frequencies. The high frequencies are dominated by the solution's resistance, metal film resistivity and connection resistances. In detail the low pressure films showed no significant variation of impedance with film thickness (figure 6.17). This indicates that their densely packed structure does not exhibit an accessible film porosity. The samples deposited at high pressure in contrast display decreased impedance for increasing film thickness demonstrating that the pores in the columnar structure are sufficiently large to increase the effective surface area of the film. Furthermore it shows that this increase is proportional to the height of the columns. It must be noted that even for the shortest deposition time (3 min) and hence the thinnest film the impedance already differs by half an order of magnitude illustrating the significance of film structure and its effect on the interface. For 9 min the impedance differed by a full magnitude of scale, which is a significant improvement of the interface impedance and has the

potential for further improvement by increasing the film thickness. After the frequency cut-off both film types plateau at roughly the same value of about 40 Ω, which means that there is no appreciable difference in bulk film conductivity and the columnar structure does not interfere with current conduction.

The examination of the corresponding Nyquist plots (figure 6.18a) shows that they are composed of nearly straight lines with slight bending. This means that at least a constant phase element in parallel with a charge transfer resistance must be used as circuit model. The presence of a Warburg impedance could also be justified as the phase angle of the curves is close to 45°. Gold is considered a capacitive electrode material so that a high charge transfer resistance should be assumed and diffusion limiting through a Warburg element should not occur. Both variants with and without Warburg impedance are used for data fitting in order to determine which model delivers better results (table 6.4). The tendency in all the circuit parameters is the same as for the impedance plot. While the values for low pressure samples show little variation, the high pressure circuit parameters scale accordingly to the proportionality laws in table 6.1. The capacitance increases while R_t and Z_w magnitudes decrease. Using a Warburg element leads to slightly better fits as the residuals are generally lower compared to charge transfer resistance alone. As an example the results obtained for the 160 nm thick high pressure sample are shown in figure 6.18. As stated before, from the physical point of view the model without the Warburg impedance is a more accurate representation of the real situation. The similarity of the curve fits obtained for the two models, which represent different electrochemical situations, serves to illustrate the ambiguity encountered when using equivalent circuits to model complex processes such as double layer interfaces.

The results of the chronoamperometry and cyclic voltammetry further consolidate the better properties of the columnar film structure over the granular one. While no change in current was observed in the chronoamperometry for the low pressure process, it showed an increase with thickness for higher pressure (figure 6.19a). The values for $\mid I \mid$ are substantially larger then for the low pressure coating. Given that $\mid I \mid$ increases with surface area, it leads one to conclude that the columnar samples have a larger effective surface area that is proportional to film

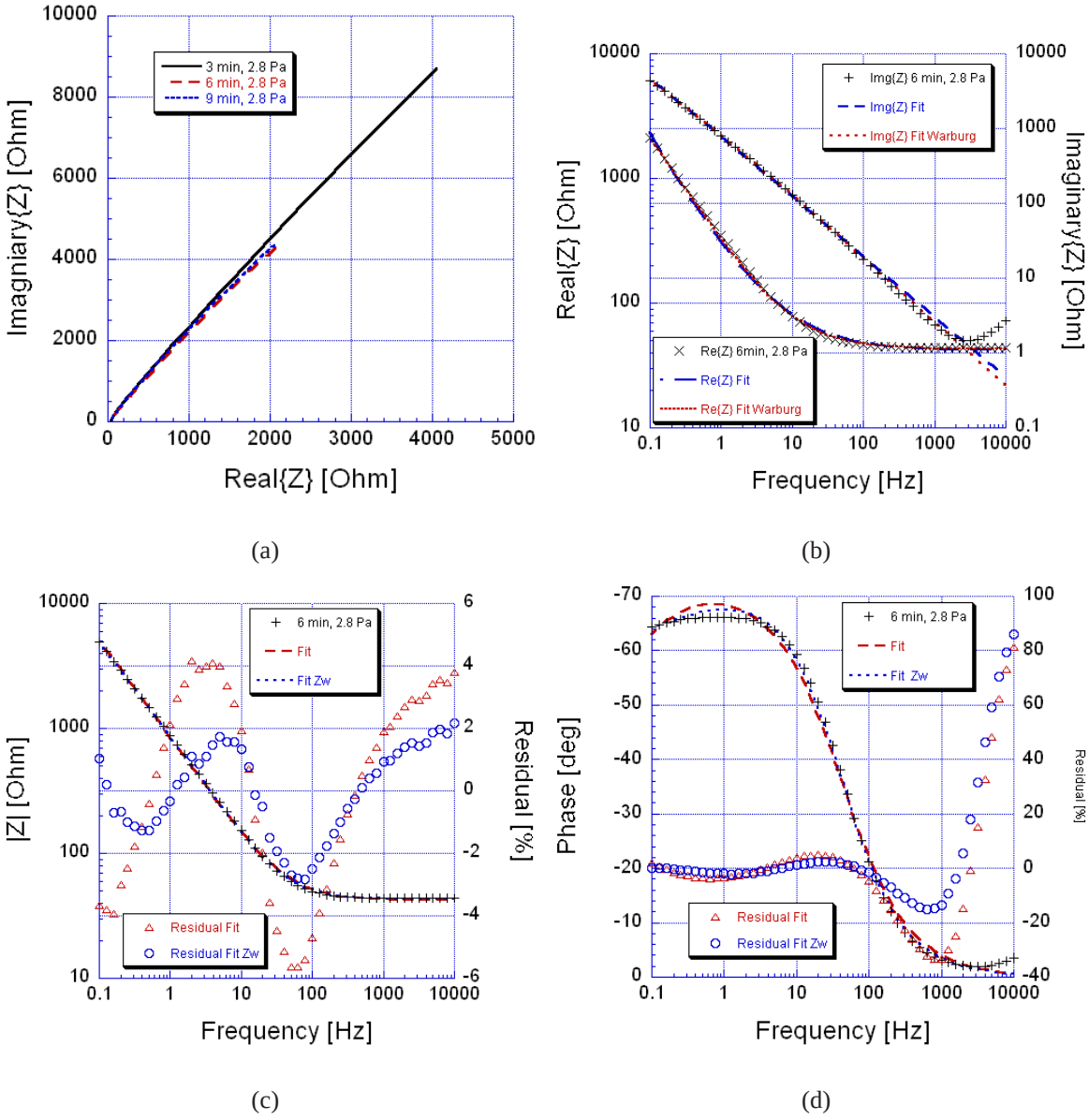

Fig. 6.18: Comparison of equivalent circuit fitting with and without a Warburg element for the 6 min - 2.8 Pa sample

Tab. 6.4: Results of equivalent circuit fitting for gold samples of both pressure settings with relative errors

Sample	R_s [Ω]	CPE		R_t [Ω]	Z_w [Ω]
		Q [$S \cdot s^n$]	n		
3 min	40.47 (2.05%)	47.13 x 10^{-6} (1.49%)	0.88 (0.38%)	180 x 10^3 (12.9%)	-
0.9 Pa	41.23 (0.89%)	40.24 x 10^{-6} (0.69%)	0.91 (0.17%)	10.1 x 10^3 (25.08%)	50 x 10^3 (12.86%)
6 min	39.19 (1.57%)	41.25 x 10^{-6} (1.12%)	0.89 (0.28%)	200 x 10^3 (11.93%)	-
0.9 Pa	39.86 (0.82%)	35.33 x 10^{-6} (0.63%)	0.92 (0.15%)	7.7 x 10^3 (34.76%)	60.6 x 10^3 (5.38%)
9 min	39.04 (1.59%)	43.24 x 10^{-6} (1.15%)	0.9 (0.17%)	190 x 10^3 (11.55%)	-
0.9 Pa	39.69 (0.79%)	37.35 x 10^{-6} (0.61%)	0.92 (0.15%)	10.2 x 10^3 (27.4%)	57.3 x 10^3 (15.49%)
3 min	40.85 (2.7%)	135.6 x 10^{-6} (2.27%)	0.81 (0.69%)	61 x 10^3 (20.65%)	-
2.8 Pa	41.92 (1.44%)	105.06 x 10^{-6} (1.37%)	0.86 (0.39%)	2.7 x 10^3 (28.58%)	13 x 10^3 (3.83%)
6 min	41.86 (1.88%)	270.08 x 10^{-6} (1.84%)	0.81 (0.63%)	30 x 10^3 (17.68%)	-
2.8 Pa	42.65 (1.09%)	215.16 x 10^{-6} (1.2%)	0.85 (0.37%)	1.7 x 10^3 (23.95%)	7 x 10^3 (3.84%)
9 min	38.43 (1.5%)	436.57 x 10^{-6} (1.64%)	0.84 (0.6%)	24.5 x 10^3 (21.77%)	-
2.8 Pa	38.85 (1.06%)	374.75 x 10^{-6} (1.26%)	0.87 (0.43%)	1.7 x 10^3 (34.46%)	6 x 10^3 (5.62%)

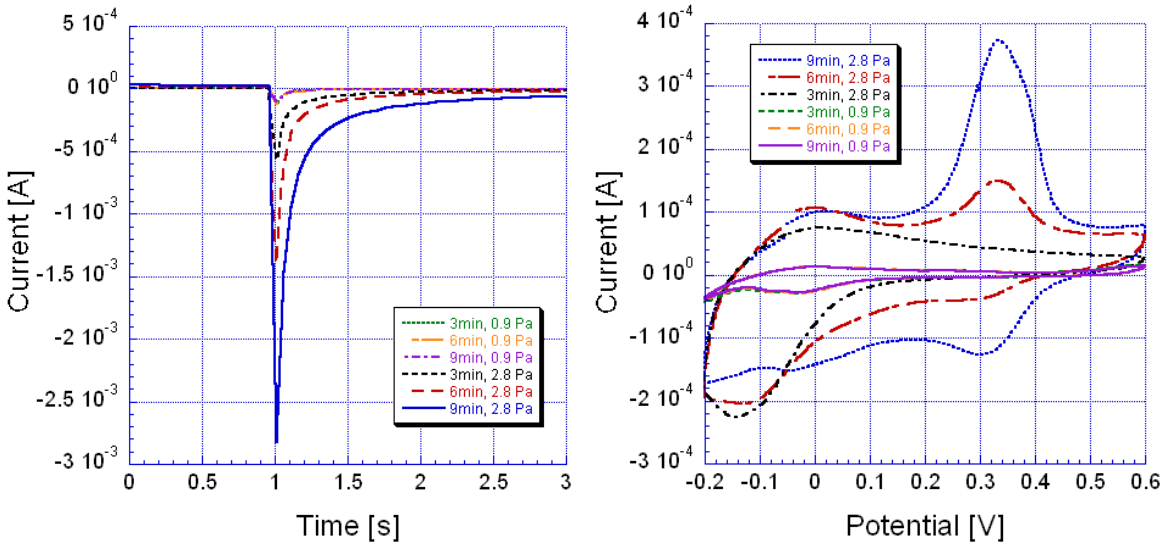

(a) (b)

Fig. 6.19: Results of (a) chronoamperometry and (b) cyclic voltammetry for both low and high pressure gold films

thickness. For the CV again all three low pressure films feature almost the same characteristics independent of film thickness while the samples prepared at 2.8 Pa experience broadened CV curves for thicker films (figure 6.19b). In addition a peak develops in both scan directions for the high pressure films around 0.33 V with the height of the peak increasing with film thickness. The peaks are again attributed to the adsorption and desorption of chloride ions. The peaks then grow in height for thicker films because more electrode surface area is available for chloride adsorption. In summary the gold films with columnar morphology show better properties compared to the grained gold with regards to the application as electrode material in neural devices. They also have the possibility of further improvement by scaling of the film thickness.

As an assessment of the quality of the porous gold films they are compared to titanium nitride. TiN is a well known neural electrode material whose excellent properties are also based on a porous, columnar film structure. The TiN films were grown by Dr Zoe Barber and Dr Kartik Senapati from the Department of Material Science of the University of Cambridge. The titanium nitride was deposited on silicon chips with an RF power of 120 W at pressures of 3 and 4 Pa in a 40% nitrogen atmosphere at room temperature. Film thickness was determined as

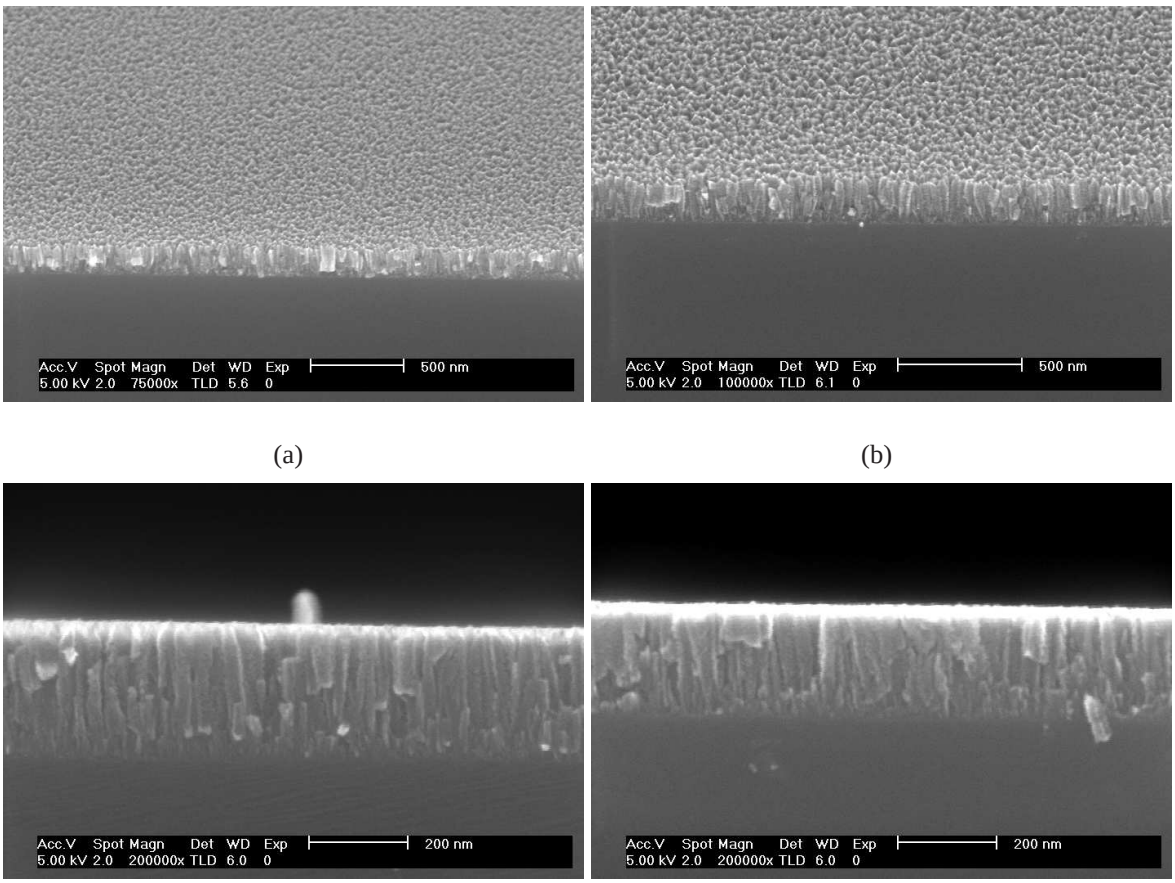

Fig. 6.20: SEM images of titanium nitride surfaces at 45° angle for (a) 290 nm at 3 Pa and (b) 255 nm at 4 Pa and the corresponding cross sections (c-d)

135 nm and 290 nm for 3 Pa and 170 nm and 255 nm for 4 Pa. The values are close enough to the thickness of the gold films to allow comparison. Figure 6.20 shows the structure of the TiN samples to be composed of columns as well.

Similar to the columnar gold, the impedance of the TiN also decreases with increasing film thickness corresponding to larger column heights (figure 6.21a). In addition the rise in deposition pressure from 3 to 4 Pa increases the porosity so that a larger surface area is accessible by the electrolyte causing the impedance to drop further. This effect is likely to be seen in gold films as well but the gold was already deposited at the maximum pressure possible with the used sputter coater. As gold films deposited at 2 Pa still show the morphology and electrochem-

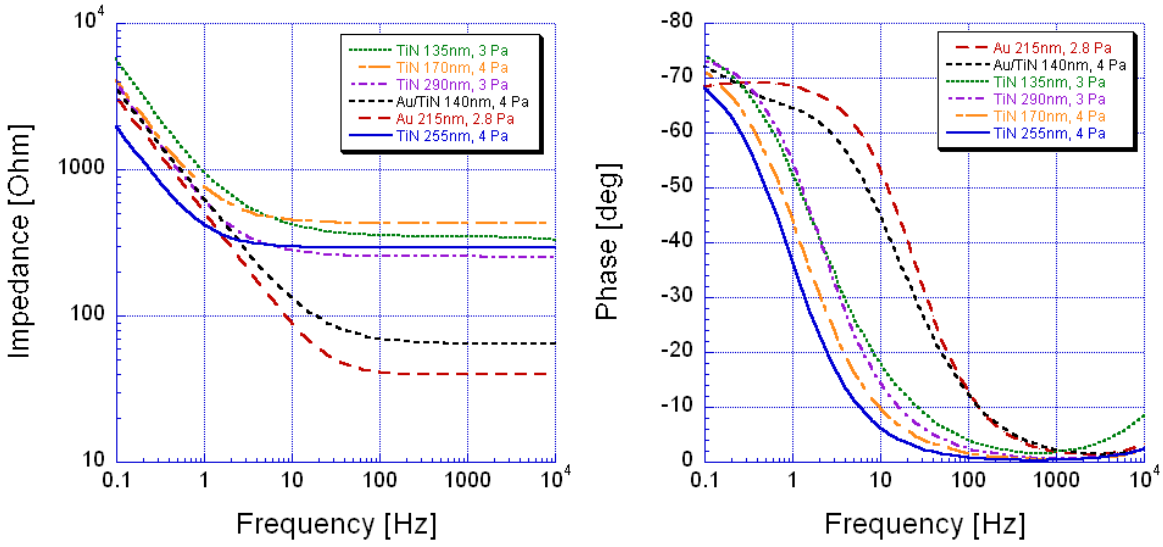

(a) (b)

Fig. 6.21: (a) Impedance and (b) phase measurements of titanium nitride films in comparison with the thickest columnar gold sample

ical behaviour of densely packed grain films it is presumed that the value of 2.8 Pa lies within a region where the columnar structure is just beginning to evolve and there is still a certain margin left to further increase gold porosity at higher pressures. The conductivity of the TiN films is assumed to be lower than for gold as they plateau at higher values compared to the gold films. This is confirmed by depositing a 140 nm TiN film on a 150 nm gold layer, which offers a shunt pathway and leads to a smaller impedance value at higher frequencies. While the best TiN sample possesses an impedance that is slightly smaller then for the best gold film it must be kept in mind that the TiN film thickness is roughly 40 nm thicker and was deposited at a higher pressure resulting in higher porosity. This indicates that even though TiN was considered to be a superior material compared to plain gold surfaces, gold potentially has better properties if the film structure is optimised for use in neural devices. For comparison the fitted values of the equivalent circuit parameters are summarised in table 6.5. In contrast to the gold films the data was fitted best by a simple series circuit of a resistance and a constant phase element. Consideration of a charge transfer element was not necessary as it did not improve fitting results and its role on material behaviour can be neglected.

Tab. 6.5: Results of equivalent circuit fitting for TiN samples with relative errors

Sample	R_s [Ω]	CPE	
		Q [$S \cdot s^n$]	n
135 nm, 3 Pa	362.81 (2.16%)	264.97 x 10^{-6} (0.57%)	0.854 (0.4%)
290 nm, 3 Pa	252.03 (1.11%)	391.2 x 10^{-6} (0.3%)	0.86 (0.21%)
170 nm, 4 Pa	427.87 (0.32%)	378.14 x 10^{-6} (0.14%)	0.857 (0.1%)
255 nm, 4 Pa	289.34 (0.58%)	796 x 10^{-6} (0.37%)	0.856 (0.26%)

Chronoamperometry and cyclic voltammetry further demonstrate the similarity of the two materials as they show the same scaling tendencies and the values for the films with the best properties are similar (figure 6.22). Unlike with gold the chloride possesses no particular affinity to TiN so the CVs do not show peaks and remain flat within the scanned voltage window. Both materials are considered to be capacitive neural electrode materials because no faradaic charge transfer mechanism exists in the materials themselves and their behaviour is dominated by the charge double layer capacitance [96]. Their properties then mainly dependent on the exposed surface area. Since they show comparable behaviour and properties within acceptable limits for similar film thickness this leads to the conclusion that they possess a comparable film structure. The advantage of gold is a simpler fabrication process and its properties do not depend on the amount of nitrogen incorporated into the film, which can lead to quite different properties. The film conductivity of gold is higher evidenced by the lower impedance at higher frequencies and the film properties are more stable and reproducible.

6.4 Conclusion

The analysis using the electrochemical methods discussed at the beginning of the chapter demonstrated that all the nanostructuring methods developed were able to improve the properties important for neural applications. The structured gold thin films achieved a maximum reduction in interface impedance by half the value of unmodified reference electrodes. The polyimide pillars could lower the impedance by an order of magnitude similar to the porous gold films discovered

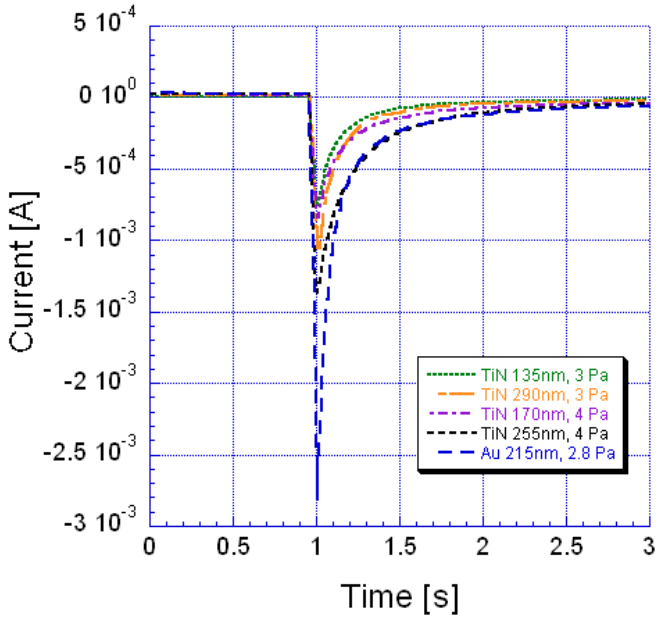

(a)

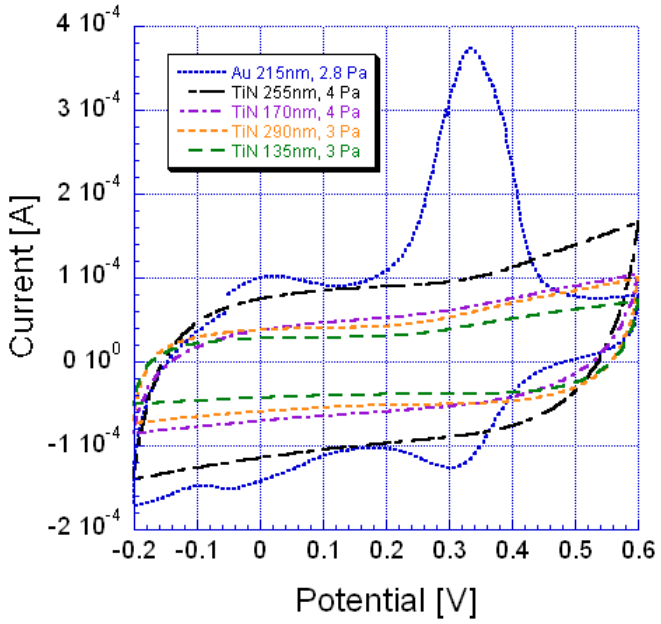

(b)

Fig. 6.22: Results of (a) chronoamperometry and (b) cyclic voltammetry for titanium nitride films compared to the thickest columnar gold sample

during the electrochemical measurements. Both the pillars and the porous film could easily feature even better properties by increasing pillar height and film thickness. The polyimide pillar process is still not perfect and optimisation should lead to more improvement in the interface properties. Together with the economical use of the expensive gold material it makes this the best approach towards nanostructured neural electrodes.

7. IMPLANTS FOR RECORDING FROM NERVES

The implants developed in this thesis serve two purposes, to test the integration of nanostructured surfaces into the fabrication of neural devices and to evaluate the effect of the nanotexture in neural tissue. The nanostructure process was originally developed for incorporation into the polyimide microchannel device but they have to be implanted in animals for an extended time period before they can be tested. Therefore it was decided to additionally design and fabricate a set of neural implants for in vitro assessment in the Department of Neurophysiology at the medical school of the University of Birmingham. The implants are intended for different applications and requirements so that their designs differ as discussed in the first section. The subsequent sections describe the fabrication process and the modification of the electrodes for each of the designs.

7.1 Requirements for implant devices

The implants are classified according to their application locations into two distinct types. In order to be integrated well in the biological tissue they have to accommodate the structure of the target organ. The polyimide roll intended for the peripheral nervous system uses the ability of the axon to regrow after injury. The injured axon fibres regrow through the roll from the cell body side to innervate the muscle. The device has to be a three-dimensional structure in order to completely envelope the axon requiring a sophisticated fabrication process. As the axon needs to be supplied with oxygen and nutrients the device channels have to provide enough space to support both axons and blood vessels as well as connective tissue.

The needles on the other hand represent penetrating devices which are directly inserted into the brain tissue. Their stiffness has to be sufficient enough to allow insertion without device

buckling. The brain tissue itself is relatively soft but covered with a tough skin layer. During the surgical implantation procedure this layer is normally incised with a scalpel and peeled back to expose an area for insertion. While a certain stiffness is required for insertion, the implant should be flexible enough to withstand deformation and stresses caused by minute movements of the brain without breakage or damaging the brain tissue. To minimise injury caused to the brain by device insertion, a near-planar shape with a smallest possible cross section is desirable. This helps to limit the inflammatory tissue response and cell death. It also prevents the neurons from being pushed away too far from the recording sites.

7.2 Silicon needle process

The first attempt at neural implant fabrication was made with silicon needles produced from 500 μm thick 4-inch silicon wafers. A Bosch process was used to pattern the wafer into a needle shape as seen in figure 7.1. This process uses a short isotropic silicon etch step with sulphur hexafluoride (SF_6) followed by a deposition step of a thin polymer layer from octafluorocyclobutane (C_4F_8) gas, which passivates the side walls while the surface perpendicular to the plasma is cleared off the polymer by ion bombardment. The two steps are alternated continuously until the desired depth is reached. Almost perpendicular side walls can be achieved otherwise impossible with an isotropic etch alone. The needles have a square base with contact pads for electrical connection. From the base the silicon tapers linearly into a sharp tip. The design included single needles with one or three electrodes and multiple arrays of the single version. Contact pads and electrode tracks were made from thermally evaporated gold, lithographically patterned and wet etched in potassium iodine or milled by ion beam. As the devices are released during etching, the wafer has to be mounted on a carrier wafer with double-sided carbon tape to prevent the devices from being scattered throughout the chamber. The devices were then coated with a thin insulation layer of polyimide PSPI 7505 exposing only the electrode tip and the contact pads.

In order to use them for recording neurological data from brain slices they were attached to custom-made printed circuit boards (PCB). The electrodes were connected to the PCB by

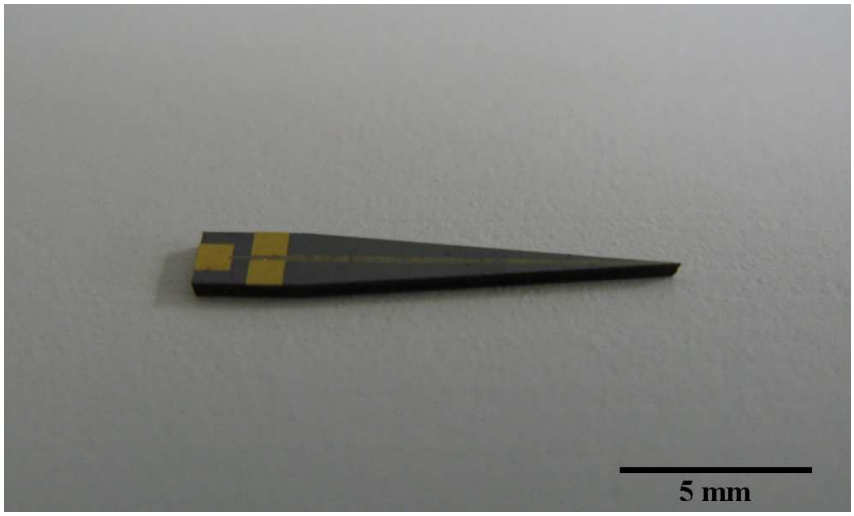

(a)

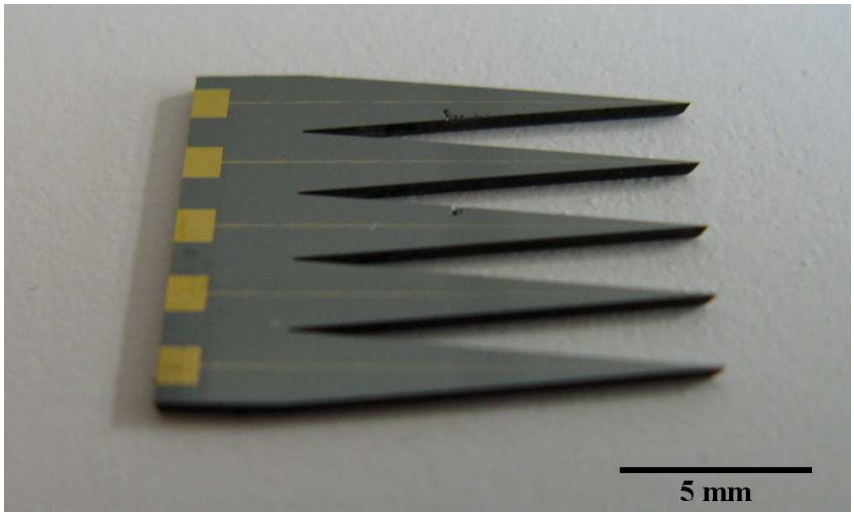

(b)

Fig. 7.1: Prototypes of the first silicon needle devices: (a) single device (b) array

wire bonding. Pin connectors mounted on the PCB allowed the connection to the electrophysiology rack. Unfortunately no viable signals could be acquired. Dr Jiruska, who conducted the experiment, suggested that the device thickness might be too large to record any useful information because the devices deform the tissue too much and push the neurones away from the electrodes. In an effort to reduce the needle thickness the fabrication was repeated with 200 μm thick silicon wafers. It was the smallest available thickness for single wafers that could be safely handled and even these were fragile and occasionally broke during processing. Repeating the recording experiment with the thinner needles single, spiking events were distinguishable but signal quality was very poor. The decision was then made to aim for a much smaller thickness to ensure minimal impact on the tissue and allow intimate contact between neurones and electrodes to boost signal quality and enable reliable recording of neurological signals. A target thickness of 20 μm was chosen, which is well below the average neuron size of 30 μm and should be sufficient to ensure good performance. Single wafers of such thickness are not readily available as they are very fragile and fracture easily under point loads making their handling very difficult.

The Michigan probes [7] solve this problem elegantly by using deep boron diffusion to define the desired device shape into the surface layer of a conventional silicon wafer. After device patterning it is released in ethylene diamine pyrocatechol, which etches pure silicon but not the boron doped parts. As the devices are expensive and the equipment to apply this technique was not accessible another solution was sought. One idea is to change the material for device fabrication to spin-on photopatternable polymers as described in the SU8 needle process section. The other option is to use silicon-on-insulator (SOI) wafers instead. A SOI wafer is produced by oxidising the surface of two silicon wafers and bonding them together at the oxide layer side. Mechanical polishing is then used to thin one of the wafers down to the desired thickness while the other one acts as the handling wafer. This way the thin silicon can be processed without the risk of breakage during handling. The SOI wafers obtained were 4-inch in diameter with a 400 μm thick handle wafer, a 2 μm oxide layer and 20 μm top silicon layer.

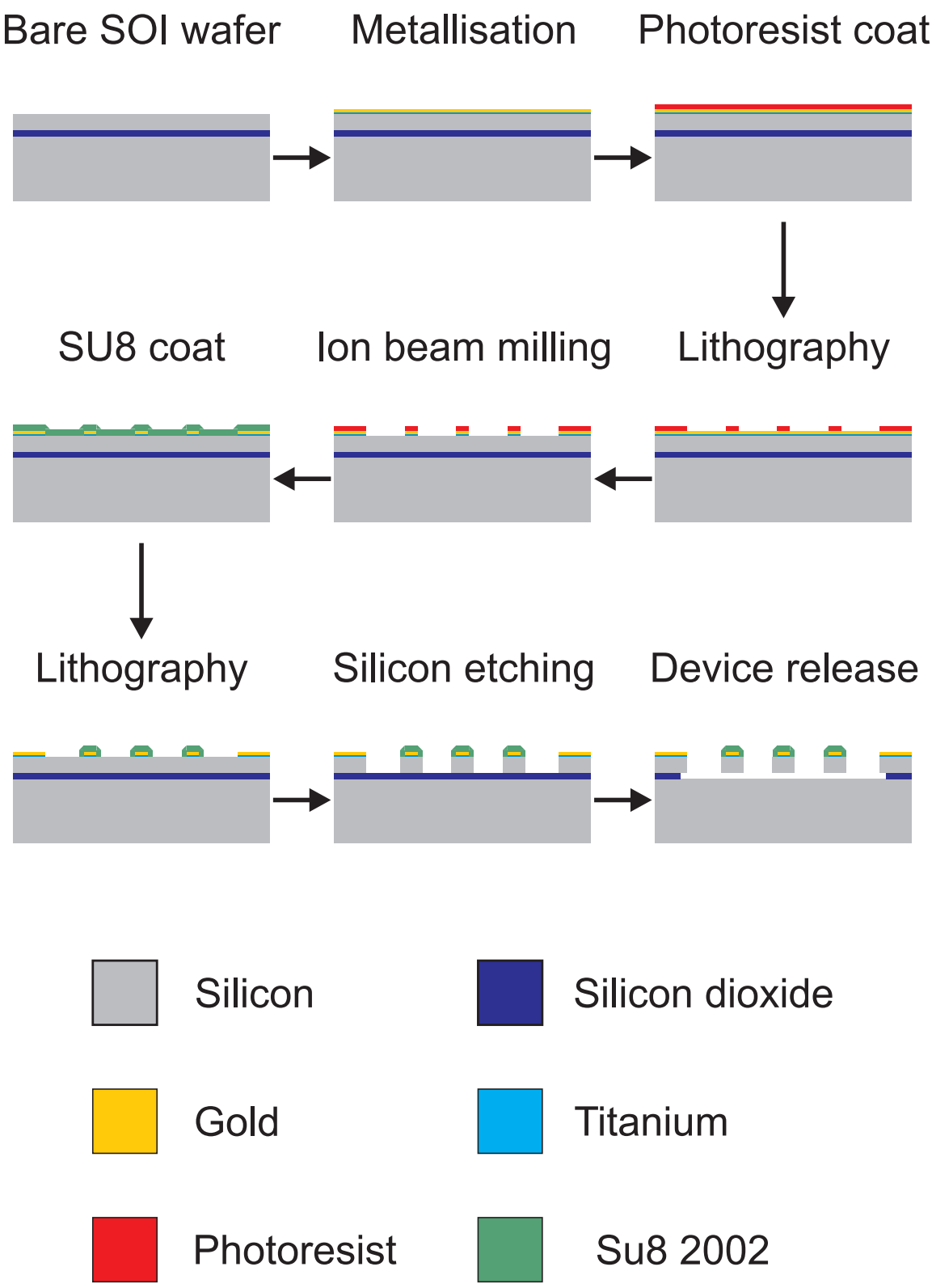

Fig. 7.2: Fabrication process for the SOI devices

The lithography masks were modified to opt for a design with reduced impact on the tissue. The width of the tip was reduced step-wise from 100 μm down to 20 μm over the maximum possible insertion depth of 400 μm. Sharp corners were avoided to minimise the risk of breakage. For fabrication the insulation material was replaced by SU8 as it is easier to process and does not require extensive curing (see figure 7.2). The device shape is again defined into the thin silicon layer by the Bosch process removing unmasked silicon down to the buried silicon dioxide layer. The oxide serves as a natural etch stop for the SF_6 etch leaving the silicon oxide exposed after the Bosch process. In principle the devices can then be released by etching the silicon dioxide layer using hydrofluoric acid (HF). Attempting this however quickly revealed a flaw in the design which neglected the actual dimensions of the device for release. The strongest available concentration of HF is a 40% solution with a corresponding etch rate of ~1.5 μm/min. The largest dimension of the device is the width of the base of 2 mm. As the oxide is etched from both sides it needs to dissolve the oxide under the device on a lateral length of 1,000 μm. The oxide layer is only 2 μm thick, which means that fresh etch species have to diffuse from the bulk solution into the narrow gap formed between the device layer and the handling wafer. The release of the device on a realistic time-scale is then impossible.

In microelectromechanical systems (MEMS) fabrication free-standing membranes of large dimensions are commonly perforated with holes to allow etchant species to reach the bottom side of the membrane and dissolve the sacrificial layer underneath. As the implant devices are released completely without any further support, the perforation reduces the mechanical stability and they become even more fragile. Therefore the size of the perforations has to be balanced so they are big enough to allow sufficient etchant species diffusion and small enough to maintain mechanical stability. The smallest feature the photomask company was able to reliably produce is a 5 μm square, which is approximately also the limit of the available mask aligner system. Since this value is above the thickness of the silicon dioxide it also ensures that the hole size is not the limiting factor for species diffusion. To realise a realistic release time the holes were placed on a 40 μm by 40 μm grid. The holes have to be replicated in the metallisation and insulation layer as well so that they are not blocked by any material, which

requires highly accurate alignment between the layers. To reduce the number of layers that need to be aligned, the devices are masked during the Bosch etch by the combination of the SU8 insulation and the gold metallisation without the use of a separate masking layer for this process. As a consequence the device tip takes the shape of the gold electrode.

The through holes for release formed well in the metallisation layer because of the polarity of the S1813 photoresist used for masking during the gold patterning. It is a positive resist so that areas exposed to UV light are washed away by the developer while unexposed parts remain. Therefore the holes are defined in the photolithographic mask for the electrode as openings in the chrome film. Scattering of light from the edges of these patterns exposes some of the resist otherwise blanked by chrome. As a result the holes were slightly bigger then defined by the mask. Patterning the holes in the insulation layer is more difficult as SU8 is a negative tone resist with exposed areas remaining on the substrate while the unexposed part is dissolved in the developer. The holes were defined by chrome squares on the mask, which prevents the SU8 underneath from cross-linking. Again light scattering is responsible for non-perfect feature reproduction. But in this case because of the opposite polarity the holes were smaller or even not patterned at all. The thickness of the SU8 layer becomes critical as it approaches the size of the feature to be patterned. Thicker resists increase the amount of area affected by scattering.

For the insulation layer SU8 2002 was used. The formulation of the product is optimised for a 2 μm thickness, which is close to the hole size of 5 μm. On the other hand SU8 is etched by the SF_6 during the Bosch process. A too thin layer will be completely etched away and expose the silicon device to the etchant. The two aspects have to be balanced for successful fabrication. Applying a postbake to the SU8 layer just beneath the glass transition temperature improved the shape of the holes as the SU8 started to re-flow slightly and excess material blocking the hole was absorbed by the surrounding SU8. The postbake also improves the durability of the material during the Bosch process. However, using the standard recipe for the Bosch process the SU8 still failed and the silicon surface underneath was etched. Reducing the ICP power of the reactor lowered the etch rate of the SU8 enough to survive until the silicon dioxide layer was reached. The reduced etch rate of silicon was compensated by performing more Bosch cycles

increasing the overall etch time. Alternatively the SU8 could be successfully masked with an aluminium layer protecting it from etching. The aluminium was later selectively removed again by a wet etch. As the masking adds an additional layer for alignment, it is a less favourable option.

According to the spin speed - thickness relation for the SU8 a coating of 2.2 μm was used. While it survived the Bosch process, erosion of the resist was visible and measurements with a DEKTAK surface profiler gave a total device thickness smaller than the theoretical 22.2 μm (20 μm silicon device and 2.2 μm insulation). Therefore the use of a thinner insulation layer to improve the definition of holes was not considered. Problems with the mask aligner meant that not all needles had visible defined holes. A part of the needles only had shallow holes or none at all in the resist. It was observed that the substrate holder was not plane so that the wafer did not contact the mask plate everywhere properly and minute gaps were visible. After 50 Bosch cycles (see appendix for details) the silicon was completely etched through over the entire area and the oxide layer was exposed, which was visible inside the chamber during etching by a change in optical appearance.

The wafer was then immersed in 40% concentrated HF solution to remove the silicon dioxide and release the devices (figure 7.3). The first needles started to come off the substrate after about 2 hours and the last devices were released after 5 hours. They were then transferred to deionised water and left soaking to wash out any HF contamination. Even though not all the devices had holes in the SU8 layer still most of them detached from the wafer. Optical inspection of the device backside under a microscope showed holes only in those parts that are solely covered by the patterned gold on the top side (figure 7.4c). Regions covered by the patterned SU8 layer did not result in holes being etched through the silicon. Given the delicate nature of the needles it is impossible to remove the SU8 layer again to see whether the silicon underneath was etched. It is left to speculation whether all the perforations in the resist were not patterned well enough or if the silicon was not completely etched through as a result of a reduced etch rated caused by the narrow holes in the SU8. Optical microscope images of the surface as well as previous test devices on pure silicon indicate that at least some of the pores are good enough

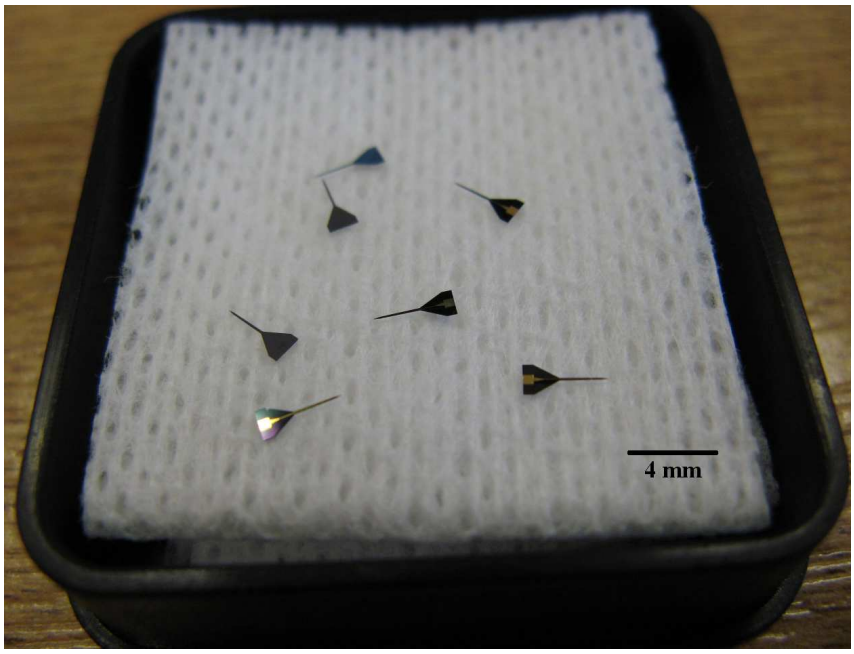

(a)

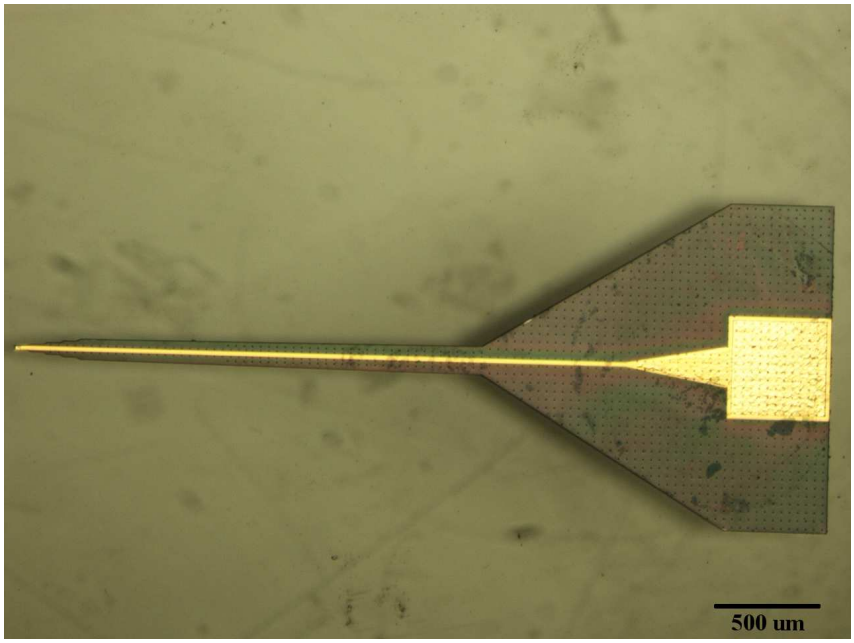

(b)

Fig. 7.3: SOI needle devices: (a) released devices (b) close-up of single device

to expose some silicon at the bottom so that the second possibility seems more likely (figure 7.4a,b). The addition of holes at the location of the gold pad still was beneficial as it made device release possible. For the devices that took longer to release, the prolonged soaking in the HF solution degraded the device surface to some extent as the SU8 took on a dark brownish tone giving it a burned appearance. Also the gold metallisation appeared to be attacked by the acid (figure 7.4d). The removal of native oxide from the silicon surface prior to device patterning might prevent this problem.

To reduce the necessary soaking time more holes in particular at the needle base have to be generated. Adding more cycles for the Bosch process might be sufficient to etch holes completely through but carries the risk of destroying the SU8 insulation. To reliably reproduce the holes in the insulation layer and ensure complete silicon etching their size should be increased but this comes with a trade-off in reduced mechanical stability for the fragile devices. As the holes were consistently etched in the metal masked parts, alternatively the size of the gold pad with the perforations could be enlarged to increase the number of pores in the bulk base. Another option is a more profound redesign of the fabrication process. The idea is to eliminate the need of releasing the base of the device at all. Instead it would be left on the carrier wafer and only the actual shank is released. This requires a more elaborate and difficult process with photolithography being carried out on both sides of the SOI wafer for backside etching of the silicon so that the shank only rests on the silicon dioxide membrane prior to release. The devices would have to be separated with a dicing saw. An advantage of this approach is the increased mechanical stability and ease of handling as the needle is now attached to a thicker silicon piece and no perforations are necessary as the oxide is completely exposed on the back for release. Because of time constraints and successful production of devices completely made from SU8 none of the mentioned options were explored any further. Applying the nanotexture process to the electrode is principally the same procedure as for the SU8 needles and is discussed in detail in the next section.

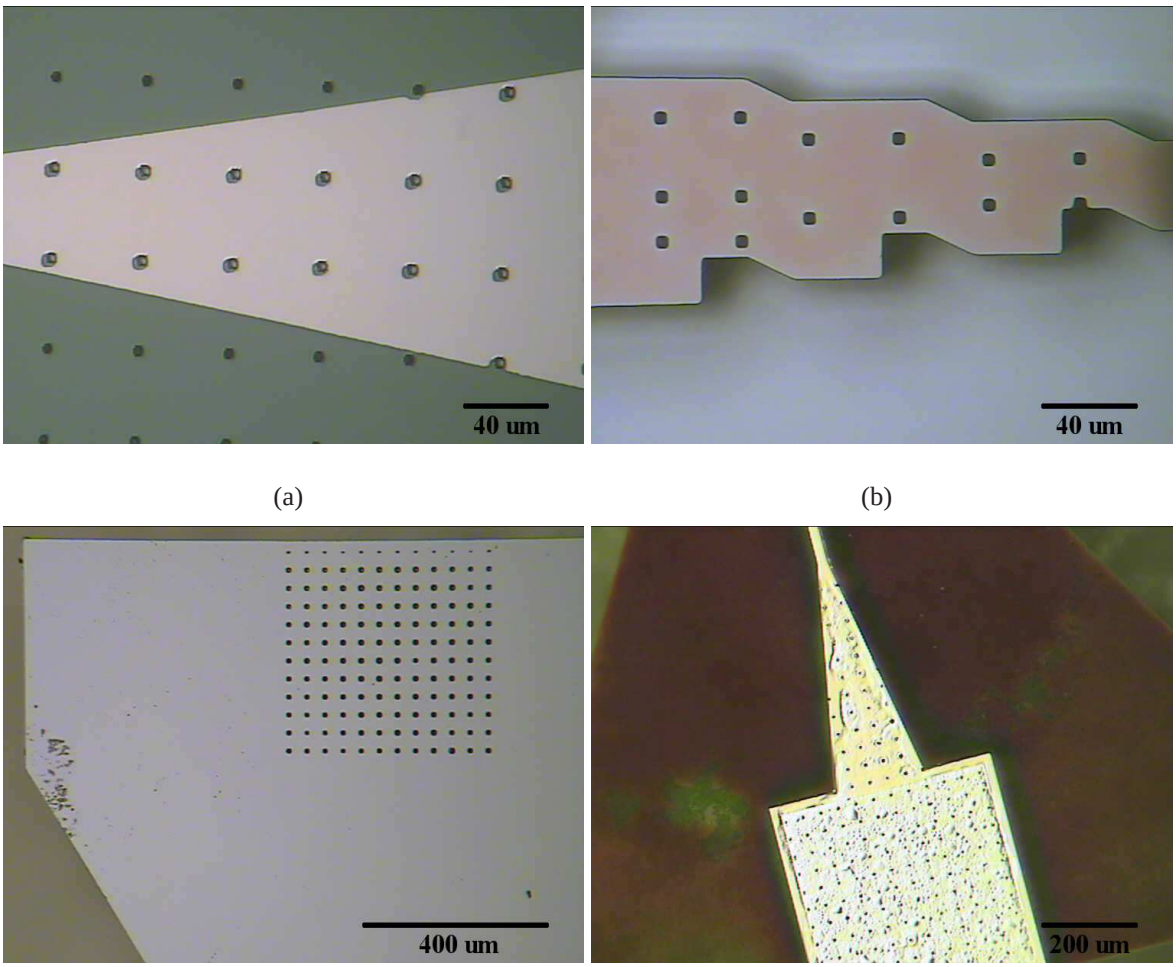

(a) (b)

(c) (d)

Fig. 7.4: (a) Holes patterned into the SU8 top layer, (b) visible etched holes in test devices on pure silicon wafers, (c) holes etched through to the back of the SOI needles, (d) erosion of the SU8 and gold by the HF releasing solution

7.3 SU8 needle process

As an alternative to the use of SOI for small device thickness photo-patternable polymers can be used for device fabrication by spinning them on to substrates for patterning. The chosen material was SU8, a negative photoresist originally developed for semiconductor fabrication. High aspect ratios with thickness up to 2 mm can be achieved and it is now commonly used in microfluidics and BioMEMS because of its good biocompatibility [97]. Upon exposure to UV light the liquid monomer solution becomes highly cross-linked to form very durable polymer chains with high chemical stability making it very hard to remove once cured. Because of this property creation of free-standing structures is possible. The material is supplied in different formulations each specified for a certain thickness range by changing the viscoelastic properties and concentration of the liquid precursor. Within this range the thickness can be adjusted through variation of the spin speed during the coating process. It is straight forward to fabricate devices with the desired thickness of 20 μm by choosing the appropriate formulation and spin speed.

The design of the devices is essentially the same as the SOI devices. The masks were adapted to the negative tone behaviour with devices defined as clear areas and the surrounding blanked by chrome. The design consists of the gold electrode sandwiched between two layers of SU8. The bottom SU8 layer acts as the electrode carrier while the top layer forms the insulation exposing only the device tip and the pad for electrical connection. The recording electrode is formed by leaving the last 20 μm of the gold track uncovered by the SU8 insulation. Because of SU8's optical transparency it is impossible to distinguish between the bottom and the top side by optical inspection once the device is released, which is important for device mounting and connection. Therefore the bottom SU8 layer mask was modified to carry a label reading the word "UP", which is only displayed correctly when the device is placed with the exposed gold facing up.

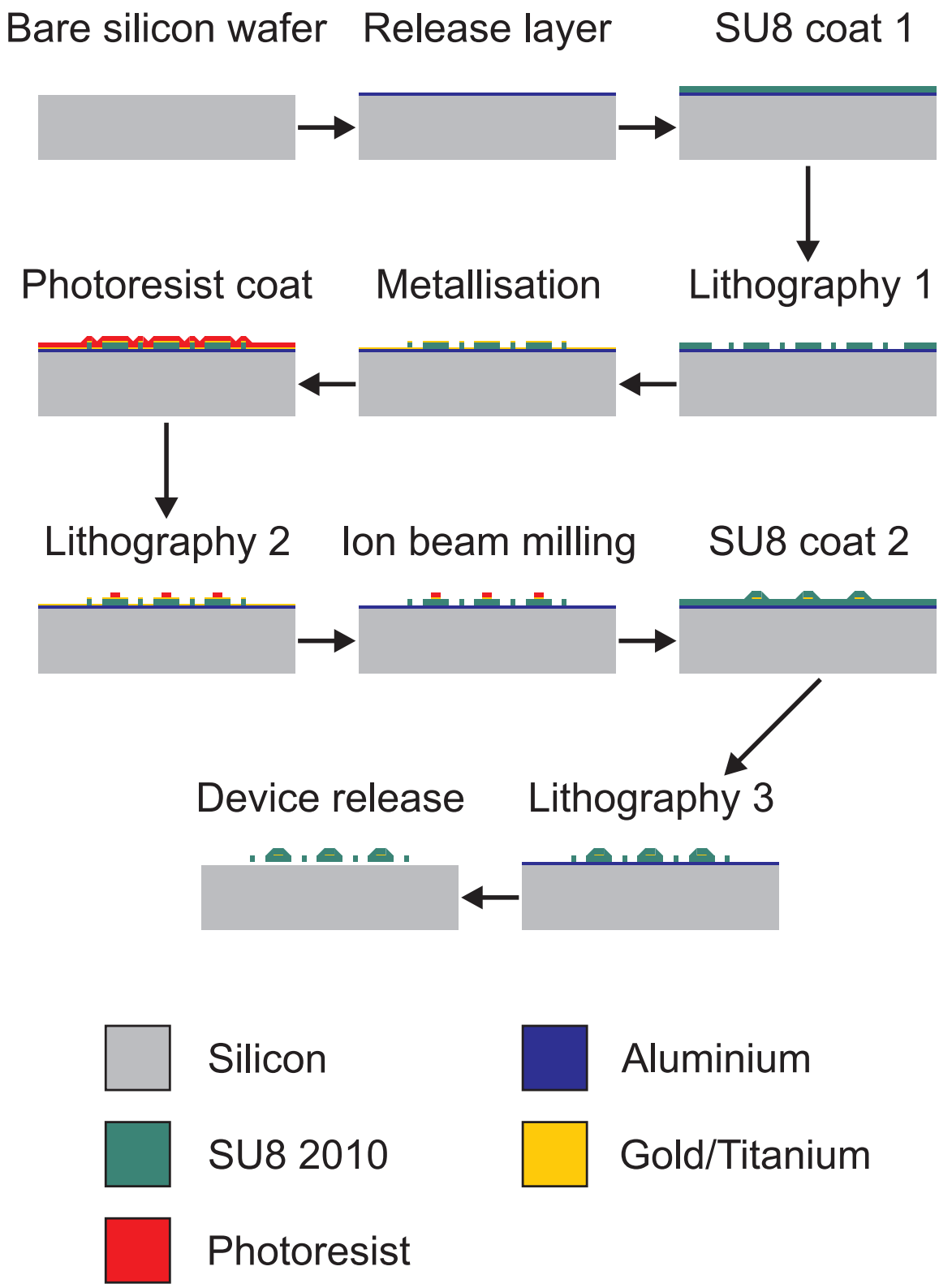

Fig. 7.5: Fabrication steps for the SU8 devices

7.3.1 Implant fabrication

The principle fabrication process is shown in figure 7.5. SU8 2010 was used as resist with a possible coating thickness ranging from 10 to 20 μm. A difficulty is that the substrate is no longer planar after patterning the first SU8 layer and forms a three-dimensional surface instead, making further lithography steps non-trivial. The use of a thinner SU8 type for the insulation layer would cause the material to flow off the elevated structure only partially covering the device with resist. Therefore the SU8 2010 with its sufficiently high viscosity had to be used for both layers and the insulation layer could not be much thinner than the bottom layer. As the minimum thickness of SU8 2010 is around 10 μm both layers were set to this value to obtain a total device thickness of ~20 μm. Alternatively the device could be build upside down with a thin insulation layer patterned first on the wafer substrate.

The electrode layer consisted of 150 nm gold and 30 nm titanium, which was deposited by e-beam evaporation. A photoresist with adequate viscosity has to be used for the electrode patterning for the same reason as with the SU8 and SPR220-7.0 was chosen. It was noticed that along the edges of the device structures the resist was thicker because of the barrier represented by the devices during spinning. As a consequence a thin layer of resist remained after development at the rim of the devices using the recommended exposure time. With positive resists full exposure is necessary in order to be washed off completely by the developer. The higher thickness along the edges would require a longer exposure time risking overexposure of the thinner resist parts. The residual photoresist prevented the underneath gold from being removed during milling as seen around the edges of the device in figure 7.6. After the devices were released these thin gold stripes had to be washed off with deionised water.

After electrode patterning by ion beam milling the masking photoresist has to be fully removed. Otherwise the SU8 layers do not bond together properly and delamination occurs. An oxygen plasma step could remove resist residues and roughen the SU8 surface to improve contact between bottom and top layer. However, it was found to be effective enough to leave the wafer soaking in acetone for 30 minutes followed by the use of an ultrasonic bath for 1 minute. For the release of the devices a 100 nm thick aluminium layer was deposited on the silicon wafer

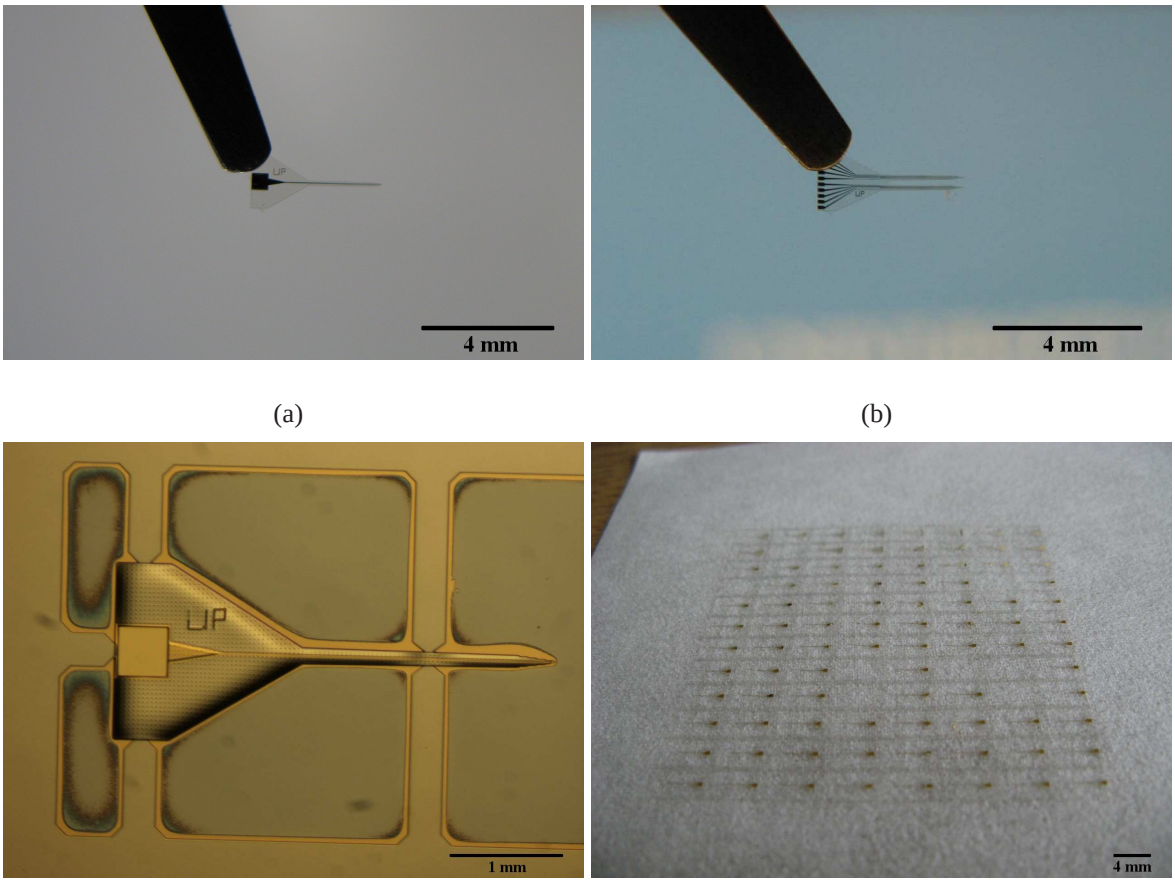

(a) (b)

(c) (d)

Fig. 7.6: SU8 needle devices: (a) single electrode, (b) 2 shanks with multiple electrodes, (c) single device with supporting grid prior to release, (d) complete array of devices with supporting grid

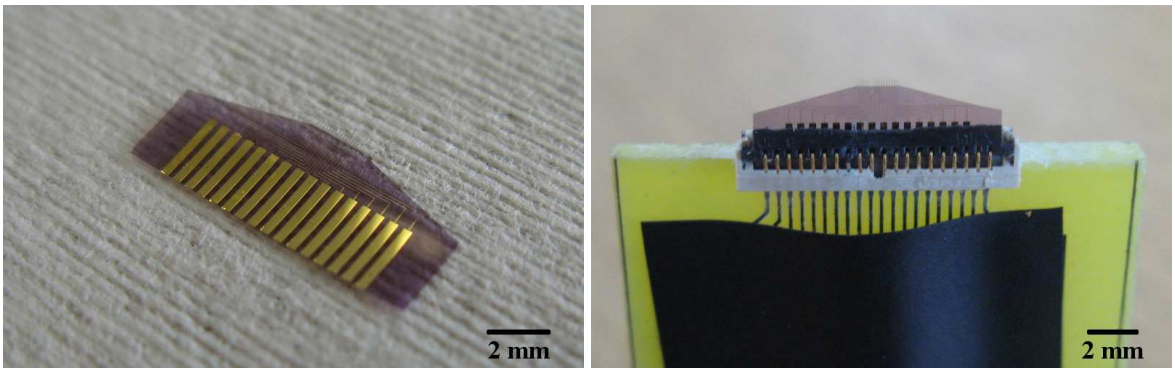

(a) (b)

Fig. 7.7: (a) multi shank array and (b) mounted in a ZIF connector

before device fabrication. After the devices were completed, they were released by immersing the wafer in a TMAH solution overnight. The TMAH etches the aluminium away lifting off the devices from the substrate. For convenience the photoresist developer MF319 was used as it provides a readily available weakly concentrated solution of TMAH (2-3%). To avoid time-consuming collection of the singular devices one by one from the solution a supportive grid was introduced in the bottom layer mask to which the devices are connected through narrow tear off connections. To separate a device from the grid these connections were broken with the tip of a pair of tweezers or a scalpel blade.

7.3.2 Electrical connection

A problem when using SU8 as material for the needles is the electrical connection of the device. Wire bonding was not successful as the bonds did not stick to the gold on the SU8. It is suspected that the elastic properties of the material caused the absorption the ultrasonic vibrational energy used for the wire bond by the SU8 so that no durable bond connection could be formed.

For single electrode devices conductive silver paint was used to connect device and PCB traces but for higher density interconnects as required by multiple electrode devices it is more difficult. The pads need to have a minimum size and separation for silver paint application to avoid formation of bridges between adjacent pads, which limits the number of possible connections. A device design created for the medical school for research on neuron behaviour during

epilepsy featuring an array of shanks with one electrode each was used to test an alternative way for electrical connection, a zero insertion force (ZIF) connector originally developed for flexible printed circuits and cables (figure 7.7). The exposed connection pads of the cables are slid over the flat gold pins inside the connector and the base is pressed down on the back by a clamp. The base of the SU8 device has to match the footprint and geometry of such a connector. It was also large enough to use silver paint as an alternative. In order to be safely clamped, a silicon back support had to be glued to the devices as their thickness was not sufficient for proper clamping. A major issue during testing was the suction of electrolyte through the relatively short shanks into the connector where it shorted the pads. The deposition of a thin line of silicone on both sides of the device above the shanks kept the electrolyte away from the connector. Future devices will feature longer shanks, which should prevent this as well. The recordings obtained with the array are discussed in chapter 8.

7.3.3 Nanopatterning

There are two possible ways for nanopatterning of the needle devices. Either single devices can be modified after device fabrication or the method for the nanotexture creation is incorporated into the device fabrication to obtain a batch process for nanostructured needles. To modify single devices the tips were covered with a sphere array assembled on a water surface by dip coating similar to the gold chips in chapter 5. As both gold and SU8 are hydrophobic surfaces the devices were soaked in sodium dodecyl sulfate (SDS) surfactant to improve the spreading of the water film on the devices and prevented it from dewetting during dip-coating, which would destroy the monolayer. The pretreatment in piranha solution can not be used as it attacks the SU8 material causing the gold film to peel off as well as device detachment from the substrate. As shown in figure 7.8 some defects appeared during transfer but the overall ordering of the spheres on the electrode is maintained. For further processing they must be mounted on a carrier in order to load them into the necessary equipment. For this purpose silicon substrates were cut and the needles mounted by either vacuum grease or double-sided sticky tape. After coating the sample with titanium, the spheres were lifted off with scotch tape. Care has to be

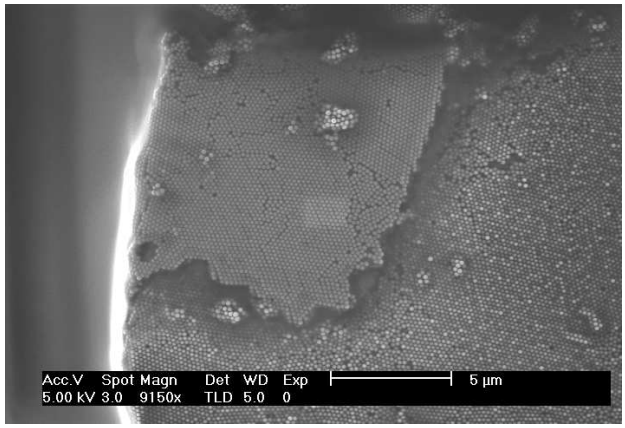

(a)

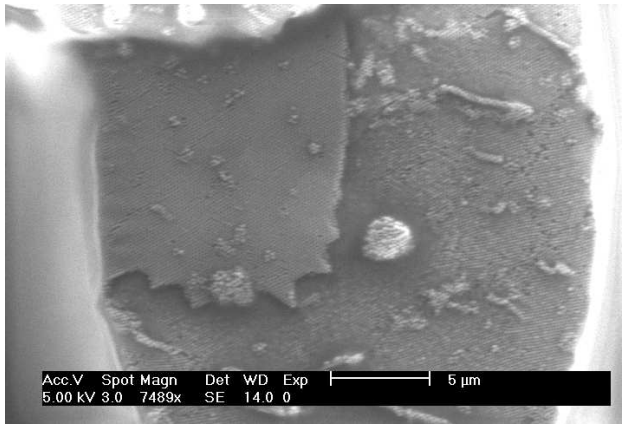

(b)

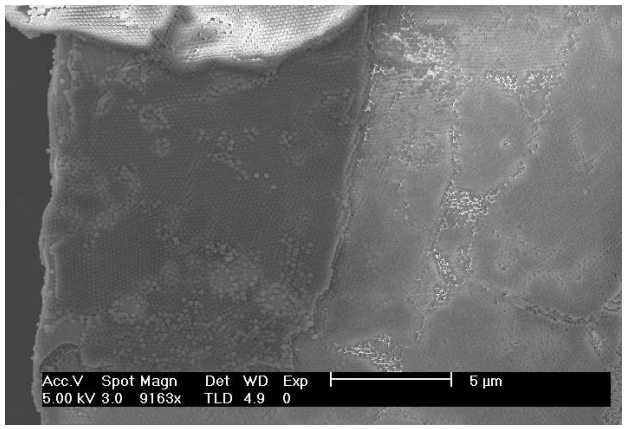

(c)

Fig. 7.8: Three examples of single needles with sphere arrays deposited by dip-coating

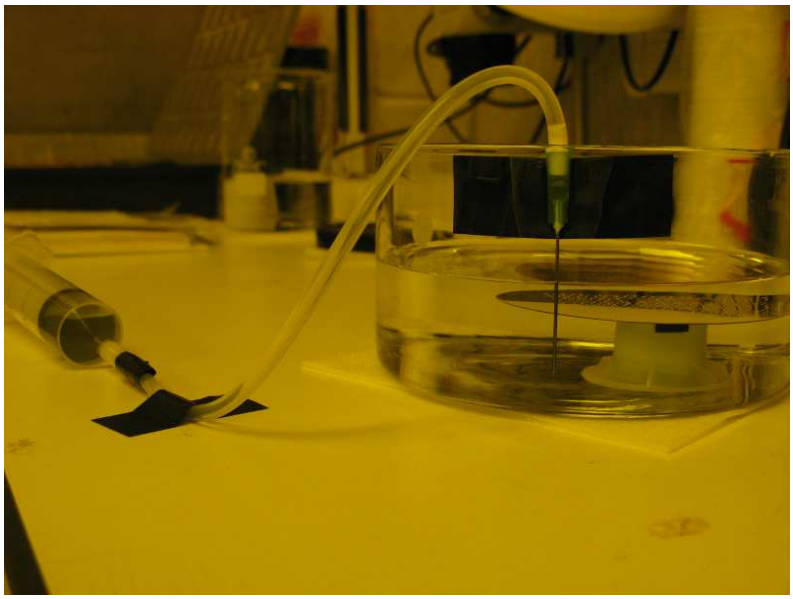

Fig. 7.9: Setup for NSL on large wafer

taken to prevent tearing off the shanks when removing the scotch tape. Subsequent sonication in chloroform often released the device from the carrier as chloroform is a organic solvent and had to be mounted to the silicon again for ion beam milling. After etching the remains of the titanium mask the device modification is completed by removing it from the carrier through soaking in solvent.

Single device modification works well but it is time-consuming to structure them one by one. A better quality can be produced by batch fabrication as will be demonstrated. The structuring steps are performed after patterning the bottom SU8 layer and the evaporation of gold. This way the whole gold layer is nanostructured before the actual electrode is patterned. Arrays of devices fabricated on 2-inch wafers have been successfully covered by dip-coating. For bigger samples dipping is an impractical method as it is difficult to control larger substrate sizes with tweezers and hold them steadily during withdrawal from the water. An improved procedure was developed instead. The consideration was that the biggest advantage would be if the sample does not have to be moved at all. The idea was to control the water level in the beaker while the sample sits on a holder in the water. Slow reduction of the level by extraction of water transfers the spheres on to the wafer as the water level sinks below the wafer surface. To avoid disruption

of the transfer process by interaction of the water with the bottom of the beaker or the water flow, the wafer is placed a few centimetres above the bottom of the beaker. Water is extracted via a syringe needle taped to the side of the beaker. The needle is connected to the syringe with silicone tubing. This helps decoupling vibrations from the syringe to the beaker, which might disrupt the sphere order. The experimental set-up used is shown in figure 7.9. Ideally an air table should be used as well to cancel any environmental vibration.

A 20 ml syringe is slowly filled by hand with beaker water at a rate below 2 ml/min. It is important to limit the resultant flow and prevent excessive drag on the surface to leave the sphere layer intact. Whenever the syringe is full it can be detached from the silicon tubing via a custom made connector to drain it and reattach. When the wafer is in close proximity to the water surface and visibly deforms the surface along the edges of the substrate, the water extraction is slowed down further until drying starts to occur at the edges. Water removal is then stopped completely and the sample is left to dry solely by evaporation. Extracting too much water can cause dewetting and subsequently destroy the sphere layer. The risk of dewetting is given because the wafer remains in water for a longer period as the water extraction takes more time then simple dip-coating. Also an additional rest period is necessary. Once the spheres are dispersed on the water surface, the beaker has to be left undisturbed until spheres that were dragged into solution have completely dissolved in the water. Otherwise there is the risk that they are deposited on the wafer during water removal causing defects and multilayers. Because of the prolonged immersion the SDS is washed off the wafer surface through diffusion and the surface is not hydrophilic any more, which facilitates dewetting. In addition large sample sizes are coated with a significant amount of surfactant. Mixing the surfactant with the water in the beaker affects the surface tension, which in return has an impact on the sphere assembly. In this case the water is not covered by a continuous sphere layer any more but broken into several smaller, fringy islands. Furthermore, the prolonged soaking of the wafers in SDS seems to induce shrinking of the SU8. The resulting stresses were large enough to partly detach the devices from the carrier wafer making them unusable for further processing steps. In conclusion the use of SDS is actual adverse for this approach.

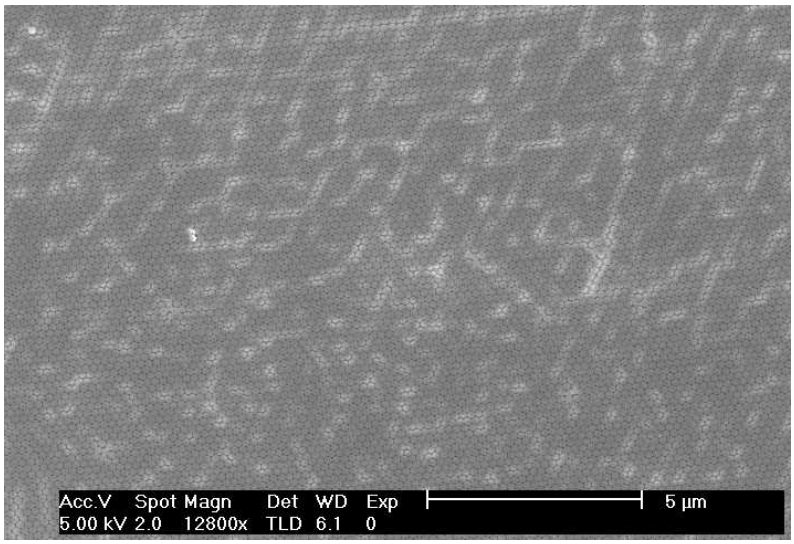

Fig. 7.10: Coating produced by the syringe method on a flat gold chip

Instead it could be shown that in contrast to conventional academic belief of the necessity of hydrophilic surfaces for NSL hydrophobic SU8 and gold can be used without further pretreatment. A small tilt was introduced through the substrate holder. As a result only a small part of the substrate breaks the water surface at a time. The surrounding water then acts as a cushion to prevent the water from receding and the contact line is pinned to the exposed edge so that no dewetting occurred. Caution is necessary when immersing the untreated substrate into the water. The hydrophobic nature of the top material facilitates the entrapment of air bubbles at the wafer surface. The bubbles interfere with the NSL and shield the underneath part from sphere coating. The best approach in this regard was to fill the beaker up to the height of the substrate and then use the syringe to inject water at a slow rate to cover the wafer. The slow controlled filling reduces the number and size of air bubbles to a minimum. Since a large portion of the substrate remains in the water the sample cannot be left to dry on its own once the upper edge is exposed. Instead it was necessary to continuously extract water during drying until the whole wafer has emerged from the water surface, which must still be done slowly to avoid dewetting. The best way to do this was by detaching the syringe from the silicone tubing and letting it hang down on the side of the beaker. The water then starts to continuously drop out of the tube at a slow rate because of the pressure difference.

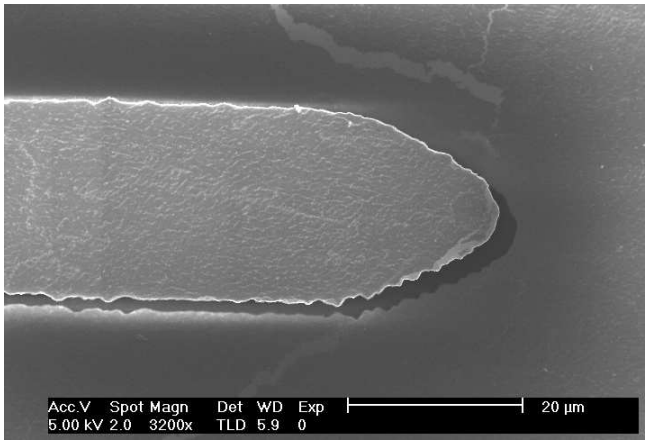

(a)

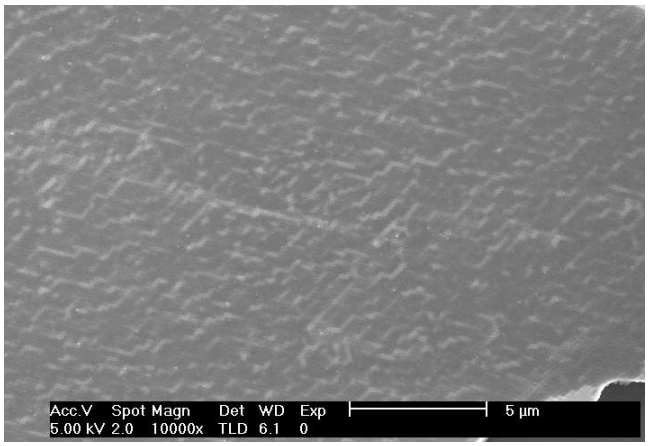

(b)

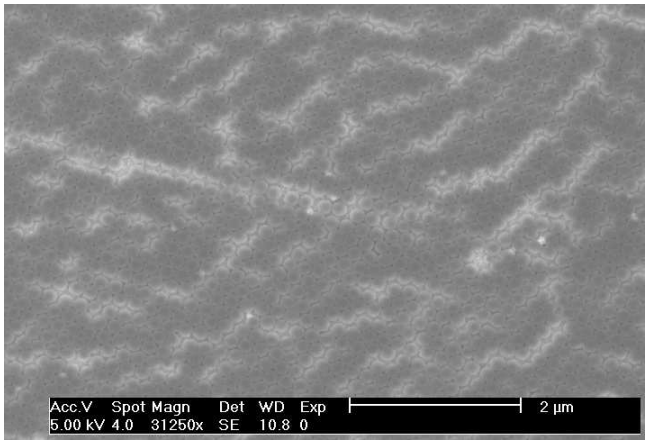

(c)

Fig. 7.11: SEM images of device coated by syringe method with cracks visible in the background (a) and higher magnifications of the spheres (b,c)

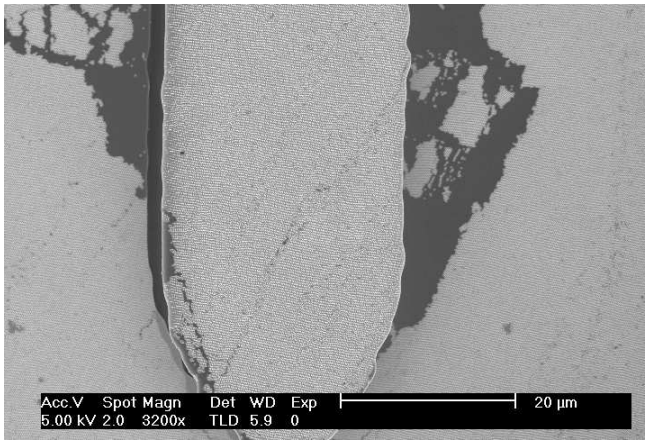

(a)

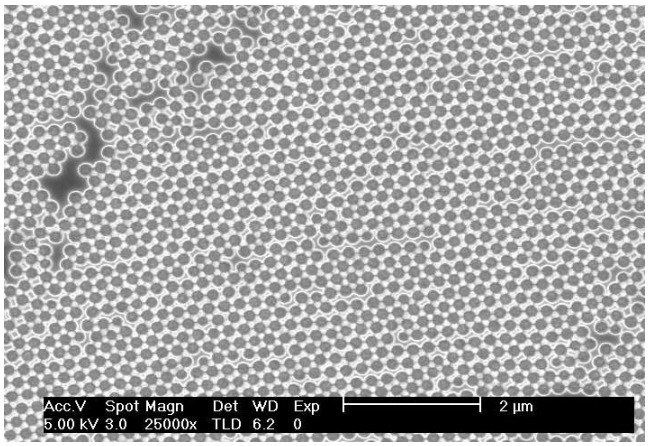

(b)

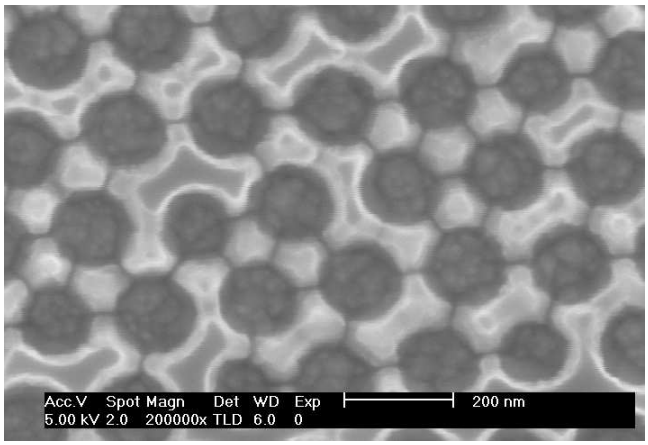

(c)

Fig. 7.12: SEM images with increasing magnification of a device coated by syringe method after surface patterning

The quality of the produced coating with this method was better compared to dip-coating. The spheres were better packed with less irregularities. Ruptures in the sphere film did not occur as often as the substrate stays fixed during coating. In fact the procedure was also used for any nanostructured gold chips produced since the development of this method because of the improved quality and good reproducibility. Flat samples are completely covered with a continuous mono-layer over the whole surface (figure 7.10). Substrates patterned with devices had cracks in the sphere layer (figure 7.11). They are attributed to the structured surface. As the sphere array wraps around the devices a mismatch between the locally available monolayer area (determined by the substrate size) and the larger surface area caused by device structure develops and cracks appear to compensate for this. As the top of the devices comes into contact with the spheres first when the layer is still intact the shanks are mostly coated well. Wafers of 3-inch diameter could reliably be coated, which was impossible using dip-coating. With larger beakers and sufficient amounts of nanoparticle solution the procedure should be scalable to bigger substrates without problems.

The previously described steps for nanopatterning were carried out then. The entire wafer was subjected to a oxygen plasma treatment prior to titanium deposition. Since the nanotexture is solely desired on the electrode tip, the scotch tape was applied only to the a sufficient portion of the shank while the rest of the device stayed covered by titanium. Some titanium is lifted off during the sonication in chloroform but most parts were still masked. After ion beam milling and titanium removal the shank surface was covered by nanostrutures as shown in figure 7.12. Upon completion of the nanopatterning the device fabrication was carried on as described earlier. Once the devices were released they were ready for use with the nanotexture incorporated into the electrodes.

7.4 Polyimide microchannel process

The microchannel channel implants differ from the needle devices not only in structure but also in the materials used for fabrication. They are formed by a multilayer structure (figure 7.13) with a non-photosensitive polyimide serving as the device substrate. After metal deposition

and electrode definition the tracks are passivated by a layer of thin photopatternable polyimide (Durimide 7505). Windows are patterned by photolithography to define the electrode sites. A layer of thick photosensitive polyimide (Durimide 7020) is then used to create the channel walls separating the electrode sites. When rolling the polyimide the top of each open channel is automatically sealed by the following turn of the roll to confine the extracellular space. The gold electrodes survive the rolling process and remain operational which is attributed to the elastic nature of the substrate material [98]. Research suggests that nerve fibres can regrow through these kind of channel devices [99]. The electrode incorporated in the bottom of the channel is used to record or stimulate the regenerated nerves.

One specific characteristic of the polyimide is the requirement of extensive curing after device fabrication is completed. This has to be carried out in a nitrogen atmosphere to avoid the material from being burned. A rigid temperature profile has to be used to ensure proper curing. First the sample is heated from room temperature to 200° C with a ramp of 2.5° C/min. It has to stay at this temperature for about 30 min before it is heated further to 350° C with 4° C/min. The sample is kept at 350° C for 60 min before cooling it down to room temperature again with 4° C/min. The whole curing process takes around 5 hours and is normally done overnight in a specially fitted oven.

The polyimide microchannel devices used for modification were produced by Samia Benmerah. They were successfully coated with nanospheres through dip-coating. For this purpose a single device was released from the carrier wafer by cutting along its outline with a razor blade and peeling it off with tweezers. The coating was performed before the patterning of the channels to ensure a flat surface. Because of mechanical stresses in the layers and the peeling they tend to easily roll up. Therefore the sample was glued with double-sided sticky tape to a piece of silicon that had been cut to the size of the polyimide sample with a dicing saw. Prior to dipping the device was soaked in SDS overnight. All ten electrodes on the device were coated by spheres without any significant defects to the ordering (figure 7.14). Again some cracks appeared because of the mismatch in area. Spheres can be seen covering the side wall of the window in the insulation most likely causing the cracks and minor voids. Because of charging

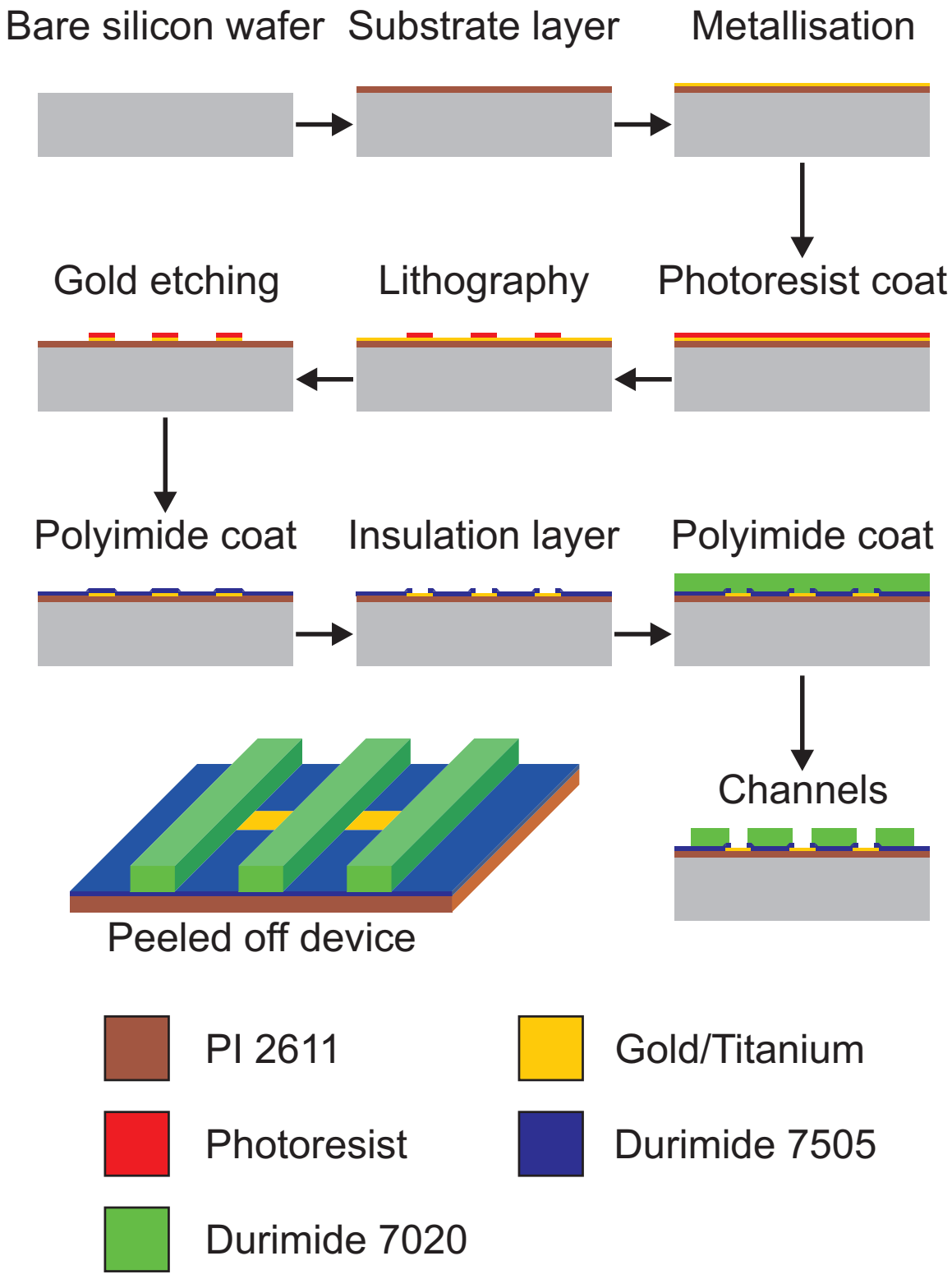

Fig. 7.13: Process steps for polyimide roll

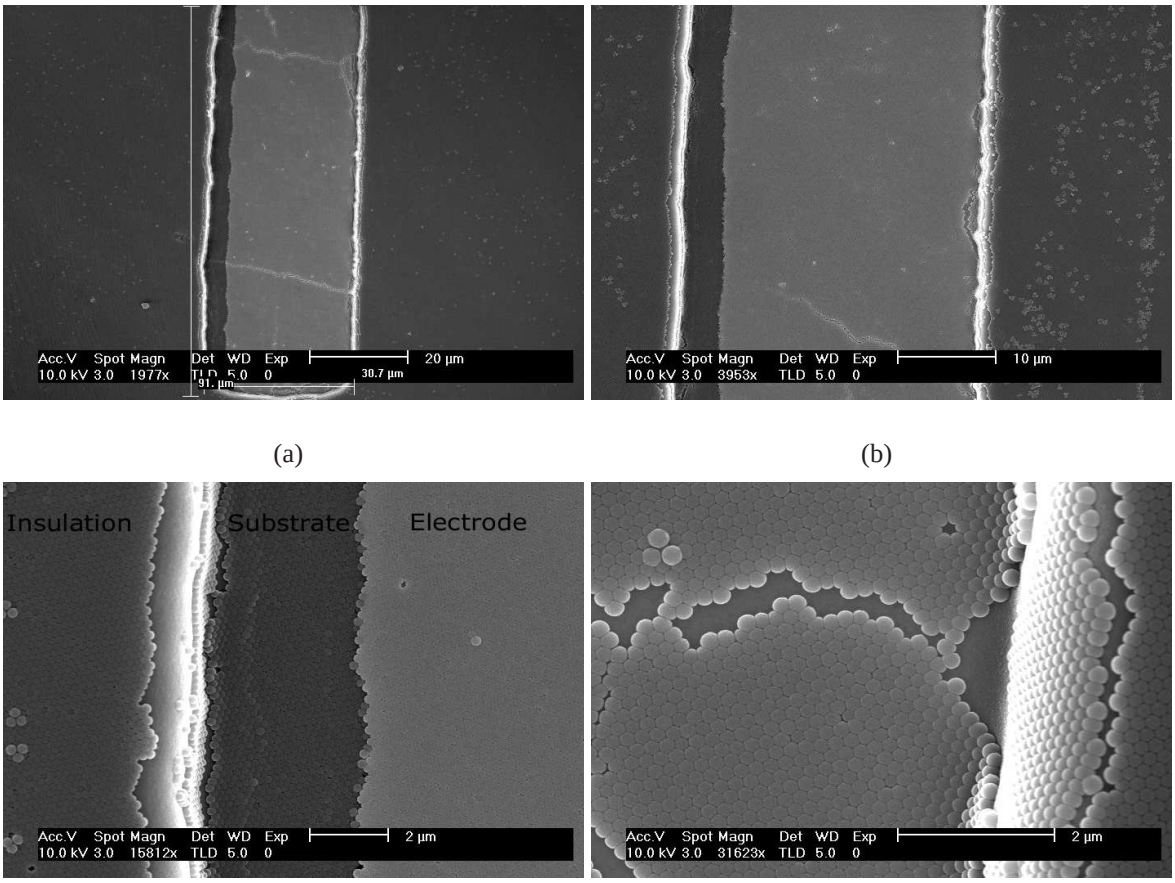

Fig. 7.14: Polyimide device after sphere deposition: (a) complete electrode window, (b) close-up of (a), (c) misalignment gap, (d) spheres on the side wall of the opening

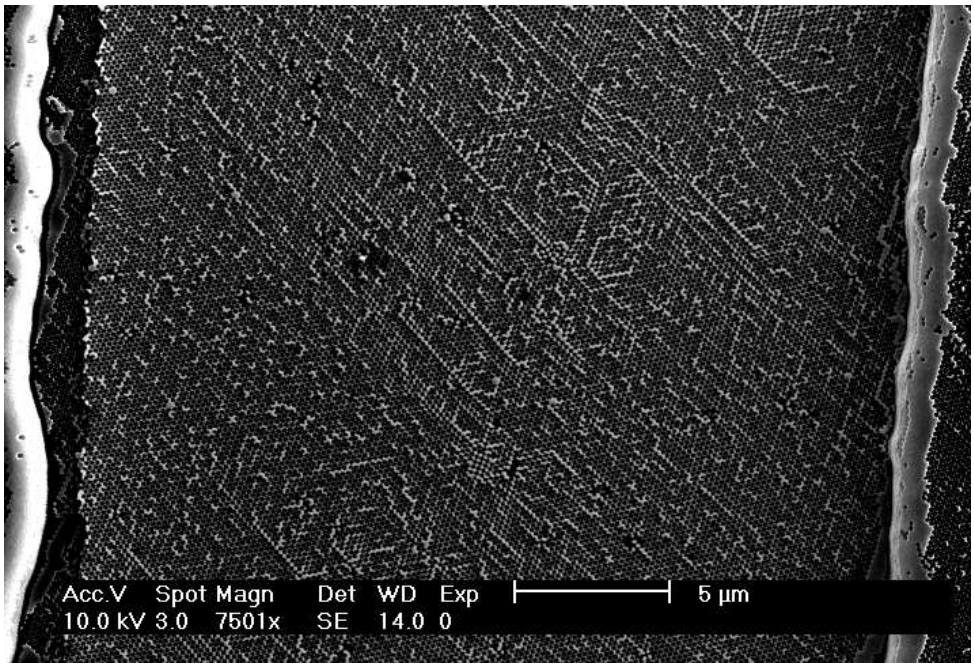

Fig. 7.15: Polyimide microchannel electrode after milling

effects during SEM imaging the pictures were taken after titanium deposition. Due to slight misalignment during device fabrication a minor part of the substrate is exposed at the bottom of the window leaving some space between the window wall and the actual gold electrode (figure 7.14c). The spheres were then lifted off as previously described and the sample was ion beam milled. The resultant surface is shown in figure 7.15 with the nanotexture clearly visible. The device is then ready for completion by the patterning of the channels. It should be possible to modify entire wafers containing this type of device using the syringe method introduced in the previous section but was not performed.

7.5 Conclusion

A SU8 penetrating electrode device for recording neural signals from brain slices was designed and fabricated. The 20 μm by 20 μm square electrode site was successfully nanostructured by the developed thin film process as was the polyimide microchannel device. To incorporate the nanostructure process into batch fabrication of nanostructured devices, the method of sphere

deposition during Nanosphere Lithography was improved to reliably coat sample sizes up to 3-inch wafers and the high yield in modified devices suggests that further up-scaling is possible.

8. RECORDING FROM BIOLOGICAL SIGNALS

The fabricated implant devices were tested in in-vitro recording set-up from slice cultures of rat hippocampus. Supply of oxygen as well as perfusion of the slices with artificial cerebrospinal fluid enables one to maintain slice functionality for more than 12 hours after the extraction from the skull. Testing was performed at the Neuronal Networks Group laboratory (under the leadership of Professor John Jefferys). This laboratory is equipped with the necessary equipment and recording devices to perform these measurements. The multi-shank array was specifically designed for the group's research aims to record neuronal and population activity during epileptic seizures from multiple sites. In addition to establishing basic operation of the devices it was also tested whether any improvement in signal quality could be observed for the use of nanostructures on the electrodes.

8.1 Experimental set-up

Electrodes were positioned individually under visual control using a microscope and eyepiece graticule. Electrodes and their positions were photographed using a digital eyepiece camera (World Precision Instruments, Inc.; Sarasota, USA). Signals were preamplified using Neuralynx headstage amplifier (Neuralynx, Inc., Tucson, USA), amplified (100x), and low-pass filtered (3 kHz) with Neuralynx Lynx-8 amplifiers. All recorded signals were digitized at a sampling frequency of 5 kHz using 1401 Plus or 1401 Power and Spike2 software (Cambridge Electronic Design, Cambridge, UK).

Initially electrodes were tested in the recording chamber without presence of brain slices. Electrode tips were submerged in artificial cerebrospinal fluid (ACSF) consisting of 125 mM NaCl, 26 mM $NaHCO_3$, 3 mM KCl, 2 mM $CaCl_2$, 1 mM $MgCl_2$, 1.25 mM $NaH_2 2PO_4$ and

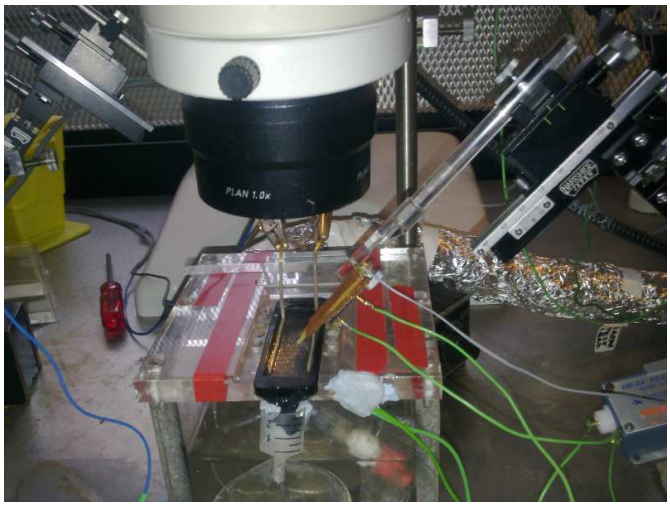

Fig. 8.1: Recording chamber with AC fields test set-up

10 mM glucose perfused with a humidified 95% O_2 and 5% CO_2 mixture. Electrode properties were established by subjecting them to alternating current (AC) fields of various frequencies and recording the electrode response. The fields were generated by applying current via Ag/AgCl electrodes (2 mm in diameter, 4 cm long) using a Bi-Phasic Stimulus Isolator DS4 (Digitimer Ltd, Welwyn, UK). These electrodes were placed on either side of the recording chamber in parallel to each other. The following frequencies of 2, 4, 8, 16, 32, 64, 128, 256 and 512 Hz were tested for two current intensities (1 uA and 10 uA) respectively. Activity from both modified and plain electrodes was recorded together with a reference wire electrode fabricated in the groups laboratory from platinum/iridium wire (Advent Research Materials, Oxford, UK; diameter $25\ \mu\mathrm{m}$, impedance $< 800\ \mathrm{k}\Omega$ at 1 kHz).

Spontaneous brain activity was recorded from hippocampal slices ($400\ \mu m$) of Sprague-Dawley rats. The slices were stored at room temperature, submerged in the holding chamber filled with normal ACSF. After 60 min, slices were transferred to the interface recording chamber, at $32\ ^{\circ}\mathrm{C}$, containing normal ACSF. To evoke spontaneous cellular and network activity, slices were perfused with high-potassium ACSF consisting of 125 mM NaCl, 26 mM $NaHCO_3$, 8 mM KCl, 2 mM $CaCl_2$, 1 mM $MgCl_2$, 1.25 mM NaH_2PO_4 and 10 mM glucose, bubbled with 95% O_2 and 5% CO_2 mixture. The tips of the electrodes were placed into the cell body layer of

hippocampal CA1 area (figure 8.4) and spontaneous evoked activity was recorded.

8.2 SU8 Needles

The ability to record electrical and also biological signals in-vitro was assessed with two devices. One was a plain needle with no surface modification. The other device possessed nanostructures patterned on the electrode with a milling time of 6 min at 60° after 15 sec of sphere thinning and titanium deposition for comparison. Successful nanostructuring was confirmed by SEM prior to testing.

First the electrodes were tested for their response in the ACSF to applied AC fields (figure 8.3). The needles were glued with nail varnish to the ends of glass capillaries, which can be clamped in micromanipulators for accurate placement. Wires for electrical connection were placed above the pads of the needles and fixed with duct tape to the glass tube. The pads were electrically connected with the wire by covering them with silver paint. A pin socket was soldered to the other end of the wire to fit into the head stage of the amplifier. The original devices without nanostructure modification picked up an external noise signal visible as a spike in the sine wave form that could not be eliminated. The modified device recorded the signals with the same amplitude as the reference wire while the original implant featured a decreased signal amplitude demonstrating the better interface properties of the modified implant. Calculation of the power spectral density revealed that each electrode type was able to record the signal of the individual frequencies from the AC fields. Main peaks in the power spectra corresponded to the individual sine wave frequency applied. Additional peaks at frequencies other than those applied represented harmonic components and sharp artefacts, which were present mainly in the original electrode. These peaks had a lower power than the main sine wave peaks. Analysis of coherence was used to examine the relation of original and modified devices to the reference. Coherence is calculated by dividing the cross spectral density between two signals by the product of the auto-spectral density of the two signals. It is a measure of the correlation of two time varying signals at each frequency. The plotted coherence statistics illustrate that the modified implant had a higher level of coherence with the reference electrode than the original electrode

Tab. 8.1: SNR for the electrodes at different frequencies

Electrode		4 Hz	16 Hz	32 Hz	64 Hz	128 Hz
Reference	STD	0.086 mV	0.088 mV	0.08 mV	0.069 mV	0.054 mV
	SNR	7.28	7.42	6.78	5.86	4.78
Original	STD	0.055 mV	0.051 mV	0.045 mV	0.037 mV	0.026 mV
	SNR	3.47	3.24	2.89	2.33	1.65
Modified	STD	0.09 mV	0.091 mV	0.085 mV	0.073 mV	0.058 mV
	SNR	6.78	6.88	6.37	5.51	4.35

over the tested frequency range and reproduced the reference signal better.

Signal-to-noise ratios (SNR) were calculated for sample frequencies of 4, 16, 32, 64 and 128 Hz. For signal amplitude estimation the data was band pass filtered from 1 to 200 Hz. Standard deviation (STD) of a one second epoch of the filtered signal at each frequency was computed. The noise level of each electrode was obtained by calculating the standard deviation from epochs of the unfiltered signals between application of the AC fields. The associated noise levels were 0.012 mV (wire), 0.016 mV (original) and 0.013 mV (modified). The SNR is the signal STD divided by the noise STD and the obtained values are tabulated in table 8.1. They were averaged over the chosen frequencies and plotted with the standard deviation (figure 8.2). The difference in SNR for the two gold electrodes is clearly visible. The SNR of the modified gold electrode was close to the reference wire. The original gold electrode had a value of less then half the SNR of the modified device. This suggests that the increase of surface area has improved the recording capability of the electrode but extensive and repeated testing of a larger number of devices is required for final conclusions.

Both electrodes were able to record spontaneous brain activity which in this case was characterised by spontaneous action potential firing (unit firing) of multiple neurons and manifested extracellularly as multi-unit activity (figure 8.4). The data was high-pass filtered at 700 Hz to isolate spike events. A large amount of action potentials could be discerned from the noise background for both electrodes. The registered units featured larger amplitude signals in the

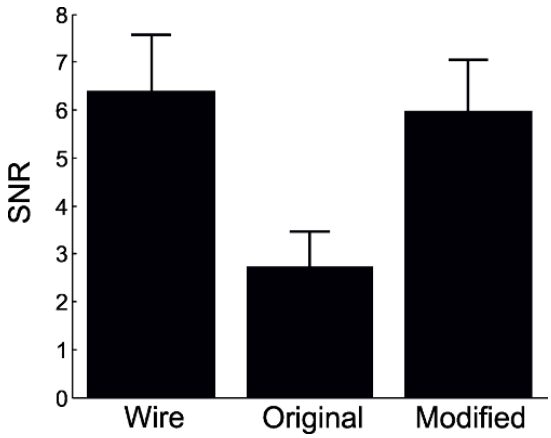

Fig. 8.2: Averaged SNR for analysed frequencies of each electrode

modified electrodes. However, the distance of the source neuron to the electrode also has an impact on the amplitude so that for single electrodes these results must be taken with caution. For more reliable data a higher number of each type of electrode spread out over the brain section of interest should be used to ensure a close location to the neurones. The largest obtained signals would then be used for a more detailed analysis but time restrictions and the experimental set-up did not allow this. The shank arrays would be suited for this approach as they possess a larger number of electrodes in a small space. But as described in the next section they do not work reliably yet.

Gold-coated polyimide pillars were not tested as needle devices made of this material had not been fabricated. One concern is that needle devices made of polyimide might not possess the necessary mechanical stability for insertion. Additionally the thermal stress from curing will most likely cause curling of the devices after peeling them off the substrate as experienced with the polyimide rolls. A straight device is a prerequisite for insertion so that insertion direction and insertion force are aligned in parallel and lie in the plane of the thin film device to avoid deflection. Even slight bends in some of the shank arrays have proven them difficult to use. Solutions have to be found to address these issues, for example the use of a thin polyimide layer on top of a SU8 base for nanopatterning.

Devices containing electrodes fabricated using the columnar sputtered gold also suffered

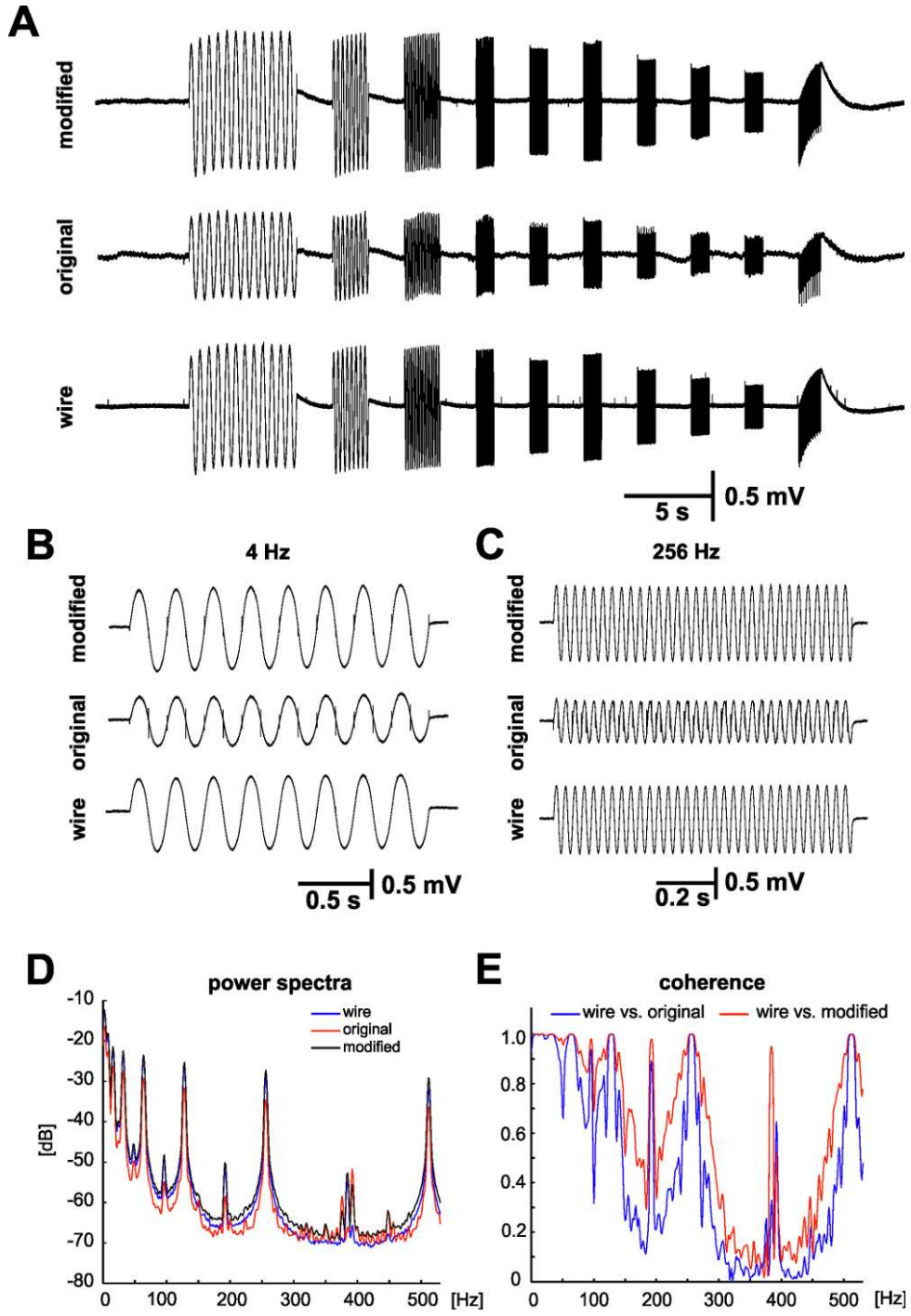

Fig. 8.3: Results of sine wave testing: (A) complete recording for all three electrodes, the last waveform in each curve is a square pulse; (B) magnified view for details at 4 Hz; (C) magnified view for details at 256 Hz; (D) calculated power spectrum distribution; (E) electrode coherence compared to reference wire

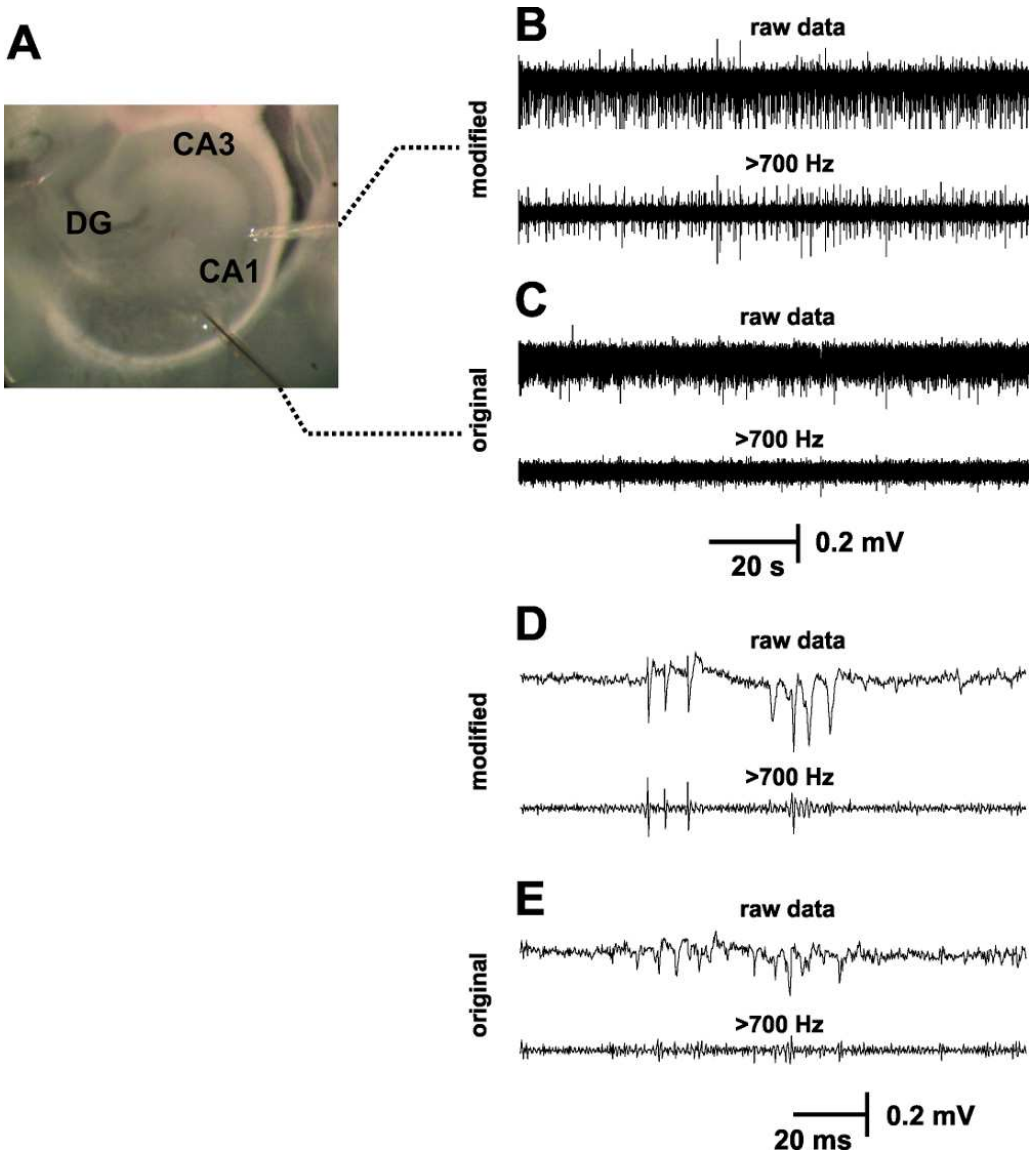

Fig. 8.4: Extracellular recording of spontaneous brain activity: (A) Placement of the electrodes in the slice; (B,C) Potential recordings before and after high pass filtering; (D,E) section of the recordings with higher temporal resolution for more detail

from device curling that made them unusable. The prolonged heating during sputtering caused the gold to be deposited with an intrinsic thermal stress. This led to curling of the thin tips of the devices preventing their use in the set-up. Because the substrate holder in the sputter coater was not cooled, the gold atom bombardment heated up the sample. The use of a machine with sufficient cooling should prevent this. The cooling will also ensure that the columnar structure is maintained for thicker deposits as an increase of substrate temperature can shift the surface morphology to different zones according to the Thornton model [94].

8.3 Multi-shank array

The shank devices were tested by recording antidromic responses from a hippocampal slice perfused with low-calcium artificial cerebrospinal fluid and complemented by sine wave testing. The separation between individual shanks was $100\ \mu\mathrm{m}$. As a result the distance of each shank to firing neuron populations varies, which causes a difference in amplitude for the recorded signal in the shank electrodes enabling the identification of the source location.

The shank device was inserted along the CA1 area and a stimulation electrode was placed in the alveus. The response to stimulation obtained with the multishank electrodes partially resembled an antidromic response. Each individual spike corresponds to a synchronous and repeated action potential firing of populations of pyramidal cells. The shape of the spikes appeared distorted and had a lower amplitude compared to typical responses. The distortion might be due to a wrong position of electrodes where they were not placed exactly in the cell body layer. But the presence of similar waveforms in each individual electrode suggests the existence of heavy cross-talk as no difference in amplitude was detected. The sine wave testing with a 100 Hz signal applied to the stimulation electrode further confirmed that the signals were all the same magnitude. Some of the electrodes also showed a low frequency drift indicating a general problem in the device.

At present it is unclear whether the cross talk is caused by the ZIF connector or if it is a problem of the device design. A modification of the design to incorporate a ground plane could help to eliminate the cross talk and signal deformation as well as reducing noise. Initial

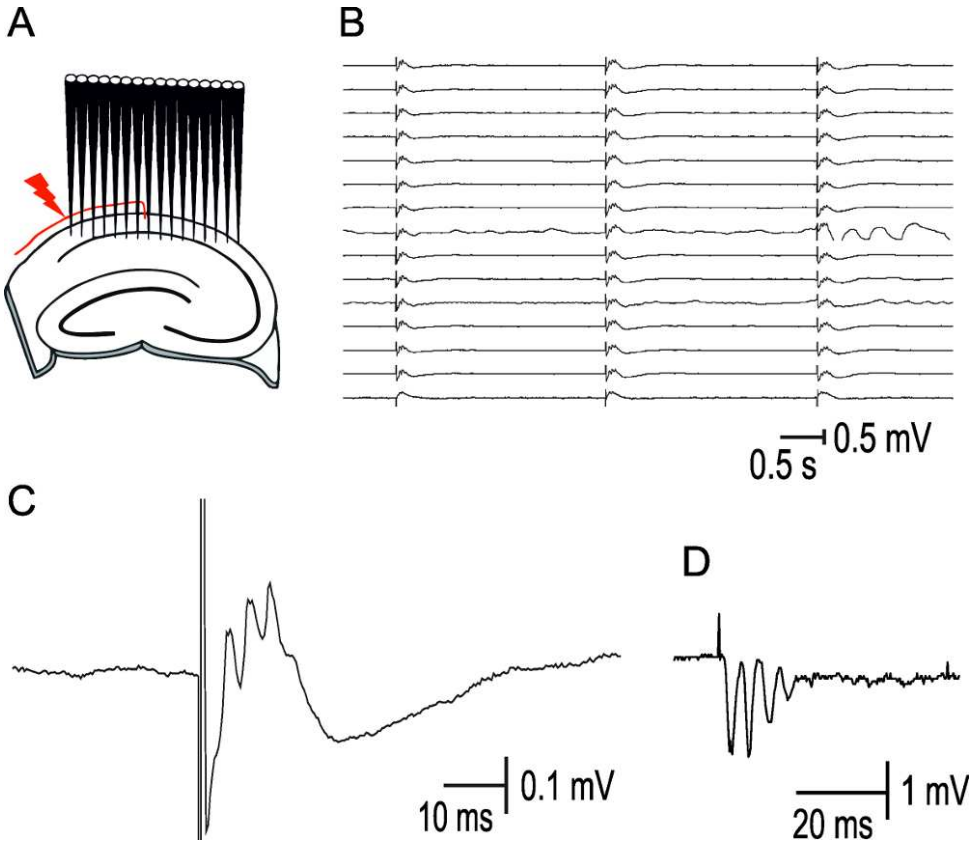

Fig. 8.5: (A) experimental set-up for recording with shank device; (B) recorded signal for each channel; (C) detail of the recorded features; (D) ideal antidromic response

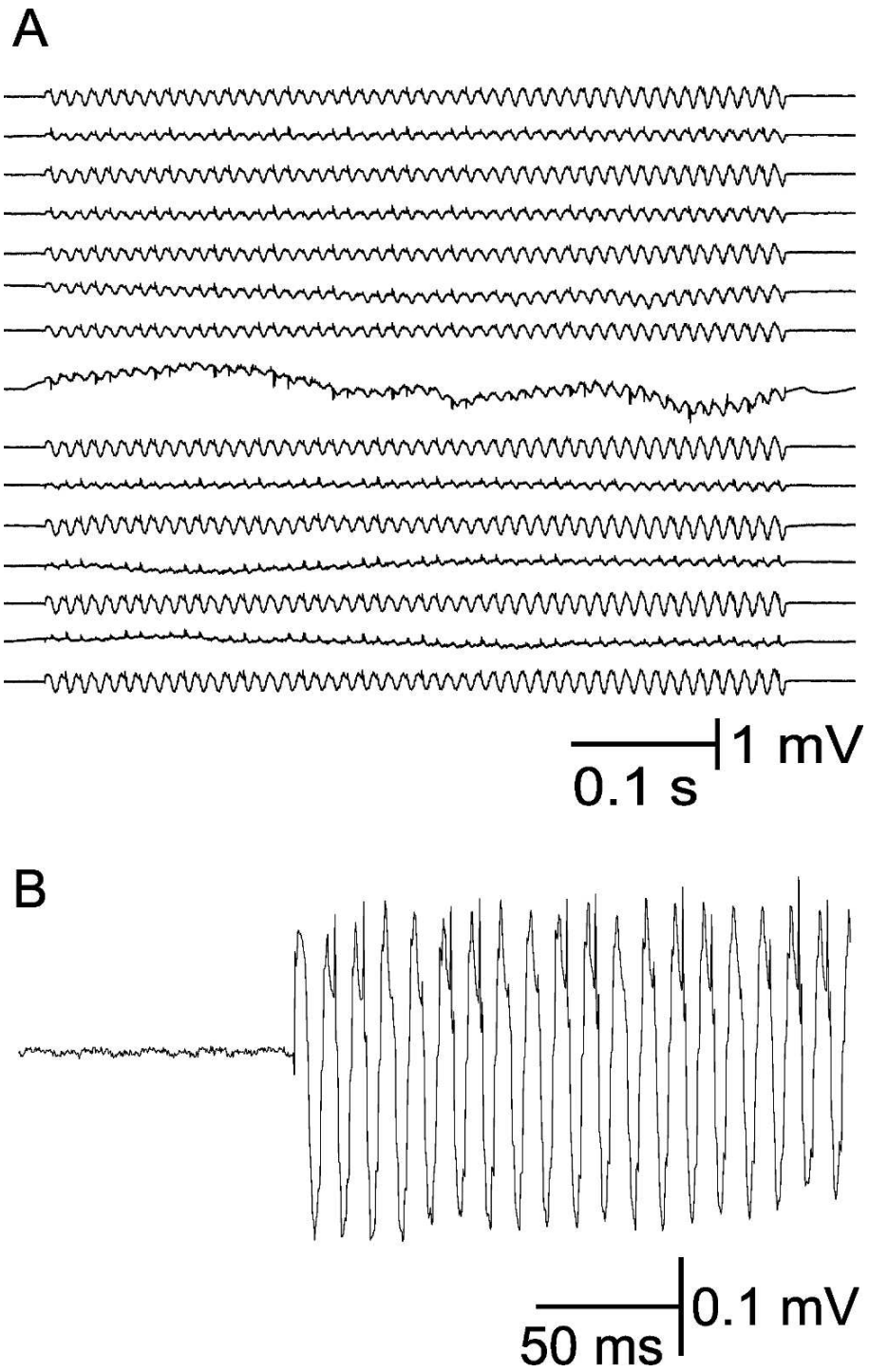

Fig. 8.6: Sinewave testing: (A) Recordings from each channel; (B) close-up of recorded sine wave

recordings could be obtained with the device but further optimisation is necessary for reliable signal acquisition. The influence of the ZIF connector will be established by glueing the device directly to PCB and connecting it electrically with silver paint. Design and fabrication of the arrays was handed over to Samia Benmerah to continue the work.

8.4 Conclusion

Both results from the AC fields set-up and in-vitro slice recordings indicate a better performance of the nanostructured device over the plain reference device. The nanostructured device possesses a higher signal to noise ratio, which means that better quality recording can be obtained with this device compared to the unmodified one. Because only one device of each type could be assessed, additional testing of a larger number of devices has to be performed to statistically quantify the exact degree of improvement in recording quality.

9. SUMMARY AND FUTURE WORK

A new methodology for the fabrication of gold nanostructures for the use in neural implants was developed. The aim was to increase the available surface area at the electrode site in order to improve the characteristics of the electrochemical interface between implantable electrodes and the neurological tissue. This approach is justified by the inverse proportional relation between interface parameters and surface area.

The nanostructures were fabricated by deposition of a nanometre-sized etch mask with Nanosphere Lithography and subsequent anisotropic etching. The gold films were directly patterned by ion beam milling into pillars and honey-comb like structures. The variety in fabricated surface structures was possible because of the good control of multiple process parameters. The developed process is easily extendible to other materials by simply choosing a suitable combination of masking material and etch process. This was demonstrated by the fabrication of polyimide pillars through oxygen plasma etching with silicon masks. Coating these pillars with gold resulted in another kind of gold nanostructure. In addition to the development of a nanostructuring process a porous form of gold was found that is characterised by dense arrays of nanometre-sized columns.

The interface properties of surfaces modified with the different nanostructure types were probed with electrochemical methods and compared to flat gold references. The results of those measurements showed that all the produced nanostructures types were able to reduce the interface impedance and increase the charge injection capabilities, the most important parameters for recording and stimulation with neural devices. The maximum reduction in interface impedance was one order of magnitude. As the surface area increased with the structures aspect ratio, the polyimide nanopillars were identified as the most suitable structure because preliminary devices already showed significant impedance reduction and the highest charge injection of all tested

devices. Their height is easily increased by etch time to achieve even further impedance reduction. They also require less amount of gold material as they only use a thin metal layer. Because the pure gold structure process possesses only limited aspect ratios the interface property improvement was less effective. Another etch process is required to resolve this issue.

The nanostructuring process was successfully incorporated into the fabrication process of neural implants for use in the brain and the peripheral nervous system. The method of NSL was refined to coat sample sizes up to 3-inch reliably with high quality masks. The brain implants were custom-designed for in-vitro neural recording while the peripheral microchannel devices originated from a multidisciplinary collaboration. The results showed that the developed method is suitable for application in different implant shapes.

Their capabilities to record neurological signals was tested in-vitro and from Ac fields. Initial results showed a better recording quality for the modified implant evidenced by a higher signal to noise ratio. The signal amplitude recorded with the nanostructured implant in AC field set-up was comparable to a high grade medical recording wire used as reference. Spontaneous activity from brain slices could be recorded with both devices and the spikes in the modified implant had larger amplitudes. However, results were inconclusive as the signal amplitude also depends on implant position and only two devices could be tested, but the overall better performance of the nanostructured implant leads one to assume an improvement of recording quality by the nanostructures.

The developed process is a valuable technology that extends the capabilities of nanosphere lithography for nanofabrication. The structured surfaces could also find applications in other fields. For instance it is planned to use them for surface enhanced Raman spectroscopy. Rough metal surfaces are known to enhance the Raman scattering of molecules adsorbed to the surface. This leads to larger signal amplitudes and higher sensitivity in detection. The ability of the new process to tailor the surface structure might improve the enhancement factor, which depends on shape and size of the nanostructures. Another possibility is the incorporation into biochemical sensors to improve the detection limit. Nanometre-sized electrodes have a different diffusion profile compared to planar ones. If the spacing between the nanostructures is larger than the

diffusion length the profile switches from planar to radial increasing the mass transport to the electrode. Utilising surface chemical reactions, the increased mass transport would then improve the detection limit for species that are only present in tiny amounts. With the developed process the distance between nanostructures is simply controlled by the sphere diameter and can easily be adjusted.

Compared to other methods the maximum improvement of interface properties is on the same level or a bit less than the best methods discussed in the literature review. However further optimisation should potentially close this gap or even get ahead of it. Where the introduced method excels is its simplicity combined with a mechanical stability avoiding many of the disadvantages of the other methods like electrode delamination or cracking because the nanostructures are directly shaped into the surface of the devices. Furthermore all used materials have proven their biocompatibility and no toxic materials are involved in any step of the process. The reduction of the interface impedance is not so important any more in this area as today's amplifiers used for neural recording have input impedances far above typical microelectrodes. Instead the value of the interface modification is that it allows to reduce the electrode size without a loss in sensitivity and signal quality as discussed in the introduction.

Future work should aim to optimise the process for surface area increase to determine the maximum of improvement possible for the recording of nerve signals with neural implants. The polyimide pillars demonstrated the most potential as they possess the best scaling properties, but the technique needs to be perfected so that straight pillars are completely coated with gold. It is planned to incorporate the polyimide pillars into polyimide roll devices to assess their performance in biological systems. The mechanical properties of the pillars will be assessed by seeding the modified surface with cells and measuring the pillar deformation by atomic force microscopy. The multi-shank devices are a valuable research tool but need further improvement to ensure reliable operation and high quality recordings. They could be modified with nanostructures as well to optimise the interface properties. Finally larger quantities of modified devices need to be produced for in-vitro testing to allow for a statistically complete data analysis.

APPENDIX

A. PHOTOLITHOGRAPHY MASK DESIGNS

A.1 Needle devices

- base width: 1.6 mm
- needle length: 4 mmm
- shank length: 2.3 mm
- minimum shank width: 20 μm
- electrode width: 20 μm
- gold pad: 500 μm x 500 μm

A.2 Multishank array

- base width: 10.5 mm
- base length: 4 mm
- shank length: 300 μm
- shank width: 10 μm
- separation between shanks: 100 μm
- electrode width: 6 & 10 μm
- electrode tip: 50 μm x 10 μm

- gold pad: 2.3 mm x 300 μm
- separation between pads: 200 μm

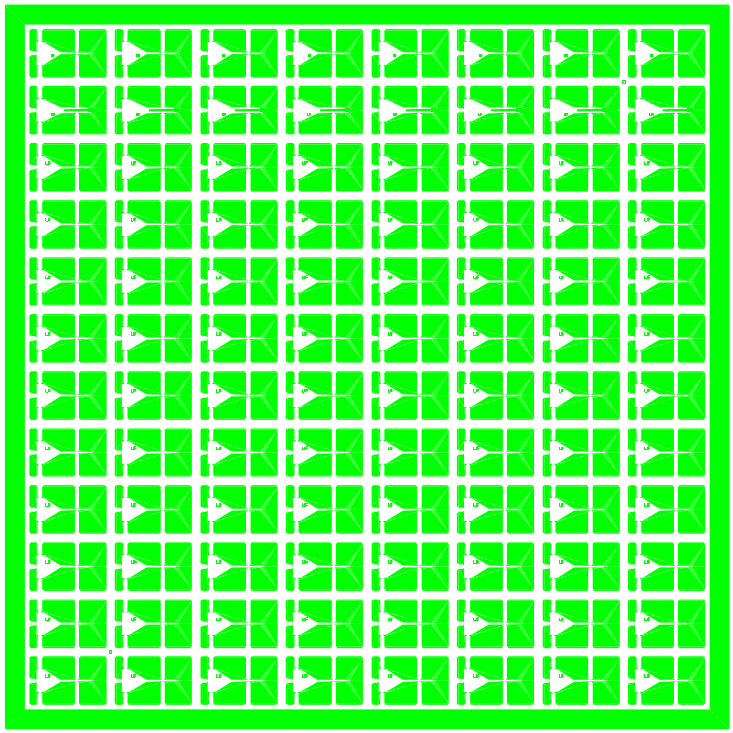

(a)

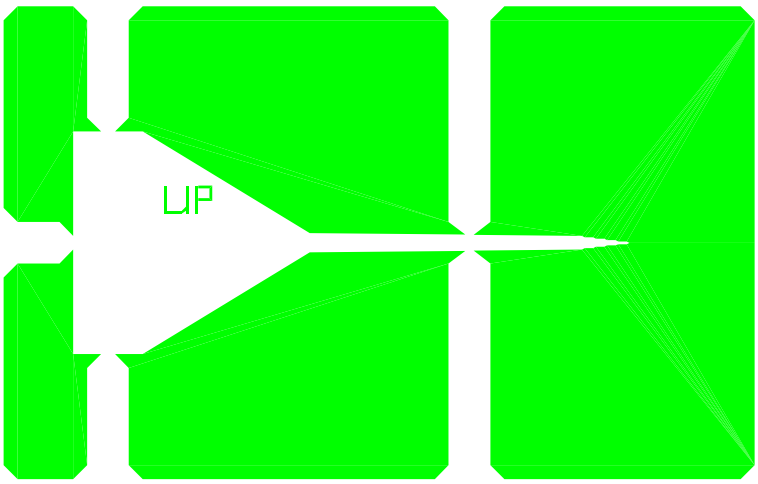

(b)

Fig. A.1: Photomask for the SU8 substrate layer of the needle device

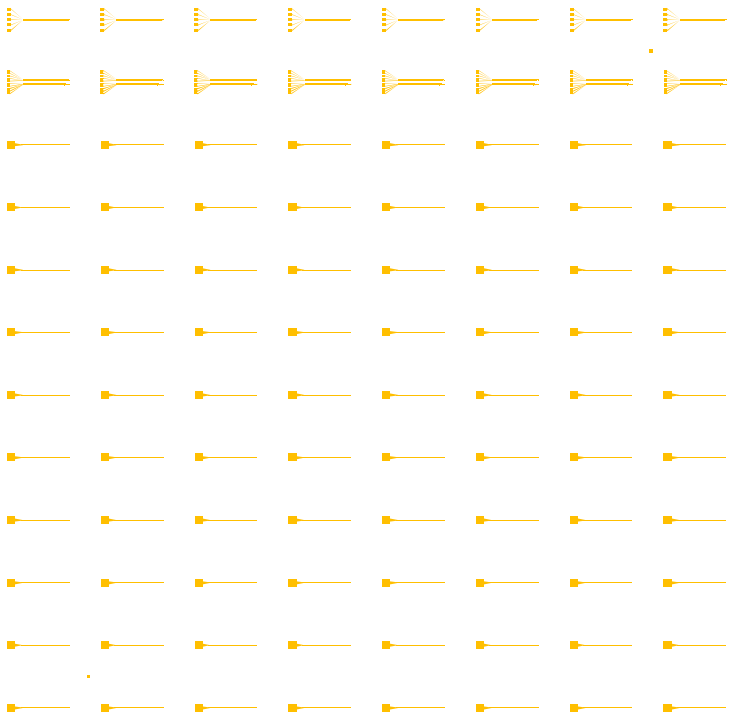

(a)

(b)

Fig. A.2: Photomask for the gold electrode layer of the needle device

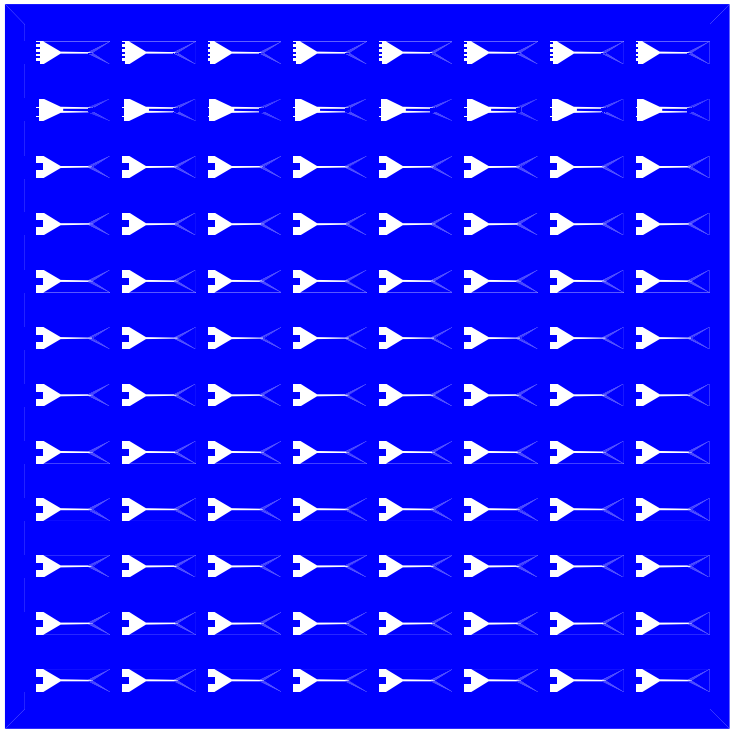

(a)

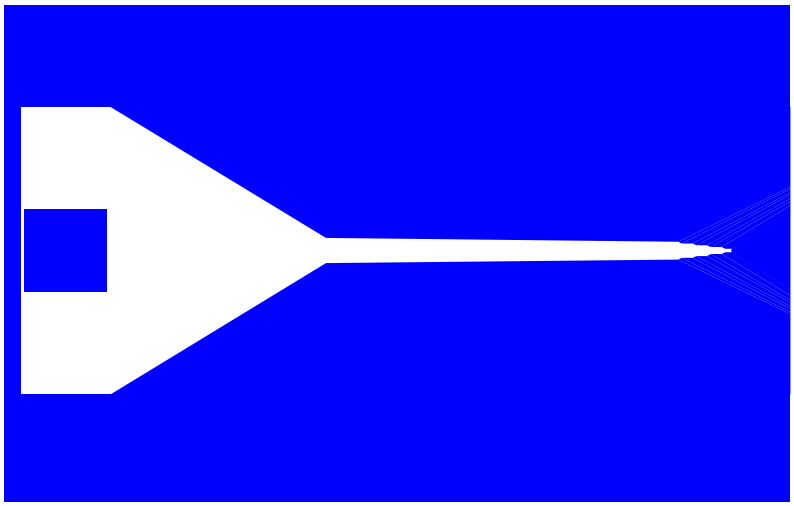

(b)

Fig. A.3: Photomask for the SU8 insulation layer of the needle device

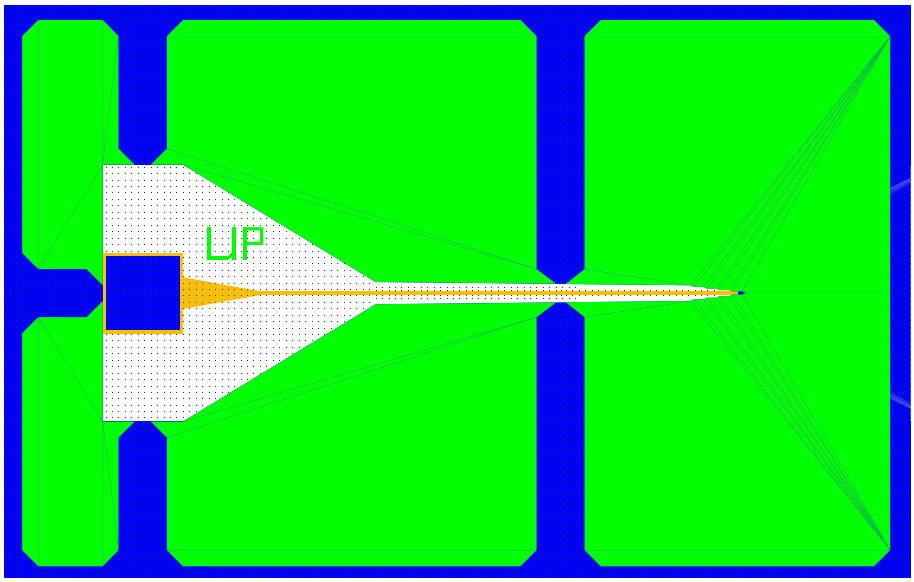

(a)

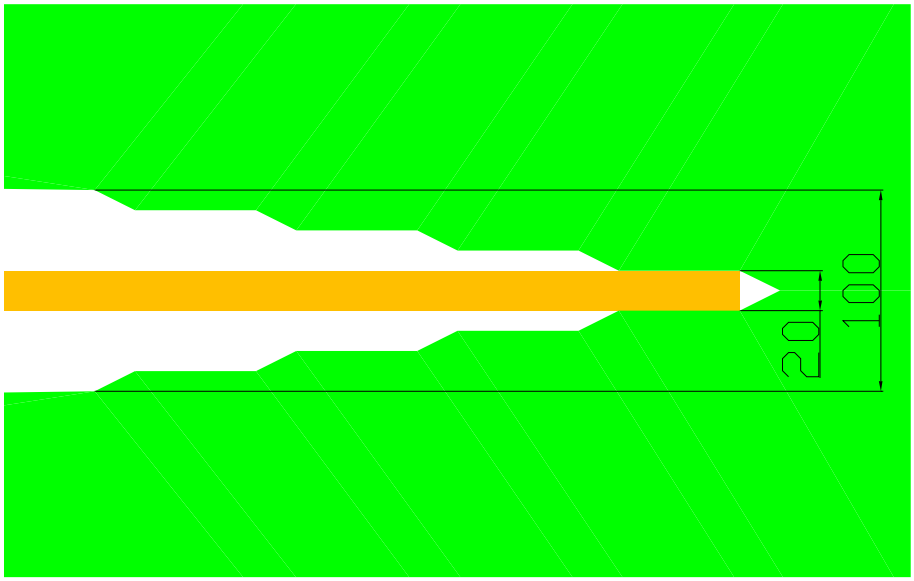

(b)

Fig. A.4: Assembled photomasks for a single device (A) and enlarge view of the electrode tip (B) of the needle device

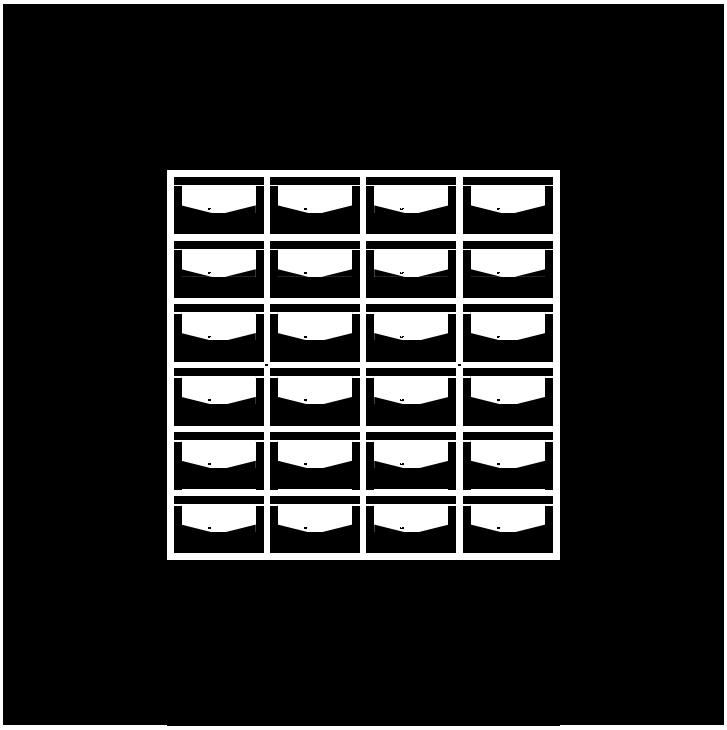

(a)

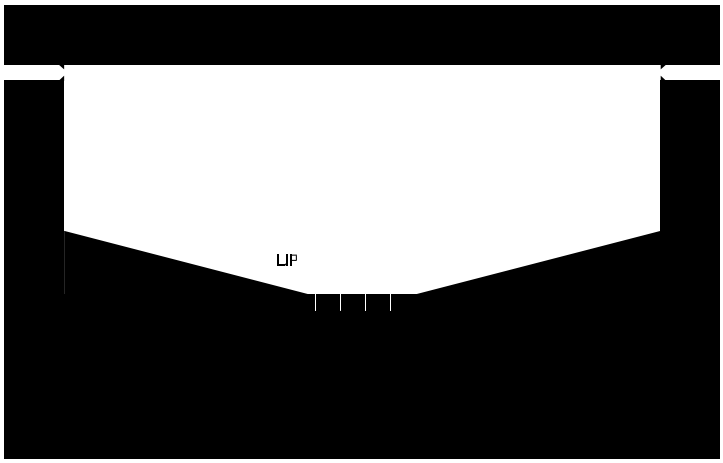

(b)

Fig. A.5: Photomask for the SU8 substrate layer of the multishank array

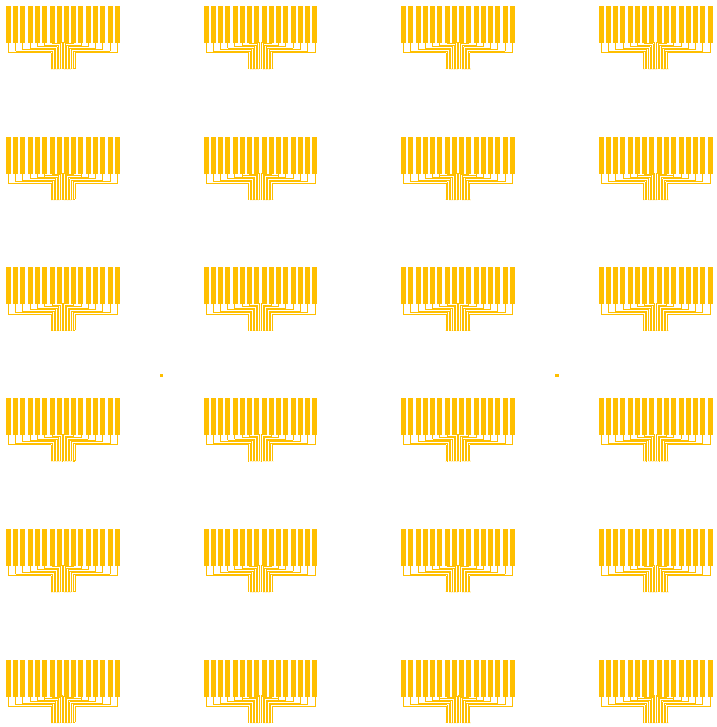

(a)

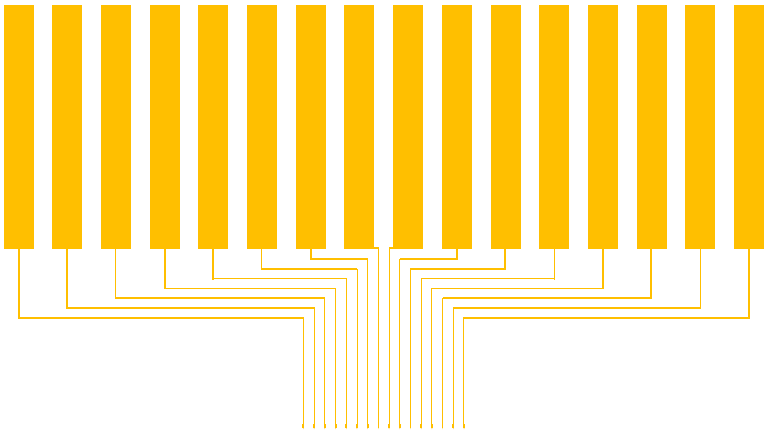

(b)

Fig. A.6: Photomask for the gold electrode layer of the multishank array

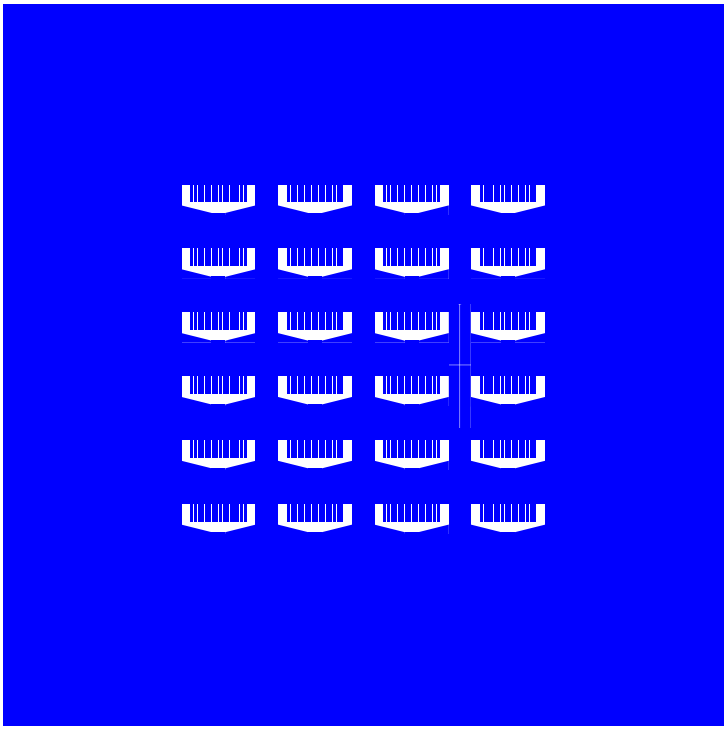

(a)

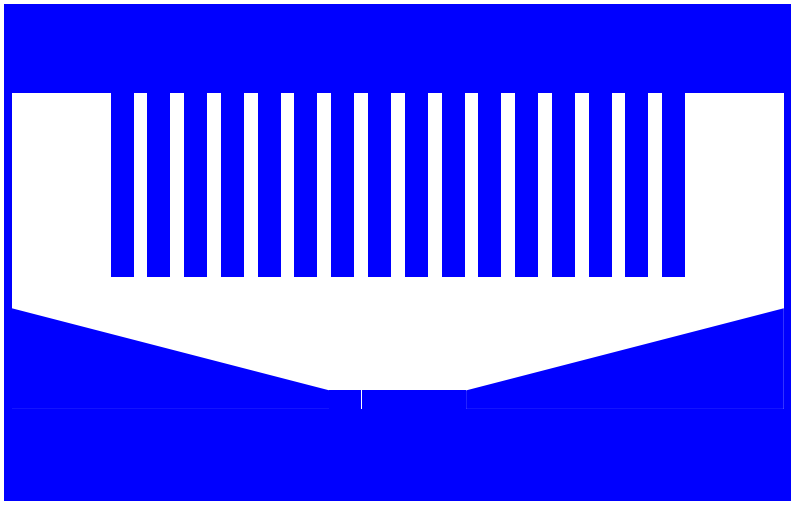

(b)

Fig. A.7: Photomask for the SU8 insulation layer of the multishank array

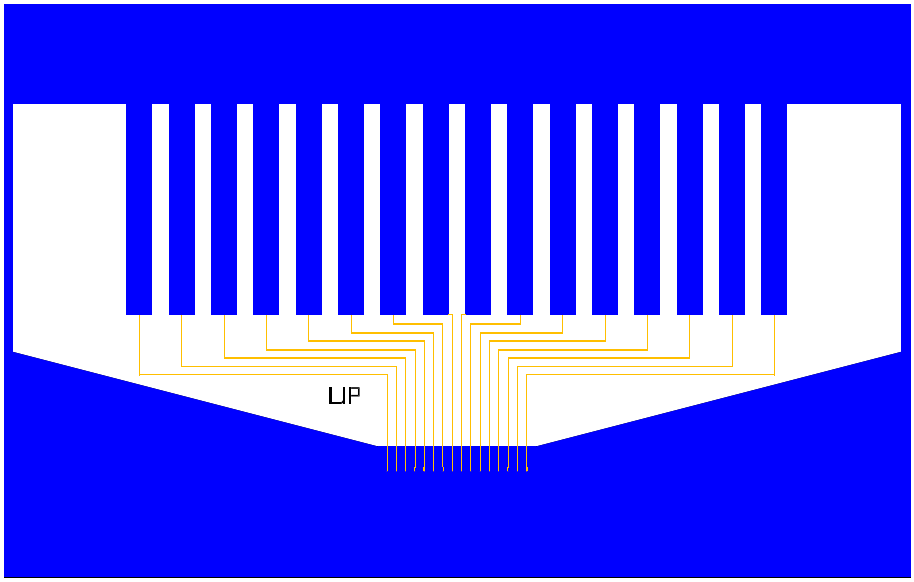

(a)

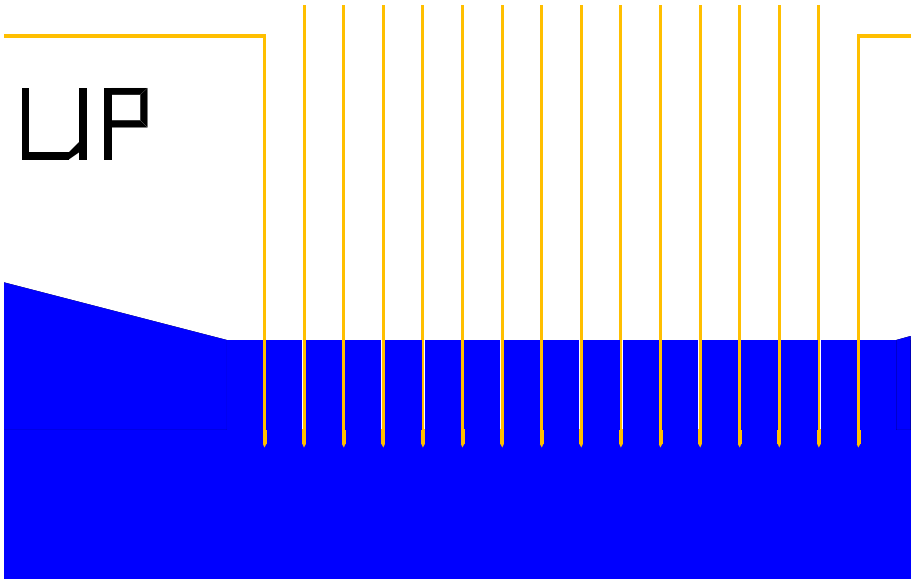

(b)

Fig. A.8: Assembled photomasks for a single device (A) and enlarge view of the electrode tip (B) of the multishank array

B. PROCESS RECIPES

B.1 Resist processing

SU8 2002

1. Spin at 500 rpm for 10 sec then increase to 3000 rpm for 30 sec
2. Soft bake on hotplate at 65° for 30 sec followed by 95° for 1 min
3. Expose for 55 sec in Karl Suess MJB3 mask aligner
4. Post bake on hotplate at 65° for 1 min followed by 95° for 2 min
5. Develop in EC solvent for 1 min followed by IPA rinse and deionised (DI) water
6. Hard bake on hotplate at 200° for 10 min

SU8 2010

1. Spin at 500 rpm for 10 sec then increase to 3000-4000 rpm for 30 sec
2. Soft bake on hotplate at 65° for 1 min followed by 95° for 3 min
3. Expose for 120 sec in Karl Suess MJB3 mask aligner
4. Post bake on hotplate at 65° for 1 min followed by 95° for 4 min
5. Develop in EC solvent for 4 min followed by IPA rinse and DI water
6. Hard bake on hotplate at 200° for 10 min

S1813

1. Spin at 500 rpm for 10 sec then increase to 2000 rpm for 30 sec
2. Soft bake on hotplate at 120° for 1 min
3. Expose for 12 sec in Karl Suess MJB3 mask aligner
4. Develop in MF319 developer for 1 min followed by DI water rinse

SPR220-7.0

1. Spin at 500 rpm for 10 sec then increase to 6000 rpm for 30 sec
2. Soft bake on hotplate using a 30 sec ramp in temperature to 115° and then bake for 90 sec
3. Expose for 50 sec in Karl Suess MJB3 mask aligner and let it rest for 30 min before development
4. Develop in MF-26 developer for 3 min followed by DI water rinse

B.2 Etch recipes

Bosch

- Strike Step
  - 20 sccm SF_6
  - 50 sccm C_4F_8
  - pressure 10 mTorr
  - 300 W ICP power
  - 45 W RF power
  - temperature 20 °C
  - backside helium 15 Torr

  - time 5 sec

- Deposition Step
  - 1 sccm SF_6
  - 100 sccm C_4F_8
  - pressure 25 mTorr
  - 200 W ICP power
  - 10 W RF power
  - temperature 20 °C
  - backside helium 15 Torr
  - time 5 sec

- Etch Step
  - 100 sccm SF_6
  - 1 sccm C_4F_8
  - pressure 30 mTorr
  - 200 W ICP power
  - 30 W RF power
  - temperature 20 °C
  - backside helium 15 Torr
  - time 12 sec

Polyimide etching

Sufficient cooling is necessary for polyimide etching so the temperature was set to the minimum of 1 °C.

- Strike Step
  - 100 sccm O_2
  - pressure 10 mTorr
  - 0 W ICP power
  - 100 W RF power
  - temperature 1 °C
  - backside helium 15 Torr
  - time 10 sec
- Etch Step
  - 30 sccm O_2
  - pressure 10 mTorr
  - 0 W ICP power
  - 100 W RF power
  - temperature 1 °C
  - backside helium 15 Torr

Silicon etching

- Strike Step
  - 1 sccm SF_6
  - 50 sccm C_4F_8
  - pressure 15 mTorr
  - 300 W ICP power
  - 50 W RF power

  - temperature 10 °C
  - backside helium 10 Torr
  - time 5 sec

- Etch Step
  - 20 sccm SF_6
  - 30 sccm C_4F_8
  - pressure 15 mTorr
  - 220 W ICP power
  - 20 W RF power
  - temperature 10 °C
  - backside helium 10 Torr

Sphere etching

- Strike Step
  - 100 sccm O_2
  - pressure 10 mTorr
  - 0 W ICP power
  - 100 W RF power
  - temperature 20 °C
  - backside helium 10 Torr
  - time 7 sec

- Etch Step
  - 30 sccm O_2

- pressure 10 mTorr
- 0 W ICP power
- 100 W RF power
- temperature 20 °C
- backside helium 10 Torr
- time 10 sec - 1 min

C. PUBLICATION PLAN

- published: Andreas Frommhold, Edward Tarte, "Modification of the electrical characteristics of the interface electrode to nervous tissue by Nanopatterning", Sensor Letters, Vol. 8, No. 3, pp. 470-475, June 20102
- submitted: Andreas Frommhold, Edward Tarte, "Effect of film structure on the electrochemical properties of gold electrodes for neural implants", Electro-chimica Acta
- in preparation: paper describing the silicon and polyimide nanopillar process

BIBLIOGRAPHY

[1] L.R. Hochberg, M.D. Serruya, G.M. Friehs, J.A. Mukand, M. Saleh, A.H. Caplan, A. Branner, D. Chen, R.D. Penn, and J.P. Donoghue. Neuronal ensemble control of prosthetic devices by a human with tetraplegia. *Nature*, 442(7099):164–171, 2006.

[2] Associated Press. Man controlled robotic hand with thoughts, 2009.

[3] E. Zrenner, R. Wilke, H. Sachs, K. Bartz-Schmitdt, F. Gekeler, D. Besch, U. Greppmaier, A. Harscher, T. Peters, G. Wrobel, B. Wilhelm, A. Bruckmann, and A. Stett. Visual sensations mediated by subretinal microelectrode arrays implanted into blind retinitis pigmentosa patients. In *Proceedings of the 13th Annual Conference of the IFESS*, pages 218–220, 2008.

[4] A. Branner, R.B. Stein, and R.A. Normann. Selective stimulation of cat sciatic nerve using an array of varying-length microelectrodes. *Journal of Neurophysiology*, 85(4):1585–1594, 2001.

[5] K. Najafi, J. Ji, and K.D. Wise. Scaling limitations of silicon multichannel recording probes. *IEEE Transactions on Biomedical Engineering*, 37(1):1–11, 1990.

[6] K.E. Jones, P.K. Campbell, R.A. Normann, K.W. Horch, and R.B. Huber. A glass/silicon composite intracortical electrode array. *Annals of Biomedical Engineering*, 20(4):423Ű437, 1992.

[7] K. Najafi, K. Wise, and T. Mochizuki. A high-yield ic-compatible multichannel recording array. *IEEE Transactions on Electron Devices*, 32(7):1206–1211, 1985.

[8] R.B. Stein, D. Charles, L. Davis, J. Jhamandas, A. Mannard, and T.R. Nichols. Principles underlying new methods for chronic neural recording. *Canadian Journal of Neurological Sience*, 2(3):235–244, 1975.

[9] X. Navarro, S. Calvet, F.J. Rodríguez, T. Stieglitz, C. Blau, M. Butí, E. Valderrama, and J.U. Meyer. Stimulation and recording from regenerated peripheral nerves through polyimide sieve electrodes. *Journal of the Peripheral nervous System*, 2:91–101, 1998.

[10] S. Benmerah, S.P. Lacour, and E. Tarte. Design and fabrication of neural implant with thick microchannels based on flexible polymeric materials. *Conference Proccedings of the IEEE Engineering in Medicine and Biology Society*, 2009:6400–3, 2009.

[11] J.J. FitzGerald, S.P. Lacour, S.B. McMahon, and J.W. Fawcett. Microchannels as axonal amplifiers. *IEEE TRANSACTIONS ON BIOMEDICAL ENGINEERING*, 2008.

[12] J. Malmivuo and R. Plonsey. *Bioelectromagnetism*. Oxford University Press, 1st edition edition, 1995.

[13] E.R. Kandel, J.H. Schwartz, and T.M. Jessel. *Essentials of neural science and behavior*. Appleton and Lange, 1995.

[14] G.M. Shepherd. *Foundations of the neuron doctrine*. Oxford University Press, 1991.

[15] A.L. Hodgkin and A.F. Huxley. A quantitive description of membrane current and its application to conduction and excitation in nerve. *Journal of Physiology*, 117:500–544, 2010.

[16] www.mathworks.com.

[17] Sonny Martin. Modelling of the neuron/electrode interface. Master's thesis, University of Cambridge, 2003.

[18] W. Penfield and T. Rasmussen. *The Cerebral Cortex of Man: A Clinical Study of Localization of Function*. Macmillian, 1950.

[19] S.E. Mackinnon and A.L. Dellon. *Surgery of the Peripheral Nerve*. Thieme Medical Publishers, 1988.

[20] J.O'M. Bockris and A.N. Reddy. *Modern Electrochemistry*. Plenum, 1970.

[21] A.J. Bard and L.R. Faulkner. *Electrochemical Methods*. John Wiley and Sons, 1980.

[22] A. C. Fischer. *Electrode Dynamics*. Oxford University Press, 1996.

[23] Gregory T.A. Kovacs. *Technology Development For A Chronic Neural Interface*. PhD thesis, Stanford University, 1990.

[24] D.A. Robinson. The electrical properties of metal microelectrodes. *Proceedings of the IEEE*, 56(6):1065–1071, 1968.

[25] R.S.C. Cobbold. *Transducers for Biomedical Measurements: Principles and Applications*. John Wiley and Sons, 1974.

[26] D.R. Lide. *CRC Handbook of Chemistry and Physics*. CRC Press, 2002.

[27] J. Newman. Resistance for flow of current to a disk. *Journal of the Electrochemical Society*, 113(5):501–502, 1966.

[28] C.D. Ferris. *Introduction to Bioelectrodes*. Plenum Press London, 1974.

[29] C.A. Marrese. Preparation of strongly adherent platinum black coatings. *Analytical Chemistry*, 59(1):217–218, 1987.

[30] K.W. Horch and G.S. Dhillon. *Neuroprosthetics - Theory and Practice*. World Scientific Singapore, 2004.

[31] E.T. McAdams, A. Lackermeier, J.A. McLaughlin, and D. Macken. The linear and non-linear electrical properties of the electrode-electrolyte interface. *Biosensors and Bioelectronics*, 10:67–74, 1995.

[32] J.D. Weiland and D.J. Anderson. Chronic neural stimulation with thin-film, iridium oxide electrodes. *IEEE TRANSACTIONS ON BIOMEDICAL ENGINEERING*, 47(7):911–918, 2000.

[33] A. Blau, Ch. Ziegler, M. Heyer, F. Endres, G. Schwitzgebel, T. Matthies, T. Stieglitz, J.U. Meyer, and W. Goepel. Characterization and optimization of microelectrode arrays for in vivo nerve signal recording and stimulation. *Biosensors and Bioelectronics*, 12(9):883–892, 1997.

[34] S.C. Mailley, M. Hyland, P. Mailley, J.M. Mc Laughlin, and E.T. McAdams. Electrochemical and structural characterizations of electrodeposited iridium oxide thin-film electrodes applied to neurostimulating electrical signal. *Material Science and Engineering C*, 21:167–175, 2002.

[35] S.F. Cogan, A.A. Guzelian, W.F. Agnew, T.G.H. Yuen, and D.B. McCreery. Over-pulsing degrades activated iridium oxide films used for intracortical neural stimulation. *Journal of Neuroscience Methods*, 137:141–150, 2004.

[36] M. Janders, U. Egert, M. Stelzle, and W. Nisch. Novel thin film titanium nitride microelectrodes with excellent charge transfer capability for cell stimulation and sensing applications. In *18th Annual Conference of the IEEE Engineering in Medicine and Biology Society*, pages 245–247, 1996.

[37] J.D. Weiland, D.J. Anderson, and M.S. Humayun. In vitro electrical properties for iridium oxide versus titanium nitride stimulating electrodes. *IEEE TRANSACTIONS ON BIOMEDICAL ENGINEERING*, 49(12):1574–1579, 2002.

[38] N.K. Guimard, N. Gomez, and C.E. Schmidt. Conducting polymers in biomedical engineering. *Progress In Polymer Science*, 32:876–921, 2007.

[39] X. Cui, J.F. Hetke, J.A. Wiler, D.J. Anderson, and D.C. Martin. Electrochemical deposition and characterization of conducting polymer polypyrrole/pss on multichannel neural probes. *Sensors and Actuators A*, 93:8–18, 2001.

[40] X. Cui and D.C. Martin. Electrochemical deposition and characterization of poly(3,4-ethylenedioxythiophene) on neural microelectrode arrays. *Sensors and Actuators B*, 89:92–102, 2003.

[41] M.R. Abidian and D.C. Martin. Experimental and theoretical characterization of implantable neural microelectrodes modified with conducting polymer nanotubes. *Biomaterials*, 29:1273–1283, 2008.

[42] X. Cui and D.D. Zhou. Poly(3,4-ethylenedioxythiophene) for chronic neural stimulation. *IEEE TRANSACTIONS ON NEURAL SYSTEMS AND REHABILITATION ENGINEERING*, 15(4):502–508, 2007.

[43] R.A. Green, L.A. Poole-Warren, and N.H. Lovell. Novel neural interface for vision prosthesis electrodes: Improving electrical and mechanical properties through layering. In *Proceedings of the 3rd International IEEE EMBS Conference on Neural Engineering*, volume 97-100, 2007.

[44] X. Cui, V.A. Lee, Y. Raphael, J.A. Wiler, J.F. Hetke, and D.J. Anderson. Surface modification of neural recording electrodes with conducting polymer/biomolecule blends. *Journal of Biomedical Materials Research*, 56(2):261–272, 2001.

[45] R. Wadhwa, C.F. Lagenaur, and X. Cui. Electrochemically controlled release of dexamethasone from conducting polymer polypyrrole coated electrode. *Journal of Controlled Release*, 110:531–541, 2006.

[46] R.A. Green, N.H. Lovell, G.G. Wallace, and L.A. Poole-Warren. Conducting polymers for neural interfaces: Challenges in developing an effective long-term implant. *Biomaterials*, 29:3393–3399, 2008.

[47] K.A. Ludwig, J.D. Uram, J. Yang, D.C. Martin, and D.R. Kipke. Chronic neural recordings using silicon microelectrode arrays electrochemically deposited with a poly(3,4-ethylenedioxythiophene) (pedot) film. *Journal of Neural Engineering*, 3:59–70, 2006.

[48] M.R. Abidian, K.A. Ludwig, T.C. Marzullo, D.C. Martin, and D.R. Kipke. Interfacing conducting polymer nanotubes with the central nervous system: Chronic neural recording using poly(3,4-ethylenedioxythiophene) nanotubes. *Advanced Materials*, 21:3764–3770, 2009.

[49] T.D.B. Nguyen-Vu, H. Chen, A.M. Cassell, R. Andrews, M. Meyyappan, and J. Li. Vertically aligned carbon nanofiber arrays: An advance toward electrical-neural interfaces. *Small*, 2(1):89–94, 2006.

[50] T. Gabay, M. Ben-David, I. Kalifa, R. Sorkin, Z.R. Abrams, E. Ben-Jacob, and Y. Hanein. Electro-chemical and biological properties of carbon nanotube based multi-electrode arrays. *Nanotechnology*, 18:1–6, 2007.

[51] K. Wang, H.A. Fishman, H. Dai, and J.S. Harris. Neural stimulation with a carbon nanotube microelectrode array. *Nano Letters*, 6(9):2043–2048, 2006.

[52] J. Kolosnjaj, H. Szwarc, and F. Moussa. Toxicity studies of carbon nanotubes. In Warren C.W. Chan, editor, *Bio-Applications of Nanoparticles*. Springer, 2007.

[53] F. Tian, D. Cui, H. Schwarz, G.G. Estrada, and H. Kobayashi. Cytotoxicity of single-wall carbon nanotubes on human fibroplasts. *Toxicology in Vitro*, 20(7):1202–1212, 2006.

[54] C.W. Lam, J.T. James, R. McCluskey, and R.L. Hunter. Pulmonary toxicity of single-wall carbon nanotubes in mice 7 and 90 days after intratracheal instillation. *Toxicological Sciences*, 77:126–134, 2004.

[55] A.E. Porter, M. Gass, K. Muller, J.N. Skepper, P.A. Midgley, and M. Welland. Direct imaging of single-walled carbon nanotubes in cells. *Nature Nanotechnology*, 2(11):713–717, 2007.

[56] M. Hughes, G.Z. Chen, M.S.P. Shaffer, D.J. Fray, and A.H. Windle. Electrochemical capacitance of a nanoporous composite of carbon nanotubes and polypyrrole. *Chemistry of Materials*, 14:1610–1613, 2002.

[57] R.A. Green, C.M. Williams, N.H. Lovell, and L.A. Poole-Warren. Novel neural interface for implant electrodes: improving electroactivity of polypyrrole through mwnt incorporation. *Journal of Materials Science: Materials in Medicine*, 19:1625–1629, 2008.

[58] E. Jan, J.L. Hendricks, V. Husaini, S.M. Richardson-Burns, A. Sereno, D.C. Martin, and N.A. Kotov. Layered carbon nanotube-polyelectrolyte electrodes outperform traditional neural interface materials. *Nano Letters*, 9(12):4012–4018, 2009.

[59] M. Hyland, J.A. McLaughlin, D.M. Zhou, and E.T. McAdams. Surface modification of thin film gold electrodes for improved in vivo performance. *Analyst*, 121:705–709, 1996.

[60] E.T. Kim, J.M. Seo, S.J. Woo, J.A. Zhou, H. Chung, and S.J. Kim. Fabrication of pillar shaped electrode arrays for artificial retinal implants. *Sensors*, 8(9):5845–5856, 2008.

[61] H.B. Zhou, G. Li, X.N. Sun Z.H. Zhu, X.H. Lou, H. Zhang, T. Liang, Q.H. Jin, J.L. Zhao, and Q.S. Ren. Fabrication of pyramid-shaped three-dimensional flexible microelectrode array for improved neural interfacing. *Sensor Letters*, 7(1):102–109, 2009.

[62] K. Cheung, Y.K. Choi, T. Kubow, and L.P. Lee. Nanostructured electrodes for improved neural recording. *Material Research Society Symposium Proceedings*, 729, 2002.

[63] J.H. Kim, G. Kang, Y. Nam, and Y.K. Choi. Surface-modified microelectrode array with flake nanostructure for neural recording and stimulation. *Nanotechnology*, 21(8):1–8, 2010.

[64] E. Seker, Y. Berdichevsky, M.R. Begley, M.L. Reed, K.J. Staley, and M.L. Yarmush. The fabrication of low-impedance nanoporous gold multiple-electrode arrays for neural electrophysiology. *Nanotechnology*, 21(12):1–7, 2010.

[65] H. Yoon, D.C. Deshpande, V. Ramachandran, and V.K. Varadan. Aligned nanowire growth using lithography-assited bonding of a polycarbonate template for neural probe electrodes. *Nanotechnology*, 19(2):1–8, 2008.

[66] L. Leprince, A. Dogimont, D. Magnin, and S. Demoustier-Champagne. Dexamethasone electrically controlled release from polypyrrole-coated nanostructured electrodes. *Journal of Materials Science: Materials in Medicine*, 21:925–930, 2010.

[67] W.R. Hendren, A. Murphy, P. Evans, D. O'Connor, G.A. Wurtz, A.V. Zayats, R. Atkinson, and R.J. Pollard. Fabrication and optical properties of gold nanotube arrays. *Journal of Physics: Condensed Matter*, 20(36):1–5, 2008.

[68] R. Wiesendanger, M. Bode, M. Kleiber, M. Löhndorf, R. Pascal, A. Wadas, and D. Weiss. Magnetic nanostructures studied by scanning probe microscopy and spectroscopy. *Journal of Vacuum Science and Technology B*, 15(4):1330–1334, 1997.

[69] W.D. Dozier, K.P. Daly, R. Hu, C.E. Platt, and M.S. Wire. Fabrication of high-tc josephson effect devices by natural lithography. *IEEE Transactions on Magnetics*, 27(2):3223 – 3226, 1991.

[70] H. Fang, R. Zeller, and P.J. Stiles. Fabrication of quasi-zero-dimensional submicron dot array and capacitance spectroscopy in a gaas/algaas heterostructure. *Applied Physics Letters*, 55(14):1433–1435, 1989.

[71] M.C. Buncick, R.J. Warmack, and T.L. Ferrell. Optical absorbance of silver ellipsoidal particles. *Journal of the Optical Society of America B*, 4(6):927–933, 1987.

[72] E.A. Wachter, A.K. Moore, and J.W. Haas III. Fabrication of tailored needle substrates for surface-enhanced raman scattering. *Vibrational Spectroscopy*, 3(1):73–78, 1992.

[73] U.Ch. Fischer and H.P. Zingsheim. Submicroscopic pattern replication with visible light. *Journal of Vacuum Science and Technology*, 19(4):881–885, 1981.

[74] H. Deckman and J.H. Dunsmuir. Natural lithography. *Applied Physics Letters*, 41(4):377–379, 1982.

[75] J.C. Hulteen and R.P. Van Duyne. Nanosphere lithography: A materials general fabrication process for periodic particle array surfaces. *Journal of Vacuum Science and Technology A*, 13(3):1553–1558, 1995.

[76] N.D. Denkov, O.D. Velev, P.A. Kralchevsky, I.B. Ivanov, H. Yoshimura, and K. Nagayama. Mechanism of formation of two-dimensional crystals from latex particles on substrates. *Langmuir*, 8(12):3183–3190, 1992.

[77] P. Hanarp, D.S. Sutherland, J. Gold, and B. Kasemo. Control of nanoparticle film structure for colloidal lithography. *Colloids and Surfaces A*, 214(1-3):23–36, 2003.

[78] M. Giersig and P. Mulvaney. Preparation of ordered colloid monolayers by electrophoretic deposition. *Langmuir*, 9(12):3408–3413, 1993.

[79] A.S. Dimitrov and K. Nagayama. Continuous convective assembling of fine particles into two-dimensional arrays on solid surfaces. *Langmuir*, 12(5):1303–1311, 1996.

[80] B.G. Prevo and O.D. Velev. Controlled, rapid deposition of structured coatings from micro- and nanoparticle suspensions. *Langmuir*, 20(6):2099–2107, 2004.

[81] L.M. Goldenberg, J. Wagner, J. Stumpe, B.R. Paulke, and E. Görnitz. Simple method for the preparation of colloidal particle monolayers at the water/alkane interface. *Langmuir*, 18(14):5627–5629, 2002.

[82] L. Zhi-cheng, R. Wei-dong, J. Nan, R. Lu-quad, C. Qian, and Z. Bing. Fabrication of large-scale nanostructure by langmuir-blodgett technique. *Journal of Bionic Engineering*, 3:59–62, 2006.

[83] R. Micheletto, H. Fukuda, and M. Ohtsu. A simple method for the production of a two-dimensional ordered array of small latex particles. *Langmuir*, 11(9):3333–3336, 1995.

[84] M. Bale, A.J. Turner, and R.E. Palmer. Fabrication of ordered arrays of silicon nanopillars at selected sites. *Journal of Physiscs D*, 35(5):L11–L14, 2002.

[85] V. Ng, Y.V. Lee, B.T. Chen, and A.O. Adeyeye. Nanostructure array fabrication with temperature-controlled self-assembly techniques. *Nanotechnology*, 13(5):554–558, 2002.

[86] R.M. Ranade, S.S. Ang, and W.D. Brown. Reactive ion etching of thin gold films. *Journal of the Electrochemical Society*, 140(12):3676–3678, 1993.

[87] F.T. Aldridge. High speed anisotropic reactive ion etching of gold films. *Journal of the Electrochemical Society*, 142(5):1563–1565, 1995.

[88] T. Abe, Y.G. Hong, and M. Esashi. Highly selective reactive-ion etching using co/nh3/xe gases for microstructuring of au, pt, cu and 20% fe-ni. *Journal of Vacuum Science and Technology B*, 2010.

[89] K.R. Williams, K. Gupta, and M. Wasilik. Etch rates for micromachining processing - part ii. *Journal of Micromechanical Systems*, 12(6):761–778, 2003.

[90] J.L. Vossen. The preparation of substrates for film deposition using glow discharge techniques. *Journal of Physics E: Scientific Instruments*, 12:159–167, 1979.

[91] J. Turkevich, G. Garton, and P.C. Stevenson. The color of colloidal gold. *Journal of Colloid Science*, 9(Supplement 1):26–35, 1954.

[92] P. Moshayedi, L.F. Costa, A. Christ, S.P. Lacour, J. Fawcett, J. Guck, and K. Franze. Mechanosensitivity of astrocytes on optimized polyacrylamide gels analyzed by quantitative morphometry. *Journal of Physics: Condensed Matter*, 22(19):1–11, 2010.

[93] Dr Sarah Horswell. private communication, 2010.

[94] J.A. Thornton. High rate thick film growth. *Annual Review of Material Science*, 7:239–260, 1977.

[95] B.A. Movchan and A.V. Demchishin. Study of the structure and properties of thick vacuum condensates of nickel, titanium, tungsten, aluminium oxide and zirconium dioxide. *Physics of Metals and Metallography*, 28:83–90, 1969.

[96] K.W. Horch and G.S. Dhillon. *Neuroprosthetics - Theory and Practice*. World Scientific Singapore, 2004.

[97] G. Voskericiana, M.S. Shivea, R.S. Shawgoc, and H. von Recum. Biocompatibility and biofouling of mems drug delivery devices. *Biomaterials*, 24:1959Ű1967, 2003.

[98] Y. Xiang, T. Li, Zhigang Suo, and J.J Vlassak. High ductility of a metal film adherent on a polymer substrate. *Applied Physics Letters*, 87(16), 2005.

[99] S.P. Lacour, J.J. Fitzgerald, N. Lago, E. Tarte, S. McMahon, and J. Fawcett. Long microchannel electrode arrays: A novel type of regenerative peripheral nerve interface. *IEEE Transactions On Neural Systems And Rehabilitation Engineering*, 17(5):454–9, 2009.